UNIVERSITÀ
DEGLI STUDI
FIRENZE

DOTTORATO DI RICERCA IN
Energetica e Tecnologie Industriali ed Ambientali Innovative

CICLO XXX

COORDINATORE Prof. M. De Lucia

TOWARDS A UNIFIED APPROACH FOR LARGE EDDY SIMULATION OF TURBULENT SPRAY FLAMES

Settore Scientifico Disciplinare ING-IND/08

Dottorando
Dott. (*Puggelli Stefano*)
Stefano Puggelli
(firma)

Tutore
Prof. (*Facchini Bruno*)
(firma)

Coordinatore
Prof. (*De Lucia Maurizio*)
(firma)

Anni 2014/2017

Università degli Studi di Firenze
Scuola di Ingegneria
DIEF - Department of Industrial Engineering of Florence

PhD School: *Energetica e Tecnologie Industriali ed Ambientali Innovative*
Scientific Area: ING-IND/08 - *Macchine a Fluido*

Towards a unified approach for Large Eddy Simulation of turbulent spray flames.

JOINT RESEARCH DOCTORAL THESIS WITH THE UNIVERSITY OF ROUEN (FR)

PhD Candidate: Ing. Stefano Puggelli

Tutor: Prof. Ing. Bruno Facchini
Academic Supervisor: Dr. Ing. Antonio Andreini
Academic Supervisor: Prof. F.X. Demoulin
PhD School Coordinator: Prof. Ing. Maurizio De Lucia

XXX PhD School Cycle - 2014-2017

Acknowledgements

At the conclusion of a journey, it is normal to find yourself thinking about all the people who have contributed to the achievement of such an important goal. These few lines are certainly not sufficient to express my deep gratitude for you all.
First of all, I would like to thank Prof. Bruno Facchini for this growth opportunity, not only professionally, but also and foremost on a personal level.
My sincere thanks go also to Dott. Ing. Antonio Andreini for his continuous supervision. My achievements would have been unattainable without his help and patience.
I would like to thank Prof. F.X. Demoulin as well, for welcoming me at CORIA and for all the ideas/help/support has given me during this thesis. It has been great to share this work with you.
Many thanks and my warmest regards to my former colleagues: Lorenzo W., Tommaso and Lorenzo M. (without your help and patience this result would have not been possible). A special thanks to Andrea ("the best guy in England"), a continuous source of inspiration.
A special thanks also to my colleagues at UniFI, especially Davide (how many works together!.... A major part of this thesis is the result of our endless discussions), Sabrina, Daniele, Andrea, Dominique, Lorenzo (one of the most pleasant surprises in Rouen and a right-hand man during the last year), Simone, Carlo, Matteo as well as all the experimental guys Lorenzo, Tommaso, Daniele, Alessio and Riccardo.
My warmest thanks to all the CORIA guys: Antonio and Silvia (my second family in Rouen), Andres, Manuel, Felix, Javier, Aqeel, Romain, Fred, Lila and all the other guys who helped me in living a great experience. I apologize for my bad french!
Finally, I would like to thank my whole family for believing and for supporting me in all my choices. If I have been able to arrive here, I owe it to you all.

Quando ti infili in una galleria oscura, arriva il momento in cui non hai più fiato per tornare indietro. La tua unica possibilità è continuare a nuotare verso l'ignoto.... e pregare che ci sia un'uscita.
Dan Brown

When swimming into a dark tunnel, there arrives a point of no return when you no longer have enough breath to double back. Your choice is to swim forward into the unknown....and pray for an exit.
Dan Brown

Abstract

The recent limitations imposed by ICAO-CAEP, regulating NO_x emissions, are leading to the implementation of lean burn concept in the aero-engine framework. From a design perspective, a depth insight on lean burn combustion is required and Computational Fluid Dynamics (CFD) can be a useful tool for this purpose. Several interacting phenomena are involved and various modelling strategies, with huge differences in terms of computational costs, are available. Nevertheless, up to now few numerical tools are able to account for the effects of liquid fuel preparation inside reactive computations. Spray boundary conditions are normally determined thanks to correlative approaches that are not able to cover the wide range of operating conditions and geometrical characteristics of aero-engine burners. However, as highlighted in the first part of the dissertation, where several literature test cases are analysed through numerical calculations, the impact of liquid preparation can be extremely important. Considerations based on correlative approaches may be therefore unreliable. More trustworthy predictive methods focused on fuel atomization are required.

This research activity is therefore aimed at developing a general numerical tool, to be used in an industrial design process, capable of modelling the liquid phase from its injection till the generation of a dispersed spray subject to evaporation. The ELSA (Eulerian Lagrangian Spray Atomization) model, which is based on an Eulerian approach in the dense region and a Lagrangian one in the dilute zone, has been chosen to this end. The solver is able to deal with pure liquid up to the generation of a dispersed phase and to account for the breakup process through the introduction of the liquid-gas interface density.

However, several limitations of such method arise considering its application in a highly swirled reactive environment like an aero-engine burner. Therefore, particular attention has been here devoted first to the study of the turbulent liquid flux term, inside the liquid volume fraction equation.

This quantity is of paramount importance for a swirled flow-field, with high slip velocities between phases. A completely innovative modelling framework together with a new second order closure for this variable is proposed and validated on a literature jet in crossflow test case. Then, to handle a reactive environment, a novel evaporation model is integrated in the code and assessed against experimental results. Finally, an alternative way to derive the Drop Size Distribution (DSD) in ELSA context for the lagrangian injection is presented and assessed by means of Direct Numerical Simulations.
Ultimately, this work introduces an innovative framework towards a unified description of spray combustion in CFD investigations. The proposed approach should lead to a comprehensive description of fuel evolution in the injector region and to a proper characterization of the subsequent reacting flow-field. Several improvable aspects are also highlighted, pointing the way for further enhancements.

Contents

Nomenclature

c	Normalized reaction progress variable	$[-]$
C_a	Area coefficient	$[-]$
C_d	Drag coefficient	$[-]$
c_p	Spec. heat capacity at const. pressure	$[J/(kgK)]$
D	Reference diameter	$[m]$
d	Droplet diameter	$[m]$
	Diameter	$[m]$
E	Efficiency function	$[-]$
F	Thickening factor	$[-]$
FAR	Fuel to air ratio	$[-]$
G	Gauss curvature	$[-]$
g	Gibbs function	$[J/kg]$
H	Mean curvature	$[-]$
h/HTC	Heat Transfer Coefficient	$[W/(m^2K)]$
k	Turbulence kinetic energy	$[m^2/s^2]$
k	Heat conductivity	$[W/(mK)]$
L	Length	$[m]$
Le	Lewis Number	$[-]$
m	Mass flow rate	$[kg/s]$
M	Pope criterion	$[-]$
Nu	Nusselt number	$[-]$
Oh	Ohnesorge number	$[-]$
P	Pressure	$[Pa]$
Pr	Prandtl number	$[-]$
q	Momentum Flux Ratio	$[-]$
q	Spread parameter	$[-]$
R	Density Ratio	$[-]$
Re	Reynolds number	$[-]$
S_N	Swirl number	$[-]$
Sc	Schmidt number	$[-]$
Sh	Sherwood number	$[-]$
St	Stokes number	$[-]$
SMD	Sauter Mean Diamter	$[-]$
T	Temperature	$[K]$
t	Time	$[s]$
U/u	Velocity	$[m/s]$

Y	Mass Fraction	$[-]$
Y_c	Un-normalized Reaction Progress Variable	$[-]$
We	Weber Number	$[-]$
y^+	Non-dimensional wall distance	$[-]$
Ω	Flame sensor function	$[-]$
Z	Mixture Fraction	$[-]$

Acronyms

$ACARE$	Advisory Council for Aeronautics Research in Europe
ATF	Artificially Thickened Flame
BCs	Boundary Conditions
$CAEP$	Committee on Aviation Environmental Protection
CFD	Computational Fluid Dynamics
CFL	Courant-Friedrichs-Lewy
CMC	Conditional Moment Closure
DSD	Droplet Size Distribution
DNS	Direct Numerical Simulation
ECN	Engine Combustion Network
EDM	Eddy Dissipation Model
EE	Eulerian-Eulerian
EL	Eulerian-Lagrangian
$ELSA$	Eulerian Lagrangian Spray Atomization
FGM	Flamelet Generated Manifold
FTT	Flow Through Time
GIS	Grid Induced Separation
$ICAO$	International Civil Aviation Organization
ICM	Interface Capturing Method
IRZ	Inner Recirculation Zone
JCF	Jet in Cross-Flow
LDA	Laser Doppler Anemometry
LDV	Laser Doppler Velocimetry
LES	Large-Eddy Simulation
LPP	Lean Premixed Prevaporized
NDF	Number Density Function
ORZ	Outer recirculation zone
PDA	Probability Doppler Anemometry
PDF	Probability Density Function
$PLIF$	Planar Laser Induced Fluorescence
$PERM$	Partial Evaporation Rapid Mixing
PIV	Particle Image Velocimetry
QME	Quasi Multiphase Eulerian
$RANS$	Reynolds Averaged Navier-Stokes
RMS	Root Mean Square
RQL	Rich-Quench-Lean
SAS	Scale Adaptive Simulation
SGS	Sub-Grid Scale

SMD	Sauter Mean Diameter
SCD	Surface Curvature Distribution
SST	Shear Stress Transport
$TAPS$	Twin Annular Premix System
$URANS$	Unsteady RANS
VOF	Volume Of Fluid
VDF	Volume Density Function

Greeks

α_l	Liquid Volume Fraction	$[-]$
ρ	Density	$[kg/m^3]$
σ	Surface tension	$[N/m]$
Σ	Liquid-gas interface density per unit of volume	$[m^{-1}]$
$\Sigma^{'}$	Sub-grid liquid-gas interface density per unit of volume	$[m^{-1}]$
μ	Dynamic viscosity	$[Pa\ s]$
ν	Kinematic viscosity	$[m^2/s]$
κ	Principal surface curvatures	$[m^{-1}]$
ω	Turbulence eddy frequency	$[s^{-1}]$
R_{α_l}	Turbulent liquid flux	$[m/s]$
Δ	Spacing	$[m]$
Φ	Equivalence Ratio	$[-]$
Φ_D	Turbulent liquid flux due to drift	$[m/s]$
τ	Time step	$[s]$
τ_P	Dynamic Relaxation Time	$[s]$
Θ	Flame Index	$[-]$
	Injection angle	$[^\circ]$
Υ_s	Turbulent liquid flux due to slip	$[m/s]$
χ	Molar Fraction	$[-]$

Subscripts

0	Initial Value
d	Droplet
eq	Equilibrium Value
g	Gas-phase
in	Inlet
l	Liquid-phase
lag	Lagrangian Value
$mean$	Mean Value
jet	Jet
P	Particle
ref	Reference Value
v	Vapour-phase

Miscellaneous

$(\tilde{\bullet})$	Favre-averaged and Favre-filtered quantity
$(\bar{\bullet})$	Reynolds-averaged and Reynolds-filtered quantity

Introduction

The increasing demand of aeronautic transportation for civil purpose led over the last years to several research efforts devoted to the reduction of the environmental effects of aviation. The global jet fleet is projected to double in size within 2036 [1] and strong attention has to be focused to the request of a greener transportation. This is confirmed by the most recent ICAO-CAEP standards and ACARE 2050 objectives, which set a reduction of 75% of CO_2 and 90% of NO_x per passenger kilometre as a challenging goal for 2050.

Up to now, the Rich Quench Lean (RQL) technology represents the state of the art in aero-engines (see Figure 1). In this concept, a rich burning primary region is generated to ensure the flame stability. Then, a rapid mixing takes place and finally a lean zone is created to burn out smoke. In this way, NO_x levels are controlled. Clearly, the mixing region is essential from a design perspective since stoichiometric conditions can locally appear with a huge production of pollutants. The transition of the equivalence ratio towards the dilution zone has to be carefully chosen in order to reduce CO, UHC and soot levels, which can be very high in the primary region. Starting from this concept, several advanced RQL configurations have been designed. A reduction of the residence time inside the combustor, the use of more advanced injection strategies together with a more rapid air-jet mixing have been realized to achieve a drastic reduction of NO_x, without compromising the operability and the manufacturing technology. In this manner, the Pratt & Whitney TALON X (Technology for Advanced Low NO_x) combustor is able to cut down emission levels below 55% with respect to CAEP/6 standards.

Nevertheless, even if some potential improvements should be still expected from the RQL technology, the more and more stringent regulations pushed towards the development of alternative burning concepts, such as *lean combustion*. Here, the burner operates with an excess of air to significantly lower the flame temperature (e.g. up to 70% of total combustor air flow

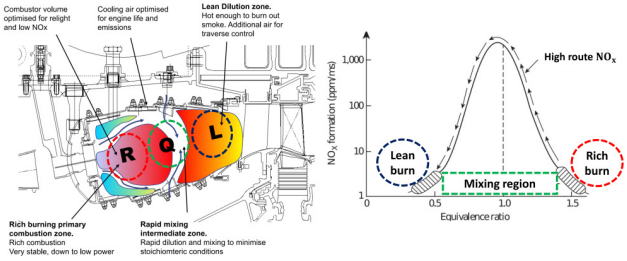

Figure 1: RQL concept together with NO_x formation rate as a function of the equivalence ratio (adapted from http://www.newac.eu and [2]).

has to be premixed with the fuel). An explicative comparison between RQL and lean combustor in terms of air splitting, as well as generated flow field, is shown in Figure 2. The burner equivalence ratio is controlled all along the reacting flow-field to ensure low levels of CO and NO_x.
The development of lean combustion in the aero-engine framework is a long-time history started with fuel-staging. Dual Annular Combustors (DAC) employed this strategy and were designed with a pilot stage in the outer annulus and a main stage in the inner one. However, several issues related to the uniformity of the exit temperature profile during staging conditions, as well as CO and UHC emission levels, limited the application of this kind of technology.
Therefore, all the engine manufacturers focused the attention on Single Staged Combustors. One of the most relevant examples in this context is surely the GE-TAPS (Twin Annular Premixing Swirler), which currently represents the only lean burn combustion system employed on a certified

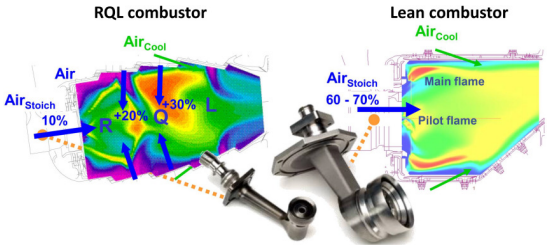

Figure 2: Comparison between Rich Quench Lean (RQL) design and a lean combustor (adapted from [3]).

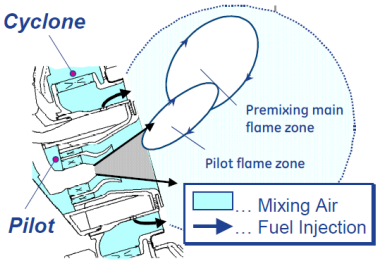

Figure 3: TAPS internally staged fuel injector concept [4].

aircraft engine (GEnx family). Figure 3 shows a schematic representation of this configuration, which is based on an internally staged pilot injector with a lean direct multi-point injection for the main stage operation. The pilot is a pressure atomizer surrounded by two co-rotating swirlers, whereas the main mixer consists of a radial inflow swirler (cyclone) and a cavity where the fuel is injected through a series of transverse jets [4, 5]. At low power conditions, a rich burn configuration takes place, whereas at higher power almost the 70% of air passes through the swirler leading to a lean burning mode [4, 5]. Recently, the TAPS II configuration has been developed leading to an additional reduction of emission levels (see [6] for further information). The improvements achieved in terms of NO_x using this technology with respect to RQL are clearly shown in Figure 4.

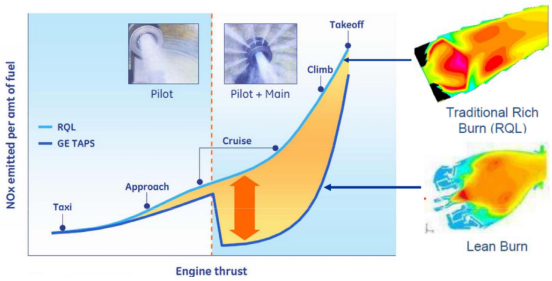

Figure 4: NO_x emission levels between conventional RQL and TAPS combustor[4]).

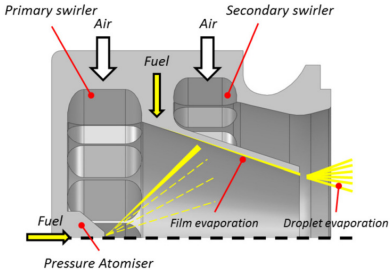

Figure 5: PERM functioning concept [9].

Several other interesting injector configurations have been as well proposed in the lean combustion framework. As an alternative to the mentioned discrete jets atomization process, a common approach is to adopt liquid film breakup by means of prefilming airblast atomizers. An interesting solution, which employs this concept, is the so-called PERM (*Partially Evaporating and Rapid Mixing*) injection system developed by GE Avio Aero [7, 8]. The injector is a double swirler airblast atomizer designed in order to achieve partial evaporation inside the inner duct and rapid mixing within the combustor. In this manner, the location and the stability of the flame is optimized as sketched in Figure 5. A film of fuel is generated over the inner surface of the lip that separates the two swirled flows. As the film reaches the edge of the lip, through the action of the gas flow, primary atomization occurs: fine droplets and rapid mixing are promoted by the two co-rotating swirled flows generated by the double swirler configuration. Furthermore, in order to ensure a stable operation of the flame, especially at low power conditions, the airblast injector is coupled with a hollow cone pressure atomizer. It is located at the centre of the primary swirler and generates a pilot flame in a configuration similar to a piloted airblast atomizer.
Nonetheless, beyond the specific adopted solution, from these observations it should be clear that one of the biggest challenges in lean devices is surely represented by the design of the injection system and how it affects the reacting flow-field.
In order to integrate information obtained by experimental campaigns in highly pressurized two-phase reactive environments, Computational Fluid Dynamics (CFD) has continuously gained importance for design scopes over the last years. It is worth mentioning that lean systems strongly suffer from the generation of large pressure fluctuations and thermoacustic

phenomena, so that numerical modelling is becoming a fundamental task to better understand these aspects. Typical industrial calculations are normally performed employing a RANS (Reynolds-Average Navier Stokes) approach, where only the mean flow is solved and turbulence effects are introduced by means of ad hoc models. However, considering the high level of unsteadiness and turbulence that normally characterize lean burn devices, they are not able or insufficient to represent the complexity under investigation. Therefore, computational techniques have been rapidly evolving towards scale resolving approaches, such as Large Eddy Simulation (LES) or hybrid RANS-LES models (i.e. Detached Eddy Simulation or Scale Adaptive Simulation), where the unsteady characteristics of spray flames can be clearly appreciated.
Nevertheless, albeit several works in technical literature are focused on detail investigations on lean spray flames, because of the lack of experimental data and of a comprehensive theory on liquid atomization, spray boundary conditions are normally determined by means of trial & error procedures or by using experimental correlations with a narrow range of application. This is normally not at all satisfactory in a design process since the uncertainty ascribed in this way in the prediction of the burner emissions is normally of the same order of magnitude of the expected improvements.
In this scenario, it looks quite evident that one major issues in the numerical simulation of lean-aero engine combustors is surely associated to the description of liquid fuel preparation and to the phenomena related to primary breakup. The development of advanced combustion models is clearly another essential research branch in this framework, but the spray, as shown in this dissertation, can deeply affect the reacting flow-field and strongly modify the whole combustion process.

Aim of the work

The main aim of the present research work has been the development of a unified computational framework for LES simulation of spray flames for lean burn aero-engine combustors. In particular, the attention here has been mainly focused on the modelling of liquid atomization, which represents a key aspect in the design of lean aero-engines. As will be clearer during the dissertation, standard Eulerian-Lagrangian or Eulerian-Eulerian models are not able to describe all the complexity associated with fuel atomization and therefore hybrid strategies have to be considered.
The Eulerian-Lagrangian Spray Atomization (ELSA) model has been chosen in the present research work. The solver, which analyses the two

phases as a single phase flow with huge density variations, beyond the equation for mixture momentum conservation, is essentially led by an equation for the liquid volume fraction and one for the liquid/gas interface density. In this way, the model is able to predict the liquid evolution and to evaluate the characteristic droplet diameter distribution without a priori assigning the carrier and the dispersed phase. In particular, the approach is based on an Eulerian technique in the dense spray region coupled with a Lagrangian tracking in the dispersed one.
The goal of the present study has been therefore the extension of the ELSA capabilities to the aeronautical context. The efforts have been mainly focused on the addition inside the solver of the most important interactions between liquid and gas, which can have a huge impact on fuel distribution inside the combustion chamber. A general tool capable of modelling the liquid phase from its injection up to the generation of a dispersed spray, subjected to evaporation, will be finally proposed as numerical method towards a unified analysis of spray combustion.
The work leading to the results presented in this dissertation was carried out in collaboration with the group "Atomisation et sprays" of the CORIA (COmplexe de Recherche Interprofessionnel en Aérothermochimie) research center, led by Prof. F.X. Demoulin, whose research activity is mainly devoted to the development of numerical models for the analysis of advanced injection systems. The proposal and validation of several advanced strategies to be included in the ELSA framework have been developed thanks to this tight collaboration.

Thesis outline

During this research activity, several aspects related to spray flames have been analysed through numerical calculations. The most important achievements shown in the following chapters are surely represented by the proposal of several novel closures in the ELSA context for its application in the aero-engine framework together with its validation on different literature test cases.
However, strong efforts have been as well devoted to deepen the knowledge on spray combustion and in particular on the impact of liquid phase modelling. Therefore, a detailed description of the state of the art in the analysis of spray flames is provided in the first part of the thesis through both a review of approaches already available in technical literature and a discussion of numerical results obtained by the author on a set of literature test cases. Such detailed introduction clearly highlights the limitations of actual numerical strategies for liquid phase modelling to

define spray boundary conditions (BCs). A huge dependency on liquid BCs, which can deeply affect the reliability of scale resolving techniques in an industrial framework, is pointed out. The lack of a general method to deal with atomization modelling is shown, justifying the research efforts then devoted to the development of ELSA.
The dissertation will be organized as described below.

Chapter 1: The most important aspects of the physics of spray combustion are here reviewed to better clarify the complexity that characterizes spray flames. An overview about numerical methods employed in this framework is as well reported in order to explain the background and the context in which this research activity has been performed.

Chapter 2: Several activities have been carried out in this study with the aim of enhancing the knowledge about the impact of liquid phase modelling on the reacting flow-field. In this chapter, three literature test cases in an increasing order of complexity are analysed to review the state of the art in the numerical analysis of spray combustion.
Different aspects in the study of liquid fuelled flames are investigated. The importance of a reliable method to determine spray boundary conditions with respect to the actual state of the art is highlighted. Such dependency justifies the research effort then focused on liquid atomization and on the development of the ELSA model that is proposed in the following chapters.

Chapter 3: This chapter is focused on a detailed introduction to the ELSA approach. The solver is thoroughly described both in its Eulerian-Eulerian and Eulerian-Lagrangian regions. The main limitations of the approach for its application in the aero-engine context are as well highlighted in order to justify the modelling efforts proposed in the present work.

Chapter 4: The development of an innovative second order closure for the *turbulent liquid flux* term inside the liquid volume fraction equation in ELSA is the main subject of this chapter. Such contribution is directly linked to the slip velocity between phases and it can have a huge impact in the aero-engine context. After a detailed overview about the limitations of gradient-based closures and a review of the state of the art on this topic, an innovative modelling framework and a novel transport equation are introduced and validated on a jet in crossflow test case.

Chapter 5: This chapter is devoted to the presentation of the approach

proposed to include evaporation in ELSA. The limitations of explicit methods are first shown. Then, an innovative model, based on the calculation of phase equilibrium, is proposed and validated using the experimental data from the Engine Combustion Network (ECN) database. This is a key step in the development of an approach able to account for all the phenomena going from the near injection region up to a dispersed spray since it represents the link between the liquid phase and the reacting flow-field.

Chapter 6: The proposition of a general framework to deal with the switching between the Eulerian region of ELSA with the Lagrangian one is the main goal of the present chapter. The innovative concept of surface curvatures to extract the Drop Size Distribution (DSD) is here introduced. The reliability of such proposal is then assessed on two numerical test cases thanks to data available from a set of two-phase Direct Numerical Simulations (DNS). A detailed analysis of the link between the curvatures evolution and the turbulence field is as well reported to justify the proposal of two completely novel transport equations for such geometrical variables.

In the last chapter, a summary of the main achievements of this research is given together with conclusions and recommendations for future works.

Chapter 1

Turbulent spray flames

The analysis of turbulent spray flames in the aero-engine context still represents one of the most challenging problems to be faced from a computational point of view. Several phenomena, normally characterized by different time and spatial scales, have to be accounted to achieve a correct prediction of the engine performances. Furthermore, beyond the aeronautical framework, a deep understanding in the evolution of spray flames is crucial in many other engineering applications such as internal combustion engines or marine motors.
After a brief introduction about the physics of spray combustion and the main interactions occurring in liquid fuelled flames, this chapter provides an overview about computational techniques employed in this context. Methods normally used to account for the presence of a liquid fuel in reactive computations are described with a particular focus on atomization and breakup.

1.1 Physics of turbulent spray flames

A very useful sketch to clearly appreciate the complexity of the physics involved in a turbulent spray flame is shown in Figure 1.1.
As explained in [10], single-phase combustion regime is represented by the first column of the picture (i.e. from gas turbulence up to combustion) since the mixing processes at macro and micro levels determine species mass fraction and combustion. As a feedback, the obtained reacting flow field affects the velocity distribution and enhances the micro mixing[10]. The remaining interactions shown in the figure are completely determined by the presence of a spray. For instance, gas phase turbulence defines the spray dispersion and therefore its evaporation, since the vaporization rate is directly influenced by the local temperature and vapour gradients, which are in turn function of the gas dispersion and micro-mixing. Evaporation can be further enhanced by radiative heat transfer and dispersed and continuous phases interact between each other with a fully two-way coupling[10]. This scenario is further complicated if liquid injection and atomization are included since additional physical scales have to be accounted.
Fuel injection aims at initiating spray formation and propagation to develop an air-fuel mixture to optimize engine performances under several operating conditions. In Figure 1.2, a simplified scheme of a spray plume

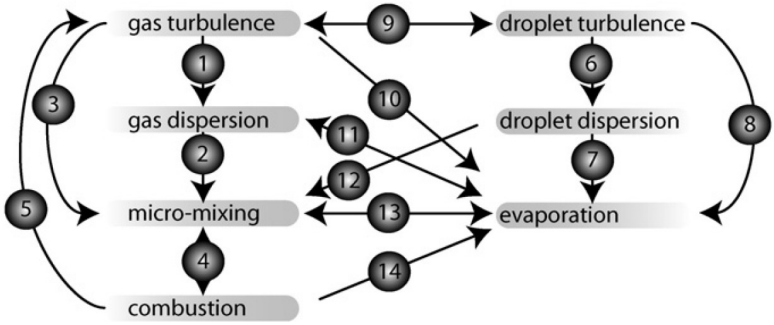

Figure 1.1: Sketch of different physical phenomena involved in spray combustion. Taken from [10].

is reported. In the near injection region, the liquid phase completely dominates over the air and it is progressively disintegrated into ligaments and droplets. Non-spherical liquid sheets are firstly generated and, at the end of such process, interactions previously shown in Figure 1.1 are recov-

ered. A detailed overview about the atomization process and numerical strategies employed for its modelling is provided in Chapter 3.
Nonetheless, it is clear that a broad range of time and length scales is involved in spray flames and, to accurately predict the performances of actual aero-engine combustors, all these phenomena should be taken into account.

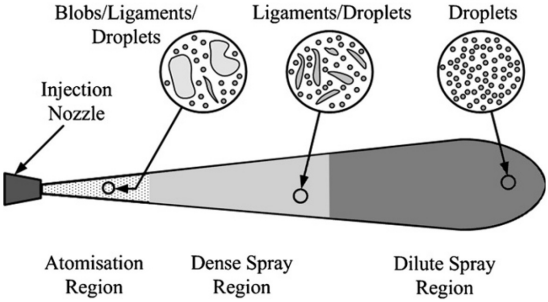

Figure 1.2: Scheme of a liquid spray. Taken from [11].

However, beyond atomization and injection steps, another important characteristic of spray flames is that evaporation and diffusion of fuel vapour into the surrounding phase precede chemical reactions between fuel and oxidizer. Therefore, characteristics of both premixed and diffusive burning modes can be observed [10]. As a matter of fact, the equivalence ratio varies continuously in space and time. The flame stabilization is led by both the generation of stoichiometric zones (i.e. diffusion like behaviour) and the heat exchange with flames already established in the neighbourhood (i.e. premixed like behaviour)[10]. The interactions between such complex chemical processes and the flow-field govern some local features of the flame such as the burning velocity in premixed zones and the extinction with the scalar dissipation rate in non-premixed regions [10].
Based on these observations, several classifications of spray combustion regimes have been proposed over the last years. A very crude distinction is the one originally introduced in [12] between homogeneous and heterogeneous combustion. In the first case, it is assumed that the spray completely evaporates before entering in the combustion chamber, where the flame is then generated. The fuel vapour mixes rapidly with the air and the liquid evaporation is not affected by the reacting flow field.

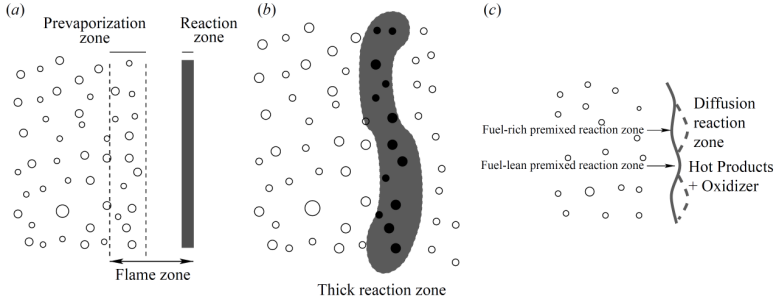

Figure 1.3: Laminar flame structures: prevaporized spray flame (a), thick flame (b) and back flame zone (c). Taken from [17].

In the latter case, droplet evaporation feeds a diffusion flame (namely *envelope flame*) around the particle. As discussed in [13], the presence of an envelope flame determines an enhancement of heat and mass transfer. Drops here act as a source of combustion products, while in the homogeneous asymptotic case they represent sources of fuel vapour. Chiu et al. [14, 15], considering a spherical domain filled with a hot oxidizer and fuel particles, developed group combustion models studying the position of the flame region with respect to each droplet and to the whole spray. Several combustion modes have been identified going from *single droplet combustion* (i.e. all droplets burn individually with a surrounding flame) to external sheath combustion, when clusters of drops are considered (i.e. all the spray is enclosed by the flame with a non-evaporating existing core). A group combustion number (G), depending on the total number of droplets as well as on their diameter and separation distance, is introduced to distinguish between these regimes.
Starting from this classification, in [16] further controlling parameters have been introduced such as the characteristic flame time and its thickness as well as the drops evaporation time (see Figure 1.3). If evaporation is extremely fast, a premixed flame develops, whereas in the opposite case a thickening of the flame takes place. Beyond these extreme situations, a partially premixed front is normally generated with a secondary back-flame reaction zone [17]. In [17], where spray flame structure is analysed through DNS analysis, the local equivalence ratio is introduced as additional parameter. More details and explanations about spray combustion regimes and their classification can be found in [15, 17] and references therein. Furthermore, the relative velocity between the spray and the

air can strongly affect the stability and the shape of the envelope flames. In presence of high slip velocities between phases, which is normally the case of actual aero-engine combustors, side or wake flames can appear with a transition that is also affected by hysteresis. All these combustion regimes can be clearly identified in laboratory test cases that are normally far from the real application. However, for instance in [18] single droplet-burning mode was also experimentally found and investigated in a partially pre-vaporized swirl-stabilized flame. It was shown that the droplet burning mode is completely determined by the instantaneous slip velocity, in particular as far as the transition to wake flames is concerned. Several numerical studies employing Direct Numerical Simulation also clearly prove the coexistence in spray combustion of premixed and diffusion flames [17]. A recent study from Luo et al. [19], where DNS is applied on a n-heptane spray flame in a model swirl combustor, shows that composite premixed-diffusive structures can be identified at the same time, as shown in Figure 1.4. Several interesting flame characteristics

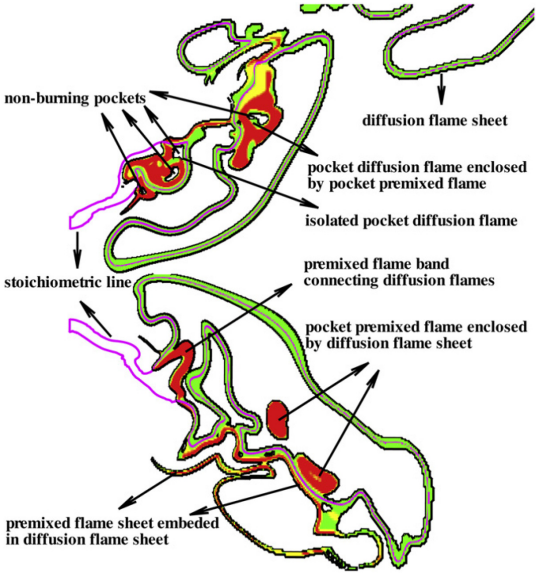

Figure 1.4: Spray flame structures in a model swirl combustor (purple: stoichiometric mixture fraction iso-line; green: diffusion flames; red: premixed flames). Taken from [19].

can be pointed out such as pockets of non-premixed flames enclosed by premixed envelopes and vice-versa. In a similar manner, non-burning pockets within burning regions can be determined. A part of the spray starts to evaporate immediately after the injection before reaching the stoichiometric line. The generated fuel-vapour mixes with the air and burns in rich conditions. Bigger droplets instead have a longer life and enter in the high temperature zones crossing the flame front. Then, they fully evaporate with a diffusive burning mode[19].
Another interesting and peculiar aspect of turbulent spray flames, which clearly points out the strong coupling between the liquid phase and the reacting flow-field, is the flame ignition. From a physical point of view, ignition in spray flames follows a different evolution with respect to the single-phase case, since a part of the energy is required to firstly evaporate the liquid. For a detailed review about ignition phenomena, the reader is addressed to the work of Mastorakos et al. [20]. Nonetheless, one of most remarkable characteristics of spray flame ignition is related to the different behaviour of small and larger droplets [10]. For instance, in [21] it was observed experimentally a primary ignition region, related to particles on the spray edges that have a low Stokes number and rapidly evaporate, together with a second flame where the remaining part of the spray burns. The same findings were reported also by Marley et al. [22], where for an ethanol spray flame, they observed a premixed reaction zone, determined by a partial evaporation of the spray after the injection, followed by a non-premixed region.

1.2 Review of spray flames analyses

A large amount of studies, both on a numerical and experimental point of view, has been dedicated to the analysis of spray flames over the past 30 years. Considering the complexity of the physics under investigation and the different interactions involved, studies have been performed from a wide range of perspectives. A complete overview goes beyond the goal of the present work and the interested reader is addressed to [10, 23, 24] among others, where several references on this topic are reported. Nonetheless, some interesting numerical modelling approaches are summarized below since they represent the theoretical background of the present research activity. Clearly, a large amount of works has been focused as well on experimental studies and in particular on the development of test articles to obtain a detailed insight in spray combustion and to validate numerical tools. The reader interested in an overview about it can refer to [10, 24].

From a numerical perspective, several works have been focused on liquid fuelled combustors from laboratory test conditions to real aero-engines. Over the last years, thanks to the increasing availability of computational power, applications of scale resolving techniques, such as Large Eddy Simulation (LES), have been becoming more widespread. In fact, it has been already widely demonstrated that classical steady state tools in RANS context are not able to represent the complex nature of turbulent spray flames, mainly in terms of flame shape and pollutant emissions. For LES, a broad range of models is still under development to properly describe the unresolved turbulence-chemistry interactions and to account for the presence of a spray [25, 26].
Thickened flame (TFM) or Artificially Thickened Flame (ATF) models for LES [27] are for instance one of the most applied group of approaches in this context. They are based on an artificial thickening of the front in order to directly solve the flame structure. The approach has been already widely validated on a broad range of applications going from partially premixed swirl burners to real aero-engine combustors (see [28] among others). One of the most important shortcomings associated with the ATF model is the exploitation of one or two steps reaction mechanisms to reduce the impact of small-scale inner flame layers. In this way, the turbulence-chemistry interactions are not properly predicted [29]. It should be pointed out that models to account for more detailed reaction mechanisms have been recently developed in the ATF context. For instance, Kuenne et al. [30] coupled the ATF model together with the Flamelet Generated Manifold (FGM), which will be introduced later, for the investigation of a premixed swirl flame, whereas Fiorina et al. [31] proposed the F-TACLES (Filtered TAbulated Chemistry for LES) combustion model. It includes a filtered chemical database in turbulent combustion and it is based on an a priori filtering of flamelets using the FPI (Flame Prolongation of ILDM) tabulation technique to account for a detailed chemistry [31].
Another important group of approaches widely employed in spray combustion is surely the flamelet based models. The turbulent flame is described here as an ensemble of one-dimensional flames, called *flamelets*, embedded within the turbulent flow field. In the steady flamelet model, the chemistry is therefore represented by separately solving the set of equations for premixed or diffusive flamelets and then mapping it into the 3D field. As an alternative to simplify combustion chemistry, historically the Intrinsic-Low Dimensional Manifold (ILDM) has been proposed, where tools for dynamic systems are used to reduce complex kinetic mechanisms. Several numerical methods have been then developed combining ILDM

with flamelet models to improve the chemical description reducing the number of parameters retained. In this context, Phase-Space ILDM and Flamelet Prolongation of ILDM (FPI) have been for instance proposed. A detailed overview about flamelet based models can be found in [32] and references therein.
Among others flamelet-based numerical methods, the Flamelet Generated Manifold (FGM) [33] and the Flamelet/Progress Variable (FPV) [34] approaches have been widely applied ranging from laminar cases to premixed and non-premixed turbulent flames [32]. Both models assume that the evolution of a general scalar, which represents a realized trajectory in the thermochemical manifold, is represented by the corresponding change in the laminar flame.
FGM has been initially developed for premixed flames and then it has been extended to the diffusive regime, while FPV was developed in the context of non-premixed combustion. In FPV, the chemical kinetic is described through one reaction progress variable (c), whereas the FGM has been in general designed to deal with multiple variables [32]. Moreover, the two approaches differ also for the employed method for the flamelet generation: considering a non-premixed case and in particular, varying the scalar dissipation rate, the region between the extinction reaction progress and c=0, in the FPV context, is resolved in the unstable middle and lower branches of the S-shaped curve [35]. It has been shown that the FPV model is able to correctly account for local extinction and re-ignition phenomena as well as for flame lift-off. Examples of the applications of the FPV in spray combustion can be found for instance in [36] and references therein, whereas for the FGM a detailed assessment has been recently performed in [37, 38].
One of the most important advantages of such group of flamelet based models is surely the opportunity to consider an arbitrary detailed reaction mechanism with a reduced computational cost. However, considering that normally both premixed and non-premixed combustion modes can be found in spray flames (see Figure 1.4), extensions of such approach are still under investigation. Multi-regime flamelet (MRF) combustion models for instance have been proposed in this scenario, where, based on the value locally assumed by a flame index [39], the premixed or diffusive solution is retrieved. Several multi-regime approaches have been proposed lately and in [40] the model has been extended to the multiphase context. It is worth pointing out also that several formulations of the regime indicator have been as well proposed (see [29] for a detailed overview).
In the context of advanced tabulated chemistry models, it is worth citing also the work of Franzelli et al. [41], where a multi-regime combustion

model combining partially-premixed and diffusive laminar solutions is proposed.
Furthermore, another interesting and recognized group of works in spray combustion area is based on the Conditional Moment Closure (CMC) [42]. Here, the chemistry is solved through values of chemical species that have been conditioned on a particular scalar, which is normally the mixture fraction. Such model has been widely employed in particular for Lean Blow Out (LBO) studies in single phase context [43] and recently it has been applied to investigate the ignition of spray flames [44]. One of the major issues related to the CMC is surely the computational cost: as noticed by Knudsen and Pitsch [29] in single regime combustion the mixture fraction is treated as an independent variable and it means that a standard three dimensional problem is solved in a 4-D space (i.e. Cartesian space plus 1 additional scalar). In the context of multiple regime combustion, a double conditional dependency on mixture fraction and progress variable would rise the dimension of the problem to 5-D [29].
Finally, in this brief review about combustion models it is worth mentioning the growing interest in technical literature towards Transported Probability Density Function (TPDF) methods, where the modelled equation for the one-point, one-time Eulerian joint PDF of variables, which characterizes the thermochemical state of a reacting medium, is transported. Several numerical approaches, ranging from Lagrangian to Eulerian realizations, have been proposed over the last years to solve such equation. One of the most important challenges in TPDF framework is the closure of the conditioned diffusive term that appears in the PDF transport equation [29]. If such term is correctly characterized, the TPDF approach should be able to fully describe the partially premixed nature of a spray flame without an a priori assumption about the asymptotic flame behaviour. TPDF methods represent a valuable and general framework for combustion modelling since several complex interactions among turbulence, chemistry, soot, radiation and spray can be directly accounted. In fact, combinations between TPDF and CMC methods (e.g. Multiple Mapping Conditioning (MMC)), including a generalisation of mapping closures, have been for instance proposed [45]. Nonetheless, they have to be considered as a tool for research and their technological readiness level is still low.
Although these works clearly represents a very small subset of turbulent combustion models available, the variety of modelling assumptions that can be performed to account for turbulence-chemistry interactions is clearly pointed out. A brief summary with particular attention on the target application is proposed in Table 1.1.

Reference	Combustion Model	Target Application
[27, 28]	ATF	From lab-scale burner up to real aero-engine burner
[34, 36]	FPV	From lab-scale burner up to real aero-engine burner
[37, 38]	FGM	Lab-scale burner
[40, 46]	MRF	Lab-scale burner
[43, 44]	CMC	Lab-scale burner
[25, 26]	TPDF	Lab-scale burner up to real aero-engine burner

Table 1.1: Tentative survey of a subset of approaches for turbulent combustion modelling.

Another peculiar aspect of numerical calculations of spray flames is surely represented by the different assumptions made on the liquid phase to include the effects of the dense region of the spray (see Figure 1.2).
Menon et al. [47] performed LES calculations of a Lean Direct Injection (LDI) burner, making a comparison between simulations including or not the secondary breakup. Different spray boundary conditions, using a Eulerian-Lagrangian (E-L) approach for liquid phase tracking, were tested. It was shown that the major impact of the breakup is on fuel evaporation in the near injector region that has a direct effect on the flame stabilization process (see Section 1).
FPV was employed, in conjunction with a standard E-L approach for liquid phase, by Moin and Apte [48] on different test cases arriving finally to a Pratt & Whitney combustor. Even if an overall good prediction of both spray and gas phase characteristics is determined, few details have been reported on the spray injection parameters and how they have been determined.
Boileau et al. [28] used instead the ATF model to simulate the ignition process in an aero-engine combustor. A mono-dispersed spray was employed within an Eulerian-Eulerian (E-E) framework and they were able to achieve an overall good qualitative representation of the ignition sequence.
In [49], a TPDF approach based on Eulerian stochastic fields was applied on the numerical simulation of a lab-scale combustor: thanks to a very detailed experimental database, it was possible to characterize the injection of the liquid phase determining a satisfactory agreement with experiments using a E-L spray tracking. The same test article for acetone flames was also studied by Chrigui et al. [37] using the FGM combustion model. Again, directly injecting a spray population derived from experimental results, calculations proved to be able to represent the investigated spray flame.
Jones and co-workers performed a wide range of LES-pdf simulations based

on the stochastics field method going from piloted flames, approaching to extinction, up to more representative liquid-fuelled aero-engines burners [25, 26]. All these studies have been realized with a standard Eulerian-Lagrangian approach and neglecting the primary breakup process: a trial & error procedure to determine spray boundary conditions was employed until a satisfactory agreement with experimental data concerning the liquid phase was achieved.
Even if just a small group of studies has been here cited for the sake of brevity, it should be sufficient to show the lack of a deep understanding on how the dense region of the spray affects the reacting flow-field. Cited research works normally rely on experimental data or on trial & error procedures, but important issues may arise when for instance the operating conditions or the injector characteristics have to be modified. Such limitations can be particularly important in the aero-engine context for lean-burn devices, where the atomization process is completely controlled by these parameters.
Very few works deal in literature with the development of numerical methods to define the liquid characteristics in a spray flame computation. A LES model to account for the evolution of the liquid film for an air-blast atomizer has been developed for instance by Chaussonnet et al. [50], where the *Primary Atomization Model for prEfilming airbLAst injectors* (PAMELA) was proposed and assessed using the experimental data provided in [51]. However, up to now such model has been always applied on the geometrical configuration proposed in [51], that is much more simplified than the actual aero-engine burners. Its validity on other geometrical configurations, as well as in reactive test conditions, has still to be addressed.
In [52] the FIM-UR (*Fuel Injection Method by Upstream Reconstruction*) methodology was instead proposed to determine spray boundary conditions for reactive calculations for simplex atomizers: based on some geometrical characteristics and on the assumption of the quantity of air entrained by the spray, injection parameters for monodispersed Eulerian and Lagrangian calculations were determined. A validation was performed in isothermal test conditions and the same set-up was then applied on a multi-point injection burner using the ATF model for turbulent combustion. Nonetheless, just simplex atomizers were investigated and the model cannot be directly employed for an injection configuration based on a liquid film or discrete jets.
In Table 1.2, a brief survey of the cited approaches to account for the presence of the liquid phase in spray flames calculations is reported.
Conversely, from a numerical perspective, several studies in literature have

Reference	Combustion Model	BCs spray	Dense spray region
[47]	FPV	Trial & Error	Neglected
[48]	FPV	Experiments	Neglected
[28]	ATF	Mono-disperse	Neglected
[49]	TPDF	Experiments	Neglected
[37]	FGM	Experiments	Neglected
[25, 26]	TPDF	Trial & Error	Neglected
[50]	No combustion	PAMELA	Modelled
[52]	ATF	FIM-UR	Modelled

Table 1.2: Tentative survey of a subset of approaches for liquid characterization in spray flame computations.

been focused just on the atomization process in the dense spray region. Several examples of DNS calculations of breakup events [53, 54] can be found, but they are limited by the CPU cost in terms of domain extension and characteristic velocities. Moreover, no combustion phenomena are clearly accounted for.
Eulerian-Eulerian methods have been as well applied in LES context to include the evolution of the liquid phase mainly in the near injection region [55], even if a Lagrangian approach is then more suitable in the dilute zone. Actually, several studies have been therefore performed for the coupling of Eulerian and Lagrangian methods in LES. The interested reader on such hybrid strategies is addressed to the review of Gorokhovski and Herrmann [56].
Among others the Eulerian Lagrangian Spray Atomization (ELSA) approach [57, 58] belongs to this class of numerical methods and it has been already employed to account at the same time for atomization and combustion [59, 60, 61] even if in RANS context.

1.3 Concluding remarks and present contribution

From the given brief presentation of phenomena and modelling approaches, it should be clear that spray combustion is a problem that can be faced from different perspectives. Several physical phenomena with different spatial and time scales interact between each other and, from a numerical point of view, the level of detail is very dependent on the specific application.
The following remarks can be stated from this preliminary review:

- Significant efforts have been focused so far on the development of advanced combustion models to deal with turbulence-chemistry

interactions (see Table 1.1).

- Minor attention has been diverted on the impact of the dense spray region, in particular as long as the flame shape and the subsequent reacting flow-field are concerned (see Table 1.2).

- Several contributions have been instead aimed at developing advanced atomization models to account for both the dense and dispersed spray regions, mainly in non-reacting test conditions.

The development and application of advanced turbulent combustion models is surely an important issue. However, the spray can completely modify the flame stabilization process and the understanding of atomization phenomena has surely to be improved in LES with respect to the actual state of the art (see Table 1.2).
This research work is introduced in this scenario and it had a twofold goal:

- To deepen the knowledge about the impact of liquid modelling in reactive calculations in order to show that without a detailed understanding of the breakup process, the flame shape can be completely misled. Considering the overview about turbulent combustion models reported so far and keeping in mind also that, in an industrial context, the computational cost is an aspect of paramount importance, the FGM model has been chosen to describe the flame dynamics. In fact, it can be considered from a theoretical point of view as a good compromise since, being based on a flamelet assumption, it is possible to consider a detailed reaction mechanism without increasing the CPU effort.
  To the best of the author's knowledge, the present work represents one of the first attempts in technical literature to analyse spray flames in LES from a lab-scale test article up to a simulacrum of an aero-engine combustor using the FGM model. This part of the study has been carried out with the aim of assessing several aspects of the proposed LES-FGM setup, which has been then applied by the candidate in the numerical simulation of the full annular rig studied within the EU-project LEMCOTEC (*Low Emissions Core-Engine Technologies*). These latter calculations are not reported in the dissertation for the sake of clarity and the interested reader is addressed to [62, 63] to find out more.
  From these set of analyses, the importance of primary breakup modelling in spray combustion and the limitations of standard numerical techniques for liquid phase will be clarified. The development of a

unified approach from atomization up to evaporation will be identified as an essential effort to enhance the reliability of numerical methods in this context.

- To develop a unified approach in LES, able to account for the evolution of the liquid phase from its injection up to evaporation in order to overcome the problems of standard lagrangian techniques. The ELSA model will be presented as possible solution in this scenario. Several novel closures for its application in the aero-engine context will be proposed and validated both on experimental and numerical test cases. To the best of the author's knowledge, the present work represents also one of the first efforts in technical literature focused on the extension of ELSA to the aeronautical framework in LES.

Chapter 2

State of the art for scale resolving modelling of spray flames

In Chapter 1 some basic concepts of spray combustion have been introduced together with an overview about computational techniques used in this context. From the given presentation, the lack of a deep understanding about how the atomization process affects the reacting flow field has been pointed out. It has been noticed that the major part of contributions in technical literature regarding spray flames deals with laboratory test conditions employing simplified boundaries for the spray. In this chapter, a state of the art about the analysis of spray combustion is proposed through the discussion of numerical results obtained on three different literature liquid fuelled flames.
The goal of this part of the work is twofold: first, the impact of a correct spray characterization in reactive calculations is pointed out. In this manner, the need of more advanced strategies to deal with the atomization process with respect to the actual state of the art is justified. Secondly, the capabilities of the FGM model in dealing with spray combustion are assessed on different configurations in order to propose it as a robust and reliable tool for spray combustion mainly from an industrial perspective.

2.1 Introduction

In this chapter, the main findings achieved in this research activity, aimed at deepening the knowledge concerning the numerical simulation of turbulent lean spray flames, are described. Particular attention is devoted to the interactions between the liquid phase and the reacting flow-field. A state of the art in the scale-resolving analysis of spray flames is reported in order to clearly point out the limits of actual techniques for liquid phase modelling. The research efforts proposed in the next chapters are finally introduced to fill this gap.
At this purpose, three test cases at increasing level of complexity and representativeness of actual lean aero-engines combustors have been considered employing a LES-FGM approach:

- **Sydney Spray Burner**: it represents one of most detailed experimental database both in reactive and non-reactive test conditions available for partially premixed turbulent spray flames. In the present work, such test case has been used to show the benefits of LES in the prediction of spray evolution and to assess the capabilities of FGM in reactive test conditions. Here, the liquid phase BCs are well defined thanks to the availability of a detailed experimental dataset.

- **Sheen Spray Burner**: the assessment of the LES-FGM numerical set-up to investigate a swirled spray flame, with several data both in terms of flow-field and pollutant emissions, has been the main aim of such second test case. As reported later, a pressure swirl atomizer is here employed involving a more difficult characterization of spray injection parameters.

- **Generic Single Sector (GSS) Combustor**: the validation of the proposed approach on a test article where both the geometry and the operating conditions are fully representative of a typical aero-engine combustor has been the goal of this part of the study. A wide range of experimental measurements is available both for flame and spray characteristics. It has been used to clearly show the link between the modelling strategy for the liquid phase and the obtained reacting flow-field.

The chapter is structured as follows: the first part is devoted to the characterization of the common mathematical models used to address the physical phenomena involved in the analysed cases. Then, the experimental test articles are described and the main results summarized.

2.2 General aspects of numerical modelling

Numerical calculations presented in the following sections have been carried out with the finite volume solver ANSYS® Fluent v16.2 using a 3D unsteady LES approach. The density-weighted Navier-Stokes system of equations for the gas phase, which takes into account also the effects of the liquid phase, arising from the filtering procedure, can be written as shown below. The reader interested in a detailed derivation of such system of equations is addressed to Sagaut et al. [64] among others.

$$\frac{\partial \bar{\rho}}{\partial t} + \boldsymbol{\nabla} \cdot \left(\bar{\rho} \tilde{\boldsymbol{U}} \right) = \overline{\dot{S}}_{mass} \tag{2.1}$$

$$\frac{\partial \bar{\rho} \tilde{\boldsymbol{U}}}{\partial t} + \boldsymbol{\nabla} \cdot \left(\bar{\rho} \tilde{\boldsymbol{U}} \otimes \tilde{\boldsymbol{U}} \right) = -\boldsymbol{\nabla} \bar{P} + \boldsymbol{\nabla} \cdot \bar{\boldsymbol{\sigma}} + \boldsymbol{\nabla} \cdot \bar{\boldsymbol{\tau}}_{sgs} + \overline{\dot{S}}_{mom} \tag{2.2}$$

where $\bar{\boldsymbol{\sigma}}$, $\bar{\rho}$, $\tilde{\boldsymbol{U}}$ and $\bar{P}$ represent the viscous stresses, density, velocity and pressure of the gas mixture. Over-bars and tildes represent respectively spatially filtered and density weighted filtered quantities based on a filter width Δ, evaluated as the cube root of the local grid cell volume.
The unclosed sub-grid stress tensor $\bar{\boldsymbol{\tau}}_{sgs}$, which appears in Equation 2.2, has been closed in all the analysed cases through a dynamic Smagorinsky-Lilly model [65].
The filtered sources terms $\overline{\dot{S}}_{mass}$ and $\overline{\dot{S}}_{mom}$ account for the contributions of the liquid phase. As detailed in Chapter 1, several numerical strategies can be employed to consider the presence of a spray.
In this first part of the work, an Eulerian-Lagrangian approach has been used [66, 67]. Such strategy is valid when the spray is highly diluted and therefore downstream of the primary break-up process. Regions in the proximity of the injector do not satisfy this assumption. Since the primary break-up is not modelled, the definition of appropriate initial conditions for the spray is required. The reader is addressed to sections devoted to the single test cases for the derivation of spray boundary conditions.
Models for droplet motion, evaporation and heat transfer have to be specified to determine the source terms for the gas phase. Drag effects have been taken into account for the liquid momentum equation, where the drag coefficient has been computed through the hypothesis of spherical not deformable droplets [68]. Concerning evaporation, a uniform temperature assumption has been adopted [69], where the integration of convection contribution on the mass transfer is included through the formulation derived by Sazhin [70]. The impact of the sub-grid temperature fluctuations on the evaporation process has been neglected. The interactions of droplets with fluid turbulent structures (i.e. *turbulent dispersion* effects)

have been instead included through the stochastic Discrete Random Walk (DRW) model, where sub-grid contributions are used to calculate velocity fluctuations. The reader interested in this topic is addressed to reference [71], where such model is presented in detail.
Properties for liquid phase have been carefully chosen based on the test case under investigation. In a similar fashion, remaining aspects of spray modelling, such as secondary breakup, are case-dependent and detailed in the following sections.
Clearly, in Equations 2.1 and 2.2 the effects of reacting phenomena are not directly included. As stated in the previous chapter, in this work the FGM model has been chosen to describe the reacting flow-field.
In FGM a two-dimensional manifold $\psi(Z, c)$ is created through the solution of a set of laminar adiabatic one-dimensional flamelets and parametrizing the chemical state only as function of two key variables, i.e. the mixture fraction Z and the normalized progress variable $c = Y_c/Y_{c,eq}$, where $Y_{c,eq}$ represents the species mass fraction at equilibrium conditions. In the present work, the un-normalized reaction progress variable (Y_c), which characterizes the transition from fresh to burnt gases, has been generally defined as:

$$Y_c = Y_{CO} + Y_{CO_2} \tag{2.3}$$

However, this general definition has not been always reliable for the test articles here investigated. Modifications to this formulation have been therefore considered and are specified in the following sections. Flamelet equations have been solved using the dedicated tool integrated in ANSYS® Fluent v16.2, creating a set of flamelets for several values of equivalence ratio and scalar dissipation rate. This last quantity is modelled by means of an algebraic function of progress variable and mixture fraction and it is not considered as an independent variable of the manifold. Both premixed and non-premixed flamelets can be generated and, considering the different topology of the spray flames under investigation, the flamelet set-up is individually specified in the next sections. A database of all species, temperature and progress variable source term as a function of mean values of Z and c and their variances is generated, as shown in Figure 2.1.
In order to include the turbulence-chemistry interactions, laminar quantities of the manifold are integrated in a pre-processing step using a presumed β-Probability Density Function (β-PDF) for both mixture fraction and progress variable, as in [73]. Hence, considering a laminar quantity $\psi(c, Z)$ and assuming that Z and c are statistically independent

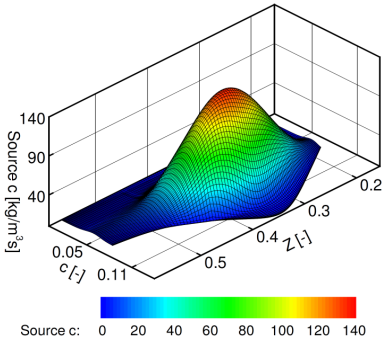

Figure 2.1: Progress variable reaction rate as a function of Z and c obtained by Ramaekers et al. [72] applying FGM on a premixed methane flame.

in the flame, its integrated value has been calculated as:

$$\tilde{\psi} = \int\int \psi(c, Z) P(c, \tilde{c}, \widetilde{c''^2}) P(Z, \tilde{Z}, \widetilde{Z''^2}) \, \mathrm{d}c\mathrm{d}Z \tag{2.4}$$

where P is the β-function, while $\tilde{c}$, $\tilde{Z}$ and $\widetilde{c''^2}$, $\widetilde{Z''^2}$ are respectively the mean values and the variances of mixture fraction and progress variable. Thus, such convolution procedure adds two additional variables to the manifold, which arrives to its final four-dimension configuration. In the present study, 21 points have been used in the manifold generation for both variances.
During the solution processing, the manifold data are recalled solving the following conservation equations for the un-normalized progress variable and the mixture fraction and performing an interpolation on tabulated values.

$$\frac{\partial \bar{\rho}\tilde{Z}}{\partial t} + \boldsymbol{\nabla} \cdot \bar{\rho}\tilde{\boldsymbol{U}}\tilde{Z} = \boldsymbol{\nabla} \cdot \left(\bar{\rho} D_{eff} \boldsymbol{\nabla}\tilde{Z}\right) + \bar{\dot{\Omega}}_z \tag{2.5}$$

$$\frac{\partial \bar{\rho}\tilde{Y}_c}{\partial t} + \boldsymbol{\nabla} \cdot \bar{\rho}\tilde{\boldsymbol{U}}\tilde{Y}_c = \boldsymbol{\nabla} \cdot \left(\bar{\rho} D_{eff} \boldsymbol{\nabla}\tilde{Y}_c\right) + \bar{\dot{\omega}}_c \tag{2.6}$$

In Equations 2.5-2.6, $\bar{\dot{\Omega}}_z$ represents the source term due to spray evaporation, whereas $\bar{\dot{\omega}}_c$ is the source term of progress variable that is directly taken from the flamelet tabulation as shown in Figure 2.1. D_{eff} represents instead the sum of molecular and turbulent diffusion coefficients.

Concerning variances modelling, the following transport equations have been solved in RANS calculations:

$$\frac{\partial \bar{\rho}\widetilde{Y_c^{"2}}}{\partial t} + \boldsymbol{\nabla}\cdot\bar{\rho}\tilde{\boldsymbol{U}}\widetilde{Y_c^{"2}} = \boldsymbol{\nabla}\cdot\left(\bar{\rho}D_{eff}\boldsymbol{\nabla}\widetilde{Y_c^{"2}}\right) + \bar{\rho}C_\phi D_{eff}|\boldsymbol{\nabla}\widetilde{Y}_c|^2 + - \frac{\bar{\rho}C_\phi}{\tau_{turb}}\widetilde{Y_c^{"2}} + \overline{2Y_c^{"}\dot{\omega}_c} \tag{2.7}$$

$$\frac{\partial \bar{\rho}\widetilde{Z^{"2}}}{\partial t} + \boldsymbol{\nabla}\cdot\bar{\rho}\tilde{\boldsymbol{U}}\widetilde{Z^{"2}} = \boldsymbol{\nabla}\cdot\left(\bar{\rho}D_{eff}\boldsymbol{\nabla}\widetilde{Z^{"2}}\right) + \bar{\rho}C_g D_{eff}|\boldsymbol{\nabla}\widetilde{Z}|^2 + - C_d\bar{\rho}\frac{\epsilon}{k}\widetilde{Z^{"2}} + \overline{2Z^{"}\dot{\Omega}_z} \tag{2.8}$$

where C_ϕ, C_g and C_d are model constants and τ_{turb} is a turbulence time scale. The following algebraic gradient based closure has been instead exploited for $\widetilde{Y_c^{"2}}$ in LES according to Donini et al. [73], whereas a transport equation has been retained for $\widetilde{Z^{"2}}$:

$$\widetilde{Y_c^{"2}} = C_{var}\frac{l_{sgs}^2}{Sc_t}\left(|\boldsymbol{\nabla}\tilde{Y}_c|\right)^2 \tag{2.9}$$

where C_{var} is a model constant, l_{sgs} is the sub-grid length scale and Sc_t is the sub-grid turbulent Schmidt number.
Finally, considering that flamelets have been considered as adiabatic during their solution, an enthalpy defect or heat loss/gain is added to the manifold. In this fashion, heat losses due to liquid evaporation are introduced. A detailed description of the enthalpy defect and its implementation in ANSYS® Fluent can be found in [74].

2.3 Sydney Spray Burner

In the first part of this section, the experimental test case is briefly described. Then, an overview of the numerical set-up is reported both for LES and RANS calculations. Finally, the obtained results in reacting test conditions are shown with a comparison against experimental data.

2.3.1 Experimental test case

The burner is composed by a round central jet surrounded by a pilot and an annular primary co-flow,, as shown in Figure 2.2. The diameter of the central jet (D) is 10.5 mm, whereas the pilot, whose outer diameter is 25.0 mm, holds 72 holes and is fixed 7.0 mm upstream of the nozzle exit plane. The co-flow has an outer diameter of 104 mm. The co flow/burner assembly is enclosed in a vertical wind tunnel with an air velocity of 4.5 m/s. The flame is fuelled with ethanol or acetone, which, compared to heavier fuels, do not require a preheating of the carrier phase to evaporate. The liquid fuel is released upstream of the jet exit plane by an ultrasonic nebulizer generator. Its position, shown in frame B of Figure 2.2, has been optimized to reduce asymmetries in the spray distribution at the jet exit plane [75]. The nebulizer creates a cloud of droplets in a diameter range $0<d<100$ μm with a Sauter Mean Diameter (SMD) of 40 μm and approximately a log-normal distribution. The air carries droplets all along the feeding pipe and an air/fuel mixture is generated at the jet exit plane because of the evaporation within the feeding pipe.
In reacting test conditions, a pilot flame, fed by a stoichiometric mixture of acetylene, hydrogen and air, is created in order to guarantee the same C/H ratio of the main jet fuel. In isothermal conditions, this flame is replaced by air with velocity of 1.5 m/s to match the pilot unburnt velocity in reactive cases. For a detailed description of the burner assembly the reader is addressed to Gounder et al. [76] and references therein.
The experimental apparatus has been operated at several operating points. Isothermal and reactive conditions have been considered for acetone, whereas ethanol has been used only in reactive configurations. For this reason, acetone has been chosen in the present work.
Different data at atmospheric pressure have been experimentally collected varying the fuel loading and air mass flow with a resulting different flame behaviour. Nevertheless, just one non-reactive (SP2) and the corresponding reactive (AcF2) test points have been here selected and the main operating conditions are summarized in Table 2.1.
Two sets of experiments are reported in [76] for each operating condition, i.e. “Experiment A” and “Experiment B”. In “Experiment A”

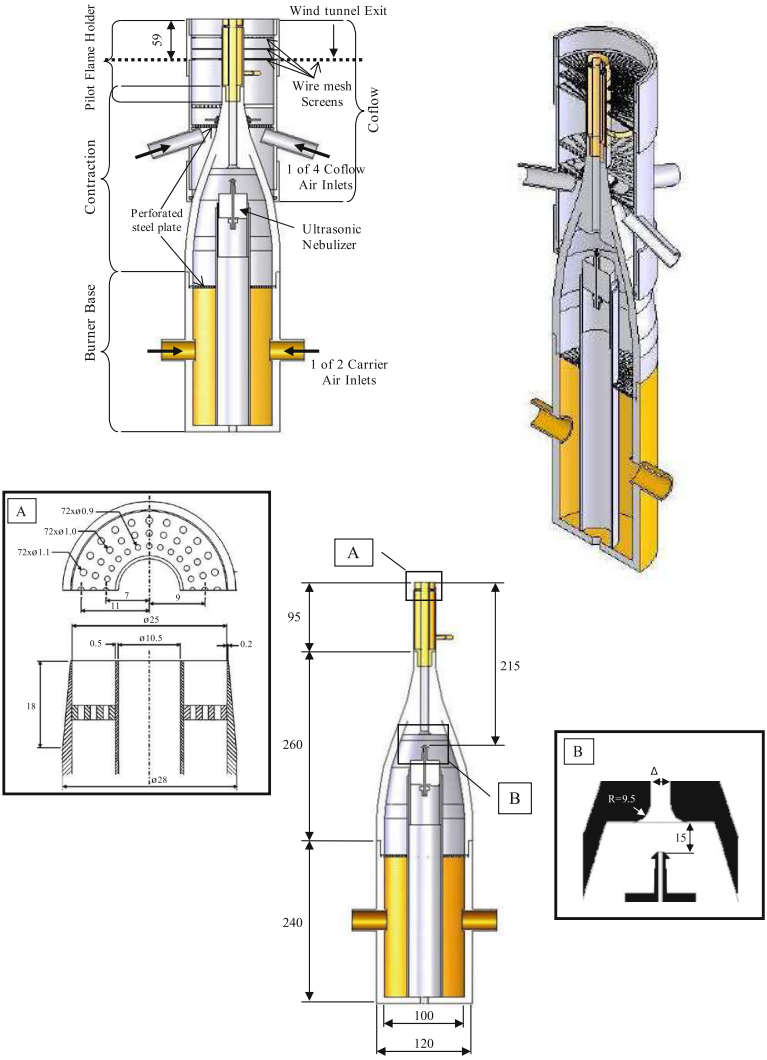

Figure 2.2: Geometric details of the experimental apparatus [75]

Acetone cases	SP2	AcF2
Bulk jet velocity (m/s)	36	36
Carrier mass flow rate (g/min)	225	225
Liquid fuel injection rate (g/min)	75	75
Temperature at jet exit plane (°C)	-5.0	-5.0
Overall equivalence ratio	-	3.2
Flame length (cm)	-	53
Experimental set A		
Measured liq. flow at exit (g/min)	28.8	23.9
Vapor fuel flow rate at jet exit (g/min)	46.2	51.1
Equivalence ratio at jet exit	-	2.2
Jet Reynolds number	31,900	32,100
Experimental set B		
Measured liq. flow at exit (g/min)	33.9	38.2
Vapor fuel flow rate at jet exit (g/min)	41.0	36.9
Equivalence ratio at jet exit	-	1.5
Jet Reynolds number	31,800	31,700

Table 2.1: Initial conditions of the simulated configurations [76]

the gas temperature is measured, whereas in set-B the droplet radial velocity component is also reported. LDV/PDA system (Laser Doppler Velocimeter/Phase-Doppler Anemometer) has been employed to measure several spray quantities such as axial and radial velocities, shear stresses, diameter, droplet number density and liquid volume flux. All the measurements have been performed at different axial locations, i.e. x/D = 0.3, 5, 10, 15, 20, 25 and 30.

2.3.2 Review of previous numerical works

Considering the wide and detailed dataset available on this spray flame, such test case has been widely used for the assessment of LES in spray combustion in technical literature. An Eulerian-Lagrangian approach is normally employed so that comparisons with the experimental database can be directly performed.
LES calculations of different acetone spray flames (i.e. from AcF3 to AcF8), using a two-dimensional FGM approach for turbulent combustion modelling, have been carried out by Chrigui et al. [37]. A non-equilibrium evaporation model was employed, assuming that it may have a strong impact in reacting test conditions. Subgrid scales effects on droplet dispersion and vaporization were neglected and the feeding pipe was included in the computational domain in order to ease boundary conditions. An overall reliable prediction of temperature levels and liquid phase characteristics was pointed out. Some remarkable discrepancies, mainly in the near axis region, were as well determined.

Ukai et al. [77] instead coupled LES with CMC for the computation of a set of acetone flames. The results showed a fair agreement of mean temperature especially along the centerline, which positively influences the accuracy in the prediction of droplet statistics.
LES calculations of the set of spray flames fuelled with ethanol have been instead performed by Rittler et al. [78], using a premixed FGM combined with the ATF model. A fair agreement with the experimental data has been again achieved. The attention has been mainly focused on the impact of sub-grid variances modelling both for mixture fraction and for progress variable.
In Figure 2.3, a brief summary of such works for test conditions similar to the test point AcF2 here investigated is reported in terms of temperature radial profiles. The data obtained on test conditions 6 (EtF6 and AcF6 respectively) have been considered for Rittler et al. [78] and Chrigui et al. [37] since representative of AcF2 in terms of Reynolds jet number and air mass-flow rate.

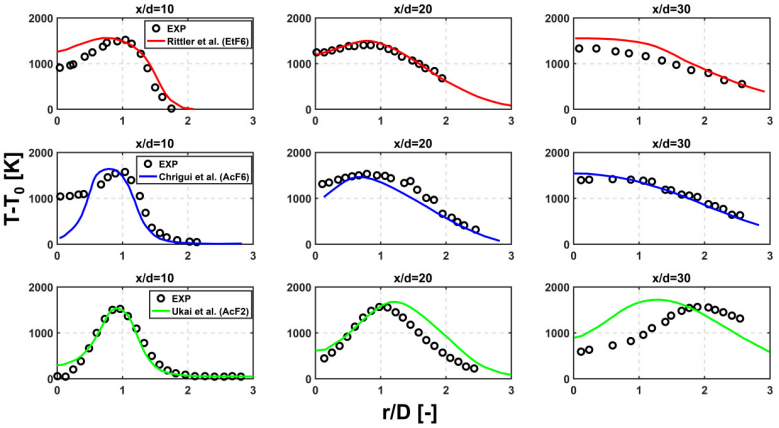

Figure 2.3: Comparison of numerical results obtained on the Sydney spray burner taken from Rittler et al. [78] for EtF6(top), from Chrigui et al. [37] for AcF6 (middle) and from Ukai et al. [77] for AcF2 (bottom).

Therefore, this test case has been here employed since detailed information of both liquid and gas phases are experimentally available. Several numerical studies have been already performed using different modelling strategies for turbulent combustion. This should lead to a comprehensive assessment of the proposed LES-FGM approach on a basic geometrical

configuration. The accuracy of the obtained results is indeed strongly determined by each numerical model (i.e. evaporation model, combustion model, spray tracking) and in the next section the most important features of RANS and LES calculations are briefly resumed.

2.3.3 Main features of the numerical set-up

In this section, the main aspects of the numerical setup are summarized. The reader interested in the different sensitivies carried out on this test case is addressed to [79, 80] to find out more.
As far as spray boundary conditions are concerned, the wide experimental dataset at x/D=0.3 has been used to derive the characteristics of the injection. In this manner, droplets properties, such as diameter, velocity and mass flux have been extrapolated and imposed at the domain inlet. Therefore, for each position, ten parcels, corresponding to ten equispaced diameter classes ranging from 0 μm to 100 μm, have been injected at several radial and tangential locations (see Figure 2.4)[79, 80]. In order

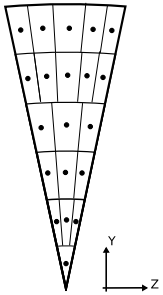

Figure 2.4: Sketch of the chosen injection setup on a 15 degrees sector of the jet inlet [79, 80].

to reduce the impact of the discrete injection, a radial and temporal staggering [74], which consists in a time-dependent random variation of the injection location around mean positions, has been included.
Acetone liquid properties have been derived from Reid et al. [81] and NIST database as a function of temperature. As reported by Chrigui et al. [37], the values of Weber and Ohnesorge numbers are very low ($We < 0.3$,$Oh < 0.006$) in the entire domain, so that secondary break-up effects can be safely neglected.
Regarding the carrier phase boundary conditions, the velocity at jet inlet has been derived starting from experimental data on axial velocity for the

0-10 μm class, i.e. particles that follow the carrier phase [75]. A scaling has been then carried out in order to retrieve the experimental mass flow rate (see Table 2.1). The velocity profile provided by Masri and Gounder [75] has been instead employed to calculate the coflow velocity, obtaining a value of 5.9 m/s with a turbulence intensity of 9%. A fixed ambient pressure has been finally imposed at the domain outlet.
In LES calculations, a turbulence generator has been employed at the inlet patch to promote the generation of turbulent eddies and a spectral synthesizer method has been employed to this end [82].
Comparisons with a reference RANS solution will be also shown for this spray flame to better appreciate the impact of LES. Following De et al. [83], a standard k-ϵ model with the correction $C_{\epsilon 1} = 1.6$ has been used.
For FGM, the detailed chemical mechanism for acetone provided by Pichon et al. [84] has been employed to generate the flamelet solution and the PDF table. A set of 64 opposed-jet non-premixed flamelets have been therefore used for the FGM database. As already mentioned in Section 2.2, a different definition of the un-normalized progress variable with respect to Equation 2.3 has been here adopted. The following expression suitable in the frame of spray combustion, has been used. A similar expression was suggested also in [37] to correctly represent the reacting flow-field. Here, the CO-mass fraction has been also included.

$$Y_c = \frac{Y_{CO_2}}{M_{CO_2}} + \frac{Y_{CO}}{M_{CO}} + \frac{Y_{H_2}}{M_{H_2}} + \frac{Y_{H_2O}}{M_{H_2O}} \tag{2.10}$$

where M_ϕ are the molar mass, used as weighting factor for the species mass fraction.
The chosen computational domain takes the region downstream of the exit plane and the feeding pipe has not been included.
In RANS simulations, a prismatic mesh of a 15 degrees sector has been simulated to reduce the CPU cost and to ease the convergence. Instead, a 360° domain, composed by hexahedral elements, has been used for LES (see Figure 2.5). The mesh quality has been verified thanks to the Pope criterion [85] in non-reacting test conditions [79, 80]. Details of the employed computational domains are summarized in Table 2.2. Second-order schemes have been employed both for spatial and time integration. A PISO algorithm with 12 iterations per time step completed the numerical set-up.
For the sake of clarity, in the following section only the results achieved in reacting test conditions (i.e. ACF2) are resumed. The numerical data obtained for the test point SP2, which show a great agreement, can be instead found in Puggelli et al. [79].

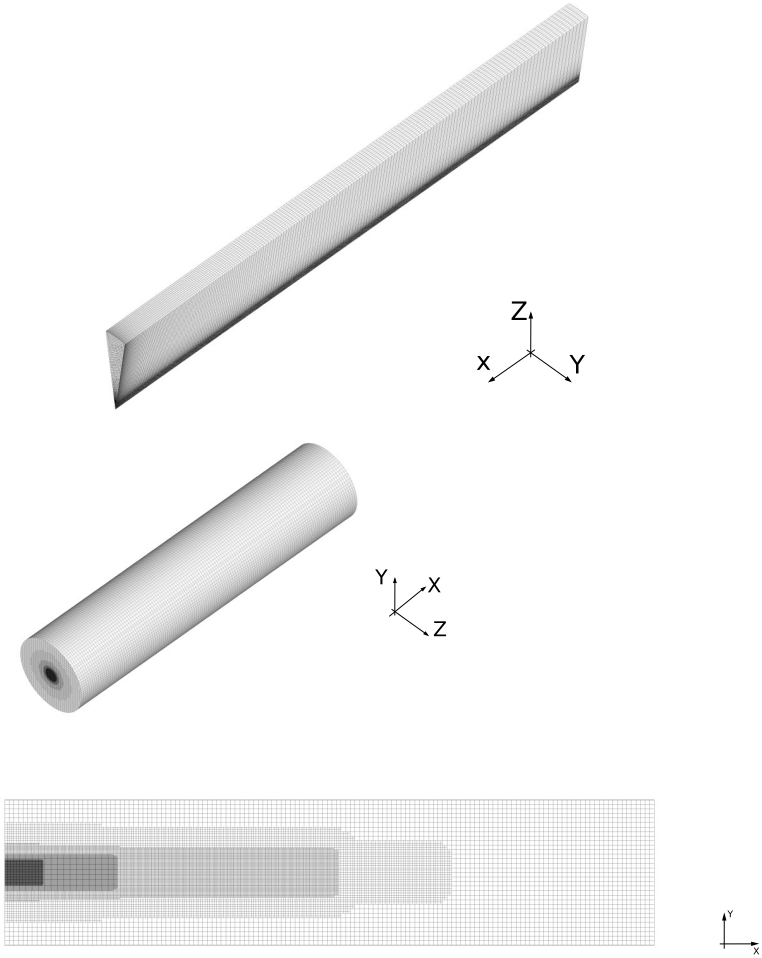

Figure 2.5: Mesh adopted in RANS (top) and LES (bottom) simulations. Taken from [80].

Case	**Angle** [°]	**Extension** [mm] (ax·rad)	**Cells** (10^5)	**Nodes** (10^5)
RANS	15	900x140	2.98	1.87
LES	360	900x100	21.35	22.18

Table 2.2: Mesh details

2.3.4 Reactive analysis

The main aim of this section is to carry out a first assessment of the proposed LES-FGM set-up in reacting test conditions. The significant amount of experimental data on this fundamental geometrical configuration leads to a detailed validation of the proposed methodology. The presence of a combustion process introduces complex interactions between the different phenomena, as explained in Chapter 1, requiring particular attention on the choice of numerical parameters.

Further details on numerical set-up Considering the overall good agreement obtained in non-reacting test conditions with LES in terms of discrete phase variables [79], the computational domain described in the previous section has been retained also for the reacting test point. For gas-phase solution, a time step of 1×10^{-5} s has been used in LES and considering a flow-through time around 0.1s, nearly 20000 time steps were performed to flush out boundary conditions and allow the flow-field to develop. Statistics were then gathered over nearly two FTT.
Considering the reacting test point, boundary conditions for the mixture fraction and progress variable have to be carefully chosen. The mixture fraction at the jet inlet has been calculated based on the experimental mass fraction of acetone vapour at the pipe exit (i.e. Z=0.141), whereas Z=0 has been imposed at the co-flow inlet. Considering that at these inlets the mixture is unburned, the progress variable has been set c=0. Instead, the pilot has been modelled as a burnt mixture (c=1) with Z=0.095, i.e. the stoichiometric value.
In reacting test conditions, boundary conditions for the gas-phase temperature are not experimentally available and therefore T=293 K has been assumed both for the co-flow and jet inlets. At the pilot exit instead, temperature (T_{pilot}) has been imposed equal to the adiabatic flame temperature corresponding to pilot mixture fraction. As reported by De et al. [83], T_{pilot}=2493 K. The rise in temperature augments the pilot velocity and, in order to respect the flow-rate shown in Table 2.1, a value of 12.76 m/s with no turbulence has been imposed.

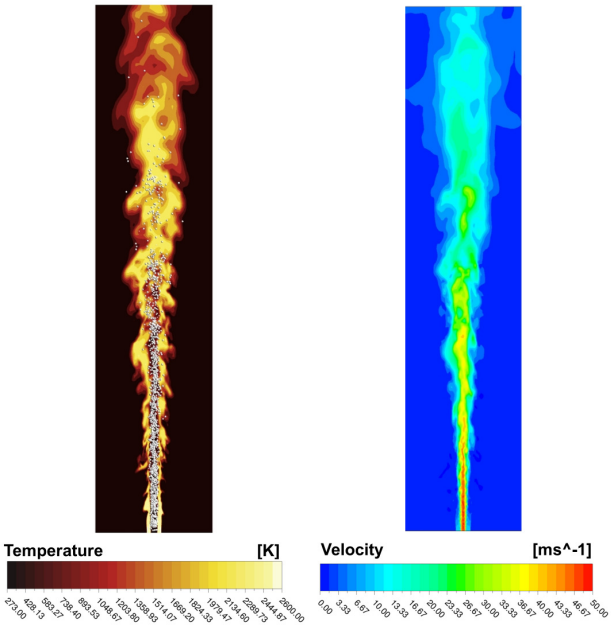

Figure 2.6: Instantaneous Temperature (left) and velocity (right) contours obtained in LES.

Results and discussion As already said in Chapter 1, in reacting conditions the adoption of a scale resolving approach, such as LES, leads to strongly improve the spray flame solution. This is mainly related to a better resolution of turbulent mixing that is a key process in flame development. In Figure 2.6, the LES instantaneous temperature and velocity contour plots are shown. The spray evolution is also super-imposed on the temperature field.
The liquid enters in the combustion chamber with a high momentum with respect to the air and in the near injection region it is nearly unaffected by the carrier phase. Further downstream, the spray evaporates and gradually feeds the flame with new reactants. The spray tends progressively to be relaxed to the gas phase velocity by the drag force and the turbulent fluctuations determine the dispersion of the liquid. This is clearly shown in Figure 2.7, where the discrete phase liquid volume fraction (α_l) together with its axial velocity is reported. The reduction of α_l all along

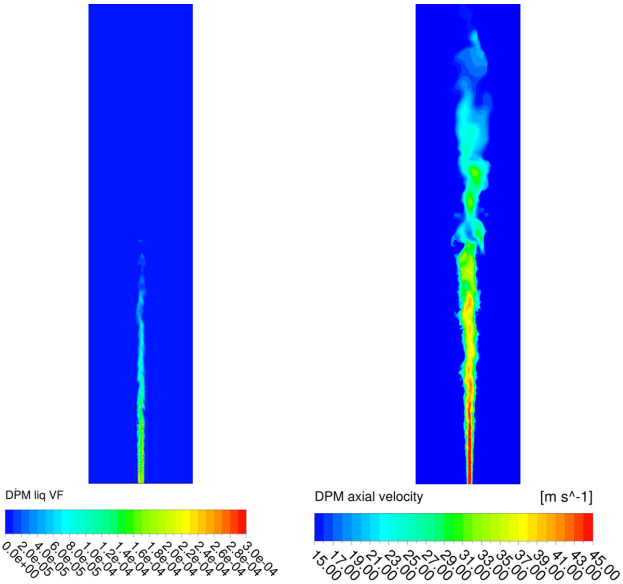

Figure 2.7: Instantaneous liquid volume fraction (left) and liquid velocity (right) contours obtained in LES.

the domain due to evaporation and radial dispersion is associated to a lower slip velocity between phases that tends to disappear at the end of the domain.
A non-uniform mixture fraction field is therefore produced leading to a partially premixed flame behaviour. Shears generated in the first part of the combustion chamber are essential to correctly characterize the dispersion of parcels and the vapour release in the carrier phase. Such a process is reproduced in LES and RANS in a very different manner as can be pointed out in Figure 2.8. In RANS, the Z field is narrower in radial direction because the reduced spray mixing tends to keep the droplets closer to the centreline. Less fuel vapour is produced and this moves the position of the Z peak downstream with respect to LES.
Moreover, the progress variable field shows that in LES the gas mixture in the near injection region is not completely burnt. The increased turbulence levels cause a slight flame lift-off. This is also confirmed in Figure 2.9, where both time averaged velocity field and OH mass fraction are shown. In RANS context, the pilot directly stabilizes the flame and the

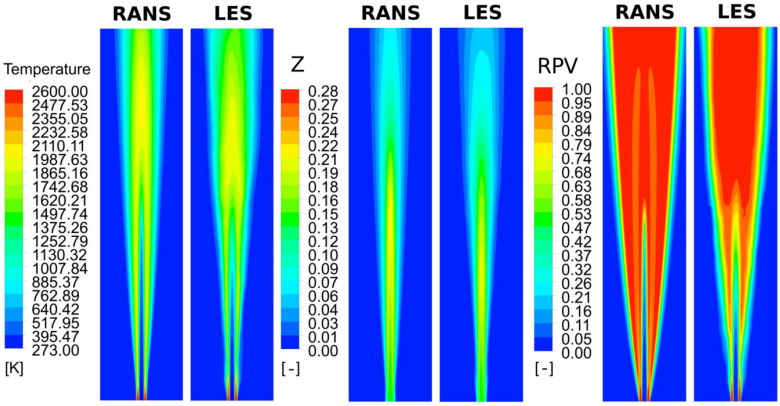

Figure 2.8: Comparisons between RANS and time-averaged LES temperature fields (left), mixture fraction (center) and reaction progress variable (left) in reactive cases [80].

simulation is not able to properly reproduce the local quenching related to the interactions with the fresh carrier phase. Moreover, with respect to LES, the axial extension of the high velocity region is higher since the turbulent dispersion model is not properly reproducing the radial spreading of the liquid phase [80].
Considering these observations, evaporation and mixing in the analysed test conditions are completely controlling the flame stabilization and topology. Based on the local vapour release rate, the spray combustion tends towards a premixed or diffusive combustion regime [37]. In the analysed test point, the evaporation rate is progressive and the modelling assumption of an asymptotic non-premixed flame behaviour is respected. This is verified in Figure 2.10, which shows contour plots of source terms of discrete phase in terms of mass, axial and radial velocity. They represents the two-way coupling of a standard Eulerian-Lagrangian calculation.
Clearly, source terms depend both on the grid sizing and on the number of parcels in each cell. It should be pointed out that all these contributions, in particular the mass source term, are nearly negligible in the near injection region. In fact, immediately after the injection, the liquid is cooled down due to the initial evaporation and this limits the heat up of the fuel. Then, going further downstream, the influence of the pilot is increasingly important leading to higher mass sources in the combustion zone. In terms of momentum, the evolution is quite similar. In particular,

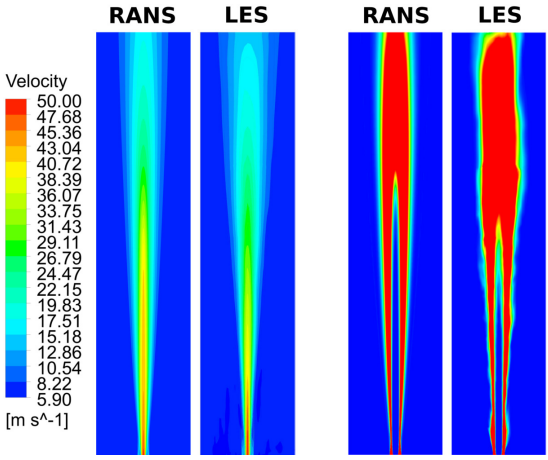

Figure 2.9: Comparisons between RANS and averaged LES velocity magnitude (left) and OH mass fraction (right) fields in reactive cases [80].

in the reacting region, the gas phase is probably accelerating and the droplets see a high slip velocity. The radial contribution is here much lower since, considering the co-flow configuration, the radial component of the gas phase velocity is nearly zero. The resulting acetone distribution is shown in Figure 2.11 to further justify the non-premixed assumption here employed.

The evolution of the evaporation process described so far is deeply affected also by the high level of temperature and velocity fluctuations reproduced by LES (see Figure 2.12). Liquid parcels are subjected locally to high temperature variations (up to 700 K), which can completely modify the stabilization of the flame. Clearly, in RANS context this effect is not captured.

The impact of the LES modelling on the temperature field is quantitatively plotted in Figure 2.13 A substantial improvement is evident and a more physical representation of the radial temperature evolution is surely achieved. This is due to a better prediction of the turbulent dispersion and evaporation of the spray and of the resulting flame shape. The obtained flame brush is in a satisfactory agreement with experiments and, in particular at higher radii, the effect of a more physical representation of the liquid-gas interactions is evident. It is worth pointing out that locally the overestimation of temperature obtained with a steady-state approach

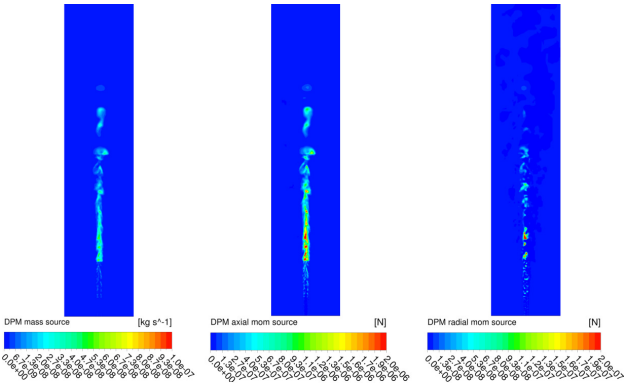

Figure 2.10: Liquid phase instantaneous mass source term (left), axial momentum (center) and radial momentum (right) source terms in LES.

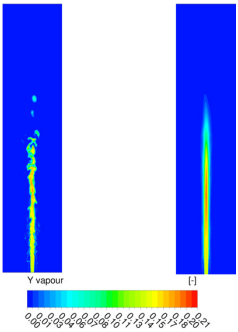

Figure 2.11: Instantaneous (left) and time-averaged (right) acetone contour plots.

is around 300-500 K with respect to experiments, mainly at higher radii. This can have a huge impact for instance on the prediction of pollutant emission or wall temperature.
Furthermore, comparing the obtained results with Figure 2.3, the reported agreement is in line with the data achieved with further advanced combustion models leading to a further assessment of the proposed set-up on this geometrical configuration.
The spray evolution obtained in this way is clearly related to the temperature and velocity fields analysed so far. In Figure 2.14 the axial velocity at

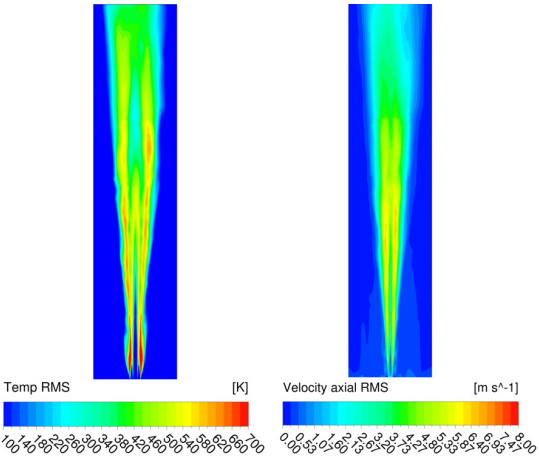

Figure 2.12: Temperature (left) and velocity (right) fluctuations provided by LES.

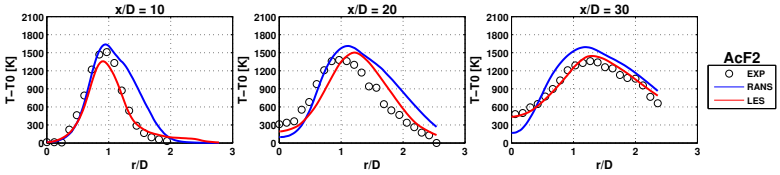

Figure 2.13: Radial profiles of the gas phase temperature field for the LES reactive case against RANS [79, 80].

three different axial positions is plotted. Also in reacting test conditions, a good agreement with experimental results is achieved. Profiles of axial velocity are also representative of the spray-opening angle, which seems to be well reproduced.

It is interesting to point out that also in terms of axial velocity fluctuations, experimental data agree well with numerical calculations (see Figure 2.15). The presence of the flame enhances the turbulence and the droplet *rms* velocity profile becomes monotone increasing because close to the flame front velocity fluctuations are higher. The *rms* values are well reproduced also increasing the axial distance, suggesting that the sub-grid scale model is properly reproducing the physics under investigation. As long as the

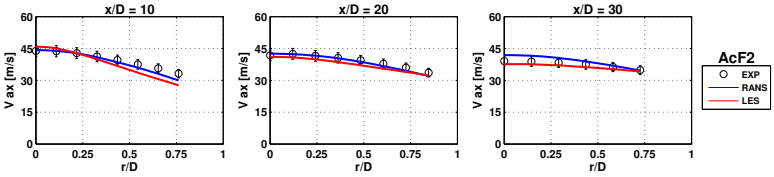

Figure 2.14: Radial profiles of the droplet axial velocity at three axial distances from the jet exit plane [79, 80].

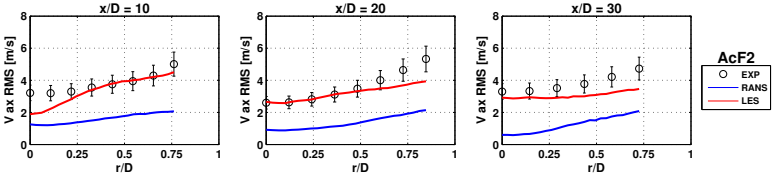

Figure 2.15: Radial profiles of the droplet rms axial velocity at three axial distances from the jet exit plane [79, 80].

spray evaporates and droplet diameter is reduced, liquid particles become a seeding and their evolution perfectly represents the gas phase.
Furthermore, the agreement obtained in terms of *rms* suggests that calculations are reproducing also the bimodality of the spray at the edge of the fuel nozzle that propagates downstream and determines the spray fluctuations [37, 76]. In fact, experimentally a wide range of droplets with different Stokes numbers is generated inside the feeding pipe and small particles follow the carrier phase in terms of fluctuations, whereas bigger ones yield to generate high slip velocity and locally lower *rms*. Such evolution seems to be here correctly reproduced.
In Figure 2.16, volume flux profiles are also shown. Again, an enhancement with respect to RANS is obtained thanks to a realistic resolution of the spray turbulent dispersion. Some discrepancies may be still detected since the spray seems to be gathered from a computational point of view in the near axis region. At the last experimental section (x/D=30) the disagreement is not much significant since the major part of the spray is already evaporated. It should be pointed out that similar results have been obtained also in [37], where a non-equilibrium evaporation model was also employed. Furthermore, as suggested by Chrigui et al. [37], on an experimental point of view, volume flux measurements can present strong under-predictions since some parcels may be not detected by the

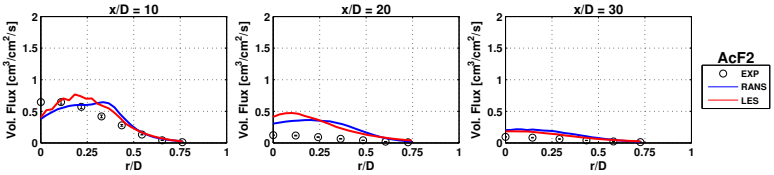

Figure 2.16: Radial profiles of the droplet volume flux at three axial distances from the jet exit plane [79, 80].

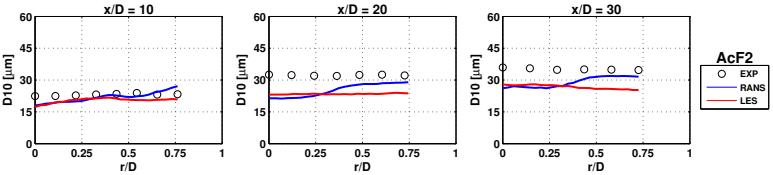

Figure 2.17: Radial profiles of the droplet mean diameter at three axial distances from the jet exit plane [79, 80].

PDA. Finally, in Figure 2.17 radial profiles of mean droplet diameter are shown. The agreement is again reasonable. Going downstream, even if the evaporation is acting, the diameter remains nearly constant since just the small classes are evaporating. Only the bigger particles survive and arrive until the last experimental section. Calculations are able to reproduce such experimental trends.

2.3.5 Concluding remarks on Sydney Spray Burner

A turbulent lean spray flames belonging to the database of the University of Sydney has been investigated in both RANS and LES frameworks. A standard Eulerian-Lagrangian approach coupled with the FGM combustion model has been employed from a numerical point of view.
The non-reactive case, which was not reported here for the sake of brevity, showed a substantial improvement in the prediction of spray evolution when a scale-resolving technique was employed thanks to a more accurate representation of turbulent dispersion. The interested reader is addressed to Puggelli et al. [79] for further details.
In reacting test conditions, the different interactions between spray, combustion and turbulence lead to much more complex physical phenomena. Especially in terms of temperature field, LES provides a general good fit

with experiments. Several characteristics of both liquid and gas phases have been analysed in order to show the impact of liquid phase modelling on the resulting reacting flow-field.
On a test case where the liquid boundary conditions are clearly defined, the proposed LES-FGM set-up leads to a satisfactory agreement with the experimental data, consistently with previous numerical works realized on the same test case.

2.4 Sheen Spray Burner

The capabilities of the LES-FGM set-up in correctly representing the interactions between turbulence, spray and reacting flow field were highlighted in the previous section. However, a more representative case for aero-engine applications, with measurements of typical gas-phase quantities (i.e. flow-field, temperature, and pollutant emissions), has to be as well considered. Therefore, the experimental set-up studied by Sheen [86] has been chosen as a second test article. In this section, the main results are summarized and the interested reader is addressed to the works of Puggelli et al. [87, 88] for further details and investigations on this spray flame. The author would like to express his gratitude to ASME (*American Society of Mechanical Engineers*) society for the permission to use parts and figures of his papers.

2.4.1 Experimental test case

The Sheen burner consists of a cylindrical combustion chamber fed by a swirled air jet flowing through an annular duct. A sketch of the experimental domain is shown in Figure 2.18, where the main geometrical features are also reported. The combustor chamber is 500 mm long with a diameter D_0 of 200 mm. The annular duct has an inner diameter D_{in} of 21 mm and an outer D_{out} of 42 mm. The outer radius of the annulus (R=21mm) is used in the following as reference length. The swirler is composed by 20 equally spaced vanes with a discharge angle of 30° with respect to the axis. The fuel injector is located at the center of the combustor (x=0 mm) and it injects Jet A-1 through a pressure swirl atomizer generating a hollow spray cone. Air and fuel enter into the combustion chamber at ambient temperature and all tests were carried out

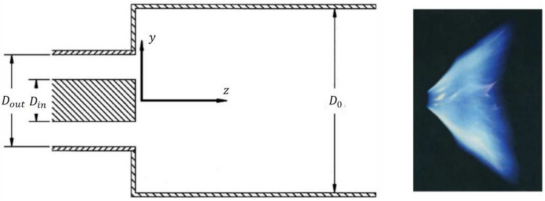

Figure 2.18: Sketch of the geometry experimentally studied and of the spray flame under investigation (adapted from [86]).

Inlet pressure [bar]	1
Inlet temperature [K]	300
Burner AFR [-]	27.88
Burner airflow rate [g/s]	26.1
Burner fuel flow rate [g/s]	0.951

Table 2.3: Operating conditions for Sheen burner [86].

at atmospheric pressure. Experimental data in terms of gas phase velocity, temperature and species (O_2, CO_2, CO and H_2) concentration in reacting test conditions are available at several axial positions downstream the swirler exit. In Table 2.3, the operating conditions are briefly summarized. It should be pointed out that, here, no experimental information on the generated spray is available.
With respect to the previous test case, a swirled flow field is under investigation and both the chosen liquid fuel and the injection strategy are almost consistent with a real aero-engine application.

2.4.2 Review of previous numerical works

Considering the characteristics of the swirled reactive flow-field analysed in this section, numerical studies can be challenging. In literature, significant results in predicting the flow behaviour and the flame topology on this test article have been achieved for instance by Jones and co-workers [89]. Here, the BOFFIN-LES code has been employed to realize a set of LES simulations both in isothermal and reacting test conditions. Considering the lack of geometrical details for the swirler, it was not included in the computational domain. As shown in [89], a reliable representation of the swirling flow-field can be even obtained locating the inlet 50 mm upstream of the jet exit and accounting for the swirler effects by imposing a swirling velocity component. Jones et al. [90] carried out a very detailed analysis in non-reacting test conditions to determine the value of the swirler number (S_n) to be used at the inlet. Finally, S_n equal to 1.22 was suggested to match the experimental velocity profiles at the first measurement section [89, 90].
Instead, for the burning test point, the evolution of the N_s scalar quantities, which determine the thermo-chemical state of the multicomponent reacting mixture (i.e. N species mass fraction and the enthalpy), was described by Jones and coworkers [89] thanks to the TPDF approach developed by O'Brien [91]. All the terms related to liquid evaporation or

reactions are directly closed and the modelling acts just at sub-grid scale (sgs) and micro-mixing levels [25, 89, 92]. A dynamic Smagorinsky model [65] was employed for sgs terms and a Linear Mean Square estimation closure for the latter one. The reader interested in this topic is addressed to references [25, 92], where it is discussed in detail. A stochastic Eulerian field method is then employed to solve the resulting transport equation for the PDF [25, 89, 93]. A four step global reaction mechanism for $C_{12}H_{23}$ was employed to reduce the computational cost. Regarding the liquid phase characterization, the state of the dispersed phase is characterized in terms of droplet radius (R), velocity ($\mathbf{V}$), temperature (T) and number (θ) leading to the joined PDF $\bar{P}_{spr}(\mathbf{V}, R, \theta, N, T, x, t)$ [92]. A set of stochastic Lagrangian parcels, which are inertial particles and follow the Stokes law [92], is then tracked in the phase space $(\mathbf{V}, R, \theta, N, T, x, t)$ to determine the liquid evolution. Such stochastic approach leads to directly account for the effects of small scales on the droplets motion, which can be important mainly in zones where the mesh is not fine enough to minimize the impact of sub-grid scales. As reported also in [94], in regions where the sub-grid scale turbulent kinetic energy is about the 30% of the total one, the effects of small scales on droplets evolution can be important and cannot be neglected. To the best of the author's knowledge, this represents one of the few attempts in technical literature to consider the sgs-droplet interactions. The major part of spray combustion studies (see for instance [37, 95]) assumes that more than the 80% of the turbulent kinetic energy is resolved in all the domain and therefore the effects of sgs-droplet interactions are considered as negligible. The same approach has been also employed in the present work.

As long as spray boundary conditions are concerned, a sensitivity analysis was as well performed by Jones and co-workers in [93]: it was shown that the spray distribution has here a huge impact since, using for instance a mono-disperse spray of droplets smaller than 55 μm, the flame can be shorter than the experimental one and it is characterized by high temperature values. In a similar fashion, it was pointed out that if the spray is composed by big droplets (i.e. d $>$ 65 μm), the mixture becomes very lean in the first region of the burner and temperature would be under-estimated [93]. The resulting flow-field together with data obtained on the first experimental section are reported in Figure 2.19. A fair agreement with respect to the experiments was pointed out both in terms of flame shape and chemical species.

The same test article was also numerically investigated by Fossi et al. [96] using a standard steady laminar flamelet model. A computational domain similar to Jones et al. [89] was employed and the most interesting aspect

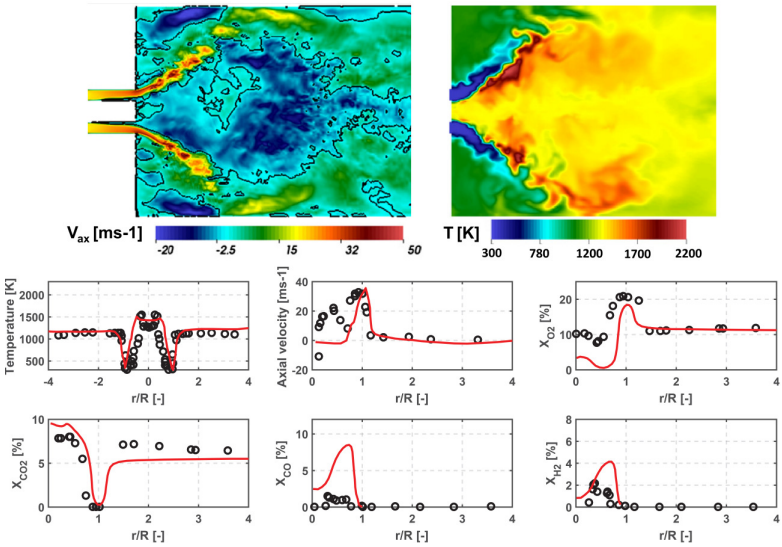

Figure 2.19: Numerical results obtained by Jones et al. [89] in terms of flow-field and temperature contour plots (top) and radial profiles at $z/R = 0.5$ (bottom). Modified from Jones et al. [89].

is surely the comparison between pure n-decane (i.e. 100% $C_{10}H_{22}$) and a mixture of n-decane and toluene (i.e. 60% $C_{10}H_{22}$ and 40% C_7H_8) as surrogates for liquid Jet A-1. No appreciable differences were observed between the two cases and a good agreement in terms of flow-field characteristics was obtained, even if major discrepancies were pointed out as far as chemical species are concerned.

2.4.3 Main features of the numerical set-up

Calculations were carried out on the computational domain shown in Figure 2.20. A coarse grid (M1) consisting of 2.8×10^6 tetrahedral elements and 0.59×10^6 nodes with 5 prism layers for near-wall modelling, with a sizing of 2 mm at the annular duct exit, was firstly generated. A further refined grid (M2), with a minimum size of 1 mm, was then created counting 9.9×10^6 elements and 1.8×10^6 nodes. A cross-section of the two generated meshes is shown in Figure 2.21. As in the previous test case, the quality of the mesh in LES has been verified using the well-known

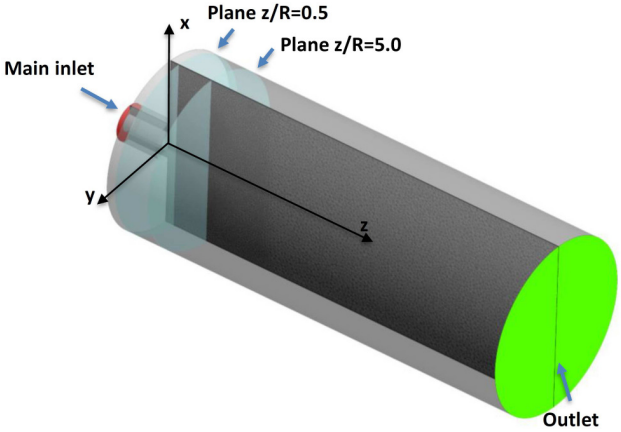

Figure 2.20: Computational domain and boundary conditions used for Sheen Burner.

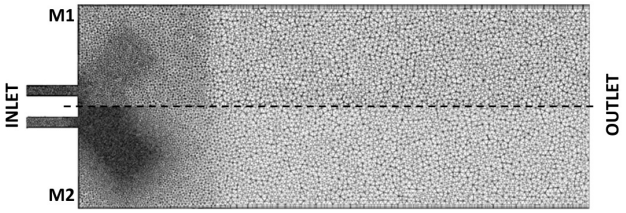

Figure 2.21: Computational grids M1 (top) and M2 (bottom) employed in LES simulations.

Pope criterion [85], that was valid in the entire region where reactions take place for both the computational grids.
From the picture, it is possible to notice the inlet (on the left), located upstream the front plate of the combustor, and the outlet of the domain. In the same figure, the axial position of first and last experimental sections, using R as reference length, is also shown. As in Jones et al. [89], the swirler was not included in the numerical domain and a S_n of 1.22 was prescribed.
Resulting uniform top-hat profiles have been imposed at the inlet, con-

sidering an axial velocity component determined from the experimental mass flow rate (see Table 2.3). From a theoretical point of view, this is not an ideal approach for LES since turbulent inflow boundary conditions are normally required. To verify this simplification, the effect of inflow boundaries has been investigated in isothermal conditions where a good capability of LES in describing the flow field was observed. This can be explained considering that turbulence is mainly generated in the sudden expansion of the swirling jet inside the combustion chamber. Such analysis in non-reactive test conditions is not shown here for the sake of clarity.
The numerical set-up is completed by a uniform static pressure value prescribed at the outlet of the domain, whereas all the other boundaries have been considered as smooth, no slip and adiabatic walls.
Special attention has been also devoted to the liquid fuel modelling and again from a numerical point of view a Lagrangian tracking has been here employed. The injection consists in a hollow wide angle cone (70-80°) for which experimental information of injection temperature and velocity are available from Sheen [86]. Here, with respect to the Sydney Spray Burner, the characterization of the spray BCs is much more challenging since no experimental information is available on the generated drops population. Nonetheless, several experimental works over the last years have been focused on pressure and pressure-swirl atomizers (see [12, 97] and references therein) and different experimental correlations have been derived. Therefore, using an initial guess Sauter Mean Diameter (SMD) determined from the experimental correlation for pressure atomizers reported in [12] and assuming a Rosin-Rammler spray distribution [89], a preliminary RANS sensitivity analysis on both SMD and injection angle has been realized. Consistently with data reported by Jones et al. [89], a mean diameter of 60 μm and a spread parameter for Rosin-Rammler distribution of 3 have been determined as reliable spray boundary conditions for this test case, together with an injection cone angle of 74°.
As far as combustion modelling is concerned, taking into account that in the experimental work a non-premixed behaviour of the spray flame is observed [86], 64 opposed-jet non-premixed flamelets have been used for the FGM database. In all the reported simulations, fuel kerosene has been modelled assuming $C_{10}H_{22}$ (n-decane) as single species surrogate and a detailed reaction mechanism taken from [98] with 96 species and 856 reactions has been used for kinetics.
A time step of 5×10^{-6} s has been chosen for mesh M1 in order to properly control the Courant number in the near injection region. Then, it has been further reduced to 1×10^{-6} s with mesh M2 in order to accurately reproduce the main unsteady features of the flow field.

Considering that the geometry under investigation is 0.55 m long and that in reactive test conditions a bulk velocity of 9 m/s is determined, a flow through time of 6.1×10^{-2} s has been evaluated. Thus, after 2 flow through times required to flush out the initialization and to allow the unsteady flow field to evolve, statistics were collected on 3 FTT in order to achieve a statistically representative solution.
In terms of numerics, bounded central difference schemes for momentum discretisation and a second order implicit formulation for time have been employed. A PISO algorithm with 8 iterations per time step for both M1 and M2 completed the numerical set-up.

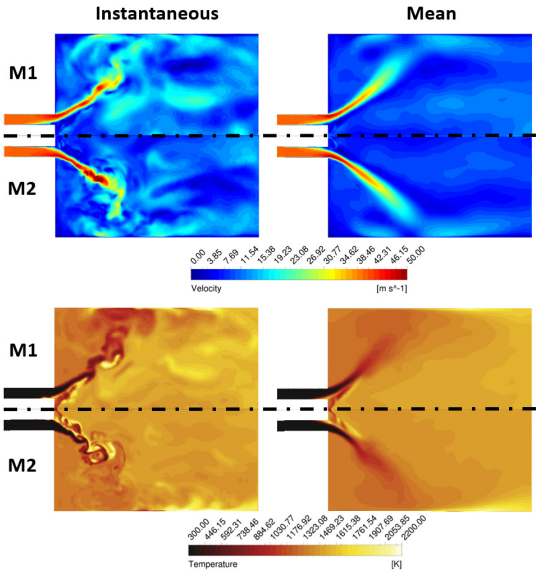

Figure 2.22: Instantaneous (for τ_{ft}=3.5 for M1 τ_{ft}=2.5 for M2) and mean temperature and velocity distributions for Sheen Burner for M1 and M2 [88].

2.4.4 Reactive analysis

Instantaneous and time-averaged contour plots of velocity and temperature obtained on the two grids are shown in Figure 2.22. The air stream,

due to its high tangential component, enters inside the combustion chamber and expands radially creating through the vortex breakdown two main flow structures, i.e. the inner recirculating zone (IRZ) and the outer one (ORZ). Two mixing layers are therefore generated, i.e. one in the region where the swirling jet mixes with the reacting gases and one between the oxidizer and the corner recirculation region. Droplets are injected with high velocity and some of them, characterized by smaller diameters, tend to evaporate immediately after the injection as demonstrated by the low temperature region near the injection location. Conversely, larger droplets are able to pass through this zone and cross the air stream with a reduction of the evaporation rate. Such droplets come up to the side-walls where they complete their evaporation or are captured by the corner recirculation zone. The refined mesh is capable of reproducing smaller turbulent flow structures enhancing the mixing between kerosene vapour and fresh gases.
In Figure 2.23 the resulting axial velocity and temperature profiles for M1 and M2 at several axial distances from the injector location are compared with experimental data. The two series of symbols used for experiments represent the left and right sides of radial profiles in order to provide evidence of the experimental asymmetry.

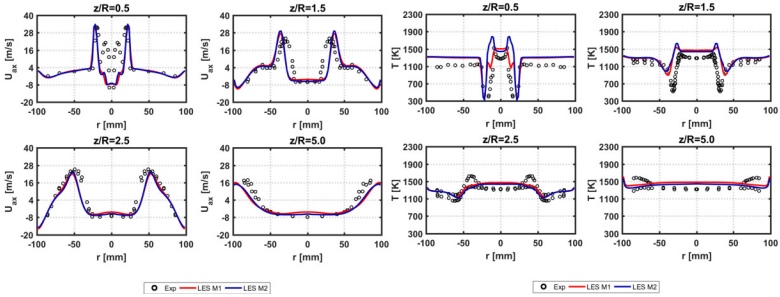

Figure 2.23: Axial velocity (left) and temperature (right) profiles at several axial positions [88].

It should be pointed out that at the first section ($z/R = 0.5$) the experimental velocity profiles show a non-physical double peak probably due to the liquid injection. In this zone, the spray is dense and it probably acts as a noise source in the measured signal. With the exception of this region, the agreement obtained with LES in terms of axial velocity profiles is satisfactory, suggesting that the chosen numerical set-up is able to reliably

describe the topology of the flow field under investigation. A similar agreement has been obtained also in terms of radial and circumferential velocity components, which are not here reported for the sake of brevity. Some remarkable discrepancies can be still determined at $z/R = 1.5$, where the extension of the recirculation region in radial direction is slightly overestimated. A comparable behaviour is also shown by Jones et al. [89] for such section and the authors argued that velocity measurements are still significantly affected by the presence of droplets and that important uncertainties in accuracy of experiments can be therefore inferred.
Regarding temperature profiles a good correspondence with experiments in the outer recirculation region is obtained in all the analysed sections. Performed simulations correctly catch the generation of the mixing layer between fresh air and burnt gases leading to a consistent prediction of temperature evolution at high radii. In particular, the agreement obtained in the corner vortex region is due to the scale-resolving resolution of the flow-field: the intensity of the recirculation is significant and some droplets, which have still to be evaporated, are captured by the carrier phase and burn in the ORZ.
However, a non-physical double-peaked evolution is recovered at $z/R = 0.5$ for grid M1, whereas the finer mesh, even if it avoids such discontinuous evolution, shows a higher maximum value than the experimental data. This is probably related to the spray evaporation that determines a strong sink in the gas phase temperature that is not shown in the experiments. In Figure 2.24, the instantaneous mixture fraction distribution is analysed in order to better understand such a behaviour. Once the spray is injected, considering the high velocity difference between liquid and air in that region, convective heat transfer is high and, because of it, the liquid quickly heats up. Fuel parcels arrive soon to the wet-bulb temperature and a relevant amount of decane vapour is generated. This occurs within the zone identified through the blue line at Z=0.12 (i.e. roughly ϕ=2). This high value of the equivalence ratio leads locally to relatively low temperatures, but immediately downstream, due to the mixing with the swirled flow-field, a stoichiometric region is created that generates the temperatures peaks pointed out in Figure 2.23. Then, the liquid spray, which is not much affected by the carrier-phase interactions and tends to follow nearly the injection angle, proceeds along the combustion chamber arriving at the walls where it completely evaporates.
With respect to experiments, the evaporation rate is probably overestimated in the near injection region and the liquid is nearly immediately saturated. This problem has been detected on both the analysed computational domains. Non-equilibrium effects for instance (see [37] and

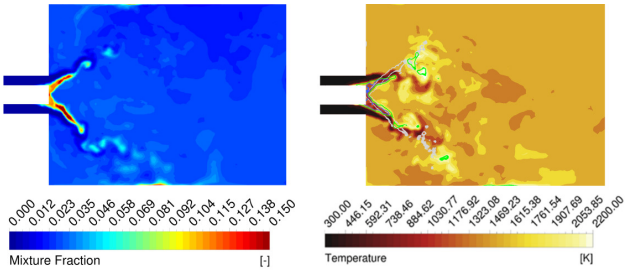

Figure 2.24: Instantaneous mixture fraction contour plot (left) and temperature distribution (right). The white line represents the iso-line at α_l=1e-05, the green line the stoichiometric Z and the blue one Z=0.012.

references therein), which are not here accounted, can be significant in this region. As reported in [37], non-equilibrium conditions normally appear if the evaporation rate is high or if a quick changing on the temperature of the liquid interface takes place (i.e. the two phase flow is subjected to a strong temperature gradient). This situation may occur when droplets from the injection zone approach to the flame front: they have to face high temperature gradients, and therefore the time to relax towards thermodynamic equilibrium is very short.
Another possible explanation of such problem is related to the chosen value of the injection angle. As highlighted in [89], together with the drop-size distribution, it completely controls the reacting flow field: if the spray angle is too narrow, droplets are directly injected in the shear region between the IRZ and the swirling flow field. This region is full of hot gases and a high evaporation rate would be determined together with an under-estimation of temperature in the far-field region since the fuel has been nearly completely consumed. Instead, a too wide injection angle would force the droplets to immediately cross the airflow and to cool down the liquid, leading to the generation of a lean air-fuel mixture with an under-estimation of temperatures in the whole burner. However, results reported so far and in the following in terms of chemical species show that, especially in the far-field, calculations seem able to correctly reproduce the phenomena involved leading to a preliminary validation of the injection set-up.
It is worth pointing out also that a very similar evolution of temperature on the first experimental section was also obtained by Jones et al. [89] with a completely different computational set-up (see Figure 2.19), thereby

validating the approach here proposed.
Moreover, near the burner axis, temperatures are slightly overestimated. Such discrepancy is probably related to the contribution of radiation, which can have a strong impact in the core region of the burner. This has been verified through a RANS sensitivity analysis, where the impact of radiation has been introduced through the Discrete Ordinate Method (DOM) and a weighted-sum-of-gray-gases approach for the calculation of the total emissivity coefficient [99]. RANS simulations highlight a strong impact of radiative heat transfer, which lower the gas phase temperature of the central recirculation zone of roughly 100 K. Therefore, an impact is also expected in LES context and further investigations are surely required on this point. However, models to account for the interactions between turbulence, radiation and liquid phase in scale-resolving simulations are currently under investigation in technical literature and it goes beyond the scope of the present work.
Nonetheless, with the exception of the near-injection zone, calculations agree reasonably well with temperature distributions and chemical species, which are key parameters during the design of spray flame systems, have been also investigated to thoroughly assess the numerical approach. Time-averaged distributions of dry mole fraction (percent) of CO_2 and O_2 are shown in Figure 2.25 for the two computational grids.

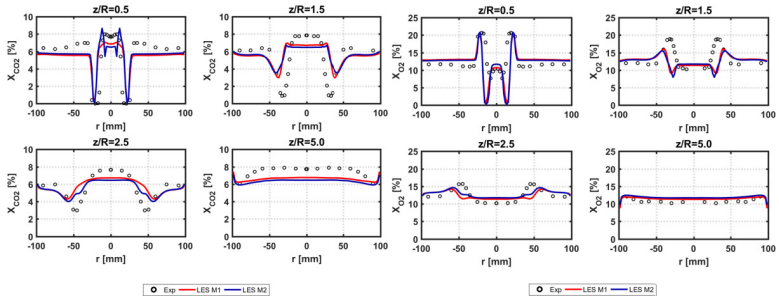

Figure 2.25: Dry (percent) mole fractions of CO_2 (left) and O_2 (right) profiles at several axial positions [88].

The CO_2 concentration levels are well reproduced by LES both in the main and corner recirculation regions. For instance, at the first experimental section, the CO_2 peak is physically captured as well as its evolution along the radius, mainly with the finer mesh. Instead, the calculated O_2 levels are underestimated mainly in the zone near the axis. In fact,

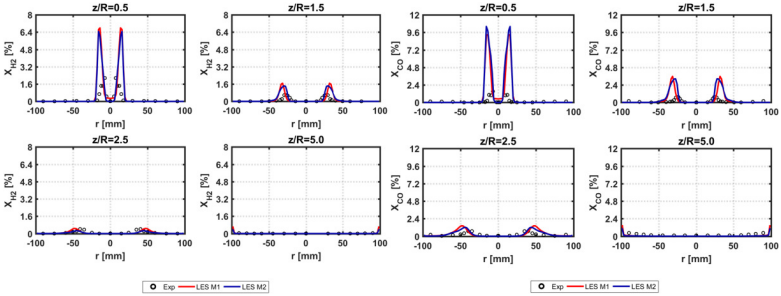

Figure 2.26: Dry (percent) mole fractions of H_2 (left) and CO (right) profiles at several axial positions [88].

experimental profiles are almost constant for r < 10 mm, whereas they show a strong peak in correspondence of the fresh air stream entering the combustor. In LES simulations such behaviour is not reproduced and a higher O_2 consumption is predicted. However, also for O_2 at higher radii, a reasonable agreement with experimental data has been achieved consistently with previous numerical works [89, 96].
It is also interesting to understand the capabilities of FGM in terms of intermediate species and in Figure 2.26, radial profiles of H_2 and CO are reported at the same axial distances. At the first experimental section, where the flame takes place, H_2 levels are overestimated but, going downstream, a good agreement is again determined up to $z/R = 5$ where no reactions occur. Results for CO are similar with an overestimation in the near field and a closer agreement further downstream: the aforementioned temperature peaks and locally the high values of mixture fraction lead to a strong generation of CO, that is quickly converted in CO_2 recovering finally the experimental distribution. An evolution consistent with Jones et al. [89] was again achieved (see Figure 2.19).

2.4.5 Concluding remarks on Sheen Spray Burner

A swirled spray flame, fuelled with Jet A-1, has been here used as further test case to analyse the capabilities of the proposed LES-FGM approach. The proposed numerical set-up was able of reproducing the main characteristics of such non-premixed flame in terms of burning and mixing regions as well as species mass fraction.
A proper description of the flame evolution has been achieved and the

LES-FGM set-up, in a test case where a diffusive burning mode can be stated, proves its potential in predicting pollutant emissions. It is worth pointing out also that the obtained agreement is coherent with results reported by Jones et al. [89] with a much more advanced combustion model, which is also characterized by a higher computational cost with respect to FGM.
Nonetheless, in regions where the effects of liquid fuel are still significant, some discrepancies have been determined. They are probably related to the performances of the employed evaporation model. Locally, an over-estimation of the evaporation rate as well as of the temperature peaks have been pointed out in the near-injection region. The subsequent mixing with the carrier phase and the development of the reacting flow-field are strongly affected by this non-physical vaporization. Then, once the liquid is completely vanished and the decane vapour mixed with air, the experimental evolution is again recovered. In a similar fashion, the chosen spray BCs can have a significant impact on such discrepancies since they completely control the evaporation and mixing of fuel vapour. Further investigations are required on this point, even if these observations clearly point out once again the impact of the liquid phase modelling and of the spray boundary conditions on the obtained reacting flow-field.

2.5 Generic Single Sector (GSS) Combustor

In the light of results shown so far, a preliminary validation of the proposed LES-FGM set-up for spray flames analysis can be stated. Now, the Generic Single Sector (GSS) combustor [100, 101], which represents a simulacrum of an actual lean aero-engine, is studied. This test article is particularly interesting since a prefilmer atomizer is here employed and a strong coupling between the atomization process and the reacting flow field takes place requiring a more detailed modelling strategy to account for the liquid film breakup. In this section, the main findings are reported and part of these results has been already published by the author in [62, 88, 102, 103]. The author would like to express his gratitude to ASME (*American Society of Mechanical Engineers*) society for the permission to use parts and figures of his papers.

2.5.1 Experimental test case

Figure 2.27 shows a schematic and a 3D view of the DLR Generic Single Sector Combustor developed in the framework of the TIMECOP-AE EU Project [100, 101]. The burner was operated in the Single Sector Combustor (SSC), that consists of a combustion chamber with a square cross section of 102 x 102 *mm* and a length of 264 *mm*.

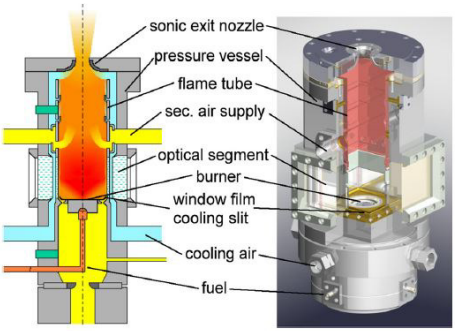

Figure 2.27: Schematic and 3D views of the Single Sector Combustor [101].

In the plenum upstream of the combustion chamber, electrically preheated compressed primary air is introduced through a sonic nozzle, which is used for metering the air mass flow. A quantity of air is diverted from

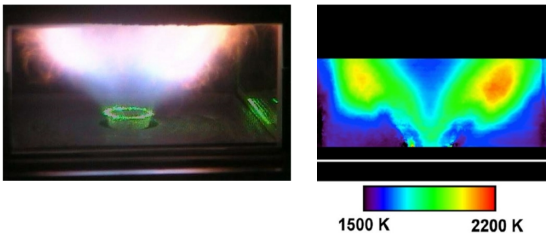

Figure 2.28: Flame visualization and temperature map from OH-PLIF for Test Point A. The white line indicates swirler exit plane [101].

the primary air supply and used to cool the windows. The ratio between the two airflows was always constant during measurements and related to the absolute burner air mass flow. This in turns depends on the main operating parameters such as the combustor pressure and the air preheated temperature [101].
Two reacting (Test A and Test C) and one isothermal configurations (Test E) have been investigated and the respective operating conditions are reported in Table 2.4. The first reacting case A is characterized by low pressure and air temperature, corresponding to the idle condition of an aero-engine burner, whereas case C is representative of a cruise operating point (i.e. with higher pressure and temperature).

Case	**A**	**B**	**C**
Inlet pressure [bar]	4	4	10
Inlet temperature [K]	295	550	650
Burner AFR [-]	-	20	20
Burner Pressure loss [%]	3.6	3.6	3.6

Table 2.4: Operating conditions analysed on the DLR Generic Single Sector Combustor.

As in previous test cases, several experimental diagnostics were employed: LDA for the measurement of the isothermal flow field, PDA for the analysis of velocities and droplet size of the evaporating spray and Planar Laser Induced Fluorescence (PLIF) of OH to determine the temperature distribution. However, beyond the temperature map shown in Figure 2.28 for test point A, no further information for the gas-phase were available in reacting conditions.

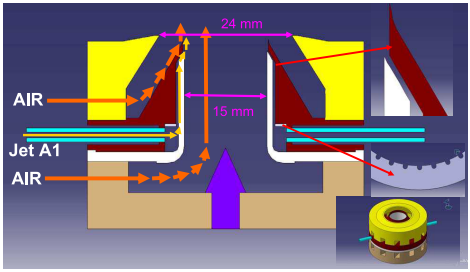

Figure 2.29: Geometrical details of the prefilmer atomizer [101].

Reactions occur especially along the inner shear layer of the spray cone, where high temperatures, determined by the inner recirculation region, and high mixing rates due to free stream turbulence support combustion. The flame shows an evident lift-off and the peak of heat release, that is represented by two distinct lobes at high temperature, is clearly located downstream of the fuel injection with a strong separation that can be justified considering the large pulse-to-pulse evolution of fuel inside the combustion chamber [101].
All the experiments were performed using a prefilming air blast atomizer for fuel injection within a dual co-rotating swirler as shown in Figure 2.29. Two opposite fuel lines supply kerosene (Jet A-1) to an annular fuel channel and to a vertical slot through a circular array of 36 orifices. At the lip, the interactions between the film and the swirled airflow lead to the disruption of the liquid and the generation of droplets, in a process typical of pre-filming air blast atomizers.

2.5.2 Review of previous numerical works

Considering the characteristics of the rig under investigation, numerical studies can be very complex and, in literature, significant results in predicting the flame shape and the spray evolution on this test article have been achieved mainly by Jones and co-workers [25]. Here, the BOFFIN-LES code has been employed to realize a set of LES simulations both in isothermal and reacting test conditions (i.e. respectively Test E and A). The same numerical set-up described in detail in Section 2.4.2 was also employed in the investigation of the present test case. Special attention was devoted to the liquid boundary conditions, which have a huge impact in this test case. As already said in the previous section, the fuel creates a thin liquid film that, due to the interactions with the gas

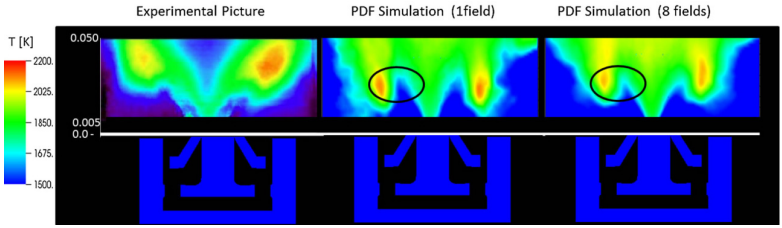

Figure 2.30: Comparison between the experimental temperature map (left) and the contour-plot obtained with one (middle) and eight (right) Eulerian fields obtained in [92]. Adapted from [92].

phase, generates a cloud of droplets at the lip. The film breakup was not modelled by Jones et al. [92], but the spray boundary conditions were determined by means of a trial & error procedure in order to reproduce the experimental data at the first measured plane (i.e. 7 mm from the prefilmer lip). The authors suggested to use a droplet temperature of 295 K and an injection velocity of 50 m/s, estimated from the experimental data at the first section (i.e. 7 mm downstream of the lip). A value of 160° was provided for the injection angle and, for what concerns the droplet size distribution, a Rosin-Rammler PDF was used with a mean droplet size of 6 μm. The spread parameter (q) was not reported in [92] and a value of q=2.5 was derived using further information found in [104]. However, strong uncertainties can be inferred on this parameter that can be extremely important to determine the whole spray evolution.
Employing the above numerical framework, Jones et al. [92] focused the attention firstly on non-reacting test conditions, where the LES set-up proved a satisfactory agreement with experiments both in terms of mean and *rms* velocity components. Then, the study was diverted on Test Point A, where the temperature contour plot shown in Figure 2.30, together with the experimental map, was obtained.
A reasonable consistency of numerical results was achieved even if an overestimation of temperature was found in the center-line region [92]. The two distinct high temperature zones were fairly reproduced, although the lift-off distance was not correctly matched since the distinct lobes are located further upstream with respect to experiments. A detailed analysis on the liquid phase characteristics has been also performed, obtaining again a good agreement with experiments both in terms of liquid velocity and SMD. In particular, one of the most interesting conclusion of the paper is that even if the gas phase temperature basically is not affected

by the number of Eulerian stochastics field employed (see Figure 2.30), spray statistics are considerably different. Remaining differences with experiments are then justified by the authors considering the uncertainty of the employed spray boundary conditions [92].

2.5.3 Main feature of the numerical set-up

As in Jones et al. [92], in this work simulations were firstly performed in isothermal conditions (test point E), so as to make a comparison with the measured velocity field. Then, test points A and C have been studied. For the sake of brevity, the main results and conclusions obtained for the non-reacting point are here just briefly summarized. The interested reader is addressed to Puggelli et al. [102] for further details.
Considering that, a simulacrum of a real burner is here under investigation, in [102] different approaches for two-phase flow turbulence modelling have been compared in isothermal test conditions.
As industrial reference, RANS has been considered with standard $k-\epsilon$ and $k-\omega$ SST models for the eddy-viscosity closure. However, considering that such well-established methods do not include any term related to curvature or rotation effects, it is expected that, in a highly swirled environment, they would lead to a wrong prediction of the recirculation zone.
Hence, a hybrid RANS-LES approach, such as SAS [105], has been evaluated to overcome these limitations. It represents a second generation URANS formulation based on the introduction of the von Karman length scale L_{vK} (see Equations 2.11) into the turbulence equations in order to dynamically adjust the resolved structures and locally reduce the eddy viscosity.

$$L_{vK} = \kappa \left| \frac{U'}{U''} \right| ; |U'| = \sqrt{\frac{\partial U_i}{\partial x_j} \frac{\partial U_i}{\partial x_j}} ; |U''| = \sqrt{\frac{\partial^2 U_i}{\partial x_j^2} \frac{\partial^2 U_i}{\partial x_k^2}} ; \tag{2.11}$$

The SAS model remains in RANS mode in zones characterized by low instability, while it provides LES-like results in the unsteady regions of the flow field. However, if spatial and temporal discretization is not adequate to correctly solve the LES part, SAS simulation will permanently stay in RANS mode due to an over prediction of turbulent viscosity. The interested reader is addressed to [105] for a detailed description of such numerical approach.
Clearly, to solve further smaller turbulent structures, LES has been also evaluated. The unclosed sub-grid stress tensor, coherently with the work shown in previous sections, has been closed through a dynamic

	RANS	SAS	LES
N° of cells (10^6)	1.00	3.28	3.28 (c) / 8.80 (f)

Table 2.5: Mesh size for the different turbulence model (c=coarse, f=fine).

Smagorinsky-Lilly model [65].
Computations were carried out on the computational grids depicted in Figure 2.31 consisting of tetrahedrons with a layer of 5 prisms close to the wall. A coarse mesh (M1) was created at first with a total amount of $3.28M$ elements and $0.76M$ nodes, with a mesh size of 0.75 mm at the swirler exit. A further refined grid (M2) with a minimum mesh size of 0.5 mm was then generated to be tested with LES, counting $8.80M$ elements and $1.82M$ nodes. RANS simulations were on the contrary performed on a 90° mesh, taking advantage of the geometric periodicity of the domain, thus easing the convergence and reducing the computational effort. A summary of the grids used in the present work is reported in Table 2.5. From Figure 2.31, it is possible to notice the inlet (on the left) and the converging outlet. Mass flow rates were prescribed at the inlets of both air and coolant (where the slot was modelled by means of a patch), whereas static pressure was imposed at the outlet, following the data previously reported in Table 2.4.

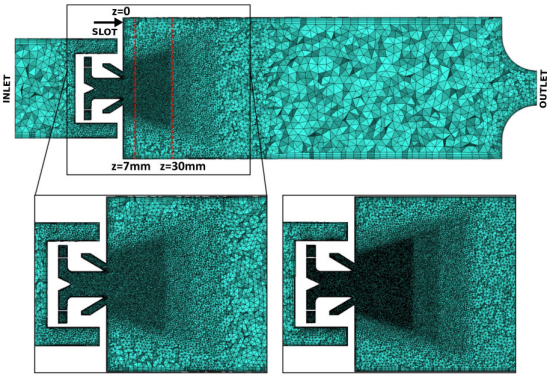

Figure 2.31: Computational grids: coarse (top and bottom left) and fine (bottom right).

No turbulence generator has been employed at the inlet boundaries, because the main turbulent structures are generated when crossing the swirler geometry. All the walls were treated as smooth, no slip and adiabatic. In the same figure is also shown the position of first and last experimental section, for which measurements of velocity and mean diameter for the liquid phase are available.
The time step ($d\tau$) used for the calculations changes depending on the mesh and the turbulence models considered. Scale Adaptive Simulations were performed with 3e-6 s, whereas the time step was reduced for Large Eddy Simulations (1e-6 s and 8e-7 s for coarse and fine mesh), so as to ensure a control on Courant number in the region of the swirler and appropriately resolve the turbulent flow structures reproduced by the scale resolving models. Moreover, considering that the geometry here studied is 0.38 m long and that, in non-reactive test conditions, an average bulk velocity of 8 m/s is predicted, a flow through time of 4.3×10^{-2} s can be evaluated. Hence, after an initialisation period of 2 flow through time required to flush out the initial conditions and to allow the underlying flow field to develop, the statistics were collected over 3.5 FTT. In reactive case, velocities are higher leading to a mean flow through time around 8.6×10^{-3} s: 17200 time steps were initially required, followed by 30100 time steps for statistics calculation. In terms of numerics, bounded central difference schemes for momentum discretisation and a second order implicit formulation for time have been employed.
Employing such numerical framework, in Puggelli et al. [102], it has been shown that, in isothermal test conditions, RANS approaches are completely unreliable. Steady state methods lead to significantly underestimate the *rms* values, which are essential for the reacting point. Instead, profiles obtained with SAS and LES proved to fit well against experiments and data previously achieved by Jones et al. [92]. In particular, it was pointed out that SAS led to a resolution of the turbulent flow-field consistent with LES with a lower CPU cost on this test case.
In order to integrate this last observation, in [102], a comparison of computational costs between scale resolving (SAS, LES) and RANS calculations has been carried out. Simulations were realized using 16 cores of a Linux cluster comprising Intel Xeon E52665 2.40 GHz CPUs. For RANS simulations, roughly 790 CPU hours were required, whereas for SAS and LES on the same computational domain 6500 CPU hours and 13000 CPU hours were respectively needed. It was pointed out that obviously RANS has undeniable advantages in terms of computational costs, but it was not able to correctly characterize the physics under investigation. Conversely, SAS approach, required half of CPU cost compared to LES.

The achieved agreement in non-reacting test conditions led to validate the employed scale resolving approaches as well as the proposed numerical set-up in terms of boundary conditions and mesh sizing. As already mentioned, these data have been not reported here for the sake of brevity and further details can be found in Puggelli et al. [102]. Considering this preliminary assessment, the attention is here diverted on the reacting test point.

2.5.4 Reactive analysis (Tp A)

Before going in detail with the main results obtained, some further aspects of the computational set-up for reactive test conditions have to be clarified.

First of all, using the same modelling assumptions reported in Jones et al. [92], no effort has been prompted at the beginning of this study to introduce liquid film breakup. Collisions, coalescence and agglomeration effects have been therefore overlooked.

In Puggelli et al. [102], where several scale resolving CFD models have been applied for the simulation of the present test case in reacting test conditions (see Figure 2.32 for a comparison between SAS-EDM and LES-FGM), a preliminary analysis on spray BCs was performed. A huge dependence of results on spray BCs was first of all highlighted. In particular, it has been pointed out that the mean diameter of 6 μm reported by Jones et al. [92] could be explained only under the hypothesis of a prompt atomization regime, which can be normally observed in different physical situations. In particular, it is effective if the air stream impinges on the liquid film at an appreciable angle or at a velocity that precludes wave formation. It does not seem the case of the present test case.

Therefore, Puggelli et al. [102] proposed another set of liquid BCs, representing a combination of SMD, injection velocity and angle. The same has been determined through a trial and error procedure relying on a geometrical analysis and correlations available from literature. This set-up of spray BCs is here used: employing a Rosin-Rammler PDF, a mean diameter of 30 μm, a spread parameter of 2.5, an injection angle of 10° and an axial velocity of 30 m/s have been employed to have a good agreement with experiments.

Secondary breakup effects have been included through the well-known Taylor Analogy Breakup (TAB) model [106] since the maximum Weber number inside the numerical domain was found to be lower than 100 in all the simulations realized. Coherently with the Sheen test case, properties taken from [107] have been employed for the decane fuel ($C_{10}H_{22}$) and the same reaction mechanism from [98] has been used for chemical

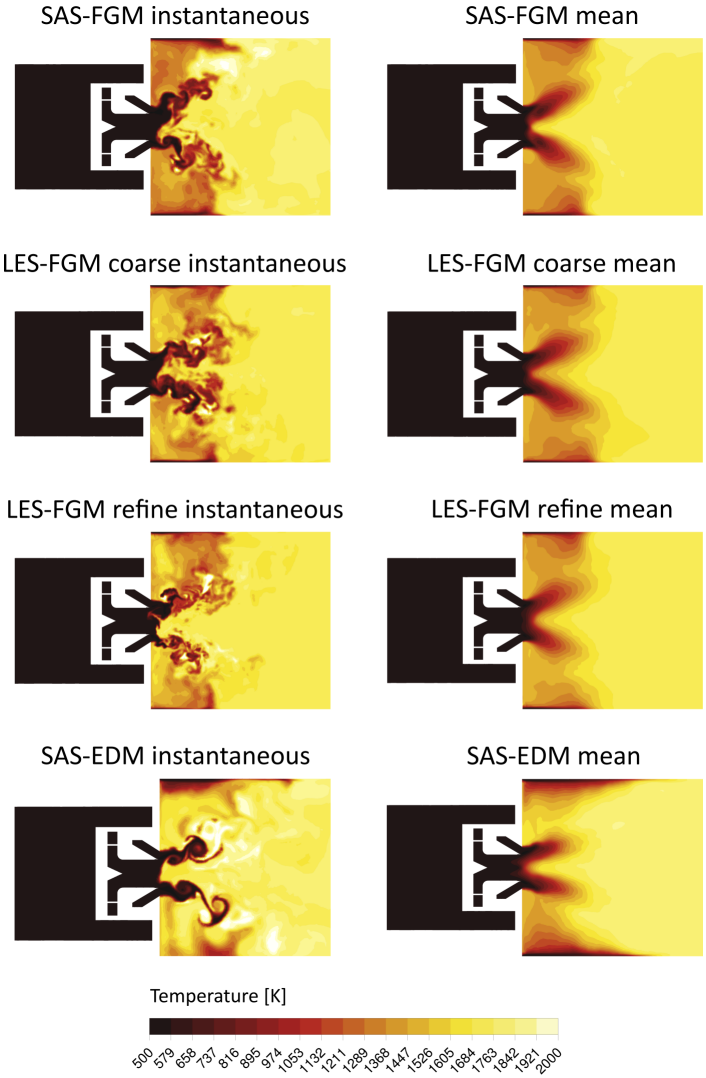

Figure 2.32: Temperature contours obtained with FGM and EDM combustion models with several resolutions of the turbulent field and mesh sizes [102].

reactions. Regarding combustion modelling, 64 premixed flamelets have been considered for the FGM database.
In this test article, in order to further assess the performances of FGM, a comparison is carried out with results obtained using the same numerical set-up with the Artificially Thickened Flame (ATF) model.
The ATF implementation available in ANSYS® Fluent v.16.2 is retained for this study and a brief description of the model is reported hereinafter. It is worth pointing out that, in technical literature, improved formulations of ATF can be recovered, based on a dynamic formulation which are able to avoid non-physical stretching of the flame [27, 108], but this is not the main focus of the present analysis.
Hence, considering a constant thickening factor $F = \frac{N\Delta}{\delta_l}$ where Δ is the grid size, δ_l is the laminar flame thickness and N is the number of points inside the flame (i.e. equal to 5 in this work), the following filtered transport equation for the generic species mass fraction Y_k is solved:

$$\frac{\partial \bar{\rho}\tilde{Y}_k}{\partial t} + \boldsymbol{\nabla} \cdot \left(\bar{\rho}\tilde{\boldsymbol{U}}\tilde{Y}_k\right) = \boldsymbol{\nabla} \cdot \left(\bar{\rho} D_{k,eff} \boldsymbol{\nabla}\tilde{Y}_k\right) + \frac{\bar{\rho} E \bar{\dot{\omega}}_k}{F} \tag{2.12}$$

where E is an efficiency function, introduced to increase the flame speed and to compensate the reduction of flame surface determined by the thickening procedure. In the present work, a formulation for E based on the Zimont turbulent flame speed closure [109] is used where the efficiency function becomes the ratio between the sub-grid turbulent flame speed at length scale $F\Delta$ and at scale Δ as reported below [74].

$$E = \frac{1 + A\left(\frac{u'}{U_l}\right)^{3/4}\left(\frac{\Delta}{\delta_l}\right)^{1/4}}{1 + A\left(\frac{u'}{U_l}\right)^{3/4}\left(\frac{\Delta}{F\delta_l}\right)^{1/4}} \tag{2.13}$$

where A is a model constant, u' represents sub-grid velocity fluctuations, whereas U_l and δ_l are the laminar flame speed and thickness. In Equation 2.12 the effective species diffusivity ($D_{k,eff}$) is also included and in the ATF modelling it is computed as:

$$D_{k,eff} = D_{k,lam} E \left(1 + (F-1)\,\Omega\right) + D_{k,turb}\left(1 - \Omega\right) \tag{2.14}$$

where $D_{k,lam}$ is the laminar diffusion coefficient of Y_k, whereas Ω is a flame sensor introduced to apply the thickening procedure just inside the flame and to avoid non-physical behaviours in regions of pure mixing or in burnout zones. In the present study, such flame sensor has been

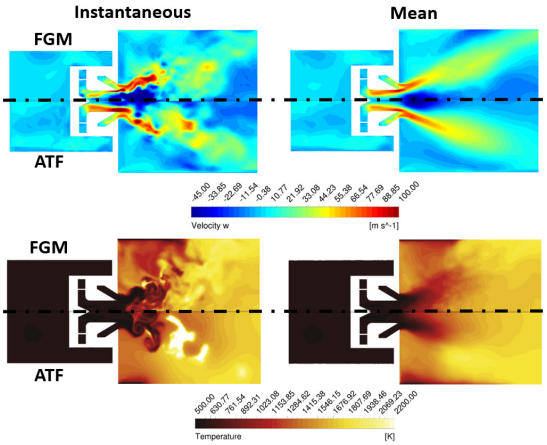

Figure 2.33: Instantaneous (for τ_{ft}=2) and mean axial velocity and temperature distributions obtained with FGM and ATF [88].

calculated following the formulation reported below:

$$\Omega = \tanh\left(\beta \frac{\bar{R}}{max\left(\bar{R}\right)}\right) \tag{2.15}$$

where $\bar{R}$ is the spatially filtered value of the reaction rate and β is a constant with a value of 10. It should be also pointed out that for the energy equation the effective thermal conductivity k_{eff} is calculated consistently with $D_{k,eff}$ by using Equation 2.14. As already explained in Chapter 1, this model is really interesting in the context of partially premixed combustion because it has been widely applied on several configurations in technical literature showing significant capabilities [27, 28]. In the ATF context, a two steps global mechanism from [110] has been employed and the laminar flame speed, which appears in Equation 2.13, has been evaluated using the experimental correlation provided by Moghaddas et al. [111].
The time step used in calculations has been therefore raised according to combustion modelling. For ATF calculation a value of 1×10^{-6} s has been chosen, as suggested in [102], in order to control the Courant number and properly reproduce also the main characteristics of the liquid phase. Then, it has been reduced to 8×10^{-7} s in FGM calculations since higher

velocity peaks in the swirling flow have been determined. Mesh M1 has been used in this part of the work since, as reported in isothermal test conditions [102], no appreciable improvements have been obtained with mesh refinement. After an initialisation of 2 flow through times, the statistics were gathered over 3 FTT. A PISO algorithm has been employed requiring respectively 10 iterations per time step for ATF and 8 for FGM computations.

Below, a resume of the main results obtained with this numerical set-up is reported and the interested reader is addressed to Puggelli et al. [88] for further details and data.

Figure 2.33 shows the resulting mean and instantaneous velocity and temperature distributions obtained both with FGM and ATF. The co-rotating double swirler provides to the incoming air a strong tangential component. This leads to the generation of a swirling flow with a stable pocket of hot gases located around the centerline. The flame shows a standard V-shape with an appreciable lift-off. From a qualitative point of view, the two combustion models show similar results in terms of instantaneous and mean flow field, whereas the hot distinct lobe, which in ATF computation is located in the shear layer between the outer and the inner regions, is completely missed in FGM. To better describe this point, the circumferentially averaged heat release rates obtained with ATF and FGM are mapped in Figure 2.34, where the same contour from experiments is also reported. The area of each image is the same specified in [101] (i.e. 105 mm $\times$ 80 mm) and pictures are scaled between local minimum and maximum values since the contour range of experiments is not declared in [100, 101]. In the same image, red colour lines indicate the 10%, 20% and 50% of the maximum of the circumferentially averaged fuel evolution, while red points represent the radial positions at z=7 mm where particles were sampled to obtain PDF spray distributions.

In both simulations the peak of heat release is located along the inner surface of the spray cone due to the high level of mixing and turbulence generated by the two recirculation zones. The fuel vapour, produced after the film breakup, mixes with the incoming swirling flow leading to the generation of a lean mixture and of a stable flame that is sustained by the high temperatures of the central recirculation bubble.

The ATF model seems to be able to reasonably reproduce such stabilization process, whereas the peak of heat release in FGM is located further downstream. This clearly has an impact on the resulting flame position and temperature distributions, which are shown in Figure 2.35 on the same experimental window. It can be clearly stated that the predicted flame height is highly overestimated, especially in FGM context. In fact,

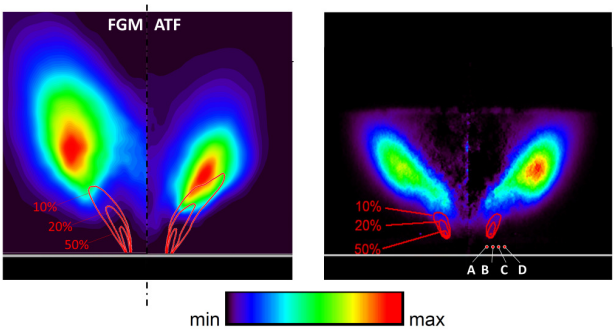

Figure 2.34: Iso-contours of heat release rates obtained with FGM and ATF against the experimental map (modified from [101]). Red iso-lines represent different levels of fuel distribution. The white line indicates the burner exit plane. The red points A, B, C, and D on the experimental map highlight the radial positions where spray PDF is evaluated (see Fig. 2.39)[88].

computing the flame position as the point of maximum gradient of OH mass fraction, accordingly with [101], a flame lift-off around 34.8 mm has been determined with FGM, which is significantly higher than the experimental value (i.e. 17 mm).
This overestimation leads to determine a non-physical interaction between the flame and the combustor walls. Such behaviour of FGM can be theoretically related to the finite rate closure used in Equation 2.6 for the reaction progress equation. In fact, as already shown in [112], to properly determine the flame position, a turbulent flame speed closure for Y_c-equation, based on the expression proposed by Zimont et al. [109], would be preferred. However, the exploitation of such closure does not lead to appreciable improvements as reported in Puggelli et al. [88].
In the light of these results, the issues detected with FGM could be explained considering that probably the premixed asymptotic flame behaviour, supposed in flamelet generation, is not completely representative for the flame under investigation. In order to verify this aspect, a regime indicator has been introduced to highlight the regions where the flame presents a premixed or diffusive burning mode. The flame index Θ has

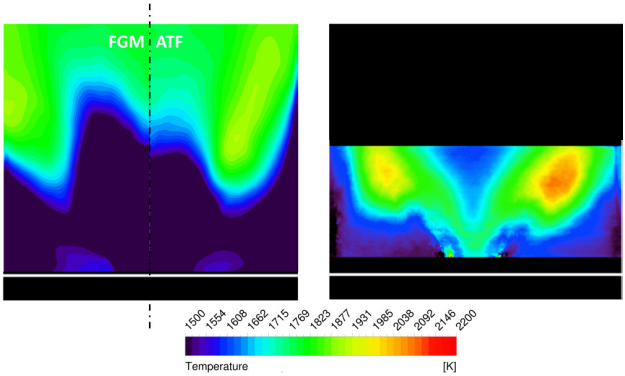

Figure 2.35: Temperature distributions obtained with FGM and ATF against the experimental map (modified from [101]). The white line indicates the burner exit plane [88].

been defined in the present work as proposed by Domingo et al. [113]:

$$\Theta = \left(\frac{\nabla Y_F \cdot \nabla Y_O}{|\nabla Y_F \cdot \nabla Y_O|} \right) \tag{2.16}$$

where Y_F and Y_O are respectively the fuel and oxidizer mass fractions. It must be stressed that the chosen definition of the flame index does not examine the underlying physical processes that contribute to flame structure in each regime and it is not able to take into account certain conditions of counterflow partially premixed flames [29]. Yet, it can be quickly evaluated for a preliminary assessment of flame evolution. It is typically argued that a positive value of Θ indicates a local premixed combustion, whereas a negative one states a diffusive condition. In Figure 2.36 the evolution of Θ obtained through LES-FGM is reported. The red iso-line states a T=1800 K, while black iso-line characterizes Θ=0. On the left side of the figure the spray evolution is also super-imposed.
The flame index accurately predicts a leading premixed behaviour even if non-premixed zones exist immediately after the liquid injection and where temperatures higher than 1800 K have been detected. In particular, it is interesting to point out that the spray is able to go beyond the red-isoline and completely evaporate in the near-wall region with a diffusive burning mode. The flame seems to be stabilized through the co-existence of a premixed flame in the primary region of the burner and a diffusive one

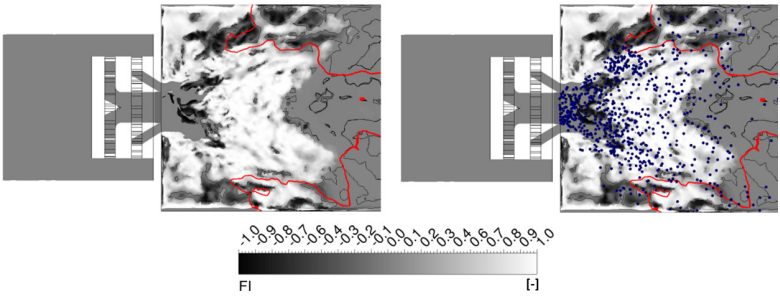

Figure 2.36: Flame Index (FI) distribution obtained with LES-FGM model on the fine mesh. See text for explanations.

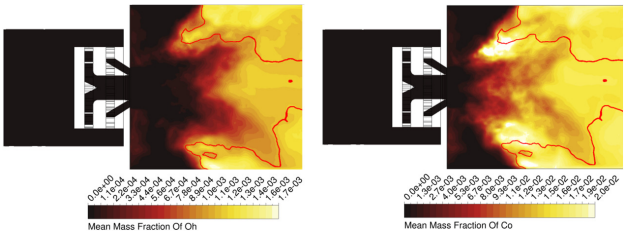

Figure 2.37: Time averaged contour plots of CO and OH mass fraction obtained with LES-FGM.

in high temperature zones. These latter regions represent also the main sources of heat release as further demonstrated in Figure 2.37 by the CO and OH mass fraction contour plots. It is worth pointing out also the presence of a diffusive zone immediately after the injection that is probably controlling the flame stabilization.

The premixed assumption is clearly not everywhere satisfied, leading locally to a wrong prediction of temperature and spray distribution that can preliminary justify the non-physical flame evolution obtained with FGM.

Nevertheless, the ATF model, which is based on completely different modelling assumptions, shows globally a similar behaviour, even if it is able to locate two lobes at higher temperature similarly to experiments. The position of heat release peaks is quite reliably determined as well as the hot zone close to 1800 K around them. It seems also to better

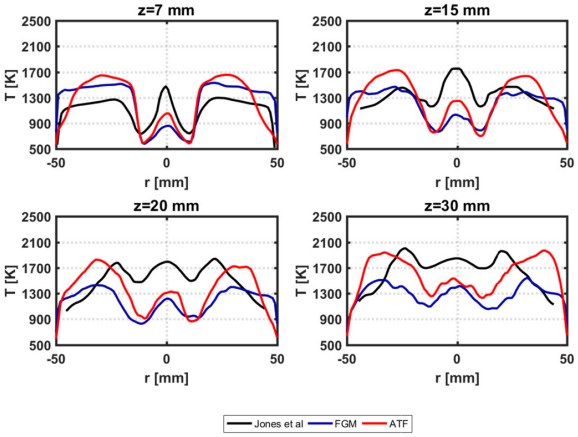

Figure 2.38: Temperature profiles obtained with FGM and ATF at several axial distances [88].

capture the flame lift-off, even if the improvements with respect to FGM are limited to the downstream region of the burner. In Figure 2.38, the radial temperature profiles obtained with FGM and ATF at several axial distances are reported and compared with the results shown by Jones et al. [92]. It should be stressed that experimental temperature profiles are not available for this test case. Therefore, the author decided to take as reference the only numerical data available in literature [92], which, as already said, shows an overall good agreement with experiments.
Even if, mainly at z=30 mm, the temperature lobes obtained with ATF are in line with those shown by Jones et al. [92], both the combustion models strongly underestimate temperature levels in the near injector region, while they over predict the heat release in the outer recirculation zones.
Hence, considering that all the analysed combustion closures lead to similar results, such strong discrepancies cannot be just related to the deficiencies of the adopted models.
On the contrary, they are probably related to the chosen spray boundary conditions. This can be proved by analysing again Figure 2.34, where contour lines of the liquid fuel distribution were also shown. It should be pointed out that the iso-lines of 20% and 10% present a stronger

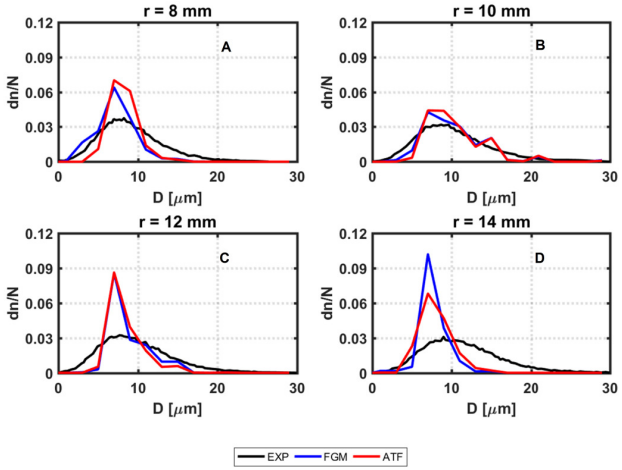

Figure 2.39: PDF spray distributions obtained with FGM and ATF at z=7 mm at four radial positions (see Figure 2.34 for details about the four locations)[88].

penetration with respect to experiments and this can be related also to an incorrect injection set-up.
Hence, the author decided to focus the attention on the spray evolution and how this is affecting the reacting flow field. Results obtained from such spray analysis are reported in the following paragraph.

Spray analysis Figure 2.39 shows the evolution of the droplet size Probability Density Function (PDF) at z=7 mm at four radial locations for both ATF and FGM calculations. The numerical distributions were obtained from a data sampling of the liquid phase over one flow-through time in order to achieve a smoothed evolution. The experimental data are characterized by a rather wide range of diameters (i.e. from 1 μm to 20 μm) and the spreading of the distribution is nearly constant in all the radial positions. The heat up and evaporation of the kerosene, caused by the flame, lead to an experimental statistic mode value around 6 μm with a significant number of droplets with higher diameters that have still to evaporate. This clearly shows the coexistence of a premixed combustion occurring with vapour already generated by fuel vaporization at z=7 mm and non-premixed combustion from liquid droplets that will

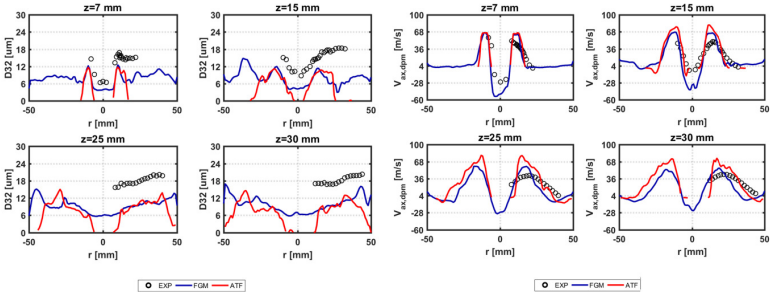

Figure 2.40: Comparison of SMD (left) and axial velocity (right) obtained with FGM and ATF against experimental data [88].

conclude their life further downstream. From a computational point of view, the broadening of the probability distributions is much smaller and, mainly at higher radii, the numerical PDFs are gathered in few microns. A considerable amount of spray volume is clearly related to diameters around 6 μm, whereas the bigger classes are characterized by a negligible number of particles. Such evolution of the PDFs along the radius is directly related to the distribution of the spray SMD and axial velocity, that are shown in Figure 2.40 for several distances from the swirler. The two considered combustion models work in a quite similar way, even if an enhanced spray spreading has been recovered in FGM. Such difference is probably related to the obtained different resolution of the flow field since in the FGM context much more turbulent structures are caught leading to a stronger interaction between spray and turbulence. Furthermore, with FGM lower temperature peaks have been appreciated and a slower evaporation process can be inferred. Nevertheless, a general underestimation of SMD can be observed, which is directly related to an overestimation of the axial velocity since the numerical parcels have a low Stokes number and are easily carried by the gas phase: the numerical spray population is therefore characterized by too low diameters.
In order to have a global overview of the spray distribution, map of liquid volume flux for the 16 μm class is shown in Figure 2.41 for ATF model. FGM is not shown for the sake of clarity since the achieved distribution is nearly the same. It should be pointed out that, in the dense spray region where experimental data are not available, the mass flow associated to 16μm is really high and tends to quickly decrease further downstream. The axial position of the volume flux peak is strongly under

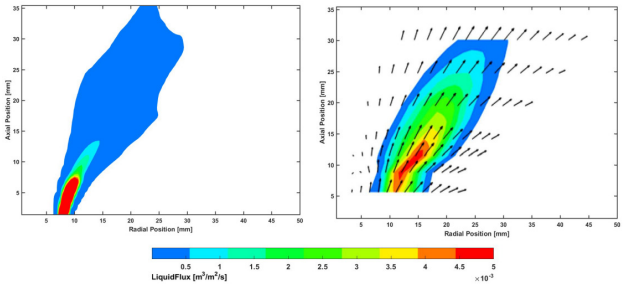

Figure 2.41: Comparison of liquid volume flux for the 16 μm class obtained with ATF against experimental data (adapted from [101])[88].

predicted and therefore the contribution of this class at z=15 mm, where the flame stabilization takes place in experiments, is nearly negligible. In order to have a deeper insight on the spray dynamics of the remaining spray population, an analysis of the axial velocity of four size classes is shown in Figure 2.42. The four classes are centered on 2 μm, 8 μm, 16 μm and 32 μm and the width of each one is $\pm$ 10 % of the central size. The 2 μm droplets can be used as a reasonable approximation of the gas phase velocity and it should be pointed out that the numerical calculations are rather in line with experiments even if higher peak values are predicted. An equivalent agreement has been obtained also for the 8 μm class whereas, considering bigger droplets, not enough particles have been collected leading to a distribution characterized by a negligible radial dispersion.
This comparison, together with the information obtained from the PDFs, proves that the employed liquid boundary conditions, which play a key role for the whole test article, are generating a spray with a mass distribution centred on too small diameters with respect to experiments.
The following preliminary conclusions can be introduced:

- The injected spray population strongly interacts with the gas phase and, at the first experimental section (i.e. z=7 mm), is composed by a high number of particles centred in a narrow diameter range. The two combustion models behave in a similar manner, suggesting once again that the spray modelling is the key parameter of the present test article.

- This phenomenon leads to completely mislead the flame stabiliza-

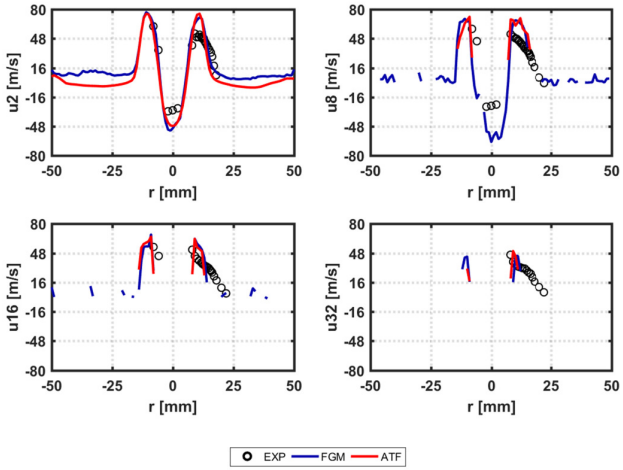

Figure 2.42: Profiles of axial velocities at axial position 7 mm for different size classes obtained with FGM and ATF[88].

tion process further downstream. In fact, the generated droplet population is largely neglecting the initial contribution of the smallest classes in producing an homogeneous mixture able to ignite the flame in the central part of the burner, and it is also strongly overlooking the effect of bigger particles in creating the two high temperature lobes.

- The proposed comparisons prove that a wider diameter distribution is required at the injection location in order to appreciate all the physical phenomena previously described. Ultimately, the liquid BCs are completely controlling the subsequent reacting flow-field.

In this work, to overcome this problem and to gain a more general resolution of spray boundary conditions, a multi-coupled approach, developed in OpenFOAM® by a former PhD student [114] and based on the inclusion of the liquid breakup through a thin film approximation, has been employed. It is worth stressing that this represents the first attempt in literature of studying the test case under investigation focusing the attention on the analysis of the film evolution coupled with the reacting flow-field. For the sake of clarity, such analysis is here briefly summarized and the interested reader can refer to Puggelli et al. [103], where all the

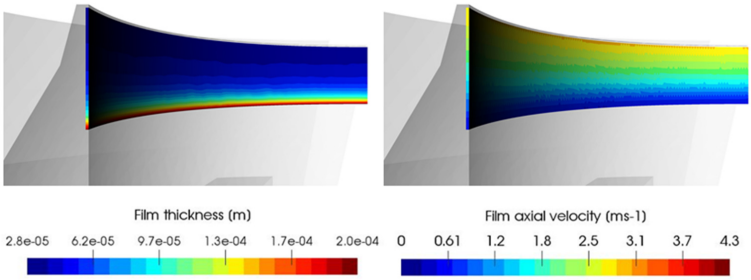

Figure 2.43: Evolution of film thickness together with its axial velocity [103].

results are presented in detail.
The solution of the liquid film evolution, shown in Figure 2.43, over the pre-filming surface suggested that the interaction between the gas phase and the liquid film is an important aspect to be considered for a reliable simulation of this air-blast systems since it has a strong impact on both velocity and fuel temperature at the atomizing edge.
The role of primary breakup has been investigated by performing a sensitivity analysis to different theoretical and correlation-based models. The impact of fuel heating-up all along the prefilmer surface has been as well investigated. The results obtained from this analysis, performed using RANS simulations, show that the various formulations predict a quite different diameter, affecting the mixing field in the downstream region. The well-known Eddy Dissipation Model (EDM) has been employed [115, 116] in this part of the study as far as turbulent combustion modelling is concerned. Table 2.6 summarizes the resulting spray BCs derived from this sensitivity analysis.
In [103], such set of spray injection parameters was then applied in SAS framework determining a fair agreement with experimental data both in terms of PDF and spray characteristics (i.e. SMD and axial velocity) as shown in Figure 2.44 and 2.45. The simulation was able to correctly represent the evolution of the spray mainly in the near injection region, where the impact of spray boundary conditions is more relevant. From an experimental point of view, initially the SMD value is nearly constant in radial direction with the exception of the recirculation region where it is abruptly reduced. Going further downstream, the diameter shows a standard evolution for a hollow-cone spray with a radial distribution that

Quantity	Value
SMD [μm]	52.4
U_{liquid} [ms-1]	1.5
θ [°]	0
T [K]	295
q [-]	2

Table 2.6: Spray boundary conditions at injection location obtained from the film sensitivity.

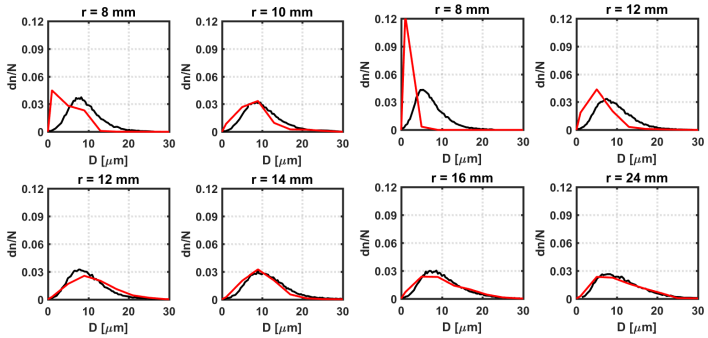

Figure 2.44: PDF spray distributions at z=7 mm (left) and z=15 mm (right) at four radial positions (see Figure 2.34 for details about the four locations) [103]. Experiments in black and numerical results in red.

tends to be progressively wider and uniform. Calculations were able to reproduce these effects even if diameters predicted at the last experimental sections (i.e. z $\geq$ 20) were still under predicted.
However, beyond such discrepancies, thanks to such detailed investigation on film breakup, the global spray evolution was reliably reproduced [103]. Based on these results, the spray BCs provided in Table 2.6 have been then applied in conjunction with the FGM combustion model. Considering the flame index distribution shown in Figure 2.36, a diffusive flamelet tabulation strategy has been adopted. A SAS approach has been instead employed as long as the turbulence resolution is concerned. In fact, based on results in isothermal test conditions [102], it was able to determine a flow-field representation coherent with LES together with a lower CPU cost.

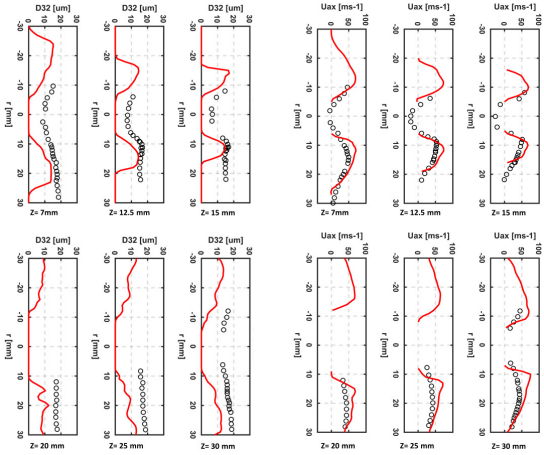

Figure 2.45: Comparison of SMD (left) and axial velocity (right) profiles obtained after the film sensitivity against experimental data [103].

In Figure 2.46, the resulting spray droplet diameter distribution superimposed on the iso-line indicating zero velocity (red line) and the one specifying a T=1500 K (black line) is shown. In the same figure, also the contour plot of discrete phase temperature is reported.
An inner recirculating zone is generated by the swirled flow field and arrives now inside the swirler. The spray evolves in the region between the IRZ and the corner vortex and its evolution is completely controlled by the shear stresses locally generated. A zero injection angle is imposed to the spray based on Table 2.6 and the liquid parcels evolve just following the instantaneous flow-field locally predicted. Another mixing region is also generated due to the air slot in the near wall zone, but it does not interact with the spray. The liquid injected is progressively heated-up by the gas phase up to the wet-bulb temperature that is reached just by the larger droplets. The spray can still be found even after crossing the iso-line at 1500K involving a very complex flame structure: immediately after the injection, smallest particles evaporate and generate a mixture that creates the flame front highlighted by the black line. Then, bigger droplets advance and evaporate further downstream where the peak of heat release is expected.
Droplets dynamics can be theoretically divided in two subsequent steps as clearly shown in Figure 2.47, where iso-lines of spray diameters to-

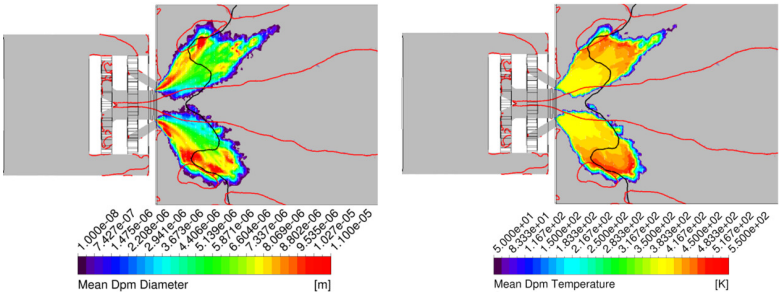

Figure 2.46: Time averaged contour plots of droplet diameter and temperature. The red line is the iso-contour of zero velocity and the red line is the iso-contour at T=1500K.

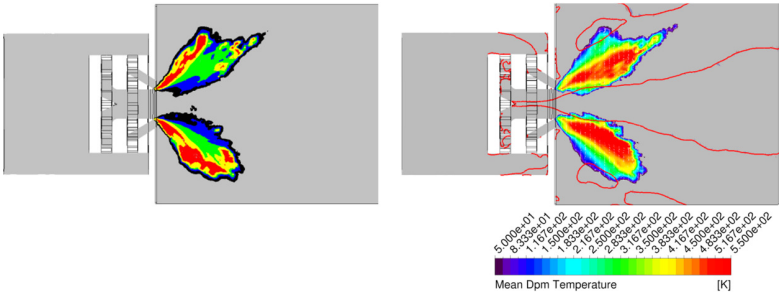

Figure 2.47: Time averaged droplet diameter (left) and axial velocity (right) contour plots. See text for explanations about iso-lines.

gether with the mean axial spray velocity plot are shown. Colours on the left-side of the figure stand for different diameter classes: black line for 1.5<d<3.5μm, blue for 3.5<d<5.5μm, green for 5.5<d<7.5μm, yellow for 7.5<d<9.5μm and red for the rest of the spray.

- A first region can be identified that is characterized by the presence of the whole injected droplet population. Smaller particles are concentrated on the spray edge and immediately assume high velocity due to their low Stokes number. Such particles evaporate and feed the flame in the first part of the burner. Bigger particles instead are enclosed in the center of the spray and tend to have a ballistic trajectory with lower velocities.

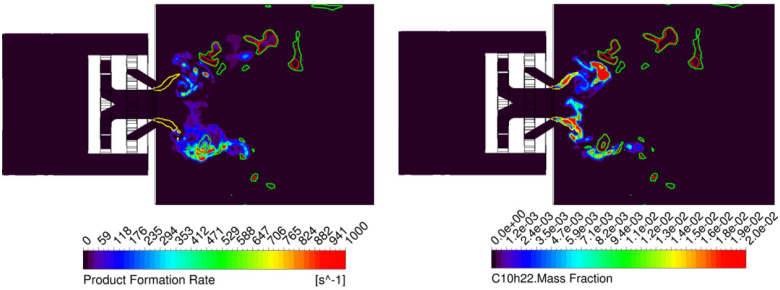

Figure 2.48: Instantaneous contour plots of heat release (left) and decane vapour mass fraction (right). See text for explanations about iso-lines.

- A second zone, pointed out mainly by red and yellow iso-lines, can be as well recognized where only larger droplets are still present. Such zone corresponds to the discontinuity in the mean spray velocity since such particles still preserve their own momentum. These droplets have still to heat-up and burn locally with a non-premixed burning mode.

Such evolution of the liquid phase completely determine the reacting flow-field. In Figure 2.48, instantaneous contour plots of heat release and decane vapour are reported to better explain the interactions between spray, turbulence and combustion. In the figure, the yellow line specifies the iso-contour of α_l=0.01%, whereas the red and green lines state the iso-values of T=2100 K and T=2000 K respectively.
A sharp separation between fuel and heat release zones is clearly apparent: as soon as the spray enters in the combustion chamber an appreciable amount of decane vapour is generated and its local mixing with the swirling flow, together with the heat provided by the main recirculating region, determines a non-zero heat release. The turbulent and unsteady flow-field has clearly a paramount importance in this process since the eddies, which are resolved in the SAS approach, strongly affect the mixing process and the flame stabilization. Immediately, regions at high temperature (i.e. red lines) are created and transported downstream by the career phase. The impact of the scale resolving resolution of the flame can be further appreciated in Figure 2.49, where the contour plot of temperature fluctuation is reported together with the decane vapour mass fraction. The local difference with the mean temperature can exceed 500 K and it is much higher where $C_{10}H_{22}$ is generated. Such unsteady contribution would be completely missed in a RANS context and it is

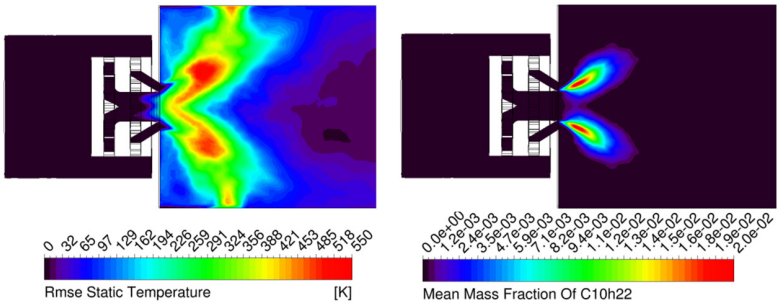

Figure 2.49: Contour plots of temperature fluctuations (left) and decane vapour mass fraction (right).

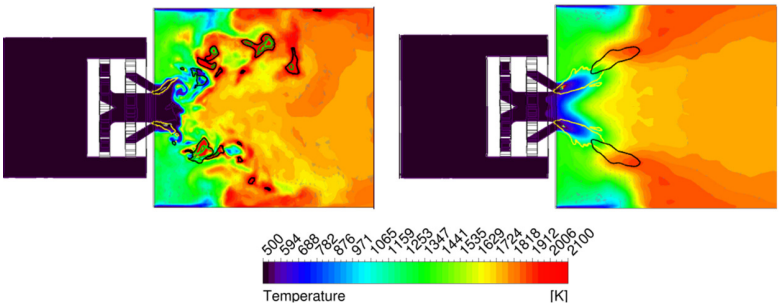

Figure 2.50: Instantaneous and mean contour plots of temperature. See text for explanations about iso-lines.

extremely relevant for the flame stabilization.
The resulting instantaneous and time-averaged temperature distributions are shown in Figure 2.50. The same iso-line of α_l is super-imposed on the contour (i.e. yellow line corresponds to α_l=0.01%), while the black marker state an equivalence ratio of 0.7. The V-shaped flame seems now to be reasonably well predicted by the proposed set-up as well as the high temperature lobes characteristic of the analysed configuration. The time-averaged plot shows once again the separation between the fuel region and the reacting flow field: the iso-line of equivalence ratio starts just downstream the spray zone and totally defines the flame lift-off distance.
This stresses the importance of a reliable set of liquid BCs for the nu-

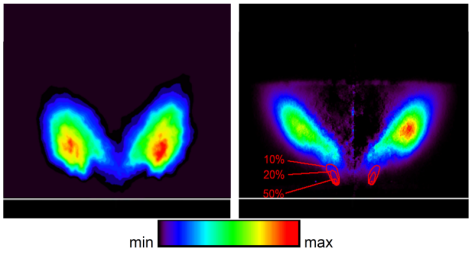

Figure 2.51: Iso-contours of heat release obtained with SAS-FGM (left) against the experimental map (right).

merical simulation of spray flames in the aero-engine context: droplets characterized by a too high momentum (e.g. too big or with too high velocity) would determine a delayed release of decane and the stabilization of the flame further downstream. Temperature would be underestimated in the primary region and the flame would arrive till the burner walls (i.e. see Figure 2.33). On the contrary, a spray characterized by a too low momentum would completely evaporate after the injection leading to an overestimation of the flame temperatures in the near-injection region and probably to miss the temperature lobes since the mixture fraction field would be nearly homogeneous everywhere (i.e. see Puggelli et al. [102]). Physically the process is much more complex and thanks to a proper set of spray BCs, a quite reasonable prediction of the flame has been finally achieved.

The interactions between the reacting flow-field and the liquid fuel seem to be now correctly predicted and it is further confirmed by the comparison in terms of heat release maps shown in Figure 2.51. The flame tends to move towards the dome of the burner with a lift off distance now in line with experiments (i.e. 22 mm using the point of maximum gradient of OH mass fraction).

Furthermore, also in terms of temperature profiles, shown in Figure 2.52, a strong enhancement can be again pointed out with respect to Figure 2.38. Even if some discrepancies are still present, mainly in the near axis region with respect to Jones et al. [92], the proposed SAS-FGM approach proves again to be able of reasonably reproducing the reacting flow-field with a limited computational cost.

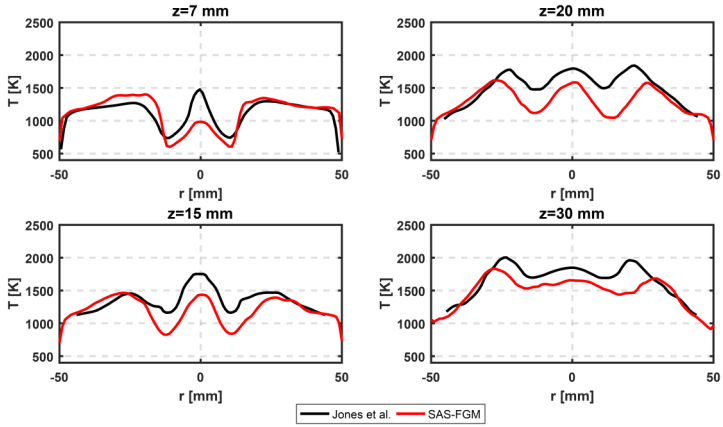

Figure 2.52: Temperature profiles obtained with SAS-FGM compared with profiles of Jones et al. [92].

2.5.5 Reactive analysis (Tp C)

The agreement finally obtained with SAS-FGM on test point A is a key step in the assessment of the proposed set-up on a test point representative of idle conditions for aero-engines.
Nevertheless, aero-engine manufacturers are normally much more interested in predicting the performances of the burner at higher power, when conditions are much more critical as far as the wall temperature distribution is concerned. It is worth pointing out that in this framework the SAS approach can be even more interesting since it avoids a too excessive mesh refinement in the near-wall region that would be required employing LES. Therefore, test Point C (see Table 2.4) has been also considered in the present study since it should be representative of a cruise operating condition. Based on results obtained for test point A, the numerical set-up is the same of the previous section. Mesh M1 has been again employed with a set of boundary conditions for the gas phase coherent with Figure 2.31. Spray BCs have been instead calculated using the method described in the previous section (i.e. see Table 2.6).
The instantaneous and time-averaged axial velocity and temperature contour-plots obtained in such test conditions are shown in Figure 2.53. The swirling flow-field shows now a much wider opening angle with respect to test point A. Thanks to a higher operating pressure and temperature,

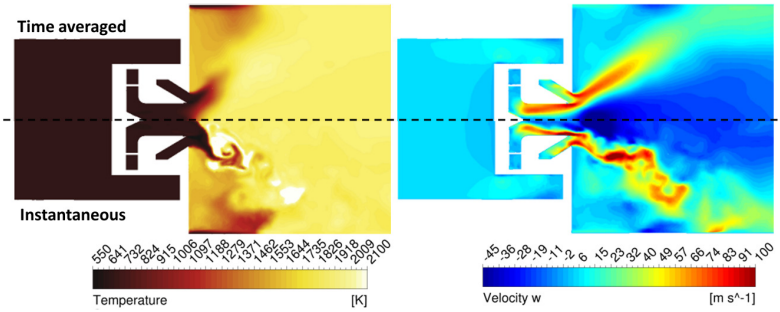

Figure 2.53: Time-averaged and instantaneous temperature and velocity contour plots obtained with SAS-FGM for Test Point C.

the inner recirculation zone now arrives nearly inside the injector. This leads to a strong augmentation of the tangential and radial component of the swirling flow-field. With respect to the previous test point, the flame moves towards the burner dome with a reduction of the lift-off distance. Focusing the attention on the instantaneous temperature contour, reactions seem to take place mainly in the inner surface of the spray cone where higher values of temperature can be observed. A comparison of the instantaneous temperature distributions between CFD and experiments is shown in Figure 2.54. In both images the red line indicates the presence of the liquid phase (iso-line at $\alpha_l = 1\%$ in numerical simulations). Clearly, the two snapshots are referred to different physical times and so the absolute local temperature is not the same. Anyway, the main characteristics of the flame can be observed and analysed.

As soon as the liquid is injected, the higher pressure and temperature here investigated lead to a strong evaporation of the fuel that is highlighted by the low temperature region inside the red iso-line. The generated kerosene vapour is mixed with air and the flame assumes a standard V-shape as for test point A. Temperature peaks are located all along the inner surface of the spray cone and the flame tends to spread out towards the burner walls (1-3). Part of the fuel is instead trapped by the turbulent structures of the swirling flow-field (2) and is burnt with the heat transferred from the hot inner recirculation region. From a numerical point of view, it should be pointed out that the sizing of turbulent structures is larger than in experiments. This is consistent with the SAS approach here employed, which is not probably switching everywhere to a LES-like behaviour. Nevertheless, a consistent representation of the aforementioned physical

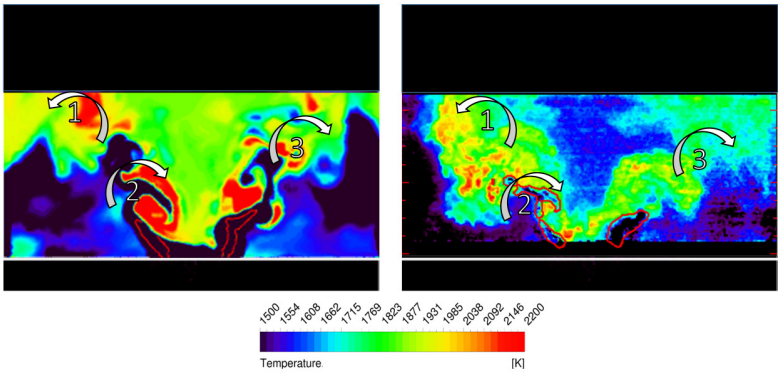

Figure 2.54: Comparison of instantaneous temperature contour obtained between SAS-FGM (left) and experiments (right) for Test Point C [62].

phenomena can be pointed out at least from an instantaneous point of view.
As long as time averaged distributions are concerned, the obtained contour plot of heat release is compared in Figure 2.55 with experimental data. A satisfactory agreement has been again obtained. As already said, the lift-off distance is strongly reduced and this leads to a much stronger interaction between the liquid fuel and the flame. The sharp separation between spray and reacting flow-field, shown in Figure 2.50 for test point A, takes place in a less evident manner. This is further confirmed in Figure 2.56, where a comparison of heat release maps superimposed on fuel distributions is shown between test points A and C.

2.5.6 Concluding remarks on GSS Combustor

In this section, main findings achieved through numerical analysis on the GSS combustor have been described.
The non-reacting case, which was not shown here for the sake of brevity, confirmed that scale resolving methods are able to properly reproduce the main flow-field features of this test rig with a good level of accuracy. RANS proved instead to be not adequate for describing in detail a highly swirled flow field.
For the reacting test point, several calculations have been performed by both varying the numerical strategy for combustion modelling and the set of spray boundary conditions. In this thesis, the comparison between

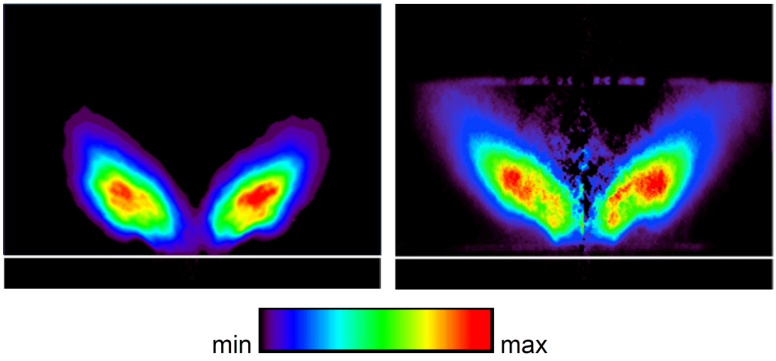

Figure 2.55: Iso-contours of heat release obtained with SAS-FGM (left) against the experimental map (right)[62].

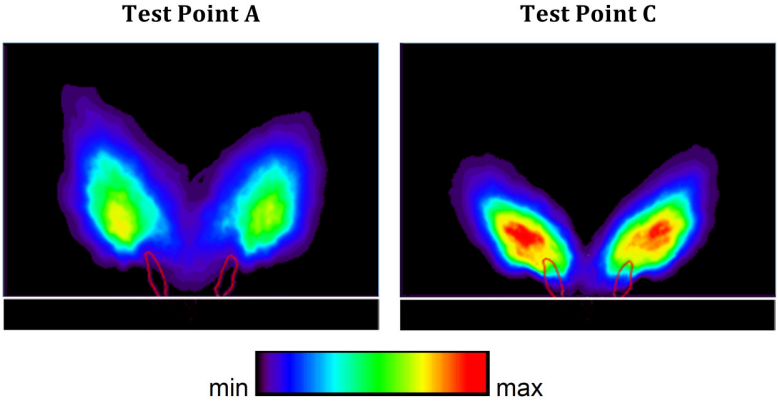

Figure 2.56: Comparison between heat release maps superimposed on fuel distribution for test points A and C [62].

ATF and FGM has been shown in LES. The ATF model, thanks to the thickening procedure, has led to improve the temperature levels, even if a strong under-prediction in the near injector region together with an overestimation in the outer recirculation zones were still evident. Discrepancies obtained with ATF and FGM with respect to the experimental data have been then justified considering the uncertainty in the employed spray boundary conditions.

A detailed analysis on spray evolution for such pre-filming configuration has been therefore realized in order to deepen how the spray resolution affects the reacting flow field. The reported comparisons have proved that the droplet population was wrongly gathered in a narrow diameter range leading to a completely modified flame stabilization process. Liquid fuel atomization has been identified as the key parameter in the analysis of such turbulent lean spray flame.
A systematic study on the main characteristics of the fuel film has been therefore performed by means of a multi-coupled numerical approach. Several aspects, ranging from liquid film boundary conditions to primary breakup modelling, have been considered allowing to identify an appropriate set of spray BCs. Results showed that the interactions between the gas phase and the liquid film are of paramount importance to reliably predict the performances of airblast injection systems. A set of spray BCs has been finally determined.
Then, a Scale Adaptive Simulation has been performed leading to a significant enhancement in the prediction of spray evolution in the combustion chamber. A reliable representation of the characteristics of the liquid phase as well as of the reacting flow field has been finally obtained. The resulting SAS-FGM approach has been also applied on Test Point C, leading again to a adequate description of the flame shape and of the main interactions between the liquid fuel and the reacting flow-field.

2.6 Concluding remarks

In this chapter, three spray flames of increasing complexity have been studied with particular attention to the interactions of the spray BCs with the reacting flow-field. It can be considered as a state of the art in the numerical analysis of spray combustion.

- The Sydney Spray Burner has been initially studied to show the impact of a scale-resolving technique on the evolution of the liquid phase and on the subsequent reacting flow-field. Thanks to an accurate estimation of the injection parameters from experimental data, the proposed LES-FGM set-up has led to a reliable representation of the flame and of the main spray characteristics.

- The Sheen Spray Burner has been then chosen as a second rig. This test case is characterized by a more representative atomization process (i.e. a pressure atomizer) and several measurements regarding the gas phase are available. An overall reliable prediction of the reacting field has been obtained even if some discrepancies in

the near injection region have been pointed out. The evaporation model, together with the employed spray parameters, have been considered as possible source of error, highlighting the impact of the liquid phase modelling on this kind of flame. Nevertheless, a fair agreement of the LES-FGM procedure has been again pointed out in line with previous works on the same test case.

- The Generic Single Sector Combustor has been finally studied as it is completely representative for actual aero-engine burners. The estimation of spray characteristics injected by airblast prefilmers is still today source of considerable uncertainties in the context of reactive simulations. It has been clearly demonstrated that, even employing several modelling strategies for combustion and turbulence, the spray breakup still remains a leading parameter.
  A detailed analysis of spray characteristics has been first realized to show how the liquid was affecting the flame stabilization in a non-physical manner. A multi-coupled approach has been then employed to analyse the liquid film with a detailed focus on primary atomization. Thanks to a more detailed representation of the film breakup, the FGM coupled with SAS finally has led to a reasonable representation of the flame for two different operating conditions.

It is worth pointing out that, to the best of the author's knowledge, the present chapter represents one of the few attempts in technical literature focused on an assessment of the capabilities of the FGM model in a scale resolving framework for the analysis of lean spray flames going from laboratory test conditions up to a real aero-engine burner. It can be considered as a thoroughly assessment of the state of the art strategies for the scale resolving modelling of turbulent lean spray combustion.
Even if some discrepancies are still evident, the obtained agreement is satisfactory mainly in an industrial perspective. Furthermore, the reliability of the SAS approach has been as well demonstrated and this represents for sure a valuable result considering the reduction of the CPU effort with respect to LES. Moreover, in all the analysed cases, the fair comparison with results previously achieved in technical literature, with more advanced and much more costly techniques for combustion modelling, assesses once again the proposed set-up. Finally, it is worth mentioning that the same approach has been also recently applied by this author and coworkers in the numerical simulation of the full annular burner investigated in the LEMCOTEC (*Low Emissions Core-Engine Technologies*) European project and the interested reader is addressed to [62, 63] for further details.

However, beyond the assessment of SAS-FGM as a numerical procedure, such a fair agreement has been achieved mainly thanks to a time-consuming and case-dependent set-up of spray BCs. Each test case requires a detailed investigation on injection parameters. This surely represents the major limit of actual strategies for the numerical simulation of spray combustion and it can deeply affect its reliability in an industrial framework.
For instance, notwithstanding the unsteady resolution of the turbulence field, in the GSS combustor the absence of droplets on the axis and outside of the swirling flow with respect to experiments points out the intrinsic limitations of the adopted Lagrangian tracking. The employed injection strategy does not account for all the processes involved in the ligament formation and droplet dispersion caused by the shedding of the liquid film. The spreading of bigger and smaller particles far from the prefilmer is in this manner completely misled. Furthermore, the multi-coupled approach adopted for the film investigation is based on a set of experimental and theoretical correlations that present normally a tight validity range (e.g. the reliability of such numerical method at high operating pressure has still to be verified).
A more general numerical strategy is required for atomization modelling in LES in order to deal with the liquid phase from its injection up to the generation of a dispersed phase. A unified numerical tool able to properly account for the effects of the dense spray region and to deal with different operating conditions (e.g. from idle to cruise) and breakup mechanisms is required.
In the present study, the Eulerian-Lagrangian Spray Atomization (ELSA) model has been chosen to this end and it will be the main topic of the second part of the thesis.
In the next chapter, such approach is presented together with the developments pursued in the present work to extend its capabilities to the aero-engine context. It is worth pointing out that the present work represents also one of the first effort in technical literature in extending the characteristics of ELSA to the aeronautical framework in LES.

Chapter 3

Introduction of a general approach for atomization modelling

In Chapter 2, the impact of liquid phase modelling on reactive spray calculations has been pointed out. Thanks to a focused modelling on the liquid film evolution and breakup, a reliable representation of the DLR-GSS burner has been finally achieved. Nevertheless, a huge dependence on liquid boundary conditions has been pointed out, highlighting the need of a more general and complete strategy to deal with fuel atomization in LES.
The Eulerian Lagrangian Spray Atomization (ELSA) model has been chosen in the present work to fill this gap.
In the present chapter, the problem of the development of a LES model for atomization is described and a coupling DNS-LES strategy based on ELSA presented as a possible solution. The complete system of equations is detailed with particular attention on the switching technique between the Eulerian and Lagrangian regions of the solver. The main characteristics of this approach are characterized together with its limitations for an application in the aero-engine context.

3.1 Atomization process

From a theoretical point of view, the spray atomization can be normally divided into three main steps as shown in Figure 3.1:

- the ejection of the liquid flow
- the primary breakup
- the secondary breakup

As soon as the liquid flow issues from the nozzle, deformations appear on the liquid interface: these instabilities grow in space and time and they result in the ejection of liquid fragments from the main liquid flow. The initial flow deformation and the consequent production of ligaments is referred as *primary atomization* mechanism.

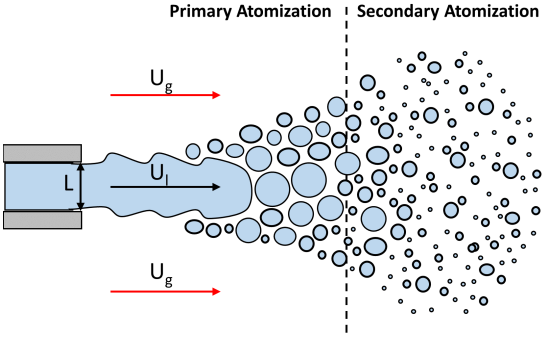

Figure 3.1: Sketch of various atomization processes in liquid jet breakup.

Then, these liquid structures may distort and disintegrate into smaller particles and this process is repeated until the surface tension forces are strong enough to ensure the cohesion of the liquid particles. A statistically stable cloud of droplets is thus generated and this step constitutes the *secondary atomization* process. The relative importance of each step depends on the initial energy of the liquid flow. In low energy cases, the primary atomization may already produce stable drops as well as greater liquid fragments that may undergo secondary breakup. For high initial energy, the secondary atomization is generally dominant in the production of the final spray.
From a physical point of view, the atomization is led by the relative importance of the following groups of forces:

- Aerodynamic force, which is related to the velocity of each phase.
- Surface tension force, which acts on the liquid/gas interface and tends to avoid breakup phenomena.
- Viscosity force, which is related to the dissipation of the liquid and gas kinetic energies and to the transfer of such energy between the two phases.

To better quantify the impact of these forces, some dimensionless parameters can be introduced. First, the so called *Weber number* (We) represents the ratio between intertial and surface tension forces [12]:

$$We = \frac{\text{Inertial Forces}}{\text{Surface Tension Force}} = \frac{\rho U^2 L}{\sigma} \tag{3.1}$$

where L is a length scale parameter (e.g. the droplet diameter or the jet diameter as in Figure 3.1), U is a characteristics velocity such as the relative velocity between liquid and gas $(U_l - U_g)$, ρ is a reference density and σ the surface tension. Based on such general formulation, it is then possible to define for example a gas Weber number (i.e. $We_g = \frac{\rho_g \left(U_l - U_g\right)^2 d}{\sigma}$) or a liquid Weber number (i.e. $We_l = \frac{\rho_l U_l^2 d}{\sigma}$).
In the analysis of droplets dynamics, the definition of a *particle Reynolds number* can be also useful. In general, the Reynolds number represents the ratio between inertial and viscous forces. In this case, it is defined in the following manner:

$$Re_p = \frac{\rho_g \left(U_l - U_g\right) d}{\mu_g} \tag{3.2}$$

where μ_g is the dynamic viscosity of the gas phase.
Combining together Weber and Reynolds, the Ohnesorge number can be also introduced. It can be considered as the ratio between the viscosity contribution inside the liquid phase and the aerodynamic and surface tension forces.

$$Oh = \frac{\text{Viscosity forces}}{\text{Inertial forces}^{0.5}\text{Surface tension forces}^{0.5}} = \frac{\sqrt{We}}{Re} \tag{3.3}$$

3.2 Computational approaches for atomization

Several strategies can be found in literature to model fuel injection and to cope with the multi-phase / multi-scale nature of the flow. A full resolution of the interface thanks to direct numerical simulation,

either using interface capturing and reconstruction methods [60, 117], is infeasible as far as industrial applications are concerned because of the computational cost. Moreover, the notion of DNS when an interface is considered has to be treated with particular attention.
Therefore, atomization modelling is required. Many approaches are based on kinetic theory, where the spray is described through a number density function ($f(t,x,m,\vec{u},T)$) that verifies the Williams-Boltzmann Equation (WBE) [118] containing terms for spatial transport, evaporation and drag (see Equation 3.4). The $f(t,x,m,\vec{u},T)dxdmd\vec{u}dT$ corresponds to the number of droplets at time t, inside a volume dx centred on x, with a velocity within $[\vec{u},\vec{u}+d\vec{u}]$, a temperature between $[T,T+dT]$ and a mass between $[m,m+dm]$.

$$\frac{\partial f}{\partial t} = -\frac{\partial \dot{\vec{x}} f}{\partial x} - \frac{\partial \dot{m} f}{\partial m} - \frac{\partial \dot{\vec{u}} f}{\partial \vec{u}} - \frac{\partial \dot{T} f}{\partial T} + Q + \Gamma \tag{3.4}$$

where $\dot{\vec{x}} = \vec{u}$ is the droplet velocity, $\dot{m}$ is the evaporation rate, $\dot{\vec{u}}$ is the acceleration (or deceleration) due to drag and $\dot{T}$ is the droplets heating or cooling. In this approach, like in many numerical models, droplets are considered spherical and are characterized with their mass m. Q and Γ are additional terms for secondary breakup and collision. It is an equation in nine dimensions: three for space, three for velocity, one respectively for time, temperature and mass.
Two main groups of approaches have been proposed to solve the WBE:

- The Lagrangian-Monte-Carlo method [119], where the liquid is tracked with a Lagrangian description and the gas is solved in an Eulerian framework. Its advantage lies in a straightforward implementation of physical processes such as evaporation and secondary break-up, even if its computational cost is generally high especially in unsteady configurations. A huge number of parcels is required in each cell of the numerical domain in order to have a statistically representative solution. In this case, one important problem is related to load balancing (see [120]) and several efforts in technical literature have been performed in this direction over the last years.

- An Euler-Euler (EE) formulation, where both phases are treated as a continuum. This solution is very attractive to describe the evolution of the spray characteristics. Reduced computational cost and high capabilities in terms of parallel computing are among the advantages of this formulation. These benefits in terms of numerical efficiency are receiving attention mainly in the context of scale resolving techniques, such as Large Eddy Simulation. However, despite the

efficiency of EE methods on actual HPC super-computers, the direct resolution of WBE is generally not feasible since the dimension of the problem is increased by the number of spray characteristics retained (position, velocity, size, temperature, etc). This constrains EE methods to address a limited description. The possible hypotheses, which can be therefore introduced, have led to an abundant research in this framework. For instance, in Multi-Fluids models [121] the diameter space is discretized in sections to represent the spray distribution, whereas a smooth reconstruction of a sum of kernels of the density function using a Quadrature Method Of Moments (QMOM) has been proposed by Yuan et al. [122].

However, all these methods based on WBE assume that individual spherical droplets, with well-defined features as position or diameter, compose the spray. Nevertheless, the liquid phase is initially a continuum (i.e. liquid jet or film) and it is not possible to determine such features up to the end of primary breakup.
Therefore, diffuse interface or mono-fluid approaches can be considered and have been developed in this work.
In these models, the interface is considered as a mixing zone so that both liquid and gas phases coexist at the same macroscopic position with an occupied portion of volume defined by the liquid volume fraction (α_l)[123].
Two families of equilibrium models have been mainly studied in technical literature.
A first possibility, proposed by Drew et al. [124], is to use the liquid volume fraction as the unique variable to describe the interface.
Another set of approaches is based instead on a transport equation for the liquid/gas interface density (Σ) [57, 60]. This quantity represents the ratio between the surface of the liquid/gas interface and the control volume. Clearly, employing such definition, Σ is defined everywhere both for a spherical droplet or for a deformed liquid jet.
In this second group, the Eulerian-Lagrangian Spray Atomization (ELSA) models are of major importance [57, 60] and in this study the application of ELSA model to aero-engine framework has been considered.
The chapter is structured as follows: issues related to atomization modelling in LES context are first pointed out and the ELSA approach, which has been used as starting point of the present work, is presented to overcome such problems. The main limitations of this approach in the aero-engine context will be as well pointed out in order to present the developments proposed in this investigation.

3.3 LES for atomization modelling

As reported in Chapter 1, the scale resolving simulation of a single phase system is a well-known and analysed problem in technical literature. The reader interested in this topic can refer for instance to [64, 125] and references therein.
However, in the context of atomization modelling and in presence of a liquid/gas interface, the filtering of the system of equations is much more challenging due to the presence of sub-grid terms related to the two-phase system under investigation. The reader interested in the mathematical derivation of the filtered system of equations valid for a two-phase flow is addressed to [126, 127], where this topic is discussed in detail. From a theoretical point of view, the filtering operation is defined as a spatial convolution using a filter G with a characteristic size Δ. Therefore, considering a general quantity $\phi(x, y, z)$, its filtered value is expressed as:

$$\bar{\phi}(x,y,z) = \int\int\int_{-\infty}^{+\infty} G_{\bar{\Delta}}\left(x-x', y-y', z-z'\right) f\left(x', y', z'\right) dx'dy'dz' \tag{3.5}$$

Applying such operation to a two-phase incompressible and immiscible system, several quantities appear such as the filtered velocity $\bar{U}_i = \overline{\chi_l U_{l,i} + \chi_g U_{g,i}}$, the filtered pressure $\bar{P} = \overline{\chi_l P_l + \chi_g P_g}$ and the filtered volume fraction $\bar{\alpha}_l = \bar{\chi}_k$, where χ_k is a phase-marker with a value equal to 1 inside the k-phase and zero elsewhere [127].
The following filtered set of equations can be therefore obtained [127]:

- Mass conservation equation:

$$\frac{\partial \bar{U}_i}{\partial x_i} = 0 \tag{3.6}$$

- Mixture momentum conservation equation:

$$\begin{aligned}\frac{\partial \bar{\rho}\bar{U}_i + \tau_{\rho u_i}}{\partial t} + \frac{\partial \bar{\rho}\bar{U}_i\bar{U}_j + \tau_{\rho u_i u_j}}{\partial x_j} = &-\frac{\partial \bar{P}}{\partial x_i} + \\ &+ \frac{\partial}{\partial x_j}\left(\bar{\mu}\left(\frac{\partial \bar{U}_i}{\partial x_j} + \frac{\partial \bar{U}_j}{\partial x_i}\right) + \tau_{S_{ij}}\right) + \\ &+ \bar{\rho} g_i - \tau_\sigma\end{aligned} \tag{3.7}$$

- Liquid volume fraction equation:

$$\frac{\partial \bar{\alpha}_l}{\partial t} + \bar{U}_i \frac{\partial \bar{\alpha}_l}{\partial x_i} + \tau_{\alpha_l} = 0 \tag{3.8}$$

where :

$$\begin{cases} \tau_{\alpha_l} = \overline{U_i \dfrac{\partial \alpha_l}{\partial x_i}} - \bar{U}_i \overline{\dfrac{\partial \alpha_l}{\partial x_i}} \\ \tau_{\rho u_i} = \overline{\rho U_i} - \bar{\rho} \bar{U}_i \\ \tau_{\rho u_i u_j} = \overline{\rho U_i U_j} - \bar{\rho} \bar{U}_i \bar{U}_j \\ \tau_{S_{ij}} = \overline{\mu \left(\dfrac{\partial U_i}{\partial x_j} + \dfrac{\partial U_j}{\partial x_i} \right)} - \bar{\mu} \left(\dfrac{\partial \bar{U}_i}{\partial x_j} + \dfrac{\partial \bar{U}_j}{\partial x_i} \right) \\ \tau_\sigma = \overline{\sigma \kappa \vec{n}_i \delta_\Gamma} \end{cases} \tag{3.9}$$

where n_i is the normal to the interface oriented towards the exterior of the liquid phase, whereas δ_Γ is a Dirac-function on the interface.
Going in detail with terms arising in the filtering procedure, it is interesting to consider the meaning of each contribution:

- τ_{α_l} is the subgrid term related to the liquid volume fraction equation. It is extremely important since it represents the contribution of the under-resolved liquid/gas interface.

- $\tau_{\rho u_i}$ is the subgrid temporal term in the mixture momentum equation.

- $\tau_{\rho u_i u_j}$ is the subgrid convective contribution in the mixture momentum equation. It is worth stressing that this quantity includes all the turbulent fluctuations, comprising also the density sub-grid correlation terms. Modelling closures coming from the single-phase context are normally applied for this term. However, as detailed in Annex-A, this approach is not theoretically consistent since the contribution of *turbulent liquid flux* is roughly neglected in this way (see Section 3.4.1 for a detailed description of turbulent liquid flux). An alternative would be to introduce a Favre averaging procedure: even if it has been widely employed over the last years for atomization modelling, it is possible to mathematically demonstrate that it presents the same limitation as far as the Reynolds stress tensor modelling is concerned. In Annex-A, a focus on this topic is reported to complete the discussion. Nevertheless, the modelling of density correlation contributions inside the momentum equation is still an open issue in technical literature for two-phase flows requiring detailed investigations that go beyond the goal of the present

study. A first modelling closure, based on single-phase models, has been therefore retained in this investigation. Some guide-lines to close this problem are then detailed in Annex-A.

- $\tau_{S_{ij}}$ and τ_σ are the subgrid terms related to the laminar viscous forces and surface tension contributions.

It is worth pointing out that all these terms are directly related to the presence of an interface that creates a discontinuity on the mixture properties [126].
The appearance of these contribution represents a significant closure problem. In fact, DNS approaches for the dynamic field coupled with interface capturing methods (ICM) for the interface description (i.e. DNS-ICM), which clearly would not present these issues, are still infeasible on real operating conditions and geometries. Conversely, the application of LES tools for atomization, based for instance on interface tracking methods, strongly suffer from the chosen mesh sizing since the sub-grid contribution can be significant. In fact, as shown in Figure 3.2 where the mesh sizing is progressively reduced for a set of DNS-ICM calculations of a Diesel jet realized by Chesnel [126], it is possible to appreciate the appearance of smaller and smaller liquid structures and a completely different atomization process [126]. Using the coarse mesh, the breakup is stabilized and the interface tracking method is not capable of representing the physics under investigation (i.e. the jet opening angle and dispersion are much lower than the fine case).
Therefore, the following preliminary conclusions can be stated for atomization modelling in LES [127]:

- If the mesh sizing is fine enough to represent the liquid/gas interface, numerical methods developed in DNS can be reliably used to simulate the atomization process. Over the last years, several approaches such as Volume of Fluid (VOF), level-set (LS), front-tracking (FT) or coupled levelset-VOF (CLSVOF) methods have been proposed in literature to track the liquid gas interface. The reader interested in a detailed description of these methods is addressed to [56] and references therein.

- If the mesh sizing is not able to capture the interface wrinkling and deformation, the sub-grid contributions detailed in Equations 3.9 become relevant and have to be introduced inside the LES atomization model.

Therefore, even if it is very tempting to apply LES for the velocity while keeping an interface capturing method for the interface, it is theoretically

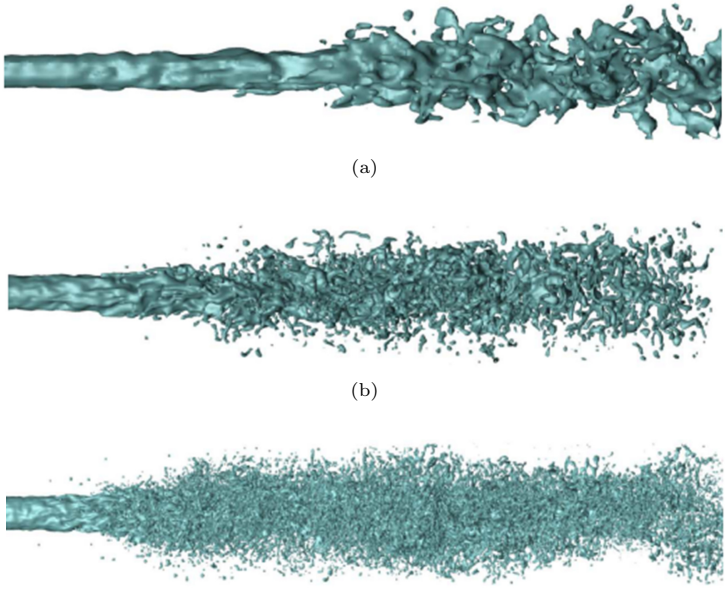

(a)

(b)

(c)

Figure 3.2: Diesel jet simulation for several mesh sizings: $32^2 \times 256$ *in Figure 3.2a,* $64^2 \times 512$ *in Figure 3.2b,* $128^2 \times 1024$ *in Figure 3.2c. Adapted from [126]*

inconsistent at least in the engineering applications of interest. In fact, in a standard atomization process, the Weber number can be high and subgrid fluctuations of the velocity field can lead to a subgrid wrinkling of the interface that cannot be handled directly with ICM. Adaptive mesh refinement [53], subgrid level set methods [128] have been proposed for instance in literature to overcome such problem. In [127] a coupled DNS-LES formalism based on ELSA has been as well implemented to this end in OpenFOAM® and it has been used as starting point for the present research study.
In the next sections, a more detailed description of such ELSA approach and in particular its implementation in OpenFOAM® is reported.

3.4 Eulerian Lagrangian Spray Atomization approach for LES

In the ELSA model, the two-phase system is studied as a single phase flow composed of two species with highly variable density. In the solution algorithm it is possible to distinguish an Eulerian framework, where the liquid distribution is calculated up to the generation of spherical droplets and a Lagrangian environment used to track the subsequent spray evolution. In Figure 3.3 a sketch of this coupling is briefly shown. The

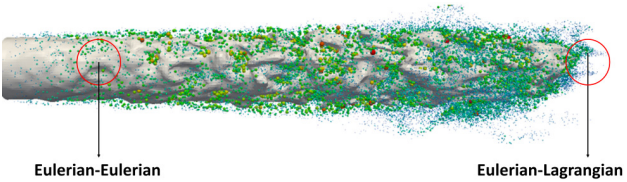

Figure 3.3: Schematical representation of the ELSA coupling proposed in [127]. Adapted from [129].

attention will be here focused firstly on the Eulerian framework, whereas some detail about the Lagrangian injection and the Eulerian/Lagrangian coupling will be provided at the end of the section.

3.4.1 Eulerian framework

Considering the depicted issues of atomization modelling in LES, one of the most challenging problems from a numerical point of view is the coupling of DNS-ICM regions with zones where the sub-grid contribution is relevant. A sketch of the strategy adopted in ELSA [126, 127, 130] is shown in Figure 3.4 using a snapshot of the atomization of a liquid jet obtained in DNS context by Vaudor et al. [131]. The dotted white lines represent, just for the sake of clarity, the theoretical mesh sizing of a really coarse LES simulation.

- In the dense regions of the spray, such as the one specified with the green circle, where the characteristic length of the surface instabilities along the liquid/gas interface is bigger than the mesh sizing (i.e. the sub-grid contribution is negligible), an interface tracking method is used. In particular, the VOF solver provided in the standard release of OpenFOAM® (i.e. *interFOAM*) is here

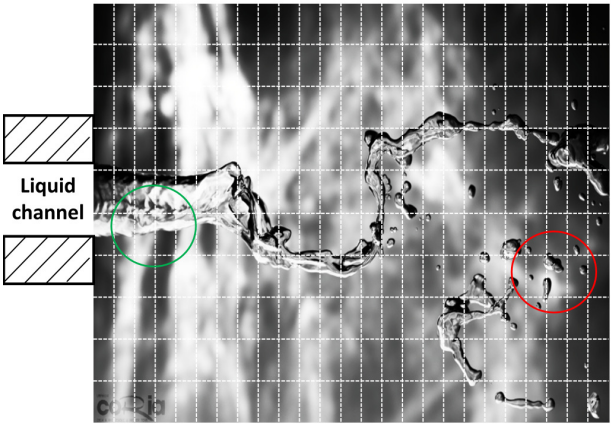

Figure 3.4: Schematical representation of the DNS-LES approach proposed in [127]. Adapted from [131].

employed. The reader interested in a detailed description of the *interFOAM* approach is addressed to [132] and references therein.

- In the more diluted spray region, such as the one identified in red, dimensions of the generated ligaments are lower than the mesh sizing (i.e. more droplets are inside one mesh element) and therefore they are accounted through a sub-grid model. The spray is therefore transferred to a sub-grid level and, based on the ELSA formalism, an equation of liquid/gas interface is used to characterize its evolution [127].

From a mathematical point of view, all the system of equations in ELSA is formulated in order to account for such coupling. First, the liquid volume fraction evolution can be entirely represented through the following equation [127]:

$$\frac{\partial \bar{\alpha_l}}{\partial t} + \frac{\partial \left(\bar{U}_i \bar{\alpha_l}\right)}{\partial x_i} + \underbrace{\frac{\partial \left(C_\alpha \bar{\alpha_l} \left(1 - \bar{\alpha_l}\right) U_i{}^r\right)}{\partial x_i}}_{ICM} + \left(1 - C_\alpha\right) \underbrace{\frac{\partial \bar{R}_{\alpha_l,i}}{\partial x_i}}_{SGS} = 0 \quad (3.10)$$

where $U_i{}^r$ is an artificial relative velocity between the liquid and the gas phases, defined in the vicinity of the interface for the ICM part, and used to steepen the gradient of the liquid volume fraction and improve the

interface resolution (see [127, 132] for further details). $R_{\alpha_l,i}$ is instead the sub-grid scale (SGS) contribution to the liquid volume fraction equation. Instead, C_α is the weighting coefficient used to switch from DNS-ICM regions (i.e. $C_\alpha = 1$) to LES (i.e. $C_\alpha = 0$). Its physical meaning and definition is detailed in the following paragraph.
Regarding the subgrid contribution $R_{\alpha_l,i}$, which is specified in the following as *turbulent liquid flux*, it can be defined as:

$$\bar{R}_{\alpha_l,i} = \overline{U_i \alpha_l} - \bar{U}_i \bar{\alpha}_l \tag{3.11}$$

Strong attention will be devoted in Chapter 4 on the strategies that can be employed to model this term. In [127], a simple diffusion law based on a turbulent diffusion coefficient (D_t) has been used and the same modelling choice is here retained for the moment (see Equation 3.12). The reader interested in a description of the consequences of such gradient closure is addressed to Section 3.5.

$$\bar{R}_{\alpha_l,i} = D_t \frac{\partial \bar{\alpha}_l}{\partial x_i} \tag{3.12}$$

Beyond the equation of liquid volume fraction, as far as the momentum equation is concerned, a single-phase formalism is retained [127] (see Equation 3.13). As already mentioned, all the density sub-grid correlation terms are included in $\tau_{\rho u_i u_j}$.

$$\begin{aligned} \frac{\partial \bar{\rho} \bar{U}_i}{\partial t} + \frac{\partial \bar{\rho} \bar{U}_i \bar{U}_j}{\partial x_j} = &- \frac{\partial \bar{P}}{\partial x_i} + \\ &+ \frac{\partial}{\partial x_j} \left(\bar{\mu} \left(\frac{\partial \bar{U}_i}{\partial x_j} + \frac{\partial \bar{U}_j}{\partial x_i} \right) \right) - \frac{\partial \tau_{\rho u_i u_j}}{\partial x_j} \end{aligned} \tag{3.13}$$

Furthermore, together with Equation 3.10, in ELSA context the breakup processes and the poly-dispersed spray distribution are accounted globally through the introduction of the quantity of liquid/gas interface per unit of volume (Σ):

$$\Sigma(x,t) = \frac{\text{Quantity of liquid-gas interface}}{\text{Control volume}} \tag{3.14}$$

It is worth noting that, with respect to the droplet diameter, Σ is a general quantity that can be defined ranging from a coherent jet up to a diluted spray.
Several works have been realized in technical literature regarding the Σ-evolution mainly in RANS context [60] and the following general formulation, initially proposed by Ishii and Hibiki [133], is normally recovered

[58, 134]:

$$\frac{\partial \bar{\Sigma}}{\partial t} + \frac{\partial \bar{U}_i \bar{\Sigma}}{\partial x_i} = \bar{S} \tag{3.15}$$

where S represents the generation or disruption of surface density due for instance to breakup or collision events. The closure of such transport equation has been the subject of several research activities and three main approaches have been pursued in literature [126]:

- The closure of the source terms for Σ is realized before the integration over the control volume. The interface density is here defined as a Dirac function centered on the interface. The mathematical identification of the unclosed terms with physical phenomena in this framework is quite challenging and not completely assessed. The reader interested in this approach is addressed to [135].

- Iyer and Abraham [136] obtained instead the interface density equation by assuming a spray PDF and then integrating it, multiplied with $4\pi D^2$, over the diameter space. Some un-closed terms appear requiring an additional modelling effort. This procedure represents an extension of multiphase approaches for discrete phase based on the kinetic equation and it can be applied only if a spray of spherical droplets has been already generated [126].

- A phenomenological approach can be also employed starting from the flame surface density equation derived in reacting environment [137] and making an analogy with the Σ transport. Several works have been realized following this strategy (e.g. [57, 58, 138, 139] among others).

In the present study, as in [127, 130], a formulation of S based on the latter criterion and in particular on the restoration of an equilibrium value of the liquid-gas interface Σ_{eq} with a characteristic time scale τ_{eq} has been adopted:

$$S = \frac{\Sigma}{\tau_{eq}} \left(1 - \frac{\Sigma}{\Sigma_{eq}}\right) \tag{3.16}$$

Σ_{eq} can be estimated considering a local equilibrium between the surface tension and the local turbulent kinetic energy k. The deviation from such equilibrium condition is then characterized through the introduction of a critical Weber number (We^*). Using this assumption, an expression of We^* based on k was firstly proposed by Lebas et al. [58, 60] (i.e. $We^* = \frac{\rho \alpha_l k}{\sigma \Sigma_{eq}}$). However, such formulation tends to infinity in very dense or diluted two-phase flows (i.e. $\alpha_l \to 1$ or 0). Then, in order to avoid

such inconsistency, Duret et al. [140] proposed a different definition which has been employed also in the present work:

$$We^* = 4\frac{0.5(\rho_l + \rho_g)\alpha_l\,(1-\alpha_l)\,k}{\sigma\Sigma_{eq}} \tag{3.17}$$

where ρ_l and ρ_g are the density of liquid and gas. Using a wide dataset of DNS simulations, We^*=1.63 was suggested as a general value [140].
Lebas et al. [60], based on Equation 3.16, derived several mathematical expressions of source terms related to primary breakup, collision and secondary atomization associating each one to a characteristic time scale. In this study, as in [127, 130], the attention is mainly focused on the near injection region and just the source term related to primary atomization is retained, where a dependency on the turbulent time scale (τ_t) is assumed.

$$\bar{S} = \bar{S}_{\text{Primary Breakup}} = \frac{\bar{\Sigma}}{\tau_t}\left(1 - \frac{\bar{\Sigma}}{\bar{\Sigma}_{eq}}\right) \tag{3.18}$$

Clearly, the developed formulation can be easily extended to include all the other phenomena.
However, from a numerical point of view, the expression of the equilibrium surface shown in Equation 3.17 presents an inconsistency when the two-phase system is at rest (i.e. for $k \to 0$, $\Sigma_{eq} \to 0$). In such condition, Σ_{eq} has to be calculated as the value of the liquid-gas interface resolved in each cell of the computational domain, i.e. assuming in this way its minimum allowed value (Σ_{min}). As derived by Chesnel et al. [130], it is possible to demonstrate that Σ_{min}, using a mesh sizing Δ, can be approximated as:

$$\Sigma_{min} = 2.4\frac{\sqrt{\alpha_l\,(1-\alpha_l)}}{\Delta} \tag{3.19}$$

Hence, the equilibrium value of the liquid-gas interface has to be computed as:

$$\bar{\Sigma}_{eq} = \bar{\Sigma}_{min} + \bar{\Sigma}^{'}\,(We^*) = \bar{\Sigma}_{min} + 4\frac{0.5(\rho_l + \rho_g)\bar{\alpha}_l\,(1-\bar{\alpha}_l)\,\bar{k}}{\sigma We^*} \tag{3.20}$$

where $\Sigma^{'}$ represents the sub-grid scale interface density, namely the generation of liquid-gas interface due to turbulence forcing in addition to the minimum value.
Based on Equation 3.20, instead of solving for Σ (see Equation 3.15), Chesnel et al. [130] proposed to consider just the transport of $\Sigma^{'}$ with the following equation, which has been employed also in [127] and in the

present study:

$$\frac{\partial \bar{\Sigma}^{'}}{\partial t} + \frac{\partial \bar{U}_i \bar{\Sigma}^{'}}{\partial x_i} = \frac{\partial}{\partial x_i}\left(\bar{\Sigma}^{'}\left(\bar{U}_i - \bar{U}_{\Gamma,i}\right)\right) + \frac{\bar{\Sigma}}{\tau_t}\left(1 - \frac{\bar{\Sigma}}{\bar{\Sigma}_{eq}}\right) \tag{3.21}$$

where $U_{\Gamma,i}$ represents the velocity of the liquid-gas interface. The complete Σ is finally calculated locally as $\bar{\Sigma} = \bar{\Sigma}^{'} + \bar{\Sigma}_{min}$. In this fashion, the primay breakup phenomena are included and a representative Sauter Mean Diameter (SMD) calculated as $SMD = 6\bar{\alpha}_l/\bar{\Sigma}$.
In Equation 3.10, the definition of C_α coefficient to switch from a DNS-ICM to LES atomization modelling is still missing and it is detailed in the next paragraph.

Switching DNS-LES criterion for ELSA In [127], two criteria are defined to transfer the interface description from DNS-ICM to LES, which are specified in the following as *Interface Resolution Quality* (IRQ) criteria:

- The first one is based on the liquid/gas interface density. In particular, considering Equation 3.19, Σ_{min}/Σ can be considered as the ratio between the resolved interface and the total one.

$$IRQ_\Sigma = \frac{\Sigma_{min}}{\Sigma} \tag{3.22}$$

  Hence, if the mesh sizing is fine enough to correctly solve all the wrinkles of the interface (i.e. $\Sigma_{min} = \Sigma$), ICM can be applied imposing $C_\alpha = 1$. On the contrary, the sub-grid contributions are not negligible if Σ is much higher than Σ_{min} and a diffuse interface approach has to be selected (i.e. $IRQ_\Sigma \to 0$ and $C_\alpha = 0$) [127].

- The second one is based on the surface curvature (κ), which is considered as a marker of regions where the interface is strongly wrinkled inside one computational cell. The higher is κ, the higher is the sub-grid contribution to Equation 3.10. In fact, considering that for a spherical droplet of radius R, $\kappa = 2/R$, the IRQ_κ is calculated in the following manner on a computational domain of Δ sizing:

$$IRQ_\kappa = \frac{1}{\kappa\Delta} = \frac{R}{2\Delta} \tag{3.23}$$

  Hence, considering the asymptotic case of $R \to 0$ (i.e. representative of a spray with a characteristic radius much lower than the mesh sizing), IRQ_κ tends to zero and the chosen Δ is not at all enough to represent the physics under investigation. In this asymptotic

condition, a diffuse interface approach has to be employed (i.e. $C_\alpha = 0$). In the opposite case, $C_\alpha = 1$ [127].

Therefore, the switching DNS-LES criteria for ELSA can be summarized as below, where ϵ_1 and ϵ_2 are two defined tolerances [127]:

$$C_\alpha = \begin{cases} 1, & \text{if } IRQ_\Sigma > \epsilon_1 \text{ or } IRQ_\kappa > \epsilon_2 \\ 0, & \text{otherwise} \end{cases} \tag{3.24}$$

In Table 3.1 the system of equations employed in the Eulerian region of ELSA in LES and used as reference in the present work is summarized.

Continuity equation:

$$\frac{\partial \bar{U}_i}{\partial x_i} = 0$$

Momentum equation:

$$\frac{\partial \bar{\rho}\bar{U}_i}{\partial t} + \frac{\partial \bar{\rho}\bar{U}_i\bar{U}_j}{\partial x_j} = -\frac{\partial \bar{P}}{\partial x_i} + \frac{\partial}{\partial x_j}\left(\bar{\mu}\left(\frac{\partial \bar{U}_i}{\partial x_j} + \frac{\partial \bar{U}_j}{\partial x_i}\right)\right) - \frac{\partial \tau_{\rho u_i u_j}}{\partial x_j}$$

Liquid volume fraction equation:

$$\frac{\partial \bar{\alpha}_l}{\partial t} + \frac{\partial\left(\bar{U}_i\bar{\alpha}_l\right)}{\partial x_i} + \frac{\partial\left(C_\alpha\bar{\alpha}_l\left(1-\bar{\alpha}_l\right)U_i{}^r\right)}{\partial x_i} + \left(1-C_\alpha\right)\frac{\partial \bar{R}_{\alpha_l,i}}{\partial x_i} = 0$$

Liquid gas interface density equation:

$$\frac{\partial \bar{\Sigma}'}{\partial t} + \frac{\partial \bar{U}_i\bar{\Sigma}'}{\partial x_i} = \frac{\partial}{\partial x_i}\left(\bar{\Sigma}'\left(\bar{U}_i - \bar{U}_{\Gamma,i}\right)\right) + \frac{\bar{\Sigma}}{\tau_t}\left(1 - \frac{\bar{\Sigma}}{\bar{\Sigma}_{eq}}\right)$$

Table 3.1: Summary of the equations implemented in the Eulerian region of ELSA to account for the coupled DNS-LES approach.[127].

3.4.2 Eulerian-Lagrangian coupling

The reduction of the liquid volume fraction all along the atomization process leads to a lower accuracy of Eulerian approaches. The sub-grid contributions become more and more important (i.e. higher values of Σ are generated) and the characterization of liquid structures with one velocity and diameter is no more meaningful. To overcome this issue, a coupling with a Lagrangian approach or with numerical methods developed to address the Williams equation (see Section 3.2) has to be provided. In the

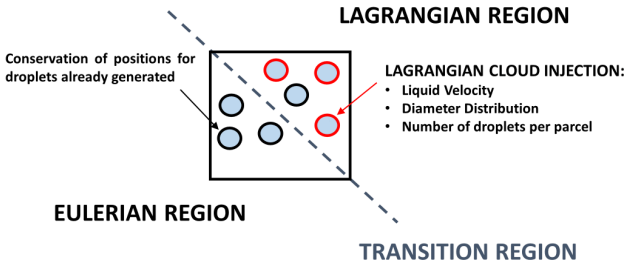

Figure 3.5: Schematical representation of Eulerian-Lagrangian coupling realized in ELSA context.

ELSA context a coupling with a lagrangian technique is adopted [127]. First, a switching criterion has to be defined and here, as proposed in [127], cells of transition inside the computational domain are determined based on values of α_l lower than 1% in order to have a distance between particles large enough to neglect the liquid-liquid interactions [127]. A sketch of the coupling procedure is shown in Figure 3.5. The lagrangian fields in transition cells have to be properly initialized from the Eulerian region and the following characteristics are considered [127]:

- **Position**: lagrangian particles are directly injected at the center of the cells identified in the transition region.
- **Diameter distribution**: this is surely one of the most representative variables for the lagrangian population since it is related both to droplet motion and evaporation. As already said in previous section, a Sauter Mean Diameter can be directly calculated from the liquid volume fraction and from the liquid/gas interface as shown below:

$$D_{32} = \frac{6\alpha_l}{\Sigma} \tag{3.25}$$

  In [127], a Dirac delta function centred on the calculated D_{32} is therefore used to define the PDF of the spray. Locally the SMD can vary all along the transition region defining a more complex diameter distribution on such a group of cells. Further developments are required on this point as shown in Section 3.5.

- **Velocity distribution**: Together with the diameter distribution, the injection velocity is the other controlling parameter for the subsequent lagrangian evolution. As described in detail in the next

chapter, Equation 3.12 entails the neglection of the slip velocity between phases and therefore in [127], lagrangian particles are injected using the mixture velocity of the cell. As advanced case, a dispersion model may be included at the injection by randomly choosing a velocity through a Gaussian velocity distribution in order to match the estimated turbulent kinetic energy. This solution should be pursued in future investigations, even if the slip velocity is still not taken into account.

- **Number of droplets per unit of volume**: the number of droplets injected at each transition cell is decided in a pre-processing step and it is specified as n_{parcel}. Hence, the number of droplets for each parcel (n_{drop}) is calculated through the local conservation of liquid mass.

Once the parcels are injected inside the computational domain, a standard lagrangian tracking is employed to determine the evolution of the liquid phase and models used in this region are described in the next section. However, it should be pointed out that, beyond the injection, the Eulerian-Lagrangian coupling developed in [127] has been realized in order to ensure also that, in the diluted spray region, the set of equations shown in Table 3.1 for the Eulerian part of the solver and the Lagrangian ones behave in the same manner. In particular, starting from Lagrangian values it is possible to re-calculate a liquid volume fraction and a surface density in an Eulerian reference in the following manner [127]:

$$\begin{cases} \alpha_{lag} = \dfrac{1}{V_{cell}} \displaystyle\sum_i \frac{\pi}{6} n_{drop,i} {d_i}^3 \\ \Sigma_{lag} = \dfrac{1}{V_{cell}} \displaystyle\sum_i \pi n_{drop,i} {d_i}^2 \end{cases} \tag{3.26}$$

where $n_{drop,i}$ is the number of droplets per parcel and d_i is the associated diameter. Hence, using these values, it is verified that Eulerian and Lagrangian approaches carry as average the same liquid volume fraction and particles diameters. If it not case, the number of droplets per parcel as well as the diameter at the injection are corrected to prevent inconsistencies [127]. Therefore, the resulting droplet diameter distribution presents information both from the Eulerian and the Lagrangian references. However, once such hybrid distribution has been defined it is also used to correct the convective velocities of the Eulerian transport equation (see Table 3.1). In fact, in each cell of the computational domain it is possible to calculate the velocities u^{α}_{lag} and u^{Σ}_{lag} that correspond to the

Lagrangian velocities in the Eulerian framework weighted respectively on the liquid volume and surface [127].

$$\begin{cases} u_{lag}^{\alpha} = \dfrac{\sum_i \frac{\pi}{6} n_{drop,i} {d_i}^3 u_{l,i}}{\sum_i \frac{\pi}{6} n_{drop,i} {d_i}^3} \\ u_{lag}^{\Sigma} = \dfrac{\sum_i \pi n_{drop,i} {d_i}^2 u_{l,i}}{\sum_k \pi n_{drop,i} {d_i}^2} \end{cases} \tag{3.27}$$

In order to introduce this contribution in the Eulerian equations, a weighting function between Eulerian and Lagrangian approaches (C_{lag}) is introduced and the number of parcels per cell (n_{parcel}) is used to this end by Hecht [127] : if n_{parcel} is equal to one, the local impact of Lagrangian cloud over the Eulerian framework is negligible, otherwise it has to be included. Equations reported in Table 3.1 are therefore corrected as shown below:

$$\begin{cases} \dfrac{\partial \bar{\alpha_l}}{\partial t} + \dfrac{\partial \bar{U}_i \bar{\alpha_l}}{\partial x_i} = \dfrac{\partial \left(C_\alpha \bar{\alpha_l} \left(1 - \bar{\alpha_l} \right) \right) {U_i}^r}{\partial x_i} + \\ \qquad + \left(1 - C_\alpha \right) \left(1 - C_{lag} \right) \dfrac{\partial \bar{R}_{\alpha_l,i}}{\partial x_i} + \dfrac{\partial C_{lag} \left(u_{lag,i}^{\alpha} - \bar{U}_i \right)}{\partial x_i} \\ \dfrac{\partial \bar{\Sigma}'}{\partial t} + \dfrac{\partial \bar{U}_i \bar{\Sigma}'}{\partial x_i} = \left(1 - C_{lag} \right) \dfrac{\partial}{\partial x_i} \left(\bar{\Sigma}' \left(\bar{U}_i - \bar{U}_{\Gamma,i} \right) \right) + \\ \qquad + \dfrac{\partial C_{lag} \Sigma' \left(u_{lag,i}^{\Sigma} - \bar{U}_i \right)}{\partial x_i} + \dfrac{\bar{\Sigma}}{\tau_t} \left(1 - \dfrac{\bar{\Sigma}}{\bar{\Sigma}_{eq}} \right) \end{cases} \tag{3.28}$$

where $C_{lag} = 1/\sqrt{N_{parcel}}$ is a measure of the effectiveness of the lagrangian methodology to shift between diffusion or lagrangian terms (e.g. $C_{lag} = 1$ if parcels are not present). The higher the number of particles, less significant are diffusion effects [127].

3.4.3 Lagrangian framework

Once injected, a standard Lagrangian approach is employed to follow the evolution of the liquid phase inside the computational domain. The reader interested in a detailed description of this approach is addressed to references [66, 67, 114] among others. However, as already detailed in Chapter 2, several models to account for drag, evaporation and secondary breakup effects have to be provided.
In this section, a brief overview about drag and evaporation modelling is given in order to introduce some basic knowledge that will be then used in the next chapters.

In lagrangian context, numerical particles (i.e. parcels) are individually tracked and the equation of motion, considering a spherical, small and non-rotating particle into a gas medium, illustrates the second law of Newton, so the sum of forces acting upon a mass determines its acceleration:

$$\frac{d\vec{u}_d}{dt} = \frac{1}{m_d}\sum_i F_i \tag{3.29}$$

where $\vec{u}_d$ is the particle velocity, m_d its mass and F_i represents a generic force on the particle.
In the conditions of interest for gas turbine applications, the particle motion is determined mainly by drag and bouyancy forces. As suggested by Faeth [13] all the other contributions, like virtual mass, Basset, Saffman and Magnus forces can be reliably neglected. With these hypotheses the Equation 3.29 can be written as:

$$\frac{d\vec{u}_d}{dt} = \vec{F}_{drag} + \frac{\rho_d - \bar{\rho}}{\rho_d}\vec{g} \tag{3.30}$$

where d_d is the particle diameter. Further information about the expression of the drag force are reported in the next paragraph.
Moreover, during their life droplets undergo heat transfer and evaporation. The evolution of mass and energy of each parcel is computed through the following conservation equations [67, 114]:

$$\begin{cases} \dfrac{dm_d}{dt} = \dot{m} \\ m_d \dfrac{d}{dt}\left(c_{p,l}\left(T_d - T_{ref}\right)\right) = \dot{Q}_d + \dot{m}h_v(T_d) \end{cases} \tag{3.31}$$

where $\dot{m}$ is the evaporation rate, $c_{p,l}$ is the liquid specific heat capacity, T_{ref} is the reference state temperature and h_v is the latent heat of vaporization. $\dot{m}$ and $\dot{Q}_d$ are calculated through specific evaporation and heat transfer models detailed in the devoted following paragraph.

Drag modelling : The drag force represents the aerodynamic interaction between liquid and gas and a general expression for this source term, to be included in Equation 3.30, is:

$$\vec{F}_{drag} = \frac{\pi d^2}{8} C_d \rho_g \left(\vec{U} - \vec{u_d}\right) || \left(\vec{U} - \vec{u_d}\right) || \tag{3.32}$$

The determination of the droplet drag coefficient C_d in a complex environment as a gas turbine chamber, where the droplets experience high

temperatures and pressures (and hence high evaporation rates) and strong deformations, is very difficult and mainly based on experimental studies. In literature, several expressions have been proposed with a direct dependency on the particle Reynolds number. In this study, the formulation proposed by Shiller-Naumann [67] for a spherical, not deformable particle has been employed:

$$C_d = \begin{cases} 0.44, & \text{if } Re_p \geq 1000 \\ \frac{24}{Re_p}(1 + \frac{1}{6}Re_p^{2/3}) & \text{if } Re_p < 1000 \end{cases} \tag{3.33}$$

Equation 3.30 can be written again introducing also the definition of a *dynamic relaxation time*, τ_p. It represents the time required for a particle to reach the 63% of the gas phase velocity. Hence, in the case of low Reynolds numbers ($Re_p < 1$), Equation(3.30) can be rearranged in the following linear form considering that in this case $C_d = \frac{24}{Re_p}$:

$$\frac{d\vec{u}_d}{dt} = C_d \frac{3}{4} \frac{\mu_g Re_p}{\rho_p d^2}(\vec{U} - \vec{u}_d) = \frac{1}{\tau_p}(\vec{U} - \vec{u_d}) \tag{3.34}$$

which for an initial droplet velocity equal to zero has the following general solution:

$$\vec{u}_d = \vec{U}(1 - e^{-\frac{t}{\tau_p}}) \tag{3.35}$$

The expression of τ_p employed in Equation 3.34 is valid only at low Reynolds numbers, but generally it is possible to define a dynamic relaxation time like:

$$\tau_p = \frac{4}{3} \frac{\rho_p d^2}{\mu_g Re_p C_d} \tag{3.36}$$

which in the case of $Re_p < 1$ becomes:

$$\tau_p = \frac{\rho_p d^2}{18\mu_g} \tag{3.37}$$

Based on the dynamic relaxation time, the *Stokes* number can be as well defined as:

$$St = \frac{\tau_p}{\tau_g} \tag{3.38}$$

where τ_g is a characteristic time of the gas-phase. It gives a measure of the relative importance of the dynamic of the liquid phase with respect to the carrier one.

Evaporation modelling: A reliable description of the spray evaporation process is another fundamental step in the prediction of the fuel

distribution inside the combustion chamber. Several models have been derived through years and the major part of the existing approaches are actually based on single spherical droplet assumption [114]. A general approach for vaporization in presence of high values of liquid volume fraction is still under development.
A complete evaporation model should take into account all the transport phenomena, around and inside the droplet as shown in Figure 3.6. The heat exchange between the gas and liquid phases by convection should be included together with conduction inside the droplet and phase change phenomena at the liquid-gas interface [66, 114]. Anyway, a comprehensive

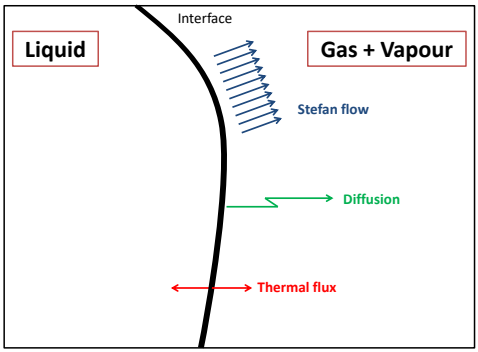

Figure 3.6: Schematic representation of the phenomena involved in liquid evaporation (adapted from [140])

modelling strategy would be extremely expensive and can be reliably employed just for single droplet investigations. Therefore, in order to take into account only the dominant processes involved, the *Biot number* is introduced for a droplet of diameter d [66]:

$$Bi = \frac{hd}{2\lambda_d} \tag{3.39}$$

where h is the heat transfer coefficient and λ_d the fuel conductivity. It represents the relative strength of the external heat transfer over the internal conduction. Based on the Biot number, different configurations can be introduced:

- $Bi \rightarrow 0$, the heat conduction inside the droplet is dominating

over the external heat transfer. The internal conduction smooths the temperature profile inside the droplet very quickly and only a small temperature gradient is established. Temperature is therefore uniform inside the droplet, thus it is referred as *uniform temperature* model.

- $Bi \to \infty$, the droplet is heated up only on the surface by the external heat and a *thin skin* approximation can be applied where only the droplet surface raises its temperature.

- $Bi = n$, a predominant process of heat transfer cannot be identified and more advanced strategies like the *conduction limit model* have to be applied [66].

In the conditions of interest of aero-engine combustors, the uniform temperature model can be reliably applied [66].
In order to derive the governing equations for evaporation and heat transfer, the domain is normally dived in three regions (see Figure 3.7):

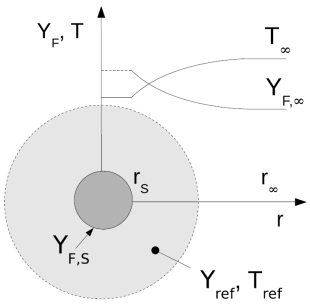

Figure 3.7: Regions considered in the uniform temperature model (adapted from [141]).

- **gas-phase**, which represents the region infinitely far from the droplet. Here, the temperatures and vapour concentrations are those of the carrier phase.

- **droplet surface**, which is a layer located at the interface between gas and liquid where transport processes take place. It is normally specified in literature as *thin film layer*.

- **droplet interior**.

In [12], starting from this domain definition, an analysis on single droplet evaporation has been carried out. Based on the main assumptions of spherical symmetry, constant fluid properties and supposing a quasi-steady evolution for the gas phase and the absence of convection phenomena, the following equation can be derived for a single evaporating droplet [12]: :

$$\dot{m} = 2\pi d \rho_{ref} D_{ref} \ln(1 + B_M) \tag{3.40}$$

where ρ_{ref} and D_{ref} are density and the mass diffusivity of the air-vapour mixture at a reference condition. B_M is instead the *Spalding mass transfer number*. Faeth [142] suggests computing all these physical properties through the so called *1/3-rule*:

$$Y_{ref} = Y_{F,S} + \frac{1}{3}(Y_{F,\infty} - Y_{F,S}) \tag{3.41}$$

$$T_{ref} = T_d + \frac{1}{3}(T_\infty - T_d) \tag{3.42}$$

where $Y_{F,S}$ and $Y_{F,\infty}$ are vapour mass fraction on droplet surface and in gas phase. It should be pointed out that the same law was used in Chapter 2 for the analysis of lean spray flames.
To derive Equation 3.40, a thermodynamic equilibrium assumption should be introduced where $Y_{F,S}$ can be calculated from T_d using the Antoine or Clasius-Clapeyron equation ($p_{sat}(T_d)$) [12].

$$Y_{F,S} = \frac{\chi_{S,eq} W_F}{\chi_{S,eq} W_F + (1 - \chi_{S,eq}) W_g} \tag{3.43}$$

where $\chi_{S,eq} = p_{sat}(T_d)/\rho_g$ is the equilibrium surface molar fraction, while W_F and W_g are molecular weight of vapour fuel and gas phase respectively. The Spalding mass transfer number (B_M) can be therefore computed as:

$$B_M = \frac{Y_{F,S} - Y_{F,\infty}}{1 - Y_{F,S}} \tag{3.44}$$

Equation 3.40 represents the fundamental expression of the evaporation rate. However, further developed formulations can be derived by removing some of the aforementioned assumptions. For instance, a correction to account for convection and Stefan flows effects can be introduced. In this case Equation 3.40 is modified as follows [69]:

$$\dot{m} = \pi d \rho_{ref} D_{ref} Sh^* \ln(1 + B_M) \tag{3.45}$$

where the Sherwood number Sh^* has been introduced. Abramzon and Sirignano [69] suggest to compute it as:

$$Sh^* = 2 + \frac{Sh_0 - 2}{F_M} \tag{3.46}$$

where Sh_0 is a reference value of Sherwood in absence of convective fluxes, which can be calculated by means of experimental correlations as a function of Reynolds and Schmidt droplet numbers. Since Reynolds number is defined on the relative velocity (see Section 3.1), convective fluxes are therefore directly included. Instead, F_M, which is a correction due to droplet evaporation derived from boundary layer theory, can be calculated as follows:

$$F_M = (1 + B_M)^{0.7} \frac{\ln(1 + B_M)}{B_M} \tag{3.47}$$

This is the so called *Abramzon-Sirignano* model [69]. In a similar manner with respect to Equation 3.45, the evaporation rate can be expressed also in terms of thermal properties [69]:

$$\dot{m} = \pi d \frac{k_{ref}}{D_{ref}} Nu^* \ln(1 + B_T^{'}) \tag{3.48}$$

where k_{ref} is the thermal conductivity at the reference state. The *Spalding heat transfer number* $B_T^{'}$ can be defined as:

$$B_T^{'} = \frac{c_{p,f}(T_\infty - T_d)}{L - \dot{Q}/\dot{m}} \tag{3.49}$$

where $c_{p,f}$ is the fuel vapour specific heat, L is the latent heat of vaporization and $\dot{Q}$ is the heat transferred into the droplet per unit of time [69]. The modified Nusselt number Nu^* can be determined similarly to the Sherwood one:

$$Nu^* = 2 + \frac{Nu_0 - 2}{F_T} \tag{3.50}$$

$$Nu_0 = 2 + 0.552 Re^{\frac{1}{2}} Pr^{\frac{1}{3}} \tag{3.51}$$

$$F_T = (1 + B_T^{'})^{0.7} \frac{\ln(1 + B_T^{'})}{B_T^{'}} \tag{3.52}$$

where the Ranz-Marshall correlation [143] was reported to evaluate the Nu_0, where the Prandtl number is:

$$Pr = \frac{c_{p,g}\mu_g}{k_g} \tag{3.53}$$

Under the assumption of Lewis number equal to one: $Sh^* = Nu^*$ and $B_M = B_T^{'}$.
Clearly, several alternative formulations with respect to Abramzon and Sirignano have been also proposed. For instance, in some commercial codes, such as ANSYS® CFX, another widely used expression is the one proposed by Borman and Johnson [144] and reported here below.

$$\dot{m} = \pi d \rho_{ref} D_{ref} Sh_0 \ln\left(\frac{p_g - p_{v,\infty}}{p_g - p_{v,s}}\right) \tag{3.54}$$

where p_g is the gas pressure, whereas $p_{v,s}$ and $p_{v,\infty}$ are respectively the partial pressure of fuel vapour at the droplet surface and far from it.
Nevertheless, Equation 3.47 surely represents one of the most known and employed laws in evaporation framework.
Vaporization has also a key role in heat transfer. The thermal energy from the gas phase to the drop can be calculated as:

$$\dot{Q}_d = \pi d^2 h (T_\infty - T_d) \tag{3.55}$$

and it can be recast in terms of Spalding heat transfer number as:

$$\dot{Q}_d = \pi d k_{ref} Nu^* \frac{\ln(1 + B_T^{'})}{B_T^{'}} (T_\infty - T_d) \tag{3.56}$$

The derived relationships can be used to compute the evaporation rate and heat transfer of a single droplet. Obviously, in order to obtain the evaporation rate of a spray cloud, it has to be multiplied with the number of droplets contained in each parcel.

3.5 Limitations of ELSA approach for aero-engine applications

The ELSA approach for LES presented so far has been already applied in the context of liquid jet atomization, compared with both DNS and experimental data.
In [126], where the coupled DNS-LES approach has been implemented in the DNS code ARCHER [145, 146], a comparison with DNS results on a Diesel like injection system was performed. In Figure 3.8, the obtained qualitative and quantitative comparisons are shown. Data calculated with a full VOF approach in LES are also reported for further comparison. As explained in detail in [126], with respect to VOF results, where the liquid column seems to be nearly unaffected and no relevant surface instabilities

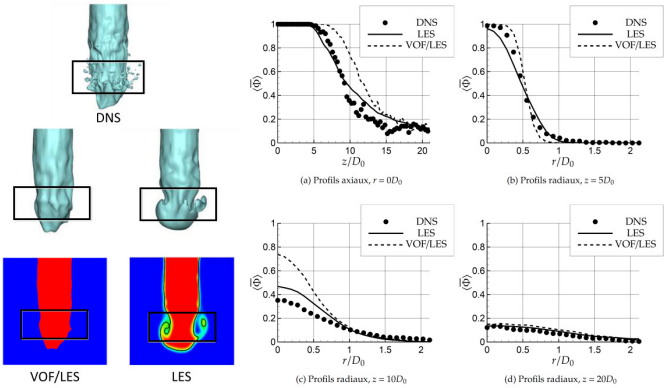

Figure 3.8: Comparison between DNS data and DNS-LES coupled approach. VOF/LES is shown as further comparison. Qualitative comparison on the left and liquid volume fraction profiles on the right. Adapted from [126].

are generated along the liquid/gas interface, the coupled DNS-LES approach based on ELSA is able to reproduce the generation of a classical mushroom shape thanks to the sub-grid scale contribution. The slice of the liquid volume fraction field, reported on the left-bottom side of the figure, clearly shows that the wrinkling of the interface in the black box is due to the diffusion at SGS level. The quantitative comparison with the DNS data confirms the capabilities of the coupled approach.
A validation on a similar jet in co-flow geometrical configuration with detailed experimental data implementing the same VOF-ELSA approach in OpenFOAM® has been performed also by Hecht et al. [127]. Obtained results show the consistency of the developed approach in terms of switching criteria describing the whole atomization process shown in Figure 3.9. Three main regions can be clearly identified: a central core of the jet where the interface is resolved with an interface capturing method, zones, where the liquid wrinkling is under-resolved and the sub-grid scale modelling acts, and a dispersed spray that is tracked in a lagrangian frame. As soon as the mesh is not fine enough to correctly solve the interface, the diffusion term is activated leading to a reliable prediction of the jet dispersion and breakup. Further results and sensitivities on the developed solver in OpenFOAM® can be found also in [147, 148, 149].

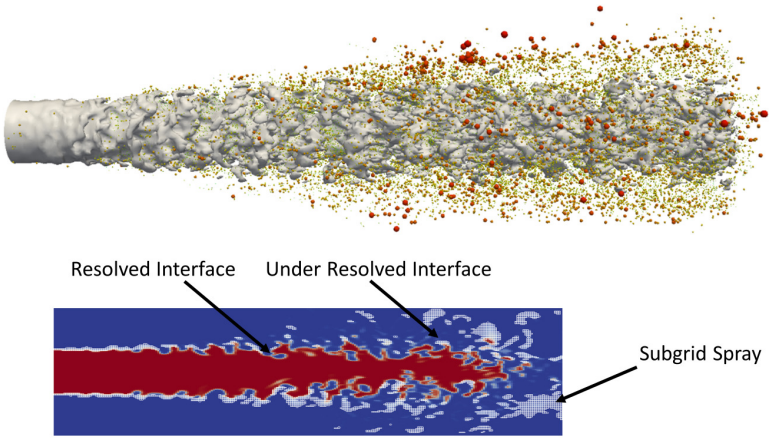

Figure 3.9: Evolution of the complete atomization process for a diesel jet from injection up to the dispersed spray. Adapted from [127].

Nonetheless, some developments are required to extend the capabilities of such approach to account for the reactive conditions and swirled flow field of lean burners.
The extension of the capabilities of the VOF-ELSA approach in LES context for aero-engines applications has been the main goal of this second part of the research activity.
It is worth pointing out that the primary aim of this piece of work was not to demonstrate the capabilities of ELSA in reproducing a breakup process since this topic has been already widely investigated by several research groups with a fair agreement in terms of diameter distribution (i.e. Demoulin et al. [60, 126, 127, 147, 148, 149]), Garcia et al. [150, 151, 152] and Schmidt et al. [153, 154] among others), but mainly to broaden its characteristics for aero-engines applications. Clearly, the validation of each one of the proposed developments represents a further assessment of such methodology.
In particular, one of the key points on which the work has been focused is the modelling of turbulent liquid flux $\vec{R}_{\alpha_l}$ (see Equation 3.11). This term is directly related to the liquid flux and it drives the fuel dispersion and evolution. As already mentioned, a simple Fick's law based on a turbulent diffusion coefficient D_t has been employed to model this term by Hecht

et al. [127]:

$$\bar{R}_{\alpha_l,i} = \overline{u_i'\alpha_l'} = -\frac{\nu_t}{Sc_t}\frac{\partial \bar{\alpha}_l}{\partial x_i} = -D_t\frac{\partial \bar{\alpha}_l}{\partial x_i} \tag{3.57}$$

However, this approach is valid only in the absence of a mean slip velocity between liquid and gas. In fact, if the phases are strictly immiscible, it is possible to derive the following exact definition for the turbulent liquid flux that shows the strong link between $\vec{R}_{\alpha_l}$ and the local relative velocity $\vec{V}_{rlg}$[138]:

$$\bar{R}_{\alpha_l,i} = \overline{u_i'\alpha_l'} = -\bar{\alpha}_l(\bar{U}_i - \bar{U}_{l,i}) = \bar{\alpha}_l(1-\bar{\alpha}_l)\bar{V}_{rlg,i} \tag{3.58}$$

It should be considered also that the local relative velocity, following the analysis developed by Deutsch and Simonin [155, 156], can be also re-arranged as:

$$\bar{V}_{rlg,i} = (\bar{U}_{l,i} - \bar{U}_{g,i} - \bar{U}_{D,i}) = (\bar{U}_{slg,i} - \bar{V}_{Dlg,i}) \tag{3.59}$$

This decomposition shows the two main components of the relative velocity in a particle two-phase flow:

- an average relative velocity, here specified as $\bar{U}_{slg,i}$, between the particle and the surrounding flow in the promixity of the interface that is directly related to the drag force acting on the liquid (see Equation 3.32).

- a drift velocity ($\bar{V}_{Dlg,i}$) that is the conditional average of the fluid turbulent velocity fluctuation with respect to the particle distribution [156].

Hereinafter, to avoid a too complex notation, the slip velocity $\bar{U}_{slg,i}$ will be specified as $\bar{U}_{s,i}$ and the drift as $\bar{V}_{D,i}$. The drift component accounts for the dispersion mechanism due to the particle transport by the fluid turbulent motion and it holds in a mixture of two different species in a single-phase flow. It is related to a random agitation that promotes homogenization of phase concentration, leading to the generation of a mean average velocity. Hence, models developed in single-phase context can be used for its closure. For example, considering the approach proposed by Bailly et al. [157], where the turbulent flux of a scalar quantity in a single-phase mixture is considered, the following classical gradient closure for drift was proposed:

$$V_{D,i} = \frac{D_t}{\bar{\alpha}_l\left(1-\bar{\alpha}_l\right)}\frac{\partial \bar{\alpha}_l}{\partial x_i} \tag{3.60}$$

where D_t represents the liquid/gas turbulent dispersion coefficient.
Thus, if the spray dynamic relaxation time τ_p and the mean effective slip velocity $\bar{U}_{s,i}$ are negligible (i.e. in the case of droplets with low intertia) the turbulent liquid flux is only due to the drift velocity and Equation 3.57 can be exactly applied.
Under the same assumptions, the first term on the RHS of Σ-equation (see Equation 3.21) can be modelled as a turbulent diffusion term [60, 158], neglecting the effects of the slip velocity on the liquid/gas interface density distribution.

$$\bar{R}_{\Sigma,i} = \left(\bar{\Sigma}'\left(\bar{U}_i - \bar{U}_{\Gamma,i}\right)\right) = \frac{\nu_t}{Sc_t}\frac{\partial \bar{\Sigma}'}{\partial x_i} \tag{3.61}$$

It should be pointed out that some modifications to these single-phase closure can be considered in order to include the effects of liquid inertia and liquid surface discontinuity [138, 156]. However, when the mean slip velocity is not negligible, these formulations have to be deeply revised.
Considering the flow-field characteristics of lean combustor atomizer, the slip velocity can have a strong impact. This has been verified using the steady-state Eulerian-Lagrangian computations realized in [114, 159] on the PERM injection system (see the Introduction for further details about the PERM system). From Lagrangian data it is possible to extract the spray evolution as in an Eulerian framework by averaging the properties of parcels cell by cell.
The chosen test condition is characterized by low pressure and by a locally high fuel-air ratio, with 20% of fuel that is injected through the pilot injector. Figure 3.10 reports the obtained evolution of slip velocity and spray volume fraction. Because of the high Sauter Mean Diameter, due to low values of air inlet temperature, droplets fully evaporate far away from the injection location and particles injected through the pilot nozzle reach the prefilming surface. Near the pilot injector, due to the high inertia of liquid droplets, particles do not follow the gas stream, maintaining a slip velocity up to the prefilming surface as high as 70 m/s. The importance of such velocity on the liquid distribution can be stressed also showing in Figure 3.11 the evolution of the ratio between the slip and the mixture velocity in the pilot region: locally U_s assumes values four time bigger than $\bar{U}$ and it gradually decreases due to the drag of the gas phase.
However, the relative importance of U_s in the pilot region with this geometrical configuration is very high and cannot be neglected as it may have a strong effect on the liquid distribution. It is worth noting that the slip velocity should have a high impact also for injector configurations different from prefilming atomizers, like those based on breakup of jets in

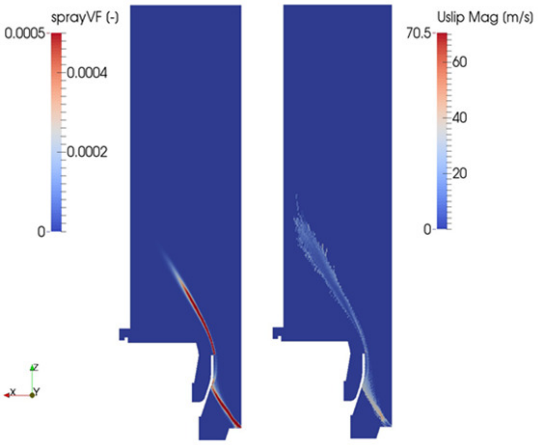

Figure 3.10: Evolution of slip velocity and liquid volume fraction on the symmetry plane [160].

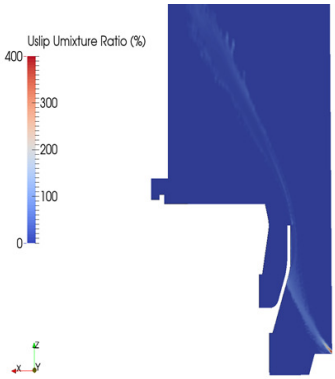

Figure 3.11: Zoom of the distribution of the ratio between the slip and the mixture velocity in the pilot region [160].

crossflow (e.g. the TAPS atomizer described in the Introduction). Here, the liquid mixing is completely controlled by discrete jets and, mainly in the region of jets impact, the slip velocity can be significant.
Therefore, strong attention has been devoted in this research work to

include the effect of slip velocity inside the ELSA context. This problem has been already faced by the author in [160] and in the next chapter the main achievements are summarized: the issues associated with the turbulent liquid flux are analysed and a novel *Quasi Multiphase Eulerian* (QME) approach is proposed and assessed on a jet in crossflow configuration.
Furthermore, considering that the attention is here focused on the analysis of the atomization process in reactive conditions, the evaporation process represents another key step in the evolution of the liquid phase. As already shown in Chapter 2, the topology of a spray flame and its stabilization are completely related to the developments of the breakup and evaporation phenomena.
Therefore, another important part of the work has been focused on the development of a compressible solver of ELSA for LES and to the introduction of an innovative modelling strategy for evaporation. Chapter 5 is completely focused on this topic.
Finally, a further limitation of the actual ELSA formulation that can deeply affect the performances of the model in the aero-engine context is the choice of a Dirac function as droplet size distribution at the lagrangian injection. In [127], the spray was assumed locally monodispersed and no spray dispersion was included. This is not generally true and it can deeply modify the evaporation and combustion processes. As reviewed in [161, 162], several types of functions can be encountered such as Rosin-Rammler, modified Rosin-Rammler, log-nomal or Nukiyama-Tanasawa distributions. A definition of their mathematical formulations can be found in [12, 161]. However, no one of these distributions is universally better than any other. In Chapter 6 this problem is discussed in detail and to overcome these issues, distributions of novel interface geometrical properties are studied thanks to DNS analyses.

3.6 Concluding remarks

In this chapter, an overview about atomization both from a physical and computational point of view is given. In particular, issues associated to the development of an LES atomization model were presented and a coupled DNS-LES strategy, based on the ELSA formalism, proposed as a possible solution. Based on values locally assumed by two quality criteria, if the mesh sizing is fine enough an interface capturing method is applied, while in the opposite case a standard diffuse interface approach is employed. The resulting VOF-ELSA solver, both in its Eulerian and Lagrangian frameworks, has been described with particular attention to

the Eulerian-Lagrangian coupling. In the last part of the chapter, some limitations of such approach in handling a swirled reactive environment like an aero-engine burner have been also highlighted in order to justify the efforts presented in the next chapters.

Chapter 4

Quasi Multiphase Eulerian approach for ELSA framework

In the previous chapter, the ELSA model has been presented together with its actual limitations for applications where slip velocity effects are significant (e.g. swirled flow-fields). In particular, the use of a gradient law for turbulent liquid flux ($\vec{R}_{\alpha_l}$) has been identified as one of the most important limiting points. Such contribution can completely modify the evolution of the liquid phase and therefore deeply affect the resulting reacting flow-field.
This chapter is devoted to the presentation of further advanced strategies that can be used to account for the effects of turbulent liquid flux. Firstly, a review of second order closures is carried out in order to highlight the characteristics of the approaches already available in technical literature. Then, a novel framework to derive a transport equation for $\vec{R}_{\alpha_l}$ is described and an innovative method to include the effects of slip velocity inside ELSA is presented. Finally, an assessment of the capabilities of the developed Quasi-Multiphase Eulerian (QME) approach is reported on a literature jet in crossflow test case.

4.1 Eulerian-Eulerian solver from ELSA

The Quasi Multiphase Eulerian (QME) solver here proposed has been initially developed starting from the mixture Eulerian-Eulerian solver derived from ELSA. Therefore, beginning from the system of equations 3.28, C_α has been set equal to zero and the lagrangian contribution has been turned off. This modelling choice is related to the fact that the slip acts in the diffuse interface region of the solver, whereas it has not impact as long as VOF is applied. Therefore, the resulting system of equations here below has been considered as starting point:

$$\begin{cases} \dfrac{\partial \bar{\rho}\bar{U}_i}{\partial t} + \dfrac{\partial \bar{\rho}\bar{U}_i\bar{U}_j}{\partial x_j} = -\dfrac{\partial \bar{P}}{\partial x_i} + \dfrac{\partial}{\partial x_j}\left(\bar{\mu}\left(\dfrac{\partial \bar{U}_i}{\partial x_j} + \dfrac{\partial \bar{U}_j}{\partial x_i}\right)\right) - \dfrac{\partial \tau_{\rho u_i u_j}}{\partial x_j} \\ \dfrac{\partial \bar{\Sigma}'}{\partial t} + \dfrac{\partial \bar{U}_i\bar{\Sigma}'}{\partial x_i} = \dfrac{\partial}{\partial x_i}\left(\bar{\Sigma}'\left(\bar{U}_i - \bar{U}_{\Gamma,i}\right)\right) + \dfrac{\bar{\Sigma}'}{\tau_t}\left(1 - \dfrac{\bar{\Sigma}'}{\Sigma_{eq}}\right) \\ \dfrac{\partial \bar{\alpha}_l}{\partial t} + \dfrac{\partial \bar{U}_i\bar{\alpha}_l}{\partial x_i} = \dfrac{\partial\left(\bar{U}_i\bar{\alpha}_l - \overline{U_i\alpha_l}\right)}{\partial x_i} = \dfrac{\partial(-\bar{R}_{\alpha_l,i})}{\partial x_i} \end{cases} \tag{4.1}$$

As already mentioned in Section 3.3, $\tau_{\rho u_i u_j}$ represents the contribution of turbulent fluctuations comprising also the density correlation terms. The reader interested in a more thorough discussion of the consequences of this modelling choice is addressed to Annex-A.

The liquid volume fraction equation contains only one unclosed term, i.e. the turbulent liquid flux ($R_{\alpha_{l,i}}$), which represents the transport of the liquid volume fraction induced by velocity fluctuations. This prevailing term describes liquid dispersion and normally, due to the high-density ratio of two-phase flow under investigation, it may dominate the evolution of the liquid. Similarly, the first contribution on the RHS of the liquid/gas interface density equation, which accounts for the mean surface velocity, should be correctly modelled.

As described in Section 3.5, first order closures for these terms are not satisfactory in the frame of aero-engine burners. The goal of this part of the work has been therefore the proposition and assessment of a novel closure for turbulent liquid flux to be applied to ELSA.

4.2 Second order closures for turbulent liquid flux

In order to overcome the issues in presence of a mean slip velocity with gradient based closure, a second order model, in which each component of the turbulent liquid flux is individually analysed, is here proposed as a solution. A general formulation of the studied conservation equation may

be the following one:

$$\frac{D\bar{R}_{\alpha_l,i}}{Dt} = \frac{\partial \overline{u_i'\alpha_l'}}{\partial t} + \frac{\partial \bar{U}_j \overline{u_i'\alpha_l'}}{\partial x_j} = \sum_{k=1}^{N} \Theta_k \tag{4.2}$$

Terms appearing on the RHS have to be properly closed and Θ_k stands for the N different physical phenomena that involve a production, destruction or transport of the turbulent liquid flux. For example, drag force, body forces, such as gravity, or any pressure gradient should be included in such term: because of the density ratio, they would lead to a different acceleration of each phase and therefore to the generation of a relative velocity.
A preliminary review of the approaches already proposed in literature to close Equation 4.2 is first provided. Then, a novel modelling framework is proposed and a new transport equation is derived and assessed on a jet in crossflow configuration.

4.2.1 Review of previous numerical works

In this section, the main efforts proposed in technical literature to address the problem of the turbulent liquid flux closure are discussed. A similar review was also proposed in [158] and the main results and conclusions are here summarized and commented. It should be pointed out that, in order to be as consistent as possible between different approaches, in this section a Favre averaging procedure is applied to Equation 4.2. It is related to the fact that previous works in this context employed a mass-weighted formulation of the proposed system of equations, while here a volume-based formalism has been adopted.
Therefore, considering a variable ϕ, the mass weighted Favre average is denoted as $\tilde{\phi} = \overline{\rho\phi}/\bar{\rho}$ and the corresponding fluctuation as ϕ''. Hence, $\bar{\rho}$ is the mean mixture density, $\tilde{U}_i$ is the Favre averaged mixture velocity and $\bar{P}$ is the mean pressure [60]. In this context, the following definition of turbulent liquid flux is introduced:

$$R_{Y_{l,i}} = \overline{\rho u_i'' y_l''} = -\bar{\rho}\tilde{Y}_l \left(1 - \tilde{Y}_l\right) (\bar{U}_{l,i} - \bar{U}_{g,i}) \tag{4.3}$$

Turbulent liquid flux closure for a mono-phase mixture. Bailly [157] considers the two-phase mixture as a single-phase system composed by gases of different volumetric mass. An analogy between a second order model for progress variable (c) in the environment of premixed combustion and an equation for liquid mass fraction (Y_l) is proposed. Thus, both c

and Y_l are used as indicator function with the following equivalence:

$$\begin{cases} Y_l = c = 1, & \text{if the point is in the liquid phase or burn gas;} \\ Y_l = c = 0, & \text{if the point is in the gas phase or fresh gas;} \end{cases} \tag{4.4}$$

Using this relation, an equation for turbulent liquid flux is derived (see Equation 4.5) [157]. Considering the single-phase environment here assumed, all the terms related to viscous forces and laminar diffusion disappear.

$$\frac{\partial \overline{\rho u_i'' y_l''}}{\partial t} + \frac{\partial \tilde{U}_j \overline{\rho u_i'' y_l''}}{\partial x_j} = \underbrace{-\frac{\partial \left(\overline{\rho u_j'' u_i'' y_l''} + \overline{p' y_l''} \delta_{ij} \right)}{\partial x_j}}_{A} \underbrace{- \overline{\rho u_i'' u_j''} \frac{\partial \tilde{Y}_l}{\partial x_j}}_{B} \underbrace{- \overline{\rho u_j'' y_l''} \frac{\partial \tilde{U}_i}{\partial x_j}}_{C} + \underbrace{- \overline{y_l''} \frac{\partial \bar{P}}{\partial x_i} + \overline{p' \frac{\partial y_l''}{\partial x_i}}}_{D} \tag{4.5}$$

The equation is unclosed, since the turbulent diffusion term (A), which relates the fluctuations of velocity to the turbulent liquid flux, and the one accounting for the fluctuations of pressure (D) have to be properly modelled. Employing a standard gradient-based closure for turbulent diffusion, the following equation for turbulent liquid flux can be derived :

$$\frac{\partial \overline{\rho u_i'' y_l''}}{\partial t} + \frac{\partial \tilde{U}_j \overline{\rho u_i'' y_l''}}{\partial x_j} = \underbrace{\frac{\partial}{\partial x_j} \left(\frac{\mu_t}{Sc_t} \frac{\partial}{\partial x_j} \left(\frac{\overline{\rho u_i'' y_l''}}{\bar{\rho}} \right) \right)}_{A} \underbrace{- \overline{\rho u_i'' u_j''} \frac{\partial \tilde{Y}_l}{\partial x_j}}_{B} + \underbrace{(C_1 - 1) \overline{\rho u_i'' y_l''} \frac{\partial \tilde{U}_i}{\partial x_j}}_{C} + \underbrace{+ (C_2 - 1) \overline{y_l''} \frac{\partial \bar{P}}{\partial x_i} - C_3 \frac{\overline{\rho u_i'' y_l''}}{\tau_t}}_{D} \tag{4.6}$$

where fluctuations of liquid mass fraction can be calculated starting from the liquid volume fraction and liquid mass fraction. On the RHS of 4.6, it is possible to recognize a source term accounting for the effects of the gradient of liquid mass fraction (B) and one that considers the influence of the velocity gradient (C) on the turbulent liquid flux. Furthermore,

with the group of terms identified with D, the effects of the mean pressure gradient and of the turbulence dissipation on turbulent liquid flux are introduced. In this latter source term, a dependency on the turbulent time scale τ_t is assumed. This hypothesis means that the slip velocity between the phases is controlled by turbulence and this can be verified only if a mono-phase mixture, composed by gases with variable density or by liquid and gas without inertial effects, is under investigation.
Considering the applications of interest in this study, this approach can be not completely representative and a formulation with a direct dependency to a dynamic relaxation time should be preferred.

Turbulent liquid flux closure from Eulerian multiphase approach. In this case, a mixture composed by two distinct phases is considered. In order to evaluate a closure for turbulent liquid flux, an equation for the average velocity of the liquid in a standard Eulerian-Eulerian multiphase framework is first derived [163]. To this end, Drew [163] applies a phase averaging process to the system of equations available for the single phase mixture, obtaining the following expression.

$$\frac{\partial \rho_l \bar{\alpha}_l \bar{U}_{l,i}}{\partial t} + \frac{\partial \rho_l \bar{\alpha}_l \bar{U}_{l,i} \bar{U}_{l,j}}{\partial x_j} = - \frac{\partial \rho_l \bar{\alpha}_l \overline{u'_{l,i} u'_{l,j}}}{\partial x_j} - \bar{\alpha}_l \frac{\partial \bar{P}_l}{\partial x_i} + \frac{\partial \bar{\alpha}_l \bar{\tau}_{l,ij}}{\partial x_j} + \rho_l \overline{\alpha_l} \overline{f}_{l,i} + \\ + \Theta_l \bar{U}_{l,int,i} + M_{l,i} + (P_{l,int} - \bar{P}_l) \frac{\partial \bar{\alpha}_l}{\partial x_i} \tag{4.7}$$

where P_l represents the pressure conditioned on the liquid phase, $f_{l,i}$ the external forces acting on the considered phase and $M_{l,i}$ the average force density on the liquid/gas interface. Moreover, with $\Theta_l \bar{U}_{l,int,i}$ evaporation is included, where the vaporization rate Θ_l can be evaluated as:

$$\Theta_l = \rho_l (U_{l,i} - U_{int,i}) n_i \delta_s = \rho_l U_{vap,i} n_i \delta_s \tag{4.8}$$

where with the subscript *int* the variables at the liquid/gas interface are evaluated. The source term $\left((P_{l,int} - \bar{P}_l) \frac{\partial \bar{\alpha}_l}{\partial x_i} \right)$ represents instead the pressure equilibrium on the droplet surface. Assuming an instantaneous microscopic pressure equilibration at the liquid-gas interface, which will be the case if the speed of sound in each phase is large compared to the convective fluxes, this contribution is normally negligible.
The transport equation for the turbulent liquid flux, recalling its theoretical definition (see Equation 4.3), can be then calculated subtracting Equation 4.7 from the following further equation (obtained by summing the equation for the liquid mass fraction multiplied by $\tilde{U}_i$ and the equation

for the mixture velocity multiplied by $\tilde{Y}_l$ [163]):

$$\begin{aligned}
&\frac{\partial \bar{\rho}\tilde{Y}_l\tilde{U}_i}{\partial t} + \frac{\partial \bar{\rho}\tilde{Y}_l\tilde{U}_i\tilde{U}_j}{\partial x_j} = \\
&-\tilde{U}_i\frac{\partial \overline{\rho u_j'' y_l''}}{\partial x_j} + \bar{\Theta}_l\tilde{U}_i - \tilde{Y}_l\frac{\partial \overline{\rho u_i'' u_j''}}{\partial x_j} + \\
&-\frac{\partial \tilde{Y}_l\bar{P}}{\partial x_i} + \bar{P}\frac{\partial \tilde{Y}_l}{\partial x_i} + \frac{\partial \tilde{Y}\bar{\tau}_{i,j}}{\partial x_j} - \bar{\tau}_{i,j}\frac{\partial \tilde{Y}_l}{\partial x_j} + \bar{\rho}\tilde{Y}_l\tilde{F}_i + \tilde{Y}_l\overline{\sigma\kappa n_i\delta_s}
\end{aligned} \tag{4.9}$$

Using this procedure, it is possible to derive the following exact closure for the turbulent liquid flux [158]:

$$\begin{aligned}
&\frac{\partial \overline{\rho u_i'' y_l''}}{\partial t} + \frac{\partial \tilde{U}_j\overline{\rho u_i'' y_l''}}{\partial x_j} = \\
&\underbrace{-\frac{\partial \overline{\rho u_i'' u_j'' y_l''}}{\partial x_j}}_{A} \underbrace{-\overline{\rho u_i'' u_j''}\frac{\partial \tilde{Y}_l}{\partial x_j}}_{B} \underbrace{-\overline{\rho u_j'' y_l''}\frac{\partial \tilde{U}_i}{\partial x_j}}_{C} + \\
&\underbrace{\underbrace{+\underbrace{M_{l,i}}_{D_1} \underbrace{-\frac{\partial \overline{Y_l P_l}}{\partial x_i} + \frac{\partial \bar{\alpha}_l\bar{\tau}_{l,ij}}{\partial x_j}}_{D_2} + \underbrace{\tilde{Y}_l\frac{\partial \bar{P}}{\partial x_i} + P_{l,int}\frac{\partial \bar{\alpha}_l}{\partial x_i}}_{D_3}}_{D} + \\
&\underbrace{-\tilde{Y}_l\frac{\partial \bar{\tau}_{ij}}{\partial x_j}}_{E} \underbrace{-\bar{\rho}\tilde{Y}_l(1-\tilde{Y}_l)(\bar{F}_{g,i}-\bar{F}_{l,i})}_{F} + \underbrace{\Theta_l(\bar{U}_{l,int,i}-\tilde{U}_i)}_{G} \underbrace{-\tilde{Y}_l\overline{\sigma\kappa n_i\delta_s}}_{H}
\end{aligned} \tag{4.10}$$

This equation is complete since all the possible physical phenomena that generate a slip velocity are considered. In addition to the source terms coming from the single-phase approach (A,B,C), different expressions to account for the interactions between liquid and gas (D_1) and for the pressure effects (D_2) are here included. The influences of viscous stresses (E), body forces (F), evaporation (G) and surface tension (H) are as well introduced. Moreover, with D_3, the source term accounting for the momentum exchange because of collisions in a eulerian framework is specified.

The main drawback of this formulation is due to the expression of the source term $\vec{M}_l$, which accounts for the integral of pressure force on the interface. It has not a general expression and it can be calculated as a drag term only if an isolated cloud of droplets is under investigation. This assumption is the basis of the approach for turbulent liquid flux modelling derived in the next paragraph.

Turbulent liquid flux closure from standard multiphase approach. Within a general multiphase Eulerian context, problems have been encountered in handling in the equation of turbulent liquid flux a source term due to drag. For this reason, in the present approach an isolated cloud of droplets is investigated. Clearly, this leads to strongly simplify the modelling framework. Simonin [164] derives an exact expression for the velocity of the liquid phase in such physical situation, integrating the Williams-Boltzmann Equation (WBE) by assuming that each droplet follow the drag force acting on a single particle injected in a infinite flow. Hence, considering a mixture composed by a continuous gas phase with liquid dispersed drops, the following momentum equation for the liquid phase can be evaluated [164]:

$$\frac{\partial \rho_l \bar{\alpha}_l \bar{U}_{l,i}}{\partial t} + \frac{\partial \rho_l \bar{\alpha}_l \bar{U}_{l,i} \bar{U}_{l,j}}{\partial x_j} = -\frac{\partial \rho_l \bar{\alpha}_l \overline{u'_{l,i} u'_{l,j}}}{\partial x_j} + \mathbf{C}_{l,i} + \rho_l \bar{\alpha}_l g_i - \bar{\alpha_l} \frac{\partial \bar{P}_g}{\partial x_i} + \\ + \Theta_l (U_i - U_{l,int,i}) + F_{drag,i} \tag{4.11}$$

The following source terms are here included [164]:

- the first term on the RHS represents the transport of momentum by the velocity fluctuations. The particle stress tensor $\overline{u'_{l,i} u'_{l,i}}$ needs to be modelled (for example through a Boussinesq approximation) or computed with an additional transport equation;

- the second term ($\mathbf{C}_{l,i}$) represents the inter-particle exchange of momentum during collisions and it is negligible in dilute flows with respect to the shear stress contribution;

- the third and the fourth term introduces the influence of the external body force field acting on the particles and the effects of the mean pressure gradient of the continuous phase. It should be pointed out that with respect to the Drew's approach, here the pressure to be introduced in the liquid flux equation is clearly apparent (i.e. the gas phase pressure P_g);

- the source term $\Theta_l (U_i - U_{l,int,i})$ considers the interphase mass transfer due to evaporation;

- the final source term corresponds to the mean inter-phase momentum transfer due to the drag force that can be evaluated through Equation 3.32.

Using a mathematical procedure similar to the one shown in the previous paragraph, it is possible to obtain the following equation for the turbulent liquid flux. This expression is formally equivalent to Equation 4.10, since all the possible physical phenomena that can generate a slip velocity are included.

$$\begin{aligned}
&\frac{\partial \overline{\rho u_i'' y_l''}}{\partial t} + \frac{\partial \tilde{U}_j \overline{\rho u_i'' y_l''}}{\partial x_j} = \\
&\underbrace{\frac{\partial}{\partial x_j}\overline{\rho u_i'' u_j'' y_l''}}_{A} - \underbrace{\overline{\rho u_i'' u_j''}\frac{\partial \tilde{Y}_l}{\partial x_j}}_{B} - \underbrace{\overline{\rho u_i'' y_l''}\frac{\partial \tilde{U}_i}{\partial x_j}}_{C} + \\
&+ \underbrace{\underbrace{F_{drag,i}}_{D_1} + \underbrace{\tilde{Y}_l\frac{\partial \bar{P}}{\partial x_i} - \bar{Y}_l\frac{\partial \bar{P}_g}{\partial x_i}}_{D_2} + \underbrace{C_{l,i}}_{D_3}}_{D} - \underbrace{\tilde{Y}_l\frac{\partial \bar{\tau_{ij}}}{\partial x_j}}_{E} + \\
&- \underbrace{\bar{\rho}\tilde{Y}_l(1-\tilde{Y}_l)(\bar{F}_{g,i} - \bar{F}_{l,i})}_{F} + \underbrace{\Theta_l(\bar{U}_{l,int,i} - \tilde{U}_i)}_{G} - \underbrace{\tilde{Y}_l\overline{\kappa\sigma n_i \delta_s}}_{H}
\end{aligned} \tag{4.12}$$

The reader can recognize the presence of the same source terms of Equation 4.10 from a formal point of view. However, the major differences rely on the expression of the interfacial momentum transfer, which presents here a closed formulation related to the drag force. In a similar fashion, the pressure contribution is here just linked to the action of the continuous phase.

Turbulent liquid flux closure for a Quasi-Multiphase Eulerian approach Beau et al. [158, 165], in the context of Eulerian multiphase flow simulations, introduces the idea of a *Quasi-Multiphase* approach where the equation of the mixture velocity ($\tilde{U}$) is coupled with the one for the turbulent liquid flux to recover a flow field description coherent with a classical multiphase method.
Starting from the modelling strategies presented so far, Beau [158] derived an additional equation for the turbulent liquid flux based on the following assumptions:

- Absence of evaporation and collision effects on the turbulent liquid flux;
- The effects of external body forces are neglected;
- Modelling of turbulent diffusion effects for $R_{Y_{l,i}}$ through a gradient based closure;

- The effects of surface tension and viscous stresses are considered as negligible considering the application at high Reynolds and Weber numbers;

- The influence of the pressure on the turbulent liquid flux is ignored.

Hence, the following simplified closure is derived:

$$\frac{\partial \overline{\rho u_i'' y_l''}}{\partial t} + \frac{\partial \tilde{U}_j \overline{\rho u_i'' y_l''}}{\partial x_j} = \underbrace{\frac{\partial}{\partial x_j}\left(\bar{\rho}\nu_t \frac{\partial}{\partial x_j}\frac{\overline{\rho u_i'' y_l''}}{\bar{\rho}}\right)}_{A} - \underbrace{\overline{\rho u_i'' u_j''}\frac{\partial \tilde{Y}_l}{\partial x_j}}_{B} - \underbrace{\overline{\rho u_i'' y_l''}\frac{\partial \tilde{U}_i}{\partial x_j}}_{C} + \underbrace{-\frac{1}{(1-\tilde{Y}_l)\tau_p}\left(\overline{\rho u_i'' y_l''} + \bar{\rho} D_{gl,t}\frac{\partial \tilde{Y}_l}{\partial x_i}\right)}_{D=D_1} \tag{4.13}$$

where $D_{gl,t}$ is a liquid/gas turbulent dispersion coefficient and τ_p, which is the dynamic relaxation time, can be evaluated through a formulation valid for a lagrangian approach (see Equation 3.36) where the relative velocity is defined as shown below:

$$U_{r,i} = \frac{1}{\bar{\rho}\tilde{Y}_l(1-\tilde{Y}_l)}\left(\overline{\rho u_i'' y_l''} + \bar{\rho} D_{gl,t}\frac{\partial \tilde{Y}_l}{\partial x_i}\right) \tag{4.14}$$

In the following table, all the introduced closures are briefly compared and the following observations are introduced:

- The closure derived from Bailly [157] is obtained for a mono-phase mixture, exploiting an analogy between the liquid volume fraction and the progress variable in the context of premixed combustion. The obtained equation for the turbulent liquid flux neglects the effects of evaporation, body forces, viscous stresses and surface tension. Above all, it is based on the main assumption that the slip velocity is controlled by the turbulence with a direct dependency on τ_t. This hypothesis is normally not representative in the context of two-phase flows.

- The closure of Drew [163] is derived in a standard multiphase Eulerian framework. The achieved equation for turbulent liquid flux is complete, since all the involved physical phenomena are introduced. However, several issues arise when the interfacial momentum transfer

source term $M_{l,i}$ is considered since it has not a straightforward expression. It can be calculated as a drag term only in presence of an isolated cloud of droplets.

- The closure of Simonin [164] is deduced starting from the momentum equation for the liquid phase in a lagrangian framework. The resulting equation for turbulent liquid flux is complete as in Drew's proposal, but here a direct expression of the drag source term is recovered with a direct dependency on the dynamic relaxation time.

- The equation for turbulent liquid flux of Beau et al. [158] can be considered as a simplified expression of the one by Simonin since, for example, the same formulation of the source term due to drag is employed, but the impact of evaporation, body forces, surface tension, viscous stresses and pressure is not included.

	Baily	Drew	Simonin	Beau	
Turbulent diffusion term	$-\frac{\partial}{\partial x_j}\left(\rho y_l'' u_i'' u_j''\right)$	$-\frac{\partial}{\partial x_j}\left(\rho y_l'' u_i'' u_j''\right)$	$-\frac{\partial}{\partial x_j}\left(\rho y_l'' u_i'' u_j''\right)$	$-\frac{\partial}{\partial x_j}\left(\rho y_l'' u_i'' u_j''\right)$	A
Source term due to the gradient of liquid mass fraction	$-\left(\overline{\rho u_i'' u_j''}\right)\frac{\partial}{\partial x_j}\widetilde{Y}_l + \frac{\partial \overline{p' y_l''}}{\partial x_i}$	$-\left(\overline{\rho u_i'' u_j''}\right)\frac{\partial}{\partial x_j}\widetilde{Y}_l$	$-\left(\overline{\rho u_i'' u_j''}\right)\frac{\partial}{\partial x_j}\widetilde{Y}_l$	$-\left(\overline{\rho u_i'' u_j''}\right)\frac{\partial}{\partial x_j}\widetilde{Y}_l$	B
Source term due to the gradient of velocity	$-\left(\overline{\rho u_j'' y_l''}\right)\frac{\partial}{\partial x_j}\widetilde{U}_i$	$-\left(\overline{\rho u_j'' y_l''}\right)\frac{\partial}{\partial x_j}\widetilde{U}_i$	$-\left(\overline{\rho u_j'' y_l''}\right)\frac{\partial}{\partial x_j}\widetilde{U}_i$	$-\left(\overline{\rho u_j'' y_l''}\right)\frac{\partial}{\partial x_j}\widetilde{U}_i$	C
Source term due to drag	$C_1\overline{\rho u_j'' y_l''}\frac{\partial \widetilde{U}_i}{\partial x_j} + (C_2$	$M_{l,i}$	F_{drag}	$\frac{1}{(1-\widetilde{Y}_l)\tau_p}\left(\overline{\rho u_j'' y_l''} + \bar{\rho} D_{glt}\frac{\partial \widetilde{Y}_l}{\partial x_i}\right)$	D1
Source term due to collisions	$-1)\overline{y_l''}\frac{\partial \overline{P}}{\partial x_j} - C_3\frac{\overline{\rho u_j'' y_l''}}{\tau_t}$	$-\frac{\partial \overline{Y_l P}}{\partial x_i} + \frac{\partial \overline{Y_l \tau_{l,ij}}}{\partial x_j}$	C_l	Neglected	D2
Source term due to pressure		$P_{l,Int}\frac{\partial \overline{Y_l}}{\partial x_i} - \widetilde{Y}_l\frac{\partial \overline{P}}{\partial x_i}$	$\widetilde{Y}_l\frac{\partial \overline{P}}{\partial x_i} - \widetilde{Y}_l\frac{\partial \overline{P_g}}{\partial x_i}$	Neglected	D3
Source term due to viscous stresses	Neglected	$\widetilde{Y}_l\frac{\partial \overline{\tau_{ij}}}{\partial x_j}$	$\widetilde{Y}_l\frac{\partial \overline{\tau_{ij}}}{\partial x_j}$	Neglected	E
Source term due to external body forces	Neglected	$-\bar{\rho}\widetilde{Y}_l(1-\widetilde{Y}_l)(F_{g,i} - F_{l,i})$	$-\bar{\rho}\widetilde{Y}_l(1-\widetilde{Y}_l)(F_{g,i} - F_{l,i})$	Neglected	F
Source terms due to evaporation	Neglected	$-\Gamma_l\left(\overline{U}_{l,int,i} - \widetilde{U}_i\right)$	$-\Gamma_l\left(\overline{U}_{l,int,i} - \widetilde{U}_i\right)$	Neglected	G
Source term due to surface tension	Neglected	$-\overline{\widetilde{Y}\sigma k n_i \delta_s}$	$-\overline{\widetilde{Y}\sigma k n_i \delta_s}$	Neglected	H

Figure 4.1: Comparison of the transport equation for the turbulent liquid flux (adapted from [158]).

4.2.2 Proposal of a new turbulent liquid flux splitting technique

Starting from this review of possible approaches that can be used to close Equation 4.2, a novel procedure to extract the transport equation for turbulent liquid flux has been here derived. For the sake of clarity, in this dissertation, the most significant passages of the proposed methodology are reviewed and the interested reader is addressed to [160] for further details.
To be consistent with the approach presented in Chapter 3, with respect to methods described above, a volume based formulation is implemented again and the whole procedure is presented in RANS context. Hence, considering a variable ϕ, its Reynolds average is denoted as $\bar{\phi}$ while its corresponding fluctuation as ϕ'. An assessment of the resulting solver in LES context is then provided here below.
First of all, an innovative splitting of $R_{\alpha_{l,i}}$ in a slip and drift contribution is introduced [160]. The major advantage of this method, as shown below, is the set-up of a robust and reliable tool from an industrial perspective to deal with turbulent liquid flux able to include the most important phenomena acting on the dispersed phase.
Hence, using Equation 3.59, the turbulent liquid flux is divided in a part due to the mean effective slip velocity (Υ_s) and one due to drift (Φ_D):

$$\begin{aligned} R_{\alpha_l,i} = \overline{u_i'\alpha_l'} &= \overline{u_{ir}'\alpha_l'} - \overline{u_{id}'\alpha_l'} \\ &= \bar{\alpha}_l(1-\bar{\alpha}_l)(\bar{U}_{s,i} - \bar{V}_{D,i}) \\ &= \bar{\Upsilon}_{s,i} + \bar{\Phi}_{D,i} \end{aligned} \tag{4.15}$$

where:

$$\begin{cases} \bar{\Upsilon}_{s,i} = \bar{\alpha}_l(1-\bar{\alpha}_l)(\bar{U}_{l,i} - \bar{U}_{g,i}) \\ \bar{\Phi}_{D,i} = \bar{\alpha}_l(1-\bar{\alpha}_l)\bar{V}_{D,i} \end{cases} \tag{4.16}$$

As already discussed in Section 3.5, the term related to the drift flux can be modelled at first order. Hence, the liquid volume fraction equation takes the following form:

$$\begin{aligned} \frac{\partial\bar{\alpha}_l}{\partial t} + \frac{\partial\bar{U}_i\bar{\alpha}_l}{\partial x_i} &= -\left(\frac{\partial}{\partial x_i}\left(\overline{u_{ir}'\alpha_l'}\right) + \frac{\partial}{\partial x_i}\left(\overline{u_{id}'\alpha_l'}\right)\right) \\ &= -\left(\frac{\partial}{\partial x_i}\left(\bar{\Upsilon}_{s,i} + \bar{\Phi}_{d,i}\right)\right) \\ &= -\left(\frac{\partial}{\partial x_i}\left(\bar{\Upsilon}_{s,i}\right) - \frac{\partial}{\partial x_i}\left(\frac{\nu_t}{Sc_t}\frac{\partial\bar{\alpha}_l}{\partial x_i}\right)\right) \end{aligned} \tag{4.17}$$

Namely, like in single-phase flows, the gradient closure for the drift contribution can be replaced with a transport equation for each component of diffusive fluxes. However, it is expected that the major part of the anisotropy is related to local interactions between liquid and gas (i.e. Υ_s) and that an isotropic diffusion flux can be employed for Φ_d.
A conservation equation for the component Υ_s is therefore required to close the problem.
The unclosed formulation of such equation can be derived formally starting from Equation 4.2 and by applying Equation 4.16. Considering all the possible physical phenomena that can be accounted in Equation 4.2 (see the review performed in Section 4.2.1), such substitution leads to the following theoretical equation [160]:

$$\begin{aligned}\frac{\partial \bar{\rho}\tilde{\Upsilon}_{s,i}}{\partial t} + \frac{\partial \bar{\rho}\bar{U}_j\tilde{\Upsilon}_{s,i}}{\partial x_j} =& \frac{\partial \bar{\rho}\overline{u_i' u_j' \alpha_1'}}{\partial x_j} + S_{gradU,i} + S_{grad\alpha_l,i} + S_{evap} + S_{coll,i} + \\ &+ S_{drag,i} + S_{pressure,i} + S_{body\ forces,i} + \\ &+ S_{surf\ tension,i} + S_{viscous,i}\end{aligned} \tag{4.18}$$

This equation is complete since all the forces that can appear in a two-phase system are accounted. Thus, the effective slip contributions have now to be extracted considering that all the source terms that are associated to a diffusion of liquid flux should be included in the drift component. Hence, $S_{gradU,i}$ and $S_{grad\alpha_l,i}$ are directly included in the drift and introduced in numerical calculations through Equation 4.17 using a first order modelling strategy. The effects on the relative flux of droplets collision (S_{coll}) can be included as well in the diffusion part because elastic collision promote an isotropic velocity redistribution. Furthermore, in order to simplify the mathematical formulation of the equation, the evaporation influence (S_{evap}) is overlooked. The reader interested in the introduction of evaporation in the ELSA framework is addressed to Chapter 5, where an innovative implicit formulation is proposed to this end. Finally, remembering that for the operating conditions of gas turbine applications, Weber and Reynolds numbers are usually high, source terms due to surface tension ($S_{surftension}$) and viscous stresses ($S_{viscous}$) are neglected.
With these hypotheses, a slip momentum equation has been derived, where remaining source terms can be calculated through a phenomenological approach starting from the momentum equation of liquid phase in an Eulerian-Eulerian framework as reported by Rusche [166]. The triple correlation term, which appears in Equation 4.18, has been instead modelled with a gradient closure.

The following expressions can be retrieved [160]:

$$\begin{cases} S_{turb\ diffusion_i} = \left(\dfrac{\mu_t}{Sc_t} \dfrac{\partial \bar{\Upsilon}_{s,i}}{\partial x_j} \right) \\ S_{drag_i} = \bar{\rho} \dfrac{\bar{\Upsilon}_{s,i}}{\bar{\alpha_l}} \dfrac{\partial \bar{\alpha_l}}{\partial t} - \bar{\rho} \bar{\alpha_l} \dfrac{\partial \bar{U_i}}{\partial t} - \bar{\rho} \dfrac{n_d \bar{\Upsilon}_{s,i}}{(1-\bar{\alpha_l})\tau_p} \\ S_{pressure_i} = \bar{\rho} \bar{\alpha_l} (1-\bar{\alpha_l}) \dfrac{1}{\rho_l} \dfrac{\partial \bar{P}}{\partial x_i} \\ S_{body\ forces_i} = {\bar{\alpha_l}}^2 \dfrac{\rho_l}{\bar{\rho}} \left(1 - \bar{\alpha_l} \dfrac{\rho_l}{\bar{\rho}} \right) (\rho_l - \rho_g) g_i \end{cases} \tag{4.19}$$

Leading to the following complete formulation [160]:

$$\begin{aligned} & \frac{\partial \bar{\rho} \bar{\Upsilon}_{s,i}}{\partial t} + \frac{\partial \bar{\rho} \bar{U}_j \bar{\Upsilon}_{s,i}}{\partial x_j} = \frac{\partial}{\partial x_j} \left(\frac{\mu_t}{Sc_t} \frac{\partial \bar{\Upsilon}_{s,i}}{\partial x_j} \right) + \\ & + \bar{\rho} \frac{\bar{\Upsilon}_{s,i}}{\bar{\alpha_l}} \frac{\partial \bar{\alpha_l}}{\partial t} - \bar{\rho} \bar{\alpha_l} \frac{\partial \bar{U_i}}{\partial t} - \bar{\rho} \frac{n_d \bar{\Upsilon}_{s,i}}{(1-\alpha_l)\tau_p} + \\ & + \bar{\rho} \bar{\alpha_l} (1-\bar{\alpha_l}) \frac{1}{\rho_l} \frac{\partial \bar{P}}{\partial x_i} + \\ & + {\bar{\alpha_l}}^2 \frac{\rho_l}{\bar{\rho}} \left(1 - \bar{\alpha_l} \frac{\rho_l}{\bar{\rho}} \right) (\rho_l - \rho_g) g_i \end{aligned} \tag{4.20}$$

The complement of such equation to recover the complete turbulent liquid flux can be theoretically exploited for the definition of a transport equation also for the drift part.
In the resulting *Quasi Multiphase Eulerian* solver [160], Equation 4.20 is coupled both with the one for liquid volume fraction and with the liquid/gas interface density. In fact, as outlined in Section 3.5, the gradient closure is not sufficient even for this second equation if the slip velocity effects are important. Therefore, the turbulent liquid flux is used in order to recover a more physical behaviour.

$$\begin{cases} \dfrac{\partial \bar{\alpha_l}}{\partial t} + \dfrac{\partial \bar{U_i} \bar{\alpha_l}}{\partial x_i} = - \left(\dfrac{\partial}{\partial x_i} \left(\bar{\Upsilon}_{s,i} - \dfrac{\nu_t}{Sc_t} \dfrac{\partial \bar{\alpha_l}}{\partial x_i} \right) \right) \\ \dfrac{\partial \bar{\Sigma}'}{\partial t} + \dfrac{\partial \bar{U_i} \bar{\Sigma}'}{\partial x_i} = - \dfrac{\partial}{\partial x_i} \left(\left(\dfrac{\bar{\Upsilon}_{s,i}}{\bar{\alpha_l}} - \dfrac{\nu_t}{Sc_t} \dfrac{\partial}{\partial x_i} \right) \bar{\Sigma}' \right) + \\ \qquad + \dfrac{\bar{\Sigma}}{\tau_t} \left(1 - \dfrac{\bar{\Sigma}}{\Sigma_{eq}} \right) \end{cases} \tag{4.21}$$

The proposed approach represents an extension of the ELSA model described in Chapter 3. It is also similar to the *Quasi-multiphase* method

Multiphase approach	Quasi multiphase approach
Equation for $U_{l,i}$	Equation for $\bar{U}_i = \bar{\alpha_l}\bar{U}_{l,i} + (\alpha_l)\bar{U}_{g,i}$
Equation for $U_{g,i}$	Equation for $\bar{\Upsilon}_{r,i} = \bar{\alpha_l}(1-\bar{\alpha_l})(\bar{U}_{l,i} - \bar{U}_{g,i})$
Equation for α_l	Equation for α_l
-	Equation for $\bar{\Sigma}$

Table 4.1: Comparison between multiphase and quasi-multiphase approach

introduced by Beau [158, 165], since the turbulent liquid flux may be used to evaluate both the liquid and the gas velocities through Equation 4.16. Nonetheless, the two approaches differ since here a formulation in terms of turbulent volume flux has been adopted. Furthermore, the contribution from slip and drift velocities have been accounted separately through the introduction of an innovative equation for $\Upsilon_{s,i}$ and the exploitation of a gradient closure for the drift component. This is surely the major modelling hypothesis since in this way all the physical phenomena are reduced to diffusion mechanisms except for the ones directly related to the slip.
As shown in Table 4.1, the proposed method is now mathematically equivalent to a classical multiphase Eulerian-Eulerian solver, since a complete kinematic description is achievable using the information obtained from the slip flux equation. However, several further advantages of quasi-multiphase framework can be highlighted:

- **Exploitation of single-phase models**: since in the Quasi Multiphase environment, as in ELSA, the two-phase system is studied as a single phase flow composed of two species, it is possible to take advantage of many models developed for mono-phase mixtures. For example, turbulent combustion models, such as the FGM, which has been widely validated in Chapter 2, can be coupled to such Eulerian solver without modifications. This is not true for methods coming from the multiphase context, where specific models have to be proposed and implemented because each phase is separately treated.

- **General flow field description**: in a multiphase approach, a choice of which phase should be considered as discrete or continuous is required. This selection is clearly not trivial in technical applications, since near the injector the carrier phase would be the liquid, but after the breakup process it is no longer true. On the contrary, the Quasi-Multiphase model, using a velocity of the mixture and the

information available from the liquid/gas interface density equation, avoids this choice and allows to describe all range from continuous phase to dilute spray with the same mathematical approach. Namely, depending on the averaged liquid volume fraction a bubbly or spray flow can be detected and an appropriate modelling closures can be applied.

- **Characterization of the dense region of the spray**: in a Quasi-Multiphase approach a description of a dense spray is achievable simply changing, in the turbulent liquid flux equation, the relative importance of the relaxation time with respect to the turbulent time scale. Conversely, the multiphase approaches, being based on the WBE, can be used only if the liquid phase is diluted. The expression of the inter-phase momentum transfer terms in a dense zone becomes therefore difficult. The use of a mixture approach with high variable density is instead required.

- **General link between homogeneous and separated phase approaches**: the proposed modelling strategy expresses a direct link between the two scenarios that can be encountered when a multiphase flow is investigated: a homogeneous approach, which is valuable everywhere not accounting for slip velocity effects, and a separated phase method, reliable in describing the different behaviour of each phase requiring an appropriate modelling to handle the homogeneous limit case. The direct computation of the slip part of turbulent liquid flux allows to benefit of the global behaviour of the homogeneous approach, together with having the opportunity to include the departure from this state if it is required.

Finally, in Table 4.2 the complete system of equations implemented in the QME solver in OpenFOAM® is briefly shown [160].
In the following sections, a validation of the developed QME solver based on Table 4.2 is reported.
It is worth pointing out that the main aim of this part of the work was not to make a validation of the complete ELSA approach in the context of liquid jets breakup, since this topic has been already analysed by several works in technical literature such as [60, 127, 152, 167, 168] among others. Here, the goal is the assessment of the improvements that can be obtained handling the slip velocity between phases with respect to a first order closure. Therefore, the selection of the validation test case is not straightforward since the impact of the turbulent liquid flux modelling in the dense spray region should be evident. Hence, the case of a single isolated droplet subjected to the drag force has been firstly considered in

Momentum equation:

$$\frac{\partial \bar{\rho}\bar{U}_i}{\partial t} + \frac{\partial \bar{\rho}\bar{U}_j\bar{U}_i}{\partial x_j} = -\frac{\partial \bar{P}}{\partial x_i} + \bar{\rho}g_i + \frac{\partial \tau^t_{ij}}{\partial x_j}$$

Liquid volume fraction equation:

$$\frac{\partial \bar{\alpha_l}}{\partial t} + \frac{\partial \bar{U}_j\bar{\alpha_l}}{\partial x_j} = -\left(\frac{\partial}{\partial x_j}\left(\bar{\Upsilon}_{s,j}\right) - \frac{\partial}{\partial x_j}\left(\frac{\nu_t}{Sc_t}\frac{\partial \bar{\alpha_l}}{\partial x_j}\right)\right)$$

Liquid gas interface density equation:

$$\frac{\partial \bar{\Sigma}'}{\partial t} + \frac{\partial \bar{U}_j\bar{\Sigma}'}{\partial x_j} =$$
$$-\frac{\partial}{\partial x_j}\left(\frac{\bar{\Upsilon}_{s,j}}{\bar{\alpha_l}}\bar{\Sigma}'\right) + \frac{\partial}{\partial x_j}\left(\frac{\nu_t}{Sc_t}\frac{\partial}{\partial x_j}\bar{\Sigma}'\right) + \frac{\bar{\Sigma}}{\tau_t}\left(1 - \frac{\bar{\Sigma}}{\Sigma_{eq}}\right)$$

Turbulent liquid flux equation:

$$\frac{\partial \bar{\rho}\bar{\Upsilon}_{s,i}}{\partial t} + \frac{\partial \bar{\rho}\bar{U}_j\bar{\Upsilon}_{s,i}}{\partial x_j} =$$
$$\frac{\partial}{\partial x_j}\left(\frac{\mu_t}{Sc_t}\frac{\partial \bar{\rho}\bar{\Upsilon}_{s,i}}{\partial x_j}\right) + \bar{\rho}\frac{\bar{\Upsilon}_{s,i}}{\bar{\alpha_l}}\frac{\partial \bar{\alpha_l}}{\partial t} +$$
$$-\bar{\rho}\bar{\alpha_l}\frac{\partial \bar{U}_i}{\partial t} - \bar{\rho}\frac{n_d\bar{\Upsilon}_{s,i}}{(1-\bar{\alpha_l})\tau_p} + \bar{\rho}\bar{\alpha_l}(1-\bar{\alpha_l})\frac{1}{\rho_l}\frac{\partial \bar{P}}{\partial x_i} + \bar{\alpha_l}^2\frac{\rho_l}{\bar{\rho}}\left(1 - \bar{\alpha_l}\frac{\rho_l}{\bar{\rho}}\right)(\rho_l - \rho_g)g_i$$

Table 4.2: Summary of the equations implemented in the QME approach (taken from [160]).

order to show that, in a dilute spray case, the QME solution is consistent with the analytical solution. Then, experimental measurements available on a jet in crossflow configuration have been employed to address the closure of turbulent liquid flux in a more interesting physical situation from an industrial perspective. As shown in the following, this test case is particularly significant for the goal of the present chapter since a strong production of slip velocity has to be expected in the region where the liquid and gas jets collide.

4.3 Validation on a single isolated droplet

To firstly clarify the improvements that can be obtained using the proposed QME solver and to underline once again the limitations of first order closure, a preliminary test case, where a homogeneous cloud of droplet, with an average velocity ΔU, is moving into a quiescent medium (see Figure 4.2) has been considered.
In such condition, the model proposed in Equation 3.57 (i.e. first order

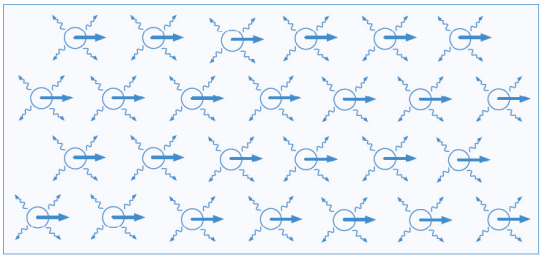

Figure 4.2: Homogenous cloud of droplet moving into a quiescent medium (taken from [158]).

closure) entails a paradox with Equation 4.32 because, since the distribution of droplets is uniform in space, a zero value of turbulent liquid flux is calculated from the gradient closure whereas a non-zero value is predicted from its definition. This is the key point: the turbulent liquid flux contains turbulent diffusion phenomena related to turbulent random fluctuations, but also the mean slip velocity between gas and liquid phases according to its exact definition. After a certain time (i.e. the particle relaxation time), because of the drag force, the slip velocity between the two-phases becomes zero, but during this transition the first order closure is not adequate and cannot be applied. On the other hand, the QME approach should be able to properly describe this situation since the slip velocity is taken into account through Equation 4.20.
Hence, a 1D-test case where a liquid droplet, with an initial velocity, is inserted in a gas flow with a non-zero relative velocity has been realized in OpenFOAM® to be representative for Figure 4.2.
It has been possible to make a comparison between the liquid velocity obtained from the QME and the one that can be analytically calculated from the definition of the dynamic relaxation time (τ_p) (for further details about its mathematical definition and derivation see Section 3.4.3):

$$U_{liquid} = U_{gas}\left(1 - e^{\left(-\frac{t}{\tau_p}\right)}\right) \tag{4.22}$$

Figure 4.3 shows that the agreement between the numerical and the analytical solution is excellent. This leads to the preliminary conclusion that the solver is able to properly reproduce the main interactions of a two-phase flow subjected to a slip velocity, where a first order closure cannot be exploited. This simple test case demonstrates also that is

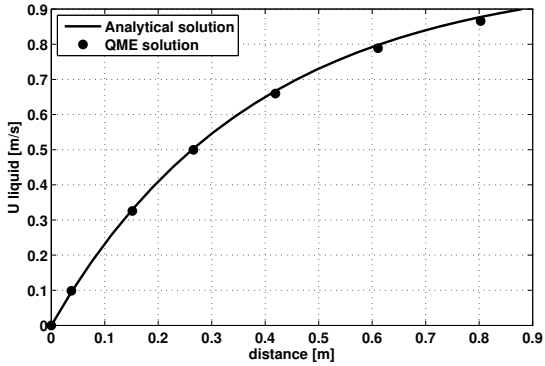

Figure 4.3: Comparison of analytical and QME results for 1D test case.

mandatory, for turbulent liquid flux approaches, to complete any closure by a dedicated two-phase flow model able to introduce the slip velocity between the gas and the liquid.

4.4 Validation on a jet in crossflow configuration

The experimental test article realized by Brown and McDonell [169] on a jet in crossflow configuration has been chosen for the validation of the QME approach because of its geometrical simplicity and the availability of accurate measurements for a wide range of operating conditions. Indeed, such test guarantees high slip velocity in the region of interaction between the jet and the crossflow and a full range of liquid volume fraction making it suitable for a simultaneous validation of different solver aspects. Furthermore, its engineering relevance, due to the high-energy transfer between phases, is proved by many applications in fuel atomization in aero-engine devices (see the TAPS injection system described in the Introduction) as well as lubrication or cooling.
It should be pointed out that this test case has been already analysed in RANS framework by the author using the QME approach in [160] for two different density ratios. Hereinafter, the main achievements obtained in RANS framework will be revised to provide the basic knowledge for LES simulations then reported. The reader interested in a detailed description of all the preliminary sensitivity realized on this test case is addressed to reference [160].

Figure 4.4 shows a schematic representation of the experimental set up. The injector consists of a long pipe of 7.49 mm diameter, followed by a 118° angled taper section and by a short pipe of diameter d_{jet} with $L/d_{jet} = 4$, whose exit is mounted flush with the lower channel wall. Jet characteristics were measured for several values of d_{jet} and here the experimental results with d_{jet} =1.30 mm are used. The experimental

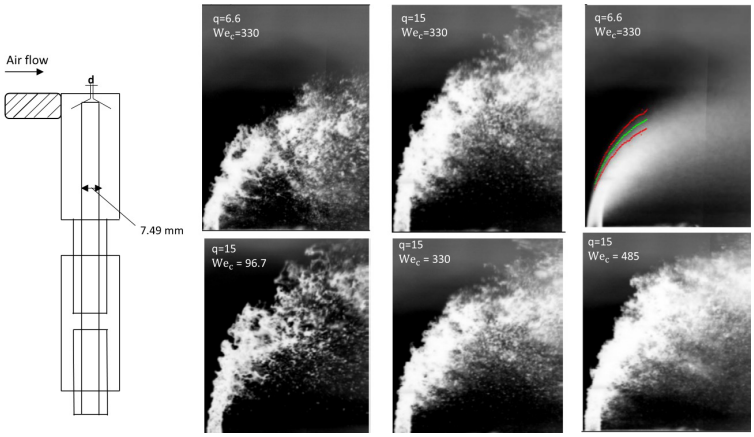

Figure 4.4: Main characteristics of the considered jet in crossflow test case (modified from [169]).

tests have been realized using a jet of water into a crossflow of air and the jet penetration has been evaluated for several values of the momentum flux ratio (q) and of the crossflow Weber number (We_c). The following definitions have been used:

$$\begin{cases} q = \dfrac{\rho_j {U_j}^2}{\rho_c {U_c}^2} \\ We_c = \dfrac{\rho_c {U_c}^2 d_{jet}}{\sigma} \end{cases} \tag{4.23}$$

Using a high-speed camera, the jet penetration has been determined measuring, for each column of pixels in the crossflow direction, the rows containing the minimum and maximum volume fraction values. Hence, for a discrete set of constant locations, starting from its corresponding maximum value, the outer edge was determined when the pixel intensity had dropped to 50 % of the maximum local value. Experimental correlations proposed by Wu et al. [170] and Stenzler et al. [171] proved to

	q	Crossflow Reynolds number	Jet Reynolds Number
Test point 1	6.6	5.7×10^5	1.4×10^4
Test point 1	15	5.7×10^5	2.1×10^4

Table 4.3: Operating conditions of the chosen test points.

determine a valuable prediction of the jet penetration:

$$\begin{cases} \dfrac{y}{d_{jet}} = 1.37\left(q\dfrac{x}{d_{jet}}\right)^{0.5} & \text{(4.24a)} \\ \dfrac{y}{d_{jet}} = 2.63\left(\dfrac{x}{d_{jet}}\right)^{0.39}\dfrac{q^{0.442}}{{We_c}^{0.088}}\left(\dfrac{\mu_l}{\mu_{H_2O}}\right)^{-0.027} & \text{(4.24b)} \end{cases}$$

As reported in [128, 169], the Equation 4.24b, including the crossflow Weber number, is more suitable for the outer edge prediction and it will be used as reference in this work.
It should be also considered that both these relations can be used up to a maximum dimensionless axial distance from the injector exit (using d_{jet} as reference length) of X=10 since the experimental measurements have been realized only in the region just downstream the injection point [54, 169]. In Figure 4.4, the experimental mean penetration is shown in green for the case with q=6.6, whereas red lines point out the measured jet oscillation. No experimental data are instead available for the subsequent spray generation.
In the present study, two test points characterized by the operating conditions reported in Table 4.3 have been considered.

Numerical set-up

Simulations have been carried out on the computational domain reported in Figure 4.9. The domain dimensions (-25d_{jet}...50d_{jet} × -23d_{jet}...25d_{jet} × -10d_{jet}...10d_{jet}), coherently with the ones employed by Herrmann et al. [54], are smaller than the channel used in the experiments (-77d_{jet}...127d_{jet} × 0d_{jet}...54d_{jet} × -27d_{jet}...27d_{jet}), but as highlighted in [54, 128], the reduced dimensions can be safely considered not affecting the obtained results. The liquid pipe is included in the computational domain in order to correctly predict the exit flow field required for a proper modelling of the interaction between the jet and the crossflow. It is worth pointing out that these effects can be predicted only employing a numerical tool able to deal with the different steps of the atomization process, like ELSA. A Lagrangian or multiphase approach would not be consistent in this near injection region.

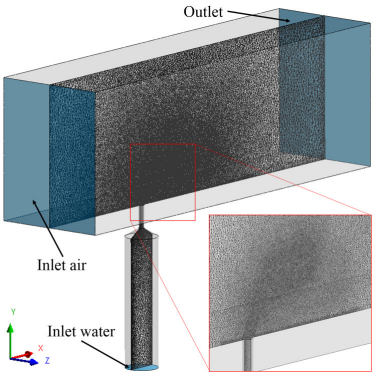

Figure 4.5: Sketch of the computational domain.

In [160], a sensitivity analysis in RANS framework on mesh sizing and wall boundary layer resolution was performed. Four meshes, with different levels of refinement in the region where the two jets collide were considered in order to assess the dependency of results on the chosen computational domain. Furthermore, considering that, based on Equation 3.57, the liquid volume fraction field with a first order closure is completely determined by the turbulent viscosity, a sensitivity analysis was realized both on turbulence model and wall treatment. Reynolds stress model (RSM) proposed by Launder et al. [172] and Launder low Reynolds (LRM) wall treatment [173] have been considered in this context. Such models have been chosen to explore possible effects of free-stream and near wall turbulence anisotropy respectively. It is known in fact that, in RANS context, simulations of a jet in crossflow may be strongly affected by the choice of the turbulence model, especially in the near wall region, also for single phase flows [174].
Finally, it has been found that in the case of two-phase flow neither the near-wall treatment nor the turbulence model have a significant impact on the liquid evolution. The controlling parameter is instead the modelling of turbulent liquid flux.
For instance, considering four axial planes normal to the crossflow direction at increasing distance from the injection location, it has been possible to appreciate the evolution of the slip velocity reported in Figure 4.6: it takes its peak value in the first transversal section, where the two jets collide, and immediately it tends to promote the growth of surface instabilities that leads to a quick atomization in the proximity of the jet

exit. The core of the spray, characterized by high values of Σ and low

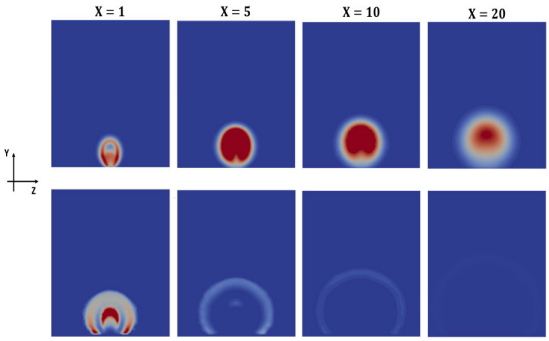

Figure 4.6: Liquid/gas interface density (top) and slip velocity (bottom) distributions at different axial distances with QME [160].

SMD, due to the drag force, follows the gas phase and spreads out in the transverse direction, while the outer part maintain a non-zero slip velocity. Going downstream, such velocity between the two-phases disappears and, at $X = 20$, the liquid/gas interface distribution determined with second order closure is similar to the one given by a first order closure. This behaviour was in agreement with experimental findings reported in [175, 176]. In a similar fashion, it was also representative for results obtained in previous numerical works on the same test case as stated by the qualitative comparison, reported in Figure 4.7, between the liquid penetration achieved with the QME solver and the liquid volume fraction field (expressed in terms of probability isolines) obtained for a density ratio (R) R=100 by Herrmann [128]. Even if the chosen density ratio is different, the relative enhancement with respect to Figure 4.7a is evident and it is due to the lift up by the turbulent liquid flux.
The predicted relative velocity sensibly modifies the liquid distribution into the domain as can be appreciated in Figure 4.8, where the jet penetration obtained in RANS is reported against first order results and the experimental correlation. According to [169], the trajectory was evaluated as the outer side of the jet and plotted as a function of direction x (distance from the centre of the hole in the downstream direction). As noticed also by Herrmann [128], the definition of the penetration in a jet in crossflow configuration is not straightforward. In [160], a detailed discussion about the numerical prediction of the outer edge penetration for the test case under investigation is reported. Finally, the compari-

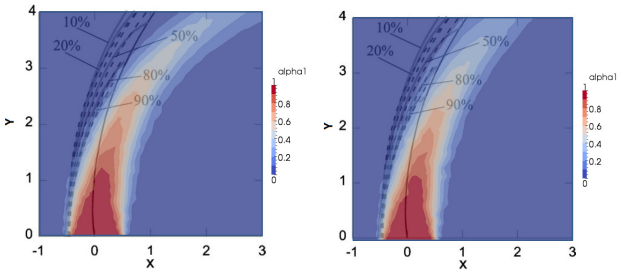

Figure 4.7: Comparison of the probability isolines in [128] for R=100 with the liquid volume fraction field obtained with first order (a) and second order (b) closure with R=1000 [160].

son with the experimental correlations has been here realized using the method suggested by Brown and McDonell [169]. Thus, the windward edge trajectory was calculated as the locus of points where, for each line in Y direction, the liquid volume fraction decreases below a specified δ% of the local maximum. A sensitivity to the chosen δ was performed on the results obtained with the first order closure for the turbulent liquid flux [160]. Results obtained for 5 different values of δ ranging from 5% to 90% reveal a moderate influence to such parameter with total spread limited to 1 d_{jet} in the investigated range. Hence, for the proposed test case it has been chosen to define the windward jet edge following the $\delta = 5\%$ curve [160]. Jet penetration was much better predicted using the QME with respect to the gradient based model. A vector plot of the slip velocity on the iso-volume within $\alpha_l = 0.05$ is also shown in the same figure to further point out the effects of the second order closure. In [160] the diameter distribution generated after the primary breakup including the slip velocity was also analysed and a reliable evolution was pointed out. Finally, an assessment on the liquid mass imbalance ($m.i. = \frac{\dot{m}_{l,out} - \dot{m}_{l,in}}{\dot{m}_{l,in}}$) was as well performed in RANS context on the developed solver and values lower than 1% have been always determined [160]. The reader interested in further results and sensitivities realized in RANS context is again addressed to [160].
Starting from these data, the model has been here applied in a scale-resolving framework. Here, the main results are summarized and the interested reader is addressed to Puggelli et al. [177] for further details. A

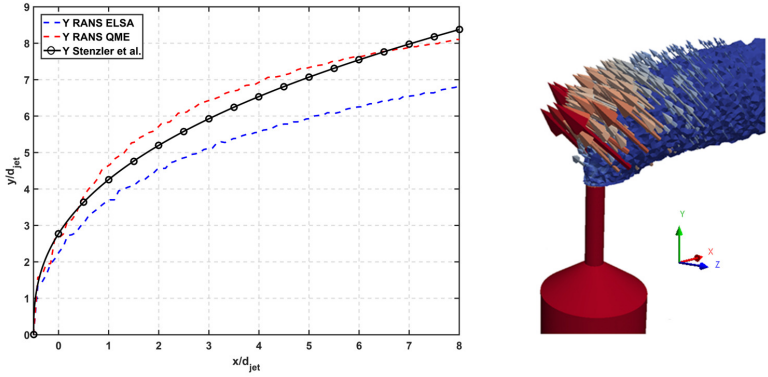

Figure 4.8: Penetration obtained with QME in RANS context compared with first order closure results (left) and vectorial representation of the slip velocity on liquid volume fraction iso-volume (right) [160].

sensitivity analysis was carried out in LES to define the most appropriate mesh sizing. With regard to the turbulence modelling, the sub-grid stress tensor has been modelled through a standard Smagorinsky closure.
Three different grids were generated consisting of tetrahedrons with prisms layers close to the wall. The mesh sizing (in the mixing region) of the grids are different, as highlighted in Table 4.4. Mass flow rates are imposed at the inlets of both air and water following data reported in Table 4.3, whereas a static pressure is prescribed at the outlet. All the walls are treated as smooth, non-slip and adiabatic, whereas the upper and the lateral surfaces are considered slip walls as done also by Herrmann et al. [54, 128]. It should be pointed out that top-hat velocity profiles for both liquid and gas phases have been used at inlets. This is not normally a reliable choice in LES. However, a preliminary sensitivity analysis has been realized using different methods for turbulence generation (e.g. the spectral synthetizer method proposed by Kornev et al. [178]) and it has been found that the liquid penetration was not affected by the chosen boundary condition.
The time step ($d\tau$) used for the simulations has been chosen in order to ensure a control of the Courant number inside the computational domain. Therefore, calculations were performed with 1×10^{-7} s for the coarser mesh, while $d\tau$ has been reduced to 8×10^{-8} s for M2 and M3. However, in simulations employing the QME approach, because of the high coupling between the equations for liquid volume fraction, turbulent liquid flux

Mesh	Hole region [mm]	Mixing region [mm]	Elements
M1	0.15	0.30	2.84×10^6
M2	0.15	0.15	9.50×10^6
M3	0.075	0.15	15×10^6

Table 4.4: Details of the computational grids.

and liquid/gas interface density, the time step for the coarser mesh has been slightly reduced to 8×10^{-8} s to avoid numerical instabilities.
Given that the hereby studied geometry is 0.65m long and that the average speed between liquid and gas is 50 m/s, a flow-through time of 0.0013 s crossing time can be calculated. Hence, after an initialisation period of 2 flow-through times required to flush out the initial conditions and to allow the underlying flow field to develop, the statistics were collected over 4.0 flow-through times. Both convective and diffusive fluxes have been discretized following second order schemes.
All the solvers employed follow a classical segregated method called PIMPLE, which is based on a PISO loop within a SIMPLE loop to solve the pressure-velocity coupling. Thanks to the small time step employed, 1 internal corrector step has been used in the ELSA computations in order to achieve the coupling between continuity and momentum together with 1 external loop. Instead, calculations based on QME have been realized with 4 internal corrector steps and 4 external loops.

Results and discussion

Considering the operating conditions detailed in Table 4.3, test point 1 has been first of all investigated for the numerical assessment of QME. The Eulerian-Eulerian solver derived from ELSA model, characterized by a first order closure, was used to determine the most appropriate mesh sizing for the following simulations. The instantaneous velocity fields obtained with grids M1 and M2 are reported in Figure 4.9 together with the obtained liquid penetration. The mesh M3 showed approximately a similar velocity and liquid volume fraction evolution and it is not reported here for the sake of clarity.
As expected, the spatial discretization seems beneficial in reducing the scale of the resolved turbulent vortices in the mixing region. However, the structure of the jet immediately downstream of the hole appears rather uninfluenced, at least from a qualitative point of view. In order to obtain a quantitative validation, the results were evaluated again in terms of time-averaged jet penetration (see Figure 4.9). The same criterion

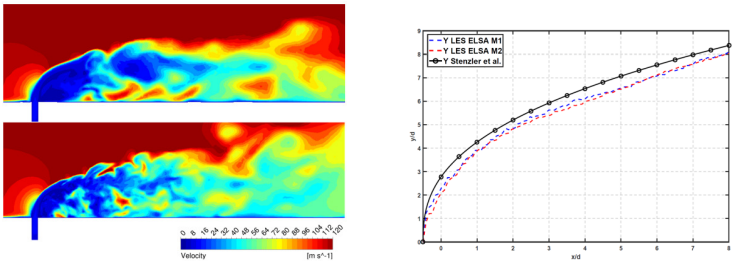

Figure 4.9: Velocity field obtained in LES framework with two different grid sizings (left) and liquid penetration using a first order closure (right).

discussed for RANS has been employed to determine the outer side of the jet.

From this comparison it is possible to draw some interesting considerations: it appears that the resulting jet outer edge is insensitive to the increasing mesh refinement, at least in time-averaged terms. This was further confirmed by the results obtained on mesh M3, where a slight improvement in the prediction of jet penetration was again obtained (i.e. lower than $0.5d_{jet}$ in all the investigated domain). In the light of these results, only the coarse mesh (M1) will be shown hereafter, since the difference in jet penetration does not justify the significant increase in computational cost ascribed to the combination of greater number of elements and smaller time step required.

In addition, it is also worth pointing out the slight underestimation of results obtained with the ELSA approach compared to the correlation by Stenzler et al. [171].

To better appreciate the capability of CFD to reproduce the jet behaviour, simulations were post-processed to allow a comparison against the experimental acquisitions obtained through high speed shadowgraphy. However, due to the strong presence of light scattering, reproducing the actual physical process involved in the image acquisition is not straightforward. To model the shadowgraphy technique, the turbidimetry theory has been used to quantify the loss of light intensity (I) due to the scattering effects ascribed to suspended particles. Hence, considering the spray as locally mono-disperse and applying the Beer-Lambert law, it is possible to express the variation of I along a given path of length L (the lateral direction y in this particular case) as the line integral of the product between the particle volume concentration (N_d), the squared Sauter Mean Diameter and an extinction coefficient (Q_{ext}), which in the present study has been

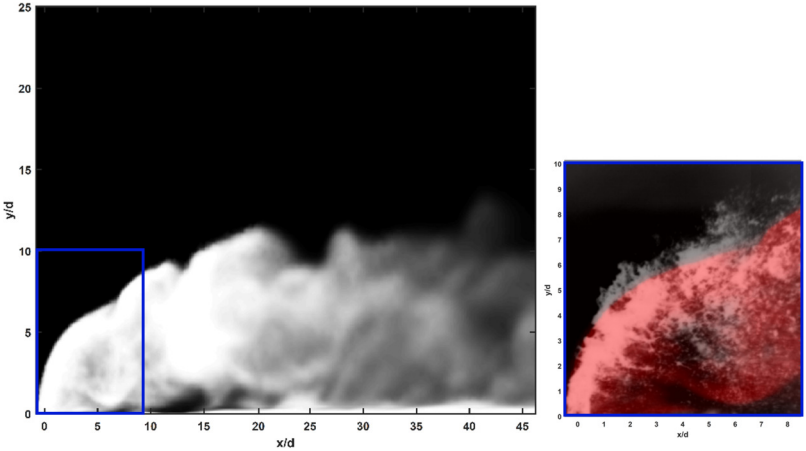

Figure 4.10: Liquid distribution obtained from ELSA calculations compared with experiments.

evaluated equal to 2 (see [179, 180] for further details). It is possible to prove that such expression can be reformulated as a function of the liquid/gas interface density Σ, as highlighted in Equation 4.25. It is worth underlining that the present approach is based on spray characteristics and therefore can be considered valid only when the spray is diluted (i.e. not for a coherent liquid jet). Therefore, the dense spray region in the present work has been identified considering values of liquid volume fraction higher than 10% (i.e. where a dilute assumption is no more verified) and assigning a constant value to the integral kernel.

$$\left(\frac{I}{I_0}\right) = -exp\left(\int_0^L Q_{ext} N_d \frac{\pi {D_{32}}^2}{4} dl\right) = -exp\left(\int_0^L \frac{\Sigma}{2} dl\right) \qquad (4.25)$$

The application of this procedure allows to obtain the liquid distribution depicted in Figure 4.10 for mesh M1. The liquid column, which can be clearly identified in the near injector region, due to instabilities generated by the interactions with the gas phase, tends to be firstly atomized in bigger liquid structures until a broad range of drop sizes (i.e. Σ) is generated. In the same figure, a comparison also with the shadowgraphy picture in the same experimental window is also reported (for the sake of clarity, the result of the ELSA simulation has been coloured in red). This representation reveals again that the penetration is not properly predicted,

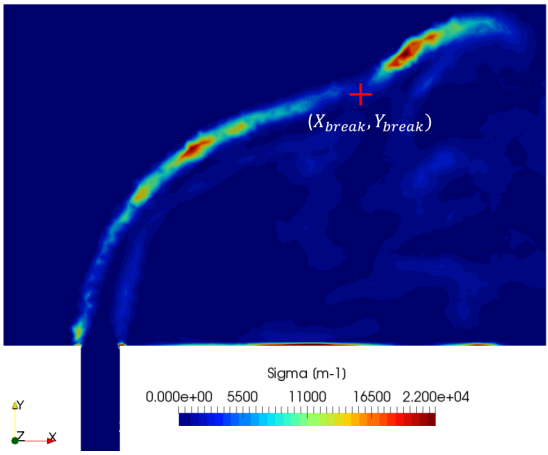

Figure 4.11: Distribution of the liquid/gas interface (Σ) obtained from ELSA computations.

mainly after x/d > 1.0. Such issue is probably due to the hypothesis of zero slip velocity between phases. In fact, once the liquid rupture begins, generated droplets and liquid structures, due to their high inertia, tend to follow different trajectories before relaxing to the dynamics of the carrier phase. This fact leads locally to important differences between liquid and gas velocities. Furthermore, the simulation is not correctly catching the liquid wrinkling due to the gas phase interactions.
Nevertheless, a further confirmation of the reliability of the LES-ELSA approach can be obtained evaluating the breakup location of the liquid column. To this end, Figure 4.11 reports the instantaneous evolution of Σ zoomed in the near injector region. The production of the liquid-gas interface, which is related to the generation of some instabilities on the liquid column surface due to the interactions with the gas crossflow, is determined on the top and bottom side of the water jet. Clearly, such generation is much higher on the top jet surface since the gas phase has a stronger impact on the liquid evolution. Going downstream, the point where these two sides of Σ connect together has been defined in the present work as the location of the liquid column breakup.
It should be pointed out that, immediately after such point, a strong production of Σ is predicted and this is related to the generation of small liquid structures, like in an intense breakup process. The location of the

liquid column breakup has been compared with the following experimental correlation proposed by Wang et al. [181], where the breakup dynamics of a plain liquid jet in air crossflow is studied.

$$\begin{cases} \dfrac{X_{breakup}}{d} = 6.9 \\ \dfrac{Y_{breakup}}{d} = 2.5q^{0.53} \end{cases} \tag{4.26}$$

The correlation, valid for a wide range of operating conditions and momentum flux ratios, gives the position of the column disintegration point as a function of the momentum flux ratio and of the jet diameter and it is shown in Figure 4.11 with the red cross. It is possible to notice that ELSA is physically reproducing the breakup length.
Considering the under-estimation of liquid jet penetration obtained with the ELSA approach and the importance that the slip velocity can have in this test article, the attention is now diverted to the QME formulation. Here, to have a deeper insight in the capabilities of different multiphase numerical methods, results obtained with a standard LES-VOF approach (i.e. *interFoam*) has been introduced as further reference.
Firstly, the resulting mean jet trajectory is plotted in Figure 4.12, where it is possible to appreciate the good agreement shown by VOF in reproducing the experimental correlation. The enhancements with respect to ELSA can be determined immediately after x/d $>$ 0, where the exploitation of an interface capturing method leads to a physical prediction of the jet penetration.
Even more important, it is evident how the introduction of a more reliable description of the slip velocity contribution (i.e. QME plot results), between the two-phases, allows to increase the jet penetration coherently with VOF. In fact, in the top part of Figure 4.12b, the iso-surface of 5% of liquid volume fraction superimposed on the slip velocity field shows that the difference of velocity between phases tends to lift up the jet. Such effect is mainly generated in the region where the two jets collide, due to the inertia of the liquid phase. The vectorial representation of the liquid and gas phase velocities on the iso-surface corresponding to the maximum value of slip velocity (i.e. in the region where the two jets collide), reported on the bottom of the same figure, proves again that such U_{slip} cannot be neglected: it is evident that liquid and gas continue to follow different trajectories while interacting between each other. Thus, the impact of a second order closure on the liquid distribution at the chosen operating conditions is significant and positively affects the agreement with experimental evidences. Then, moving downstream, the slip velocity

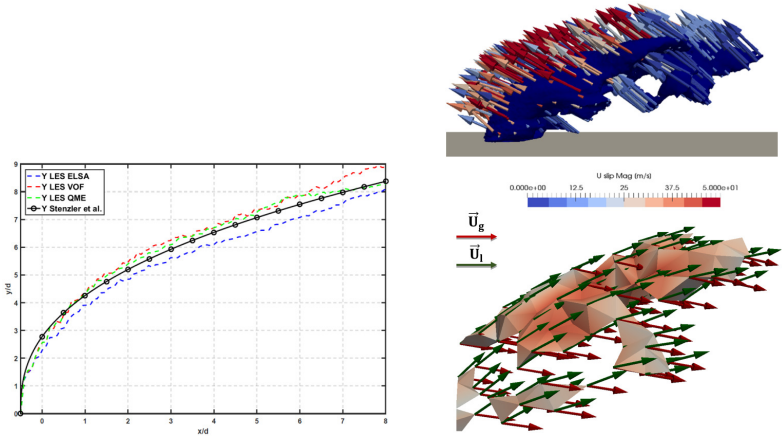

(a) (b)

Figure 4.12: Mean jet penetration obtained using different modelling strategies for liquid phase modelling (Figure 4.12a) and slip velocity effects on liquid distribution together with a vectorial comparison between liquid and gas velocities (Figure 4.12b).

is gradually reduced by the drag contribution until it becomes zero based on the local distribution of the SMD and relaxation times.
In order to complete the assessment of QME capabilities, in Figure 4.13, the results obtained from the turbidimetry analysis based on Equation 4.25 are shown for QME and VOF. Obviously, the proposed post processing tool is relevant only for QME, for which the information about the liquid/gas interface density is available. Whereas for VOF, an iso-surface of 5% of liquid volume fraction has been chosen for a qualitative comparison. It is clear that, using an interface-capturing method, the penetration and the jet behaviour immediately after the jet entrance seem physically predicted. However, due to a computational domain not refined enough to correctly reconstruct the interface (especially when breakup phenomena appear), the subsequent column breakup is roughly represented and the liquid volume fraction field undergoes an excessive numerical diffusion. Therefore, in VOF framework, the best prediction with respect to ELSA is due to a non-realistic representation of the atomisation process because all the scales of the interface are not well resolved. To overcome this problem, a highly refined mesh would be required, as already done by

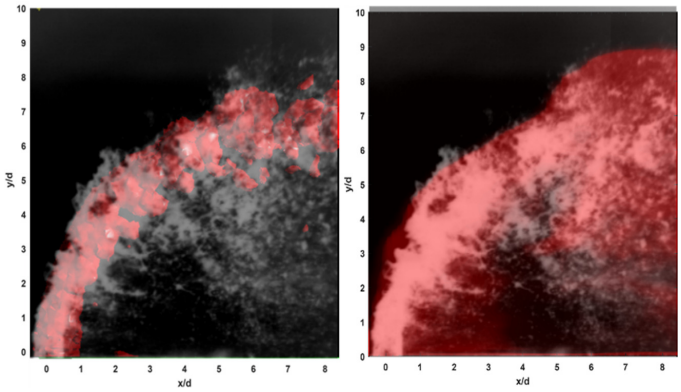

Figure 4.13: Liquid distribution obtained from VOF (left) and QME (right) calculations compared with experiments.

Herrmann [128]. However, this would clearly lead to a strong increase of the computational cost.
Instead, the QME approach can be seen as a good compromise between CPU effort and simulation accuracy: a consistent jet behaviour, in the near injection region, with regards to VOF has been obtained, but with the further opportunity of evaluating the subsequent jet breakup with a reduced computational cost.
In addition to the mean penetration, the jet oscillation has been analysed using the experimental time averaged image shown in Figure 4.4 as reference. In the experimental picture, the green line represents the steady state jet penetration, while red curves are the maximum and minimum instantaneous jet position during the experiments. Considering that no details were provided in [169] regarding the measurement of the standard deviation of the penetration, in the present work the root mean square of the liquid volume fraction field has been chosen to identify the jet unsteadiness. In Figure 4.14 such quantity is shown for each E-E method considered so far and compared with the experimental correlation (i.e. the green curve) for mean penetration of [171].
Consistently with the experimental behaviour, VOF seems to oscillate around the experimental penetration, whereas ELSA predicts a liquid volume fraction fluctuation on a lower position (i.e. coherently with Figure 4.10). Considering the VOF as the reference solution, in ELSA the higher diffusion together with the exploitation of a first order closure for

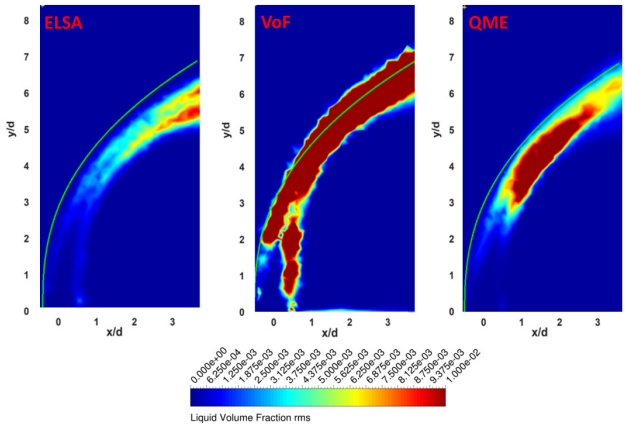

Figure 4.14: Standard deviation of liquid volume fraction obtained with ELSA, VOF and QME approaches.

turbulent liquid flux leads to a non-physical representation of liquid-gas interactions and to a strong underestimation in the liquid volume fraction fluctuations. The QME, including the contribution of slip velocity inside the liquid volume fraction equation, leads to modify the jet behaviour and therefore also the resulting standard deviation. The resolution of the turbulent liquid flux contribution reduces the liquid diffusion and leads to appreciate higher *rms* values immediately after the jet exit. The results are more consistent with VOF even if QME does not still oscillate exactly around the experimental penetration.
Nonetheless, the jet in crossflow test case clearly shows the capabilities of QME and the impact of turbulent liquid flux on liquid distribution. Considering the results obtained in Test point 1, together with the preliminary assessment shown in the previous section, the developed approach seems to be able to reliably take into account a slip velocity between phases and to improve the capabilities of the ELSA approach for an application in the aero-engine framework.
In order to completely verify the QME characteristics, Test point 2, which is characterized by an higher momentum flux ratio, has been considered. Mesh M1 has been used again in numerical calculations since at least the mean liquid penetration does not seem to be significantly affected by the mesh resolution. In Figure 4.15 the resulting mixture velocity on the symmetry plane and the liquid mean penetration obtained with a first

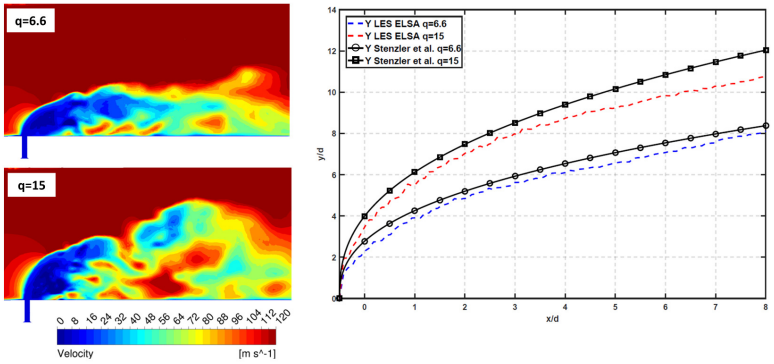

Figure 4.15: Instantaneous mixture velocity on the symmetry plane (left) and mean liquid penetration (right) for two analysed test points.

order closure for $\vec{R}_{\alpha_l}$ are shown for the two analysed test points. The accuracy with standard ELSA model is reduced when moving to higher momentum flux ratio, and it is again due to the exploitation of a first order closure for turbulent liquid flux. An higher impact of slip velocity is expected with q=15 and the error with respect to experiments is indeed increased. It should be pointed out that, mainly in the region where some liquid parcels are detached and should follow a different trajectory with respect to the carrier phase, the liquid is immediately bended in the gas direction. This is not completely consistent with the experimental data, where it seems that the liquid phase tends to show nearly a ballistic evolution.

Figure 4.16 shows a comparison of the generated instantaneous slip velocity in the two cases obtained through the QME solver. The window selected for this comparison is a zoom in the near injection region.

It should be pointed out that the field of U_{slip} is completely different in the two analysed test points. At low momentum flux ratio, the generation of the slip turbulent flux is quite reduced at the beginning. This is probably related to the fact that the inertia of the liquid column is not so high to be preserved in the jet collision and the liquid tends to be immediately bended in the crossflow direction. The production of a slip flux corresponds instead to the region where Σ is produced in consequence of the liquid breakup (see Figure 4.11). A cloud of ligament is locally generated and tends to preserve its own momentum leading to the generation of a turbulent liquid flux. It is worth pointing that in the

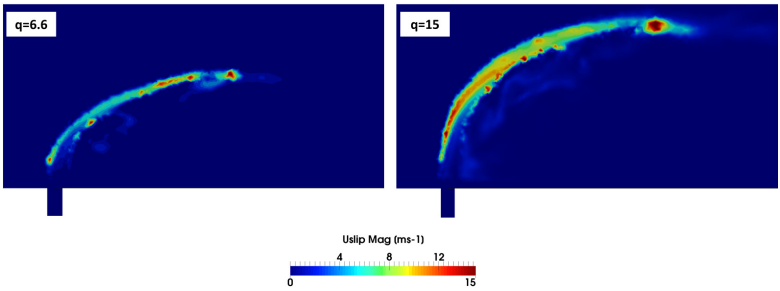

Figure 4.16: Comparison of the slip velocities instantaneously generated at two different momentum flux ratios. Zoom on the near injection region.

context of first order closures, such liquid structures are considered at the gas velocity and their trajectory and evolution would be completely misled. This effect can be really significant in the ELSA context also for the lagrangian injection step, since a non physical liquid injection velocity can be ascribed employing a standard gradient closure.
At higher momentum flux ratio, the importance of this effect is even more significant. In fact, when the liquid spreads out inside the computational domain, thanks to its higher inertia with respect to the previous case, a slip velocity is immediately generated at the injector tip. Then, due to the drag force, the liquid tends to be progressively accelerated and the slip consequently reduced. This process goes on until the breakup gets in, generating liquid parcels that are again characterized by their own dynamic evolution. In the reported snapshot, it is clear how the created parcels do not follow the gas-phase in terms of velocity magnitude and direction.
Considering these effects, the resulting liquid penetration is shown in Figure 4.17, where the result of ELSA with first order closure is shown as further comparison. It should be pointed out that again a significant enhancement has been obtained with respect to the reference correlation through the proposed closure for turbulent liquid flux. In particular, the agreement is enhanced mainly at the end of the near injection region, where now the penetration of the liquid detached structures is well represented.
Ultimately, this test point leads to an assessment of the QME formulation for this kind of configuration. The approach seems to be able to correctly handle the difference of velocity between phases, which can be significant in aero-engine burners. The proposed splitting of fluxes between drift and

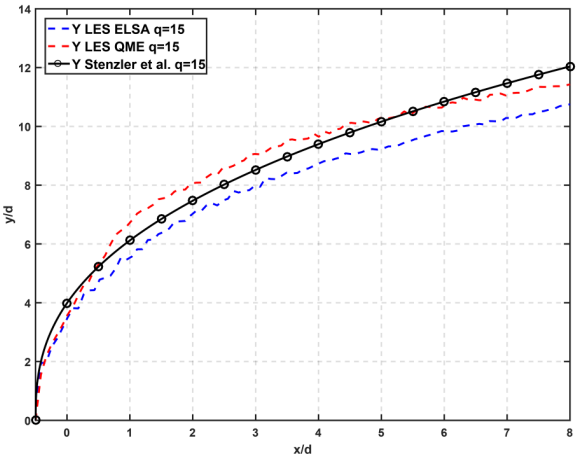

Figure 4.17: Liquid penetration obtained at q=15 using a first and second order closure for turbulent liquid flux.

slip lead to a robust and promising methodology to deal with turbulent liquid flux within the ELSA framework.
However, as shown in Figure 4.13, the exploitation of an interface capturing approach can be extremely useful in the near injection region to correctly account for the wrinkling of the interface.
Therefore, a novel coupled VOF-QME approach, based on the ELSA solver presented in Chapter 3, is analysed in the following section as a possible compromise between accuracy and computational effort.
Then, considering that Equation 4.20 has been derived by using a phenomenological approach, the last section of this chapter is devoted to a systematic derivation of a transport equation for $\vec{R}_{\alpha_l}$ and $\vec{\Upsilon}_s$. A general and novel modelling framework to deal with the slip velocity is presented and compared with the formulation described in Section 4.2.2. This paves the way for future activities in the context of turbulent liquid flux modelling and some concluding remarks are reported at the end.

4.5 Proposal of a coupled QME-VOF approach based on ELSA

Based on results shown so far, the QME appears as a valuable strategy to account for the slip velocity contribution. However, as soon as the liquid

jet is issued from the nozzle, some local characteristics of the liquid gas interface can be properly described only by using an interface capturing method. Locally, the diffuse interface methods can completely mislead the interaction between the liquid and gas phases. Conversely, a VOF approach may lead to infeasible CPU cost in an industrial context if applied in the whole domain.
Therefore, a novel coupled VOF-QME approach, based on the ELSA solver presented in Chapter 3, is proposed as a solution in this section. It is based on the addition of the equation for turbulent liquid flux to the Eulerian-Eulerian ELSA solver reported in Table 3.1 in order to include a second order closure for $R_{\alpha_{l,i}}$ at sub-grid level. The complete system of equations shown in Table 4.5 is finally proposed.

Continuity equation:

$$\frac{\partial \bar{U}_i}{\partial x_i} = 0$$

Momentum equation:

$$\frac{\partial \bar{\rho}\bar{U}_i}{\partial t} + \frac{\partial \bar{\rho}\bar{U}_i\bar{U}_j}{\partial x_j} = -\frac{\partial \bar{P}}{\partial x_i} + \frac{\partial}{\partial x_j}\left(\bar{\mu}\left(\frac{\partial \bar{U}_i}{\partial x_j} + \frac{\partial \bar{U}_j}{\partial x_i}\right)\right) - \frac{\partial \tau_{\rho u_i u_j}}{\partial x_j}$$

Liquid volume fraction equation:

$$\frac{\partial \bar{\alpha}_l}{\partial t} + \frac{\partial \bar{U}_j\bar{\alpha}_l}{\partial x_j} + \frac{\partial \left(C_\alpha \bar{\alpha}_l\left(1-\bar{\alpha}_l\right)\right)U_j{}^r}{\partial x_j} + \left(1-C_\alpha\right)\left(\frac{\partial}{\partial x_j}\left(\bar{\Upsilon}_{s,j}\right) - \frac{\partial}{\partial x_j}\left(\frac{\nu_t}{Sc_t}\frac{\partial \bar{\alpha}_l}{\partial x_j}\right)\right) = 0$$

Liquid gas interface density equation:

$$\frac{\partial \bar{\Sigma}'}{\partial t} + \frac{\partial \bar{U}_j\bar{\Sigma}'}{\partial x_j} = -\frac{\partial}{\partial x_j}\left(\left(\frac{\bar{\Upsilon}_{s,j}}{\bar{\alpha}_l} - \frac{\nu_t}{Sc_t}\frac{\partial}{\partial x_j}\right)\bar{\Sigma}'\right) + \frac{\bar{\Sigma}}{\tau_t}\left(1-\frac{\bar{\Sigma}}{\bar{\Sigma}_{eq}}\right)$$

Turbulent liquid flux equation:

$$\begin{aligned}\frac{\partial \bar{\rho}\hat{\Upsilon}_{s,i}}{\partial t} + \frac{\partial \bar{\rho}\bar{U}_j\hat{\Upsilon}_{s,i}}{\partial x_j} &= \\ +\frac{\partial}{\partial x_j}\left(\frac{\mu_t}{Sc_t}\frac{\partial \bar{\rho}\bar{\Upsilon}_{s,i}}{\partial x_j}\right) + \bar{\rho}\frac{\bar{\Upsilon}_{s,i}}{\bar{\alpha}_l}\frac{\partial \bar{\alpha}_l}{\partial t} + & \\ -\bar{\rho}\bar{\alpha}_l\frac{\partial \bar{U}_i}{\partial t} - \bar{\rho}\frac{\bar{\Upsilon}_{s,i}}{(1-\bar{\alpha}_l)\tau_p} + \bar{\rho}\bar{\alpha}_l(1-\bar{\alpha}_l)\frac{1}{\rho_l}\frac{\partial \bar{P}}{\partial x_i} + \bar{\alpha_l}^2\frac{\rho_l}{\bar{\rho}}\left(1-\bar{\alpha}_l\frac{\rho_l}{\bar{\rho}}\right)(\rho_l-\rho_g)g_i &\end{aligned}$$

Table 4.5: Summary of the equations implemented in the Eulerian region of the VOF-QME approach based on ELSA.

It is worth pointing out that this coupled method can represent a valuable approach to account for atomization phenomena in lean burn systems in the aero-engine context for several reasons:

- the VOF approach can be extremely important in the near injection region to correctly account for the effects of surface tension and to properly evaluate the generation of surface instabilities on the liquid surface. These contributions are extremely significant especially

at operating points characterized by low values of pressure and temperature in the gas phase (e.g. idle conditions), which are normally associated to small Weber numbers. In such cases a diffusive interface approach would be unreliable since the physics of the two phase flow is completely controlled by the liquid-gas interface.

- the QME approach is instead useful to describe the atomization process further downstream with respect to the injection point and in particular to account in that region for the effects of a slip velocity. It can strongly modify the liquid distribution as shown in the previous section. With respect to the approach presented in Chapter 3, where a first order closure for $R_{\alpha_{l,i}}$ was employed, now the main interactions between liquid and gas phases in terms of drag, pressure gradient as well as body forces are considered. Here, the CPU cost is much lower than a VOF and this should allow to simulate the whole evolution of a spray up to evaporation and combustion. Furthermore, the exploitation of QME can be extremely useful also in switching to the lagrangian region of ELSA. As reported in Section 3.4.2, using a first order closure for turbulent liquid flux, liquid droplets are injected with the mixture velocity neglecting the contribution of ballistic parcels that are characterized by high Stokes numbers and tend to follow their own trajectory. Employing the QME a more physical velocity is assigned to liquid parcels and, as shown in Section 2.5, this effect can have a strong impact on flame stabilization.

This approach can be considered as a general tool capable of modelling the liquid phase from its injection up to the generation of a dispersed spray in LES and in Chapter 5 evaporation is included in this framework. It is worth pointing out that, as detailed in Chapter 3, the switch between these two numerical methods takes place automatically based on the mesh sizing and on the quantity of liquid-gas interface generated [127]. A locally defined switching in space and in time should take place, which is strongly influenced by the threshold value used in Equation 3.24. Further investigations are surely required on this point to determine ϵ_1 and ϵ_2 in a dynamic manner to avoid regions where the VOF method is not strictly preserved. Anyway, in the aero-engine framework, at low power conditions (i.e. low temperature and pressure) the model should stay in VOF with QME to ensure a proper lagrangian injection, conversely it should switch to a complete diffuse interface method at cruise or take-off conditions (i.e. high temperature and pressure).

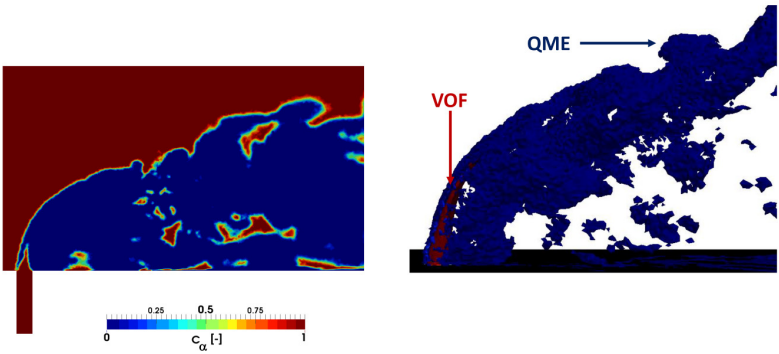

Figure 4.18: Coupling between VOF and QME methods based on ELSA. C_α contour (left-side) and iso-surfaces (right-side) are shown.

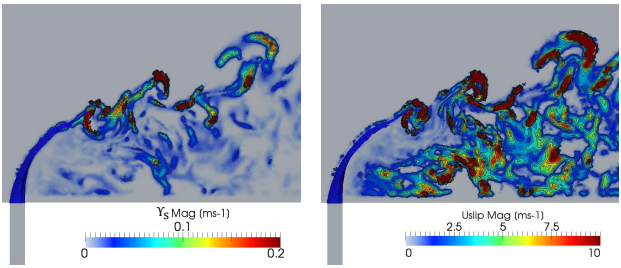

Figure 4.19: Contour plots of Υ_s (left) and slip velocity (right) obtained from the coupled QME-VOF simulation.

To better explain the idea here proposed, such method has been applied in the numerical simulation of the jet in crossflow test case described in the previous sections for Test point 1 using mesh M2 (see Table 4.4) in order to have a consistent number of elements in the hole diameter for the VOF simulation. In Figure 4.18 the coupling between VOF and QME is shown using the contour plot of C_α: in the near injection zone, the model employs an interface capturing approach (i.e. $C_\alpha = 1$), whereas, increasing the mesh sizing while going downstream, the approach automatically switches to QME (i.e. $C_\alpha = 0$). The same idea is shown in the right side of the figure by using the iso-surface of $C_\alpha = 1$ (i.e. the red one) and $C_\alpha = 0$ (i.e. the blue one). As shown in Figure 4.19 and as already described in

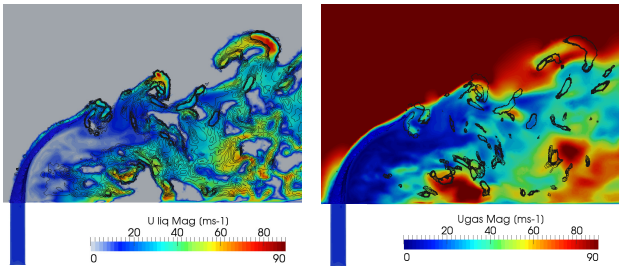

Figure 4.20: Contour plots of liquid (left) and gas (right) velocity obtained from the coupled QME-VOF simulation.

the previous section, the latter one is the zone where a high slip velocity is generated. Starting from the coherent liquid column (here highlighted through an iso-surface of α_l=0.5), some parcels are detached, leading immediately to the generation of a slip velocity. Some structures seem to maintain a ballistic trajectory and to remain of the top edge of the spray, whereas smaller particles are bounded by the gas phase towards the wall with locally high values of U_{slip}.
Such distribution of slip between phases leads clearly to modify locally the liquid and gas velocities, that are shown in Figure 4.20. On the instantaneous plot of U_{gas} the iso-contour lines of slip velocity between 6 m/s and 10 m/s are reported in black to highlight regions of slip production. Clearly, U_{liquid} tends to zero as soon as no liquid is present. Conversely, when coherent ligaments are considered like on the spray edges U_{liquid} is no more zero and its value is led by the opposite contributions of pressure gradient and drag. Locally, values of gas and liquid velocities are not the same leading to a completely different evolution of the breakup process. It is worth pointing out that all these phenomena would be completely overlooked with a first order closure, whereas with a VOF method a significant reduction of mesh sizing would be required to correctly solve all the range of liquid structures.
Finally, the lagrangian injection has been as well activated using the slip contribution to provide a more physical liquid velocity in the switching step. In Figure 4.21, the resulting cloud population is shown and on the left the instantaneous contour plot of slip is super-imposed to underline once again the impact of the employed second order closure.
Clearly, in terms of mean penetration for this configuration the leading contribution is the slip velocity and therefore a completely consistent

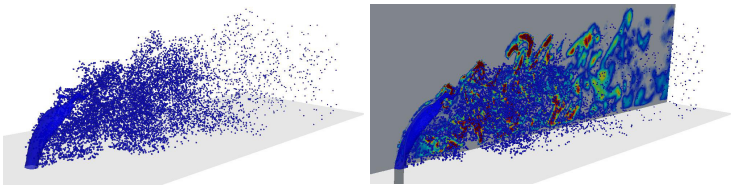

Figure 4.21: Lagrangian population obtained from the jet breakup together with the contour plot of slip velocity.

result with Figure 4.12 is expected. Further investigation are required on different geometrical configurations to completely assess the capabilities of the proposed approach, but it clearly represents a strong basis towards a unified approach for spray flame calculation.

4.6 Proposal of a new turbulent liquid flux modelling framework

Considering the results shown so far and the satisfactory agreement achieved on the jet in crossflow test case, the QME is proposed as a promising approach in dealing with a slip velocity between phases.
However, in Section 4.2.2 a phenomenological approach was used to derive Equation 4.20 [160]. This may restrict the capabilities of the present methodology on a theoretical point of view, mainly if different geometrical configurations have to be studied. The original aim of separating the turbulent liquid flux in a diffusion and a slip part in [160] was to make apparent the mechanisms that produce the slip motion and to be sure to recover a diffusion behaviour of $\vec{R}_{\alpha_l}$ when the relaxation time tends to zero. Thus, the procedure in Section 4.2.2 started from a two-phase description and then a splitting of fluxes was arbitrarily introduced.
In this section, it has been decided to carry out a systematic derivation of the equations for $\vec{R}_{\alpha_l}$ and $\vec{\Upsilon}_s$. At the end, the link with Equation 4.20 is as well described.
A different method to extract an exact transport equation for turbulent liquid flux is here employed.
The conservation equations of momentum for the liquid and gas phases, as proposed by Simonin [164], represent the starting point of the present procedure (see Equations 4.27). For such mathematical derivation, the absence of phase change phenomena is assumed. The reader interested in the introduction of evaporation in the ELSA framework is addressed to

Chapter 5, where an innovative implicit formulation is proposed to this end.

$$\begin{cases} \dfrac{\partial \rho_l \bar{\alpha}_l \bar{U}_{l,i}}{\partial t} + \dfrac{\partial \rho_l \bar{\alpha}_l \bar{U}_{l,i} \bar{U}_{l,j}}{\partial x_j} & = -\dfrac{\partial \rho_l \bar{\alpha}_l \overline{u'_{l,i} u'_{l,j}}}{\partial x_j} + \mathbf{C}_{l,i} + \rho_l \bar{\alpha}_l \bar{f}_{l,i} + \\ & \quad -\bar{\alpha}_l \dfrac{\partial \bar{P}_g}{\partial x_i} + \dfrac{\partial \bar{\alpha}_l \bar{\tau}_{l,ij}}{\partial x_j} + F_{drag,i} \\ \dfrac{\partial \rho_g \bar{\alpha}_g \bar{U}_{g,i}}{\partial t} + \dfrac{\partial \rho_g \bar{\alpha}_g \bar{U}_{g,i} \bar{U}_{g,j}}{\partial x_j} & = -\dfrac{\partial \rho_g \bar{\alpha}_g \overline{u'_{g,i} u'_{g,j}}}{\partial x_j} + \rho_g \bar{\alpha}_g \bar{f}_{g,i} + \\ & \quad -\bar{\alpha}_g \dfrac{\partial \bar{P}_g}{\partial x_i} + \dfrac{\partial \bar{\alpha}_g \bar{\tau}_{g,ij}}{\partial x_j} - F_{drag,i} \end{cases} \tag{4.27}$$

where $f_{l/g}$ represents the contribution of volume forces respectively on the liquid and gas phases and $\tau_{l/g}$ is the viscous stress tensor in the liquid and gas sides. In order to ease the discussion, in the following equation, source terms for liquid and gas phases in Equation 4.27 are gathered together into:

$$\begin{cases} \bar{S}_{|l,i} & = \mathbf{C}_{l,i} + \rho_l \bar{\alpha}_l \bar{f}_{l,i} - \bar{\alpha}_l \dfrac{\partial \bar{P}_g}{\partial x_i} + \dfrac{\partial \bar{\alpha}_l \bar{\tau}_{l,ij}}{\partial x_j} + F_{drag,i} \\ \bar{S}_{|g,i} & = \rho_g \bar{\alpha}_g \bar{f}_{g,i} - \bar{\alpha}_g \dfrac{\partial \bar{P}_g}{\partial x_i} + \dfrac{\partial \bar{\alpha}_g \bar{\tau}_{g,ij}}{\partial x_j} - F_{drag,i} \end{cases} \tag{4.28}$$

where $S_{|l,i}$ and $S_{|g,i}$ represent the contribution of the source terms acting on the mixture conditioned on being in the liquid or in the gas phase. Therefore, summing the equations valid for liquid and gas, the standard momentum equation for the whole mixture shown below can be recast.

$$\frac{\partial \overline{\rho U_i}}{\partial t} + \frac{\partial \overline{\rho U_i U_j}}{\partial x_j} = \bar{S}_i \tag{4.29}$$

where the resulting source term ($\bar{S}_i$) is related to the pressure gradient (P), viscous stress tensor ($\tau_{i,j}$) and volume forces (f). It can be calculated as $\bar{S}_i = \bar{S}_{|l,i} + \bar{S}_{|g,i}$. Considering that Equation 4.29 is verified for a homogeneous flow, such force $\vec{\bar{S}}$ is independent from the multiphase context under investigation. It acts on each phase independently from the position in space and time. Namely, it represents a homogeneous contribution to the momentum equation of each phase and it will be specified in the following as $\vec{S_H}$.

Such homogeneous part can be also identified as the force that the two-phase flow would experience in the absence of a turbulent flux between

phases. Because it is homogeneous, the source term may be decomposed by phase leading to:

$$\begin{cases} \bar{S}_{|l,i} & = \bar{\alpha}_l \bar{S}_H \\ \bar{S}_{|g,i} & = \bar{\alpha}_g \bar{S}_H \end{cases} \text{for the homogeneous case} \tag{4.30}$$

However, considering that a two-phase system is under investigation, beyond such homogeneous part, another contribution, which is related to the presence of an interface between phases, should appear and it is responsible of the generation and reduction of a slip velocity between phases. It represents the departure from the homogeneous flow of Equation 4.30. Therefore, an additional non-homogeneous and locally defined contribution (Δ_S) has to be introduced in Equations 4.30, leading to the alternative expression of liquid and gas source terms shown below:

$$\begin{cases} \bar{S}_{|l,i} & = \bar{\alpha}_l \bar{S}_H + \underbrace{\left(\bar{S}_{l,i} - \bar{S}_H \bar{\alpha}_l\right)}_{\Delta_{S,li}} \\ \bar{S}_{|g,i} & = \bar{\alpha}_g \bar{S}_H + \underbrace{\left(\bar{S}_{g,i} - \bar{S}_H \bar{\alpha}_g\right)}_{\Delta_{S,gi}} \end{cases} \tag{4.31}$$

where $\Delta_{S,li}$ and $\Delta_{S,gi}$ are the additional contributions respectively in the liquid and gas sides.

Equations 4.31 represent the key-point of the present procedure: the homogeneous equilibrium formulation, valid when the relaxation times are small enough for the two phase system to behave like a single phase flow, is the starting point and then the departure to the homogeneity is introduced.

Having in mind this innovative formalism to detail liquid and gas phase source terms, it is now possible to obtain a complete equation for turbulent liquid flux using its exact definition:

$$\bar{R}_{\alpha_{l,i}} = -\bar{\alpha}_l (\bar{U}_i - \bar{U}_{l,i}) \tag{4.32}$$

The mixture momentum equation is therefore required. Hence, starting from Equation 4.29, the following formulation has been used, where, as in Section 3.3, the unclosed terms linked to density correlations are not fully described and included in the first term on the RHS of the equation. As already mentioned, further investigations are required on this topic even employing a Favre averaging (see Annex-A for further details and to

better appreciate the impact of the modelling closure here employed).

$$\frac{\partial \bar{\rho}\bar{U}_i}{\partial t} + \frac{\partial \bar{\rho}\bar{U}_i\bar{U}_j}{\partial x_j} = -\frac{\partial \overline{\rho u_i' u_j'}}{\partial x_j} - \frac{\partial \bar{P}}{\partial x_i} + \frac{\partial \bar{\tau}_{i,j}}{\partial x_j} + \bar{\rho}\bar{f}_i \tag{4.33}$$

Hence, from the liquid momentum equation (see Equations 4.27) the following equation, which has been obtained by summing the liquid volume fraction equation multiplied by $\bar{U}$ and Equation 4.33 multiplied by $\bar{\alpha}_l$, has been subtracted:

$$\begin{aligned} &\frac{\partial \bar{\alpha}_l\bar{U}_i}{\partial t} + \frac{\partial \bar{\alpha}_l\bar{U}_i\bar{U}_j}{\partial x_j} = \\ &-\bar{U}_i\frac{\partial \overline{u_j'\alpha_l'}}{\partial x_j} - \bar{\alpha}_l\frac{\partial \overline{u_i'u_j'}}{\partial x_j} - \frac{1}{\bar{\rho}}\bar{\alpha}_l\frac{\partial \bar{P}}{\partial x_i} + \frac{1}{\bar{\rho}}\bar{\alpha}_l\frac{\partial \bar{\tau}_{i,j}}{\partial x_j} + \bar{\alpha}_l\bar{f}_i \end{aligned} \tag{4.34}$$

From this operation, assuming liquid and gas density as constant, the following exact complete equation for turbulent liquid flux ($R_{\alpha_l,i}$) can be derived:

$$\begin{aligned} &\frac{\partial \bar{R}_{\alpha_l,i}}{\partial t} + \frac{\partial \bar{U}_j\bar{R}_{\alpha_l,i}}{\partial x_j} = \\ &\underbrace{-\bar{\alpha}_l\frac{\partial}{\partial x_i}\left(-\rho_l\bar{\alpha}_l\overline{u_{l,i}'u_{l,j}'} - \rho_g\bar{\alpha}_g\overline{u_{g,i}'u_{g,j}'}\right) + \frac{\partial \bar{\alpha}_l\left(\bar{U}_j - \bar{U}_j|_l\right)\bar{U}_i|_l}{\partial x_j}}_{A} + \\ &+ \underbrace{\frac{\partial\left(-\bar{\alpha}_l\overline{u_i'u_j'}\right)}{\partial x_j}}_{B} - \underbrace{\bar{R}_{\alpha_l,i}\frac{\partial \bar{U}_i}{\partial x_j}}_{C} + \underbrace{\frac{\bar{S}_{l,i}}{\rho_l} - \frac{\bar{S}_H}{\bar{\rho}}\bar{\alpha}_l}_{D'} \end{aligned} \tag{4.35}$$

where, using the same nomenclature of Figure 4.1, term A represents the turbulent diffusion inside the turbulent liquid flux equation, term B is the source related to the gradient of liquid volume fraction, term C is the source due to the gradient of mixture velocity, whereas with D' all the contributions related to forces acting on the whole mixture or on the liquid-gas interface are gathered together.
The expression of this latter term is now straightforward: this represents one of the major advantages of the formulation proposed in Equation 4.31. In fact, the homogeneous contribution ($\bar{S}_H$) can be easily recast from Equation 4.33, whereas $\bar{S}_{l,i}$ has been already introduced previously (see Equations 4.30).
Hence, including the expression of drag force (see Equation 3.32) and con-

sidering as volume force the gravity contribution, the complete formulation of the turbulent liquid flux equation shown below can be obtained:

$$\begin{aligned}
&\frac{\partial \bar{R}_{\alpha_{l,i}}}{\partial t} + \frac{\partial \bar{U}_j \bar{R}_{\alpha_{l,i}}}{\partial x_j} = \\
&-\frac{\partial \overline{\alpha_l' u_i' u_j'}}{\partial x_j} + \overline{u_i{}' u_j{}'} \frac{\partial \bar{\alpha}_l}{\partial x_j} - \bar{R}_{\alpha_l,i} \frac{\partial \bar{U}_i}{\partial x_j} + \mathbf{C}_l + \\
&\underbrace{+\left(\left(\frac{1}{\rho_l} - \frac{1}{\bar{\rho}}\right)\left(-\bar{\alpha}_l \frac{\partial \bar{P}}{\partial x_i} + \bar{\alpha}_l \frac{\partial \bar{\tau}_{i,j}}{\partial x_j} + \bar{\alpha}_l \bar{\rho} g_i\right)\right)}_{S_{HF}} + \\
&\underbrace{+\left(\frac{1}{\rho_l}\left(-\bar{\alpha}_l\left(\frac{\partial \bar{P}}{\partial x_i} - \frac{\partial \bar{P}_g}{\partial x_i}\right) + \bar{\alpha}_l g_i \left(\rho_l - \bar{\rho}\right)\right)\right)}_{S_{N-HF}} + \\
&\underbrace{+\frac{1}{\rho_l}\left(\frac{\bar{\alpha}_l \rho_l}{\tau_p}\left(\bar{U}_{l,i} - \bar{U}_{g,i}\right) - \bar{\alpha_l} \frac{\partial \bar{\alpha}_l \bar{\tau}_{i,j}}{\partial x_j} - \bar{\alpha}_l \frac{\partial \bar{\tau}_{i,j}}{\partial x_j}\right)}_{S_{N-HF}}
\end{aligned} \tag{4.36}$$

It should be pointed out that the same contributions proposed in previous works (see [158, 163, 164]) are retrieved here and in particular the RHS of the derived equation is composed by:

1. Turbulent diffusion term. It corresponds to the transport of turbulent liquid flux related to the velocity fluctuations and it represents the only contribution that needs a modelling effort. A first order closure can be normally reliably applied for this term since it should have a lower impact than in the liquid volume fraction equation. It will be specified later on as $\vec{S}_{turbdiffusion}$.

2. Term related to the gradient of liquid volume fraction. This contribution can be significant in presence of a non-homogeneous liquid distribution. It is directly related to a first order closure for turbulent liquid flux. If this term leads the production of $R_{\alpha_{l,i}}$, a closure based on Equation 3.57 can be reliably applied. It will be specified hereinafter as $\vec{S}_{grad\alpha_l}$.

3. Term associated to the gradient of velocity. In a test article dominated by shear stresses, this term modifies the turbulent liquid flux. It will be specified later on as $\vec{S}_{gradU}$.

4. Term due to the effects of collisions between liquid parcels. Such

phenomena can determine an augmentation or reduction of liquid velocity and therefore the generation of a slip velocity between phases. It will be specified as $\vec{S}_{coll}$.

5. Term accounting for the production of turbulent liquid flux related to the forces acting homogeneously on the whole mixture. Such contribution is directly related to the inertia of each phase: considering a force homogeneously distributed on the liquid-gas mixture, a difference of velocity should be normally generated due to the higher inertia of the liquid component. It will be specified hereinafter as $\vec{S}_{HF}$.

6. Term associated to the local departure of the two-phase flows from the homogeneous assumption. It should be pointed out that this term is defined just in presence of a liquid-gas interface. Studying it in detail, the first contribution is related to the pressure difference between the gas phase and the mixture. The second term accounts locally for the gravity force that should be balanced by the third contribution, which is the drag. Finally, the laminar viscous forces are introduced. The whole term will be specified later on as $\vec{S}_{N-HF}$.

Starting from Equation 4.36, a splitting of turbulent liquid flux in a slip and drift contributions, as shown in Section 4.2.2, can be again carried out leading to the following equation for $\vec{\Upsilon}_s$:

$$\begin{aligned}
\frac{\partial \bar{\Upsilon}_{s,i}}{\partial t} + \frac{\partial \bar{U}_j \bar{\Upsilon}_{s,i}}{\partial x_j} = \\
-\frac{\partial \overline{\alpha_l' u_i' u_j'}}{\partial x_j} + \mathbf{C}_l \\
+\left(\frac{1}{\rho_l} - \frac{1}{\bar{\rho}}\right)\left(-\bar{\alpha}_l \frac{\partial \bar{P}}{\partial x_i} + \bar{\alpha}_l \frac{\partial \tau_{i,j}}{\partial x_j} + \bar{\alpha}_l \bar{\rho} g_i\right) + \\
+\frac{1}{\rho_l}\left(-\bar{\alpha}_l\left(\frac{\partial \bar{P}}{\partial x_i} - \frac{\partial \bar{P}_g}{\partial x_i}\right) + \bar{\alpha}_l g_i \left(\rho_l - \bar{\rho}\right)\right) + \\
+\frac{1}{\rho_l}\left(\frac{\bar{\alpha}_l \rho_l}{\tau_p}\left(\bar{U}_{l,i} - \bar{U}_{g,i}\right) + \frac{\partial \bar{\alpha}_l \bar{\tau}_{l,ij}}{\partial x_j} - \bar{\alpha}_l \frac{\partial \bar{\tau}_{i,j}}{\partial x_j}\right)
\end{aligned} \tag{4.37}$$

As already mentioned, this equation is complete since all the forces that can appear in a two-phase system and that can generate a slip velocity between phases are accounted.
Introducing now the same hypotheses described in Section 4.2 to extract the major contributions that generate a slip velocity (i.e. including $\vec{S}_{grad\alpha_l}$, $\vec{S}_{gradU}$ and $\vec{S}_{coll}$ in the drift component) and employing a first

order closure for $\vec{S}_{turbdiffusion}$, the following reduced equation for Υ_s can be derived. The remaining terms are related to $\vec{S}_{HF}$ and $\vec{S}_{N-HF}$, showing that the proposed methodology is theoretically based on an homogeneous assumption that is locally corrected in order to account for phenomena related to the presence of a liquid-gas interface.

$$\begin{aligned}
&\frac{\partial \bar{\Upsilon}_{s,i}}{\partial t} + \frac{\partial \bar{U}_j \bar{\Upsilon}_{s,i}}{\partial x_j} = \\
&\frac{\partial}{\partial x_j}\left(\frac{\nu_t}{Sc_t}\frac{\partial \bar{\Upsilon}_{s,i}}{\partial x_j}\right) + \\
&+\left(\frac{1}{\rho_l} - \frac{1}{\bar{\rho}}\right)\left(-\bar{\alpha}_l \frac{\partial \bar{P}}{\partial x_i} + \bar{\alpha}_l \bar{\rho} g_i\right) + \\
&+\frac{1}{\rho_l}\left(-\bar{\alpha}_l\left(\frac{\partial \bar{P}}{\partial x_i} - \frac{\partial \bar{P}_g}{\partial x_i}\right) + \bar{\alpha}_l g_i \left(\rho_l - \bar{\rho}\right)\right) + \frac{1}{\rho_l}\left(\frac{\rho_l}{\tau_p \left(1-\bar{\alpha}_l\right)}\bar{\Upsilon}_{s,i}\right)
\end{aligned} \tag{4.38}$$

The capabilities of such formulation of QME have been assessed on an analytical 0D-test case representing a liquid-gas system, evolving under the effects of forces that can generate or reduce the slip velocity (e.g. pressure gradient, gravity and drag forces). The system, shown in Figure 4.22, is at rest as initial condition and then it evolves in time based on the actions included in Equation 4.38. The convective contribution is not considered. The solution obtained from QME has been compared with the one that can be calculated starting from Equations 4.28 and solving separately each phase. Figure 4.22 shows the resulting evolution of the liquid velocity obtained with the two methods considering only the pressure gradient contribution, which is the leading one in the jet in crossflow test case. An excellent agreement is reported, proving once again the capabilities of the proposed methodology.

Finally, it is worth pointing out that Equation 4.20 represents a particular case of Equation 4.38, where the effects of slip velocity on the gas-phase have been neglected and were accounted just on the liquid. It can be considered suitable if the attention is mainly focused on the near injection region, as in the present investigation.

In fact, starting from the expressions of source terms provided in Equation 4.38 and accounting just for the contributions coming from $\bar{S}_{l,i}$ in Equation 4.35 for term $D^{'}$, Equation 4.20 can be retrieved.

Therefore, this latter formulation can be introduced from Equation 4.38 assuming a one way coupling between liquid and gas. This observation augments the theoretical background of the QME formulation proposed

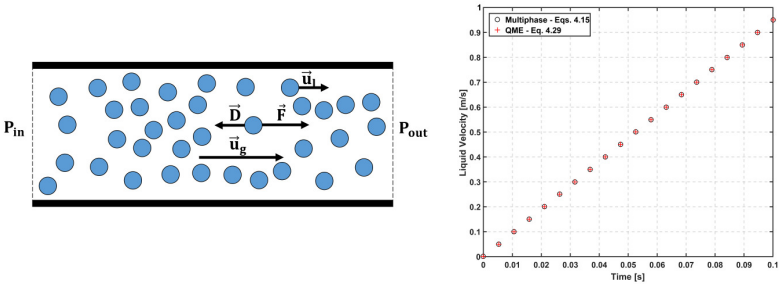

Figure 4.22: 0D-test case studied to assess the formulation for QME with a comparison with a standard multiphase flow formulation. The contribution of pressure gradient is just accounted.

in [160]. The two formulations are coherent between each other and the introduction of the general approach proposed in Equation 4.38, which overcomes some limitations of the previous modelling proposal, should be pursued in future investigations.

4.7 Concluding remarks

This chapter resumes the main activities carried out in the present research work with the aim of extending the capabilities of the ELSA approach in handling a slip velocity between phases. In Chapter 3, the effects of turbulent liquid flux on lean aero-engine burners have been highlighted justifying the need for a detailed numerical modelling of this contribution.

A novel second order closure, where one equation is solved for each component of the turbulent liquid flux, was proposed and integrated both with the liquid volume fraction and with the liquid /gas interface density equations. The approach presents an original splitting of the turbulent liquid flux in two parts: the drift, modelled according to a diffusion process, and the slip part, represented by a particular transport equation, where the effects of drag, body forces and pressure gradient are included. Such choice leads to a robust method able to introduce the leading phenomena directly linked to slip motion with significant advantages with respect to first order closures.

This approach fills the gap between single Eulerian mixture models and fully two-phase Eulerian-Eulerian approaches with the benefit to be applicable for all range of liquid volume fraction addressing both dense

and dispersed flows. Solver capabilities have been tested in a jet in crossflow test case with a direct validation against both experimental and numerical data. Improvements in terms of liquid distribution have been obtained with respect to first order results in all the analysed test conditions.
The QME approach has been as well coupled with the complete ELSA solver presented in Chapter 3, leading to the proposition of a general numerical tool able to account for the main interactions that characterize atomization processes in the aero-engine context.
Finally, a systematic derivation of the transport equation for $\vec{R}_{\alpha_l}$ has been as well carried out arriving to a general procedure to treat the liquid-gas flow, either starting from a multiphase perspective with phase separation or from a homogeneous flow and introducing the departure from homogeneity. The inclusion of this advanced and complete numerical strategy should be pursued in further investigations.

Chapter 5

Evaporation modelling for ELSA framework

In the context of the development of a high fidelity atomization model to be used in reactive simulations of aero-engine combustors, evaporation and energy transferred from gas to liquid phase are phenomena of paramount importance.
The main aim of this part of the work is the extension of the capabilities of the ELSA approach, presented in Chapter 3 and already modified to account for slip velocity effects, to include the vaporization in all the stages of spray atomization.
A novel approach for evaporation modelling is introduced and tested. An innovative implicit formulation is proposed and the first part of the chapter is focused on a theoretical explanation of the developed approach and on its implementation in the OpenFOAM® suite. It is worth pointing out that such approach is focused mainly on the dense spray region of ELSA, since, for the lagrangian one, several models have been already developed in technical literature (see Section 3.4.3). An assessment of the model on the Engine Combustion Network (ECN) database is at the end provided.

5.1 Compressible ELSA solver

Starting from the Eulerian-Eulerian mixture model presented in Section 4.1, in order to be able to deal with heat transfer and evaporation, a compressible version of the solver has been first of all developed and validated. Hereinafter, equations are written in RANS context for the sake of clarity, applying a Reynolds averaging procedure. Nonetheless, in the code, equations have been written in a general way valid both in RANS and LES. The turbulent liquid flux can be as well modelled both with a standard gradient closure, when the dynamic relaxation time tends to zero, or employing the second order strategy developed in Section 4.6. For the sake of clarity, in this chapter the development of the code and its assessment have been performed using a first order closure.
The proposed compressible solver is still based on a mixture structure with one momentum equation shared between all the phases (see Equation 5.1). As in the previous chapters, the density correlation terms are included in the Reynolds stress tensor and in the following equations a standard Boussinesq closure has been applied. The consequences of this modelling choice are detailed in Annex-A.

$$\frac{\partial \bar{\rho}\bar{U}_i}{\partial t} + \frac{\partial \bar{\rho}\bar{U}_i\bar{U}_j}{\partial x_j} - \frac{\partial}{\partial x_i}\left[\mu_t\left(\frac{\partial \bar{U}_i}{\partial x_j} + \frac{\partial \bar{U}_j}{\partial x_i}\right)\right] = \bar{\rho}g_i - \frac{\partial \bar{P}}{\partial x_i} \tag{5.1}$$

where mixture density can be obtained as $\bar{\rho} = \bar{\alpha}_l\bar{\rho}_l + \bar{\alpha}_v\bar{\rho}_v + \bar{\alpha}_a\bar{\rho}_a$, where bulk densities for vapour and air depend on temperature and pressure to include compressible phenomena. The continuity equation is written as:

$$\frac{\partial \bar{\rho}}{\partial t} + \frac{\partial \bar{\rho}\bar{U}_i}{\partial x_j} = 0 \tag{5.2}$$

A transport equation for vapour volume fraction is included together with the one for liquid. Both of them are resolved in a compressible manner and source terms due to evaporation have been added.

$$\frac{\partial \bar{\rho}_l\bar{\alpha}_l}{\partial t} + \frac{\partial \bar{\rho}_l\bar{\alpha}_l\bar{U}_i}{\partial x_i} = \frac{\partial}{\partial x_i}\left[\left(\bar{\rho}_l D_l + \frac{\mu_t}{Sc_{tl}}\right)\frac{\partial \bar{\alpha}_l}{\partial x_i}\right] + \dot{\bar{\alpha}}_{ev} \tag{5.3}$$

$$\frac{\partial \bar{\rho}_v\bar{\alpha}_v}{\partial t} + \frac{\partial \bar{\rho}_v\bar{\alpha}_v\bar{U}_i}{\partial x_i} = \frac{\partial}{\partial x_i}\left[\left(\bar{\rho}_v D_v + \frac{\mu_t}{Sc_{t_v}}\right)\frac{\partial \bar{\alpha}_v}{\partial x_i}\right] - \dot{\bar{\alpha}}_{ev} \tag{5.4}$$

where in particular μ_t is the turbulent viscosity, D and Sc_t are laminar diffusivity and turbulent Schmidt number of liquid and vapour. Furthermore, $\dot{\bar{\alpha}}_{ev}$ represents the source/sink term of evaporation, that will be discussed in detail later on. The subscripts l and v refer to liquid and

vapour properties respectively. Clearly, the air volume fraction is directly calculated from $\bar{\alpha}_l + \bar{\alpha}_v + \bar{\alpha}_a = 1$, where the subscript a refers to air.
Energy equations, formulated in terms of temperature, both for gas and liquid have been also introduced and are reported here below. The contribution of evaporation appears as additional source term ($\dot{\bar{T}}_{ev}$).

$$\begin{cases} \dfrac{\partial \bar{\rho}_a \bar{\alpha}_a c_{p_a} \bar{T}_g}{\partial t} & + \dfrac{\partial \bar{\rho}_v \bar{\alpha}_v c_{p_v} \bar{T}_g}{\partial t} + \dfrac{\partial \bar{\rho}_a \bar{\alpha}_a c_{p_a} \bar{T}_g \bar{U}_i}{\partial x_i} + \dfrac{\partial \bar{\rho}_v \bar{\alpha}_v c_{p_v} \bar{T}_g \bar{U}_i}{\partial x_i} = \\ & \dfrac{\partial}{\partial x_i}\left(\bar{\alpha}_v \dfrac{\mu_t}{Pr_{t_v}} \dfrac{\partial \bar{T}_g}{\partial x_i}\right) + \dfrac{\partial}{\partial x_i}\left(\bar{\alpha}_a \dfrac{\mu_t}{Pr_{t_a}} \dfrac{\partial \bar{T}_g}{\partial x_i}\right) + \dot{\bar{T}}_{ev,g} \\ \dfrac{\partial \bar{\rho}_l \bar{\alpha}_l c_{p_l} \bar{T}_l}{\partial t} & + \dfrac{\partial \bar{\rho}_l \bar{\alpha}_l c_{p_l} \bar{T}_l \bar{U}_i}{\partial x_i} = \dfrac{\partial}{\partial x_i}\left(\bar{\alpha}_l \dfrac{\mu_t}{Pr_{tl}} \dfrac{\partial \bar{T}_l}{\partial x_i}\right) + \dot{\bar{T}}_{ev,l} \end{cases} \tag{5.5}$$

where c_p is the specific heat and Pr_t is the turbulent Prandtl number.
As far as the $\bar{\Sigma}$-equation is concerned, the same formulation presented in Chapter 3 has been here retained non accounting for density variations:

$$\frac{\partial \bar{\Sigma}^{'}}{\partial t} + \frac{\partial \bar{U}_i \bar{\Sigma}^{'}}{\partial x_i} - \frac{\partial}{\partial x_i}\left[\left(\frac{\nu_t}{Sc_t}\right)\frac{\partial \bar{\Sigma}^{'}}{\partial x_i}\right] = \frac{\bar{\Sigma}}{\tau_t}\left(1 - \frac{\bar{\Sigma}}{\bar{\Sigma}_{eq}}\right) \tag{5.6}$$

The sink term due to evaporation for the liquid/gas interface density has been neglected. In fact, in the dense spray region, it is assumed that the turbulent breakup is the dominant phenomenon and that evaporation has a minor impact.
A brief overview about the structure of the developed compressible solver is shown in Table 5.1.
In the following, the attention is mainly focused on the method proposed for the calculation of the evaporation source terms. The reader interested in a preliminary validation of such compressible code is addressed to [182], where several aspects of the developed solver have been analysed.
The chapter is therefore structured as follows: firstly, the shortcomings of explicit methods, in the context of evaporation modelling for the dense spray region, will be presented and an assessment of the advantages of implicit approaches will be carried out. Then, the concept of the phase equilibrium is introduced for evaporative systems together with an explanation of the developed code to compute equilibrium composition and temperature. Finally, a detailed validation is performed using the available theoretical solutions for evaporation modelling and experimental data provided in the ECN database.

Continuity Equation:

$$\frac{\partial \bar{\rho}}{\partial t} + \frac{\partial \bar{\rho}\bar{U}_i}{\partial x_j} = 0$$

Momentum Equation:

$$\frac{\partial \bar{\rho}\bar{U}_i}{\partial t} + \frac{\partial \bar{\rho}\bar{U}_i\bar{U}_j}{\partial x_j} = \frac{\partial}{\partial x_i}\left[\mu_t\left(\frac{\partial \bar{U}_i}{\partial x_j} + \frac{\partial \bar{U}_j}{\partial x_i}\right)\right] - \bar{\rho}g_i - \frac{\partial \bar{P}}{\partial x_i}$$

Liquid volume fraction Equation:

$$\frac{\partial \bar{\rho}_l\bar{\alpha}_l}{\partial t} + \frac{\partial \bar{\rho}_l\bar{\alpha}_l\bar{U}_i}{\partial x_i} = \frac{\partial}{\partial x_i}\left[\left(\bar{\rho}_l D_l + \frac{\mu_t}{Sc_{tl}}\right)\frac{\partial \bar{\alpha}_l}{\partial x_i}\right] + \dot{\bar{\alpha}}_{ev}$$

Vapour volume fraction Equation:

$$\frac{\partial \bar{\rho}_v\bar{\alpha}_v}{\partial t} + \frac{\partial \bar{\rho}_v\bar{\alpha}_v\bar{U}_i}{\partial x_i} = \frac{\partial}{\partial x_i}\left[\left(\bar{\rho}_v D_v + \frac{\mu_t}{Sc_{t_v}}\right)\frac{\partial \bar{\alpha}_v}{\partial x_i}\right] - \dot{\bar{\alpha}}_{ev}$$

Liquid gas interface density Equation:

$$\frac{\partial \bar{\Sigma}'}{\partial t} + \frac{\partial \bar{U}_j\bar{\Sigma}'}{\partial x_j} = + \frac{\partial}{\partial x_j}\left(\frac{\nu_t}{Sc_t}\frac{\partial}{\partial x_j}\bar{\Sigma}'\right) + \frac{\bar{\Sigma}}{\tau_t}\left(1 - \frac{\bar{\Sigma}}{\Sigma_{eq}}\right)$$

Gas phase temperature Equation:

$$\frac{\partial \bar{\rho}_a\bar{\alpha}_a c_{p_a}\bar{T}_g}{\partial t} + \frac{\partial \bar{\rho}_a\bar{\alpha}_a c_{p_a}\bar{T}_g\bar{U}_i}{\partial x_i} = - \frac{\partial \bar{\rho}_v\bar{\alpha}_v c_{p_v}\bar{T}_g}{\partial t} - \frac{\partial \bar{\rho}_v\bar{\alpha}_v c_{p_v}\bar{T}_g\bar{U}_i}{\partial x_i} + + \frac{\partial}{\partial x_i}\left(\bar{\alpha}_v\frac{\mu_t}{Pr_{t_v}}\frac{\partial \bar{T}_g}{\partial x_i}\right) + \frac{\partial}{\partial x_i}\left(\bar{\alpha}_a\frac{\mu_t}{Pr_{t_a}}\frac{\partial \bar{T}_g}{\partial x_i}\right) + \dot{\bar{T}}_{ev,g}$$

Liquid phase temperature Equation:

$$\frac{\partial \bar{\rho}_l\bar{\alpha}_l c_{p_l}\bar{T}_l}{\partial t} + \frac{\partial \bar{\rho}_l\bar{\alpha}_l c_{p_l}\bar{T}_l\bar{U}_i}{\partial x_i} = \frac{\partial}{\partial x_i}\left(\bar{\alpha}_l\frac{\mu_t}{Pr_{tl}}\frac{\partial \bar{T}_l}{\partial x_i}\right) + \dot{\bar{T}}_{ev,l}$$

Table 5.1: Summary of the equations implemented in the developed compressible ELSA approach.

5.2 Limits of standard explicit methods for dense spray regions

As already reported in Chapter 3, in the dense zone of the spray, the assumption of spherical droplets is not at all verified. In fact, until primary breakup takes place, the liquid phase exists as coherent structures or ligaments and, mainly at low pressure and temperature conditions, their impact can be relevant.
Standard Eulerian-Lagrangian approaches, which are based on explicit formulations for evaporation modelling, can be reliably applied only if the liquid volume fraction is small. An artificial reduction of liquid volume fraction, by increasing the size of the mesh around the injection point

[183], can be considered as a solution, albeit a lower resolution in the Eulerian field is obtained in this way.
The existence of regions inside the computational domain characterized by high α_l cannot be normally avoided, considering the atomizing devices employed in lean burn combustors. Here, explicit formulations can drastically affect the obtained solution.
In this section, limits of such explicit methods are explained using results obtained in a theoretical numerical case employing the native Eulerian-Lagrangian solver of OpenFOAM® (i.e. *sprayFoam*)[182, 184]. The 1-D test case, shown in Figure 5.1, where a cloud of droplets (highlighted in red) is introduced inside a hot stagnant environment, has been considered to this end. Cyclic conditions are applied on the lateral surfaces in order to determine a one-dimensional behaviour. Liquid temperature is initially set to 288 K, while the gas phase to 773 K. On such configuration, it is possible to calculate the ratio of ambient over liquid temperature with respect to time for several values of cell liquid volume fraction [182, 184].

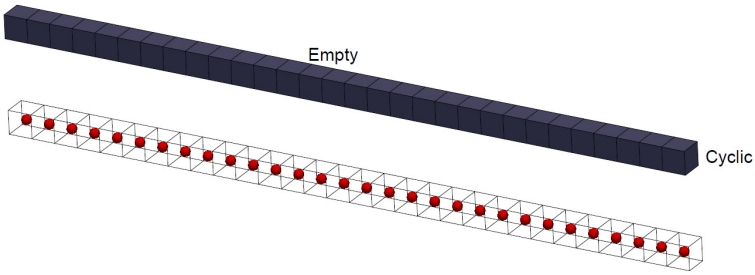

Figure 5.1: Computational domain employed to asses the limitations of explicit approaches [182, 184].

As described in Section 3.4.3, the evaporation source term employed in *sprayFoam* is based on the following expression:

$$\frac{dm}{dt} = \dot{m} = \pi d Sh D_g \rho_s \log(1 - \chi_r) \tag{5.7}$$

where d is the diameter of the droplet, Sh the Sherwood number, D_{ab} the mass diffusivity and ρ_s is the gas mixture density at droplet surface and χ_r is the relative molar fraction of vapour surrounding the droplet. As far as the enthalpy equation is concerned, the heat transfer between gas and liquid, together with the latent heat of vaporization L, compose the

sink term on the RHS.

$$\frac{dh}{dt} = \dot{h} = kA_d(T_l - T_g) - \frac{dm}{dt}L \tag{5.8}$$

Where k and A_d stand for the heat transfer coefficient and the droplet surface area. It should be pointed out that, since both terms on the RHS in Equation 5.8 become negative if evaporation takes place, undershoots or overshoots in the solution can be generated. From a numerical point of view, this scenario depends on the chosen time step value (dt): lowering dt this effect is reduced, but the CPU cost is augmented.
In Figure 5.2, the ratio between gas phase and liquid temperatures in time is reported for a set of simulations employing a $dt = 10^{-5}$s. From a

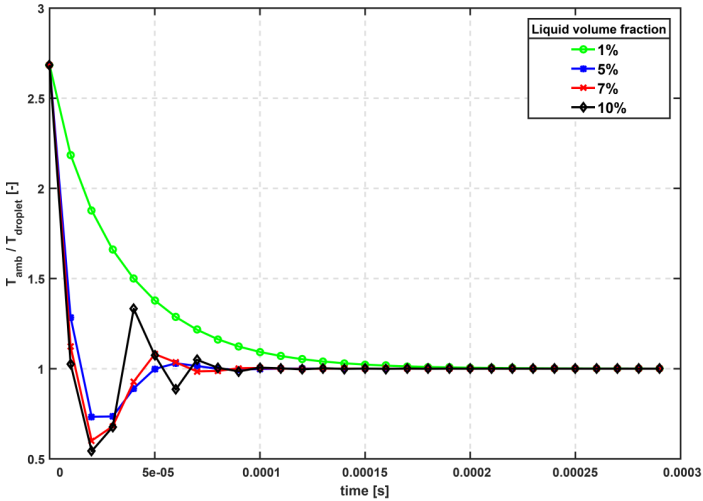

Figure 5.2: Ratio of ambient over liquid temperature with the respect to time for several liquid volume fraction values [182, 184].

physical point of view, the ratio $T_{amb}/T_{droplet}$ should never be less than 1. However, such non-physical situation happens from a numerical point of view since, increasing the liquid volume fraction, the explicit formulation leads to unbounded values of gas phase temperature. Indeed, as soon as dm/dt is calculated (Equation 5.7) and temperatures are fixed, depending on dt, a certain value of dh is computed through Equation 5.8. If dt is not sufficiently small, dh may be large enough to determine a sharp decrease of gas phase temperature. Hence, temperature undershoots can

be generated.
Clearly, this issue can be overcome by reducing the simulation time step, but with a strong increase of the computational cost. In Figure 5.3 the $\alpha_l = 5\%$ case has been simulated with two different time steps, i.e. $dt = 10^{-5}$s for the blue curve, whereas it has been reduced of two order of magnitudes for the red one [182].

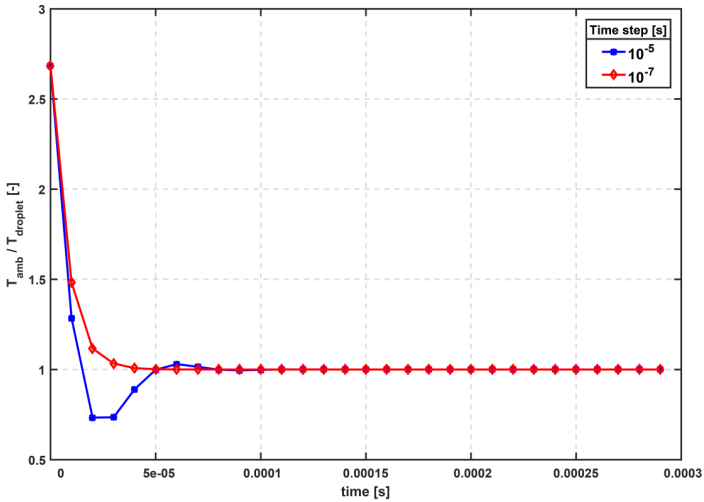

Figure 5.3: Ratio of ambient and droplet temperature with the respect to time for different time step in lagrangian simulation [182, 184].

Employing the lower time step, numerical issues are finally avoided, but CPU cost is augmented.
From these observations, it should be clear that approaching the dense spray region (i.e. $\alpha_l \to 1$), the time step should be reduced (i.e. $dt \to 0$) to overcome numerical instabilities with explicit methods [182, 184].
Therefore, considering that one of the main advantages of ELSA is being able to deal both with dense and diluted spray regions, the main purpose of this part of the work is to define a method capable of handling evaporation in the whole evolution of the spray, from pure liquid to the dispersed phase. As already explained, the attention is mainly focused on the near injection region since in the lagrangian context several evaporation models are already available (see Section 3.4.3). A novel implicit method has been developed and implemented in the framework of ELSA and it is

described in the next sections.

5.3 Implicit method for evaporation modelling

In an implicit context, source terms for Equations 5.4 and 5.5 have to be formulated as reported below:

$$\begin{cases} \dot{\alpha}_{ev} = \left(\dfrac{\alpha_{l,eq} - \alpha_l}{\tau_m} \right) \\ \dot{T}_{ev} = \left(\dfrac{T_{l,eq} - T_l}{\tau_T} \right) \end{cases} \tag{5.9}$$

where $\alpha_{l,eq}$ and $T_{l,eq}$ represent the equilibrium state that locally the liquid/gas system reaches in terms of remaining liquid volume and temperature with two rates defined by τ_m and τ_T . A similar formulation should be employed also for the gas phase in terms of temperature, which is not reported here for the sake of brevity.
Equations 5.9 lead to an unconditionally stable system on a mathematical point of view, even if a proper calculation of equilibrium state and evaporation rates has to be provided.
In technical literature, it is normally assumed that the liquid is completely evaporated at equilibrium conditions [185]. Unfortunately, this is not verified all along the atomization process, since, in the near injector region, some amount of liquid should remain. One of the few attempts to include such effects was proposed by García-Oliver et al. [151]. Here, an implicit evaporation model, based on local adiabatic saturation conditions, was proposed. However, it was assumed that the characteristic temporal scale of vaporization is the calculation time step, i.e. the vaporization was supposed quick enough to be completed within the simulation time-step. However, this is not generally true since the thermal relaxation time varies inside the domain based on the flow-field characteristics. Moreover, the equilibrium temperature for the gas-phase was calculated by using an ideal mixing without including the effects of evaporation.
To overcome these shortcomings, a novel strategy to calculate equilibrium conditions has been developed. The theoretical ground of this piece of work is mainly reported in [182], which has been realized under the author's supervision, and in the following section the main concepts and idea are summarized.

5.3.1 Definition of phase equilibrium

Different equilibrium conditions can be determined in physics and engineering, going from thermodynamic equilibrium to static equilibrium of bodies. In this study, the word *equilibrium* refers to the *phase equilibrium* that can take place between liquid and gas that coexist in the same control volume [182, 184].
The equilibrium state of a system at a defined temperature and pressure is theoretically given by the minimum of the Gibbs function [186]:

$$(dG)_{T,p} = 0 \tag{5.10}$$

Therefore, the equilibrium conditions, required in Equations 5.9, can be computed by a direct numerical minimization of G. For instance, this procedure is normally employed to calculate the equilibrium state in chemical problems. However, it can be consuming from a computational point of view and it is particularly suitable when several species are involved.
Thus, in this work a different strategy has been employed. Hereinafter, the main aspects of the proposed procedure are summarized and the reader interested in the detailed mathematical derivation is addressed to [182, 184, 187] and references therein.
Hence, considering the evaporation process in a two-phase, two-component system inside an isolated control volume at constant pressure, where mass transfer takes place from liquid to vapour phase, it is possible to calculate the equilibrium temperature of the system as [182, 184, 187]:

$$T_{eq} = \frac{m_a c_{p_a} T_a + m_l c_{p_l} T_l + m_v c_{p_v} T_v - (m_{v\,eq} - m_v) L}{m_{a\,eq} c_{p_a} + m_{l\,eq} c_{p_l} + m_{v\,eq} c_{p_v}} \tag{5.11}$$

Such equation simply represents the enthalpy conservation equation over the control volume, where the contribution of evaporation is also included. It is worth pointing out that to derive it, specific heat coefficients have been considered as constant. This represents one of the main hypothesis of the present procedure. Clearly, variations with temperature should be included, in particular in reactive test conditions, and further investigations are required on this point.
Anyway, Equation 5.11 can be further simplified. In fact, mass transfer is not allowed for air ($m_a = m_{a\,eq}$) and vapour and air have to share the same temperature T_g before achieving the equilibrium. It can be therefore

reformulated as:

$$T_{eq} = \frac{m_a c_{p_a} T_g + m_l c_{p_l} T_l + m_v c_{p_v} T_g - (m_{v\,eq} - m_v) L}{m_a c_{p_a} + m_{l\,eq} c_{p_l} + m_{v\,eq} c_{p_v}} \tag{5.12}$$

This represents the expression of the equilibrium temperature of a two-phase, two-component system subjected to evaporation.
However, another relationship is required to estimate $m_{v\,eq}$. According to Cengel and Boles [186], phase equilibrium of a liquid/air system is reached when the vapour pressure in the air is equal to the saturation pressure of liquid at the liquid temperature. The following relationship can be therefore introduced:

$$p_v = p_{sat}(T_{eq}) \tag{5.13}$$

where p_{sat} represents the saturation pressure that can be computed through the Antoine equation[186]. The partial pressure of vapour (p_v) can be instead expressed in terms of number of moles of air and vapour in the fraction of volume available for the gas phase.

$$p_v = \frac{n_v}{n_v + n_a} p \tag{5.14}$$

Hence, equilibrium conditions can be computed varying $m_{v\,eq}$, until Equation 5.13 is satisfied. An iterative cycle has been defined to this end, since both p_v and p_{sat} in Equation 5.13 depends on $m_{v\,eq}$ [182].
The iterative cycle introduced in ELSA and coded in OpenFOAM® is explained in detail in the next section.

5.3.2 Computation of equilibrium conditions

In Figure 5.4 the code employed for the computation of the equilibrium state is presented [182, 184]. The calculation is carried out in each cell where a non-zero amount of liquid is present and the input variables are directly obtained from the numerical simulation. The iterative cycle is based on $m_{l\,eq}$, since it can be easily converted in terms of liquid volume fraction using the density.
First, the saturated condition is evaluated considering $m_{l\,eq} = m_l$, which means that mass transfer does not take place [182, 184]. T_{eq} is calculated by Equation 5.12, $p_{v\,eq}$ by Equation 5.14 and $p_{sat\,eq}$ using the standard Antoine equation. If $p_{v\,eq} > p_{sat\,eq}$, no further evaporation is allowed. In this case, only heat transfer is included between phases and a proper T_{eq} is calculated[182, 184].
On the contrary, if some evaporation is possible, the case of complete

evaporation is evaluated (i.e. $m_{leq} = 0$) and two possible situations are therefore considered:

- if $p_{v,eq} < p_{sat,eq}$ the whole liquid will be evaporated and the final equilibrium temperature for the liquid is set equal to the wet bulb value (see Figure 5.5 for further details), whereas the one for the gas is computed thanks to Equation 5.12.

- if $p_{v,eq} \geqslant p_{sat,eq}$ only partial evaporation takes place. This situation leads to an iterative cycle based on Equation 5.13 and, in the present study, a simple bisection method has been employed because of his stability and boundedness. Further developments are surely required on this point to decrease the overall computational effort.

The computed m_{leq} and T_{eq} are finally used to compute source terms in Equations 5.9.
It should be pointed out that, if a complete evaporation is predicted, the equilibrium temperature calculated with Equation 5.12 is no more correct at least for the liquid [182, 184]. In fact, the evaporation hystory of a single isolated droplet [188] is usually divided in two subsequent steps:

- a *heat-up* period, when, although evaporation is taking place, the heat transfer from gas to liquid leads to increase the liquid temperature;

- a *steady* period, when the heat transfer from gas to liquid phase is balanced by the cooling effect of the vaporization. The liquid temperature attains here the wet-bulb value until evaporation is completed.

In this latter period, equilibrium temperatures for gas and liquid are different: the first one reaches the equilibrium temperature determined through Equation 5.12, whereas the other one achieves the wet-bulbe value. Another iterative cycle has been therefore employed to calculate T_{eql} and it is based on the definition of B_m and B_T (see Section 3.4.3)[182]. As reported by Lefebvre [12], if $B_m = B_T$, the steady-state period starts and the liquid temperature remains constant until the liquid is consumed. An additional iterative cycle has been developed to determine such constant temperature and it is shown in Figure 5.5 [182, 184]. A bisection method has been again employed. In this manner, a guess value of T_{eql} is computed and used to evaluate p_{sat} through the Antoine. Then, B_M and B_T are calculated and the two values are compared:

- if $B_m > B_T$, the temperature is reduced

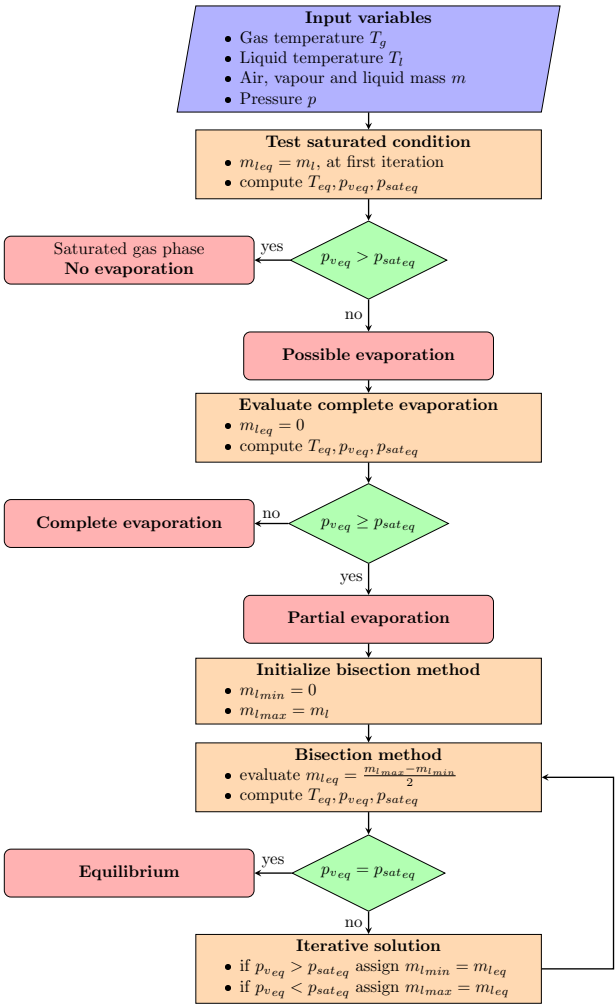

Figure 5.4: Method implemented for computation of equilibrium composition and temperature [182, 184].

- if $B_m < B_T$, the temperature is augmented

In few iterations, the correct value of liquid temperature is computed.

5.3.3 Computation of characteristic time scales

The remaining parameters that need now to be defined to close Equations 5.9 are τ_m and τ_T . Modelling proposals for the rate of vaporisation to be applied all along the atomization process are not yet available in technical literature. To overcome this difficulty, a first solution here employed is based on the Abramzon-Sirignano model [69]. In this way, a proper vaporisation rate is recovered in the dilute spray region, but the characteristic vaporisation time scale is underestimated in the dense part. However, it is worth mentioning that this error should be partially compensated by the implicit method [182, 184]. In fact, the above cycle leads to properly calculate the equilibrium conditions everywhere and the modelling approximation is only given by τ. Furthermore, in the near injection regions, the volume left for gas phase is generally small ($\alpha_l \to 1.0$) and it will be rapidly cooled and saturated by vapour. Therefore, the mass of liquid that can evaporate will be small as well as the characteristic time. Hence, at least for the near injector region, the estimation of the equilibrium state is much more significant than the time required by the system to achieve such condition. This observation leads also to the conclusion that, even if with an implicit method the time-dependent evolution can be not properly resolved, this transient phase should not impact the simulation accuracy. Further developments are required to calculate the characteristic time scales of evaporation, introducing other geometrical properties of the liquid/gas interface such as the curvature of the liquid surface. The reader interested in this topic is addressed to Chapter 6. Finally, it is worth mentioning that another key point to determine the characteristic time scales is to ensure the coherence between vaporization and heat transfer times. The employed formulation verifies this requirement.
Using the Abramzon-Sirignano model [69], it is possible to obtain the expressions of τ_m and τ_T shown below [182, 184]:

$$\begin{cases} \tau_m = \dfrac{m_{l_{eq}} - m_l}{\pi d n_d Sh^* D_g \rho_g ln\left(1 + B_M\right)} \\ \tau_T = \dfrac{T_{l_{eq}} - T_l}{\left(\frac{\dot{Q} - \dot{m} L}{c p_l m_l}\right)} \end{cases} \tag{5.15}$$

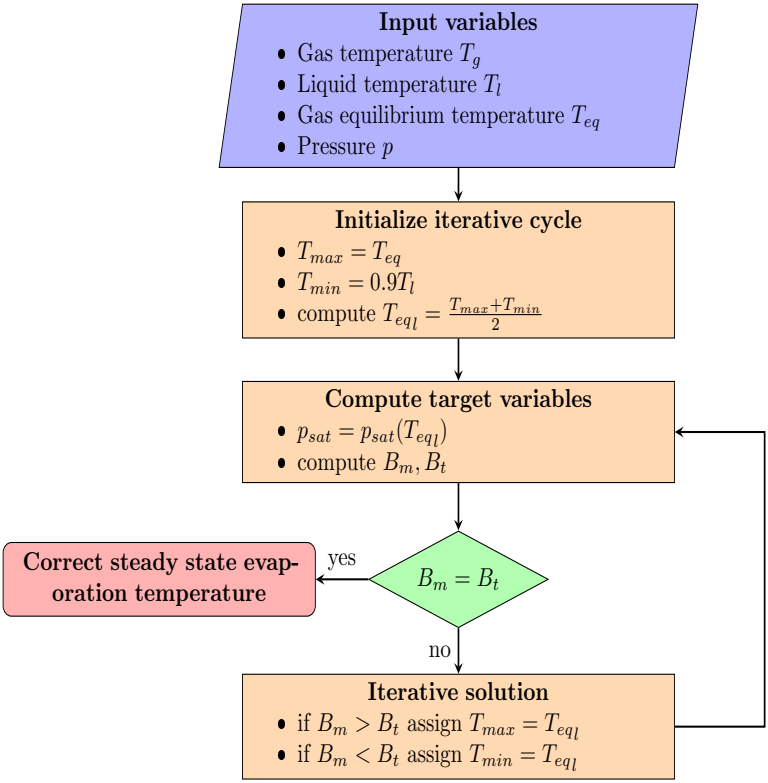

Figure 5.5: Method implemented for computation of equilibrium temperature of liquid in case of complete evaporation [182].

where d and n_d can be directly calculated from α_l and Σ as shown below:

$$d = \frac{6\alpha_l}{\Sigma} \tag{5.16}$$

$$n_d = \frac{V_{liquid}}{V_{droplet}} = \frac{V_{liquid}}{V_{cell}} \frac{V_{cell}}{V_{droplet}} = \alpha_l \frac{6}{\pi d^3} V_{cell} \tag{5.17}$$

Furthermore, in Equation 5.15, $\dot{Q}$, which is the heat transfer between phases, appears and can be calculated as:

$$\dot{Q} = \pi d n_d N u^* k_g \frac{\ln\left(1 + B_T{}'\right)}{B_T{}'} (T_g - T_l) \tag{5.18}$$

where k_g is the gas thermal conductivity, Nu^* is the corrected Nusselt number to account for the effects of Stefan flow and $B_T^{'}$ is the thermal Spalding number. The Reynolds number, employed in the definition of Nu^* and Sh^*, is instead calculated using the fluctuating component of velocity [188]:

$$\begin{cases} Sh_0 = 2 + 0.552 Re^{\frac{1}{2}} Sc^{\frac{1}{3}} \\ Re = \dfrac{u^{'} d \rho_g}{\mu_g} \end{cases} \tag{5.19}$$

For the sake of brevity, the complete expression of these terms is not here detailed, but it is possible to recast a formulation of each one through the characteristic variables of ELSA (i.e. α_l and Σ)[182, 184]. It should be pointed out that all these quantities are valid both for the dilute and dense spray regions since they are based only on geometrical properties of the droplet-gas interface, which are defined in all the domain.
In the next section, a validation of the solver is reported both on a single droplet case and on a more realistic configuration.

5.4 Analytical validation of the solver

Before going in detail with an assessment of the developed solver on the experimental test article studied in the ECN framework, in this section a preliminary theoretical validation of the solver is provided. In particular, a comparison with the results obtained with the theory of Abramzon-Sirignano [69] has been used to this end [182].
Using the computational domain shown in Figure 5.1, a small droplet (corresponding to $\alpha_l \backsimeq 10^{-4}$) evaporates in a hot stagnant environment. In Figure 5.6 a comparison of the time evolution of the squared droplet diameter is shown between the solution obtained with the Abramzon-Sirignano

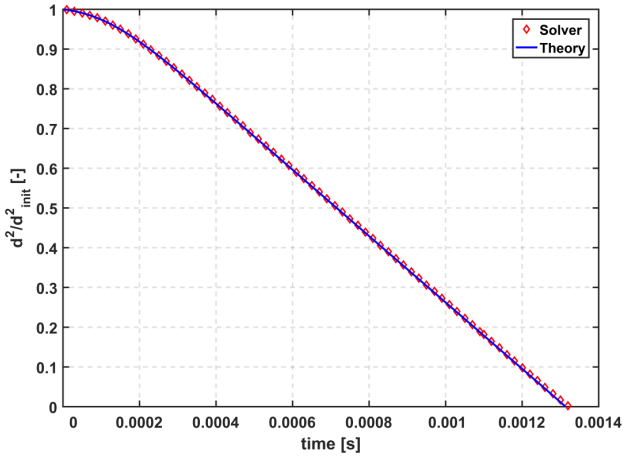

Figure 5.6: Analytical valdation of the code for a single evaporating droplet [182].

theory and calculated using the proposed solver. A fair agreement can be pointed out.

5.5 Validation on the ECN configuration

The diesel injector, studied in the Engine Combustion Network [189], has been chosen for the assessment of the proposed approach for evaporation modelling. In fact, to the best of the author's knowledge, few test articles in the aero-engine context are focused on the near injection region and the attention is normally devoted to the dilute zone.
The apparatus, shown in Figure 5.7, is based on a common rail injection system, which is used to supply fuel to a diesel injector. Several operating conditions have been tested and, in the present set of measurements, the rail pressure ranges from 50 MPa to 150 MPa. The spray is injected into an ambient with a density of 22.8 kg/m^3 (i.e. corresponding to P_{amb} = 6 MPa and T_{amb}= 900 K)[182, 184]. The injector is fuelled with a single component n-dodecane. The nominal diameter of the injector here analysed is 0.084 mm and the interested reader is addressed to [189, 190] for a detailed description of the experimental test article (i.e. referred as *Spray A*).
Since the uncertainties on the injector geometry can have a huge impact

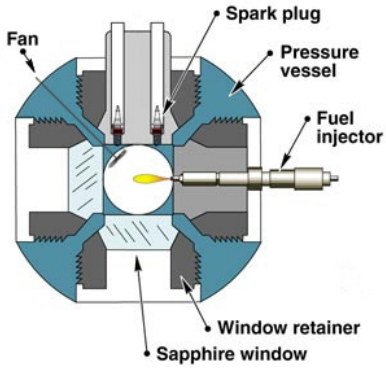

Figure 5.7: Schematic representation of ECN combustion chamber [189].

in this kind of applications [190], each atomizer has been individually characterized by x-ray tomography, x-ray phase-contrast imaging, silicone molding and optical microscopy [190]. The injector here studied, referenced as No. 210677, presents a nozzle smaller than the nominal one, with an area contraction coefficient $C_a = A_{eff}/A_0 = 0.98$. A_eff represents the effective cross-sectional area and A_0 the nominal one.
In terms of boundary conditions, the liquid fuel is injected through the nozzle at 363 K with an inlet velocity varying from 300 m/s to about 600 m/s based on the injection pressure. The injected fuel, thanks to the injection velocity and to the high temperature of the combustion chamber, rapidly breakups and evaporates, even if no combustion happens, because of the non-reactive environment.
Operating conditions are briefly summarized in Table 5.2.
The reference test point for the present work, named hereinafter as *Test point 1*, is identified by an injection pressure of 150 MPa. It is surely the most representative and challenging condition and it has been already widely investigated in technical literature [152, 189]. Two further test points, characterized by an injection pressure of 100 MPa (*Test point 2*) and 50 MPa (*Test point 3*), have been also considered to further assess the capabilities of the proposed approach.
Several experimental data are available on this test case. Mie scattering has been employed to measure the liquid length using a 3% threshold of the maximum intensity. The steady liquid penetration has been also evaluated and it has been obtained by averaging the instantaneous snapshots between 0.5 ms and 1.4 ms [189, 190].

Injector series	210677 - Spray A
Orifice nominal diameter [mm]	0.084
Injected fuel	n-dodecane
Fuel density [kg/m^3]	713
Fuel temperature [K]	363
Mean injection pressure [MPa]	150, 100, 50
Ambient density [kg/m^3]	22.8
Nominal ambient temperature [K]	900
Ambient pressure [MPa]	6.05
Discharge coefficient	0.89
Area contraction coefficient	0.98

Table 5.2: Operating conditions of the simulated configurations [182, 184].

Rayleigh scattering [189, 190] has been instead used to obtain the distributions of mixture fraction. Clearly, considering the non reacting test conditions under investigation, the mixture fraction has been directly measured using locally the vapour and air mass fractions. Instantaneous images have been averaged to compute mean contour plots provided in the ECN database. Data are available starting from 17.85 mm after the injection point until 50 mm downstream.
Hence, the ECN test case is particularly suitable to validate the proposed code since a large region, where α_l tends to one, can be found. On a theoretical point of view, this would constrain E-E or E-L solvers, based on an explicit strategy, to strongly reduce the time step size to avoid a non-physical behaviour of the vaporization source terms. Conversely, the implicit approach should lead to a robust representation of the involved phenomena and the ECN measurements on vapour mass fraction, focused on the near injection region, are surely adequate for its assessment.

5.5.1 Numerical set-up

Simulations have been carried out on the axi-symmetric domain shown in Figure 5.8, representing a 5° sector of the whole domain with 1 element in the azimuthal direction. The axial and radial extensions are smaller than the actual chamber (i.e. 108 mm x 108 mm against 100 mm x 20 mm in present calculations). However, it has been verified that this choice has a negligible impact on simulation results.
Considering that the focus of this part of the work is on evaporation modelling, the injector duct has not been included and the diameter has

been reduced based on the area contraction coefficient (see Table 5.2). Such assumption allows neglecting the cavitation inside the nozzle, which would affect the real velocity profile, and concentrating the study just on the downstream region.
As shown in [150, 151, 152], where the ELSA approach was used to study the liquid/gas interface for the same test case, a mesh sizing counting 10 elements along the injector diameter should be able to properly reproduce the main features of the flow-field as the liquid-air mixing. A structured mesh counting 12500 cells with a size of 0.008 mm at the injector exit has been therefore generated. A further refined mesh with a double number of elements in the injector diameter, has been also tested to assess the effects of the numerical domain. No appreciable effects of the mesh sizing on results have been pointed out.

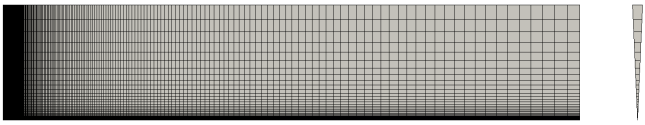

Figure 5.8: Structured grid employed in ECN test case.

Mass flow rate has been imposed at the injector inlet following the available experimental data, whereas a static pressure has been prescribed at the outlet. All the walls have been considered as smooth, non-slip and adiabatic, whereas cyclic conditions have been applied on the two lateral patches (see Figure 5.9). The employed time step ($d\tau$) has been chosen as much as high without compromising the numerical stability. Therefore, $d\tau = 1.5 \times 10^{-8}$ s for Test point 1, while it has been increased to 1.85×10^{-8} s in Test point 2 and to 2.5×10^{-8} s in Test point 3 thanks to the reduced injection velocity.
With regards to turbulence modelling, a standard k-ϵ model has been employed. Following results of previous investigations on the same test case [151, 152], a sensitivity study on the value of the characteristic constant $C_{\epsilon 1}$ has been performed in order to properly reproduce the jet opening angle. Values of 1.44, 1.52 and 1.60 have been considered but for the sake of clarity, such analysis is not reported here. In fact, it has been pointed out that standard values of $C_{\epsilon 1}$ constants are able to properly reproduce vapour jet spreading with an overall good agreement, while the modified ones are not able to catch the lateral turbulent dispersion of the vapour[184]. Both convective and diffusive fluxes have been discretized

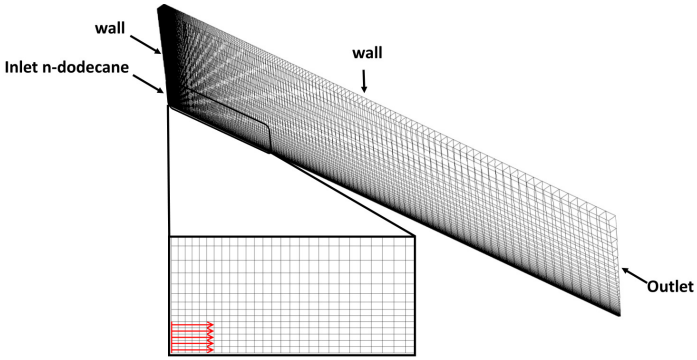

Figure 5.9: Employed computational domain and imposed boundary conditions.

following second order schemes, whereas first order Euler scheme has been employed for time advancement. Further details and sensitivies about the employed numerical setup can be found in [182, 184].
Finally, it should be pointed out that, in the next section, several results, regarding both liquid length and vapour penetration, are discussed. Nevertheless, a unified methodology to determine these parameters in numerical simulations is not available in literature on the chosen test case. A threshold on a certain value of mass or volume fraction is normally used, but no specific guidelines are prescribed in the ECN workshop [189]. In this work $\alpha_l = 0.1\%$ and $\alpha_v = 0.1\%$ have been used to this end as already done in previous works on the same test case [67].

5.5.2 Results and discussion

The validation of the vaporization model starts with the simulation of Test Point 1. Before starting with quantitative comparisons, Figure 5.10 shows velocity and liquid-gas interface density evolutions together with liquid and vapour fraction contours obtained with ELSA on a window of 10 mm x 3 mm after the injector exit. It should be pointed out that it represents the near injection region where the breakup mainly takes place. The liquid jet, due to its high Weber and Reynolds numbers, enters into the chamber and undergoes a quick atomization process, which is highlighted by the zone where the production of Σ is really high. Such violent atomization is mainly related to the growth of instabilities on the liquid surface due to the turbulent interactions with the gas phase.

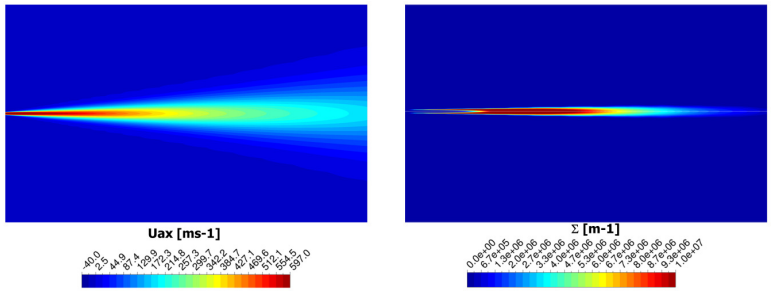

(a)

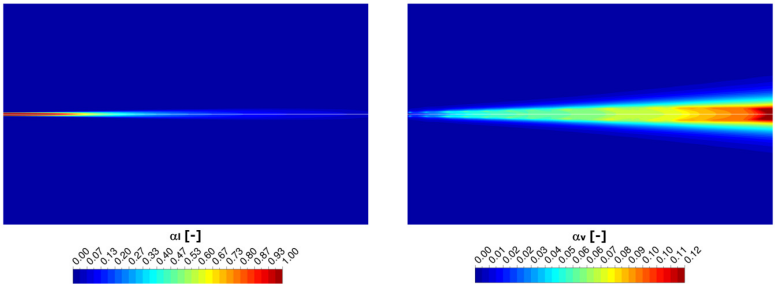

(b)

Figure 5.10: Mixture velocity and liquid/gas interface density distributions (5.10a) together with liquid and vapour fractions evolutions in the dense spray region (5.10b).

However, it is also strongly affected by the heat-up and evaporation of liquid that take place immediately in the near injection region. A liquid core is therefore generated and the spray tends progressively to evaporate producing a region with a non-negligible volume of n-dodecane vapour. It is worth noting that at the end of the selected window, the vapour volume fraction exceeds already the 10% and this can have an important effect in the stabilization mechanism if reacting test conditions would be considered. Furthermore, even in regions where the liquid volume fraction is really high (i.e. $\alpha_l \simeq$0.8-0.9) the code is able to robustly determine a non zero evaporation rate with a consequent production of α_v. In these regions, it is likely that an explicit method would present strong numerical instabilities and under-shootings in gas phase temperature.
To clearly show this limit, the implicit source term of evaporation has

been re-formulated also in an explicit fashion for Equation 5.5. The other aspects of the numerical setup have been retained as in Section 5.5.1. Employing the same time step, in Figure 5.11 the minimum value of the ratio T_g/T_l in the domain is reported for both explicit and implicit approaches [182]. Clearly, the issues shown in Section 5.2 arise again

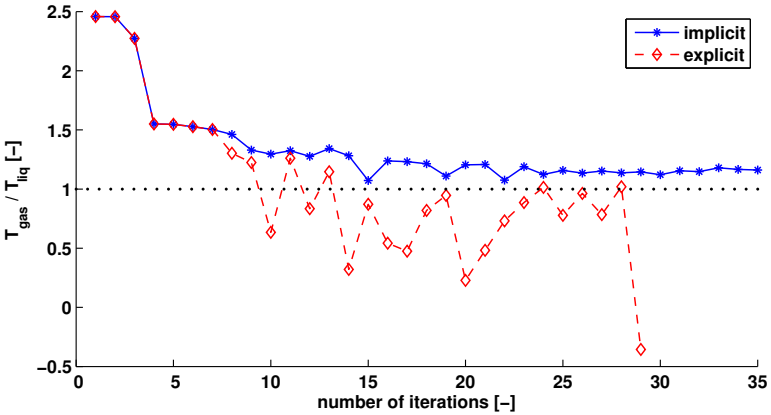

Figure 5.11: Instabilities in gas phase temperature with explicit source term in gas phase temperature [182].

with the explicit methods. A non physical behaviour is predicted and the simulation crashes after few iterations [182]. A robust and stable numerical prediction is instead obtained by using the implicit approach. Going further downstream such dense region, from a quantitative point of view, spray vapour penetration and liquid length evolution are analysed in Figure 5.12 for Test Point 1. Due to the high injection pressure here considered, the vapour penetration grows fast and this is due to the velocity at the injector-exit. The instantaneous vapour penetration is directly linked to the mass flow rate of the atomizer, but it is also the result of two conflicting phenomena: the high velocity, which determines initially the liquid penetration, and the turbulence mixing, which controls the vaporization rate reducing the liquid penetration. All these phenomena are observed experimentally and recovered by the numerical model. A slight under-prediction of vapour penetration can be pointed out and it is probably related to a low momentum exchange between vapour and the surrounding air [184]. Anyway, a reliable prediction is determined considering the RANS approach here employed.

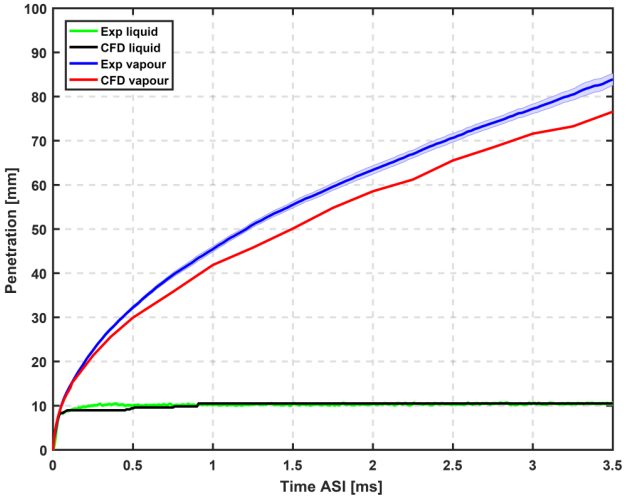

Figure 5.12: Computed and measured liquid and vapour penetration for Test Point 1.

Beyond such good agreement in terms of penetration, mixture fraction distributions, which represent the key point of the present work since they are directly related to the vaporization rate, have been analysed.
Figure 5.13 shows the results obtained for Test point 1 in terms of both axial and radial evolutions. An overall good agreement has been obtained. The shape of profiles is adequately predicted and in particular the centerline curve agrees well with experimental data. Considering the resulting contour plots (see Figure 5.14), vapour concentration seems to be slightly over-predicted mainly in the near axis zone and the difference with experiments tends to decrease going further downstream. At higher axial distances, the effect of turbulence modelling is less pronounced and numerical results properly reproduce the vapour concentration both in terms of axial and radial distributions. Therefore, based on a physical representation of the turbulence flow-field and mixing, the developed code is able to properly predict the local equilibrium state and the final vapour concentration. This has been further verified studying the velocity profiles at increasing distances from the nozzle. However, experimental data in terms of flow-field were not available for the injector under investigation. Therefore, the comparison shown hereinafter was realized using data of the nozzle 210678 (taken from [191]), which was characterized by a hole

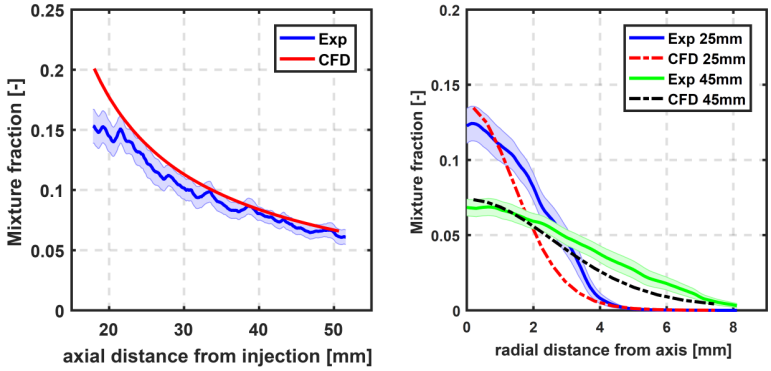

Figure 5.13: Mixture fraction distributions for Test point 1 [182, 184].

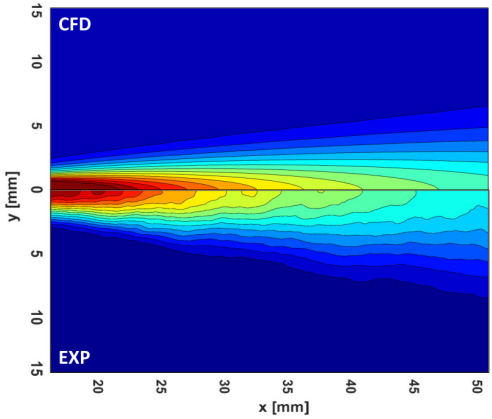

Figure 5.14: Mixture fraction contour comparison for Test point 1 [182, 184].

diameter slightly bigger (i.e. d=83.7 μm for 210677 and d=88.6μm for 210678). Hence, in order to make a proper comparison between experiments and CFD, as already done in [191], in Figure 5.15 radial profiles of axial velocity normalized by the value taken on the axis are plotted at different axial distances using an equivalent diameter as reference length (i.e. $d_{eq} = d\sqrt{\rho_f/\rho_{amb}}$).
It can be pointed out that at axial positions, where the numerical ap-

proach here employed fails in properly reproducing the jet opening angle (i.e. x=$60d_{eq} \cong 30mm$), a low accuracy was reported in the mixture fraction field (see Figure 5.13). Conversely, as soon as the distance from the injector is increased a fair agreement is retrieved both in terms of flow-field and mixture fraction distributions.

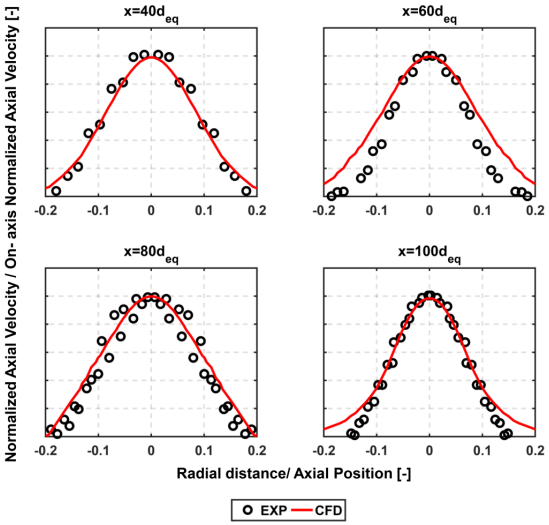

Figure 5.15: Comparison between radial velocity profiles normalized at $40d_{eq}$,$60d_{eq}$,$80d_{eq}$ and $100d_{eq}$ between CFD and experiments.

To reduce the impact of turbulence modelling and to focus the attention just on evaporation modelling, Test case 2, which is characterized by a lower injection pressure and liquid velocity, has been considered. The distribution of vapour mass fraction is now well caught on the axis (Figure 5.16). Thanks to a more consistent representation of the flow-field and of the interactions between gas and liquid phases, mixture fraction profiles mimic well the experimental evolution both in terms of axial profile and radial spreading. Pressure and velocity fields, together with liquid volume fraction, even in RANS framework, are now correctly reproduced and this leads to properly calculate both the equilibrium state as well as the global evaporation rate. This is confirmed by the overall mixture fraction field shown in Figure 5.17. A reliable prediction of vapour distribution can be again pointed out.

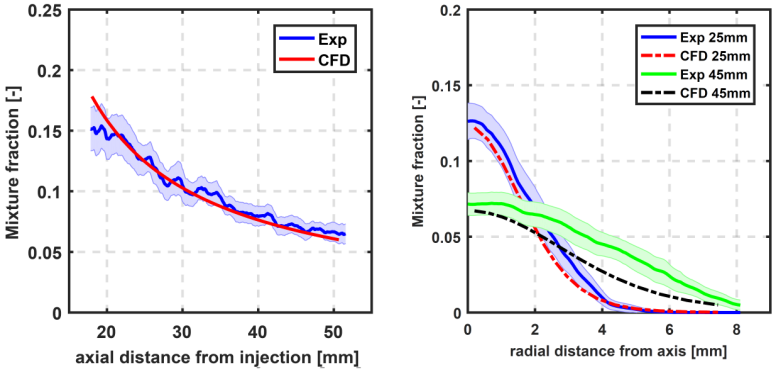

Figure 5.16: Mixture fraction distributions for Test point 2 [182, 184].

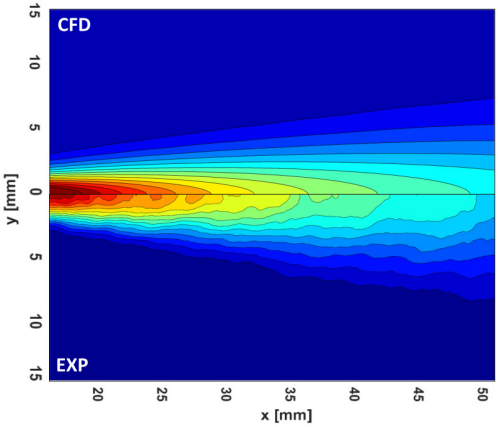

Figure 5.17: Mixture fraction contour comparison for Test point 2 [182, 184].

To further assess the solver capabilities on another operating condition, Test point 3 has been considered and results are shown in Figure 5.18. As reported also for Test point 2, numerical results agree well with experiments, both in terms of centerline and radial distributions. Contours of mixture fraction for experiments and numerical simulations are compared in Figure 5.19. A really accurate prediction of the vapour evolution is

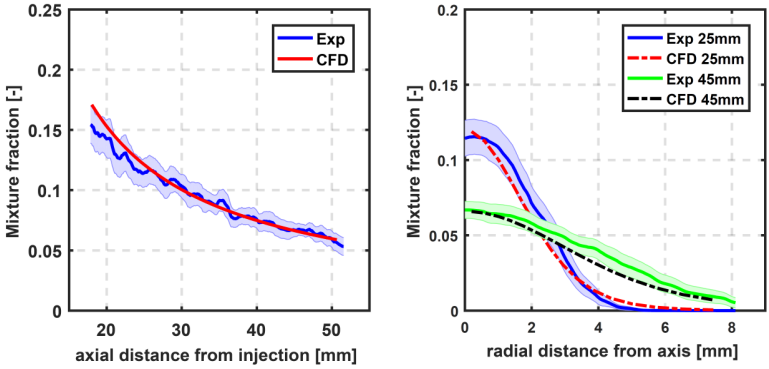

Figure 5.18: Mixture fraction distributions for Test point 3 [182].

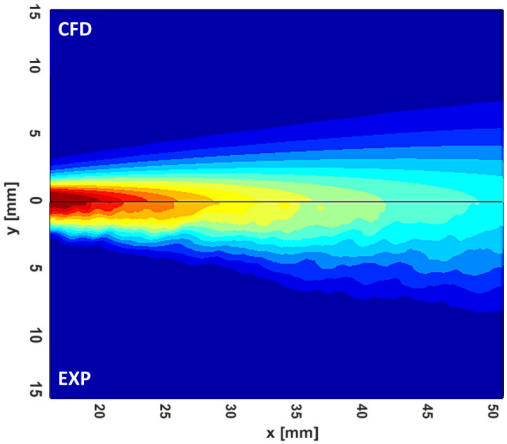

Figure 5.19: Mixture fraction contour comparison for Test point 3 [182].

obtained.

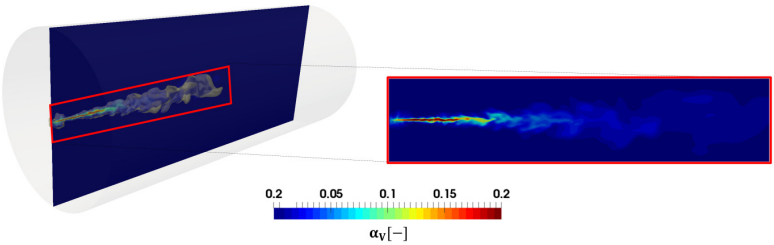

Figure 5.20: Instantaneous evolution of vapour volume fraction for Test Point 1 obtained with LES.

5.6 Concluding remarks

In this chapter, a novel method to deal with evaporation within the ELSA framework has been introduced. The approach, which is based on the formulation of evaporation rates in an implicit manner, has been described with particular attention to the calculation of the equilibrium state of the system. Its main advantages with respect to standard explicit methods have been described and the ECN dataset has been then employed for its assessment.
Three different operating conditions have been tested, comparing vapour distributions and time dependent penetration of the spray tip. Averaged contours of mixture fraction showed a good agreement with experimental data, in particular when a lower injection velocity has been considered. Moreover, a proper description of the near field of the injector has been pointed out, highlighting the characteristics of the evaporation model in dealing with the dense region of the spray. Ultimately, the obtained results assessed the code capabilities in handling evaporation in a robust and reliable manner.
This chapter represents a key step in the development of an approach able to account for all the phenomena going from the near injection region up to a dispersed spray since it represents the link between the liquid phase and the reacting flow-field. The proposition and the assessment of a numerical strategy to deal with evaporation all along the atomization process is a significant step towards an unified description of spray flames. It is worth pointing out that, even if all the calculations reported above have been carried out in a RANS context, the model has been implemented in a general way valid also in LES. Figure 5.20 shows the instantaneous evolution of vapour volume fraction that can be appreciated with a

scale-resolving technique on the full 360° geometry of the ECN case. The calculation has been realized on a coarse mesh (i.e. based on the mesh sizing of RANS calculations) to point out the capabilities of the developed method of working as well in LES. The approach seems reliably representing the unsteady evolution of the jet with an instantaneous peak of α_v higher than in RANS (see Figure 5.10). Further investigations are surely required, even exploring different geometrical configurations, but this chapter clearly represents a robust basis for further investigations.
Finally, it should be pointed out that, although the proposed strategy has been proposed and assessed starting from the Eulerian-Eulerian solver derived from ELSA, it can be easily extended to the QME-VOF approach presented in Chapter 4 since the same set of information about the two-phase flow is available.

Chapter 6

Curvature formulation for ELSA framework

The introduction of a slip velocity between phases proposed so far, together with the inclusion of an evaporation model, leads to the proposition of the QME-VOF approach based on ELSA as a numerical tool able to deal with the most challenging problems related to spray atomization in a unified manner. However, many information are still not included. For instance, a general strategy to manage the switching to the lagrangian framework inside the numerical domain, using the information coming from the Eulerian equations, is missing. The main problem is related to the definition of the Drop Size Distribution (DSD) to be used during the injection step, since the DSD can be only defined once a set of droplets or particles has been already generated

This chapter is devoted to the proposition of a general approach to study the DSD by looking to some further geometrical characteristics of the liquid-gas interface. In particular, the surface curvatures are proposed as variables to deepen the knowledge on spray atomization and to enhance the information available in ELSA. The Surface Curvature Distribution is introduced in this context and its link with the standard DSD is clarified. Then, the capabilities of such method to determine the spray distribution in a general way are assessed using data available from a set of DNS calculations on different geometrical configurations.

6.1 Extension of the concept of Drop Size Distribution

A standard output normally expected from any atomization model or theory, going from DNS studies up to experimental correlations (see Chapter 3) is the Drop Size Distribution (DSD). It surely represents the most significant quantity for engineering applications.
From a theoretical point of view, several definitions of this function can be introduced. Generally, it is $F_N(D)$ in such way that $F_N(D')dD$ is the number of droplet per unit of volume with a diameter D $\in [D', D' + dD[$. In this case, it is the Number Diameter Function (NDF) and it may be also normalized to define a probability density function $P_N(D)$.
The function $F_N(D)$ requires the possibility to count the number of droplets. A separation of the liquid phase in a set of discrete elements is therefore required. However, as widely shown in previous chapters, usual atomization processes start with a continuous liquid flow (for instance a liquid jet or film) and during the atomization a splitting occurs. Once it is created, for fixed external conditions and generally considering the whole spray, the NDF may evolve towards an asymptotic state, for which several theoretical and experimental works have been realized in techinical literature [161]. To address more complex situations or to determine its function in space and time, a transport equation for the DSD, like the Williams Boltzmann Equation (see Chapter 3), can be employed.
Nevertheless, albeit the flow inside the injector, the surface instabilities as well as the methods to solve the WBE have been the subject of several research works in technical literature (see Chapter 3 and references therein), few studies deal with the droplet generation step to estimate the DSD. One reason is the lack of data to justify any proposal, another one is the absence of a definition of the NDF during the primary breakup. In fact, considering a liquid jet before the detachment of a liquid parcel, the notion of a diameter cannot be reasonably introduced.
However, considering an initial instability over a liquid surface, such unsteadiness evolves in time and creates wrinkles at a certain length scale that is somehow related, from a theoretical point of view, to the diameter of the droplet that will be then generated. It is clear that a link between these two subsequent steps is still missing and it represents the key point to determine the droplet distribution.
Regarding the availability of data in this transition zone, lately there have been great progresses both in experimental [192] and in numerical techniques [56].
However, an extended definition of the DSD should be first introduced to

be able to deal with all the stages of atomization from primary breakup up to the final spray. It should be pointed out that the same problem appears in defining a mean diameter: it is a moment of the NDF and therefore it can be defined only once the continuous jet has been broken in a set of liquid droplets. An alternative definition has to be introduced. As widely shown in previous chapters, it is known that the definition of the mean diameter can be replaced by the more general mean surface density Σ, which represents the basis of the ELSA approach described so far. This quantity can be defined everywhere no matter what the liquid phase topology is and, combined with the liquid volume fraction α_l, it gives the SMD once the spray is generated (see Equation 3.25). Recently, Essadki et al. [123] have used high order fractional moments of the DSD for a dispersed spray, where the size is given by the surface area of the droplet, to recover some geometrical characteristics of the interface already used to describe a two-phase system in [193]. These quantities are the volume fraction (α_l), the mean surface density (Σ) and the two averaged Gauss $G = \kappa_1 * \kappa_2$ and mean $H = \frac{\kappa_1+\kappa_2}{2}$ curvatures, where κ_1 and κ_2 are the two principal curvatures of the surface.

To overcome the limits of the DSD in modelling a liquid-gas interface during the whole atomization process, the idea here proposed is therefore the exploitation of some geometrical characteristics of the interface to look at the droplet distribution. In fact, they should carry the information of the DSD that is hidden all along the wrinkling process.

In particular, the proposal is to look at the curvature (κ) distribution. In this case, the distribution of the curvature is $F_S(\kappa)$ and the $F_S(\kappa')d\kappa$ is the area of the surface with a curvature $\kappa \in [\kappa', \kappa' + d\kappa[$. This leads to the definition of a *Surface Curvature Distribution* (SCD).

Considering a 3D object, the curvature is locally defined by two parameters, i.e. κ_1 and κ_2. Thus, the SCD can be expressed as function of a global curvature $\kappa = \kappa_1 + \kappa_2$ or as a multivariate distribution, i.e. $F_S(\kappa_1, \kappa_2)$. However, an accurate description of the interface, subjected to breakup and coalescence events, cannot be restricted just to one geometrical variable as normally carried out for the DSD in a dispersed spray. Both curvatures are required to better characterize different breakup configurations.

Therefore, as already proposed in [194], the Gauss and mean curvatures are here proposed as phase-space variables, leading to the definition of the bi-variate SCD: $F_S(H, G)$.

H and G have been chosen because their interpretation is more straightforward with respect to κ_1 and κ_2, since they assume known values for some asymptotic geometrical shapes of the liquid-gas interface, e.g. $H^2 = G$

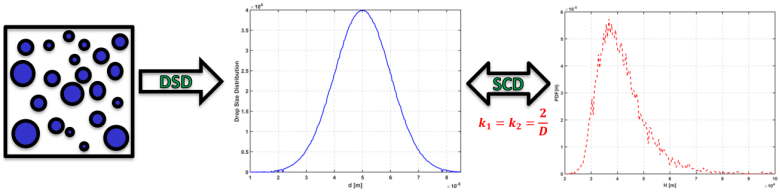

Figure 6.1: Link between the DSD and the SCD for a known cloud of spherical droplets.

for a sphere and $G = 0$ for a cylinder.
The definition of the $F_S(H, G)$ and its general link with the standard number density function is based on a significant property of separated liquid elements, namely the Gauss-Bonnet theorem [194]: considering M as a 3D object, delimited by a surface $\Sigma(M)$, the following relation stands:

$$\int_{x \in \Sigma(M)} G(x) dS(x) = 2\pi\chi(M) \tag{6.1}$$

where S is a part of Σ and $\chi(M)$ is the surface *Euler characteristic* that is equal for any object homeomorph to M.
Such quantity is particularly significant: it is equal to 2 for one sphere and, considering a set of spherical droplets, it can be used to count the number of particles. In fact, for a sphere $\kappa_1 = \kappa_2 = \frac{2}{D}$ and the Gauss curvature can be simply expressed as $G = \frac{4\pi}{S}$, where $S = \pi D^2$ is the droplet surface area. Therefore, for a cloud of n_d spherical droplets, $\chi = n_d GS/(4\pi) = n_d$.
Hence, the two functions $\frac{4\pi}{GF_S(H^2=G,G)}$ and $F_N(D)$ are equivalent, since they count the number of droplets per volume.
In Figure 6.1, the link between the DSD and the curvature distribution is shown in terms of H phase-space for a cloud of droplets with an arbitrary distribution (i.e. a normal distribution with D_{mean}=5e-05 m and σ=1e-05). A continuous link between the two distributions can be introduced and the DSD can be easily recast starting from the corresponding curvature values.
Nonetheless, the SCD is defined all along the atomization process and therefore, once the spray is generated, the DSD is a particular case of $F_S(H, G)$.
Therefore, considering that during primary atomization the liquid-gas interface undergoes different instabilities and deformations, the general idea here proposed is to determine the DSD, which has to be used in

the Eulerian-Lagrangian coupling for ELSA, by studying the interface state that can be described geometrically by the local curvatures. It is worth noting that, to the best of the author's knowledge, this represents a completely innovative modelling idea in the ELSA framework.
When the curvatures reach high values, the liquid breakup mechanism is activated and generates droplets of diameter related to the curvatures of the previous interface state. Hence, the first proposal has been to carry the curvatures by the surface. However, any spray may be characterized also by a volumetric distribution. For a spray, the DSD becomes $F_V(D)$ in such way that $F_V(D')dD$ is the liquid volume fraction of droplets with a diameter $\in [D', D' + dD[$. This volumetric distribution can be also extended to any liquid topology, leading to a volumetric distance function ($V\varphi D$), that can be a second proposal to describe the transport of curvatures. It is defined as $F_V(\varphi)$ in such way that $F_V(\varphi')d\varphi$ is the volume fraction of flow that is at a distance φ from the interface, with $\varphi \in [\varphi', \varphi' + d\varphi[$ (φ is positive in the liquid phase and negative in the gas one). With this definition the following relation stands:
The gas volume fraction is $\alpha_g = \int_{-\infty}^{0} F_V(\varphi)d\varphi$*, the liquid volume fraction is* $\alpha_l = \int_{0}^{+\infty} F_V(\varphi)d\varphi$*, and the mean surface density* $\Sigma = F_V(0)$.
The $V\varphi D$ gives the distribution of the flow with respect to the distance to the interface. The relation with the DSD is not straightforward. However, this distribution can be clearly identified on a given geometric object and in particular for a spherical droplet. A link exists between the volume fraction distribution and curvatures or at least an average curvature of the surface, i.e. $\kappa = dF_V(\varphi)/d\varphi$ at φ=0.
A similar idea to the $V\varphi D$ has been also explored by Dumouchel et al. [195] with the concept of scale distribution, $E_3(d)$. The definition of this function for a given object (for instance a droplet) is based on the total object volume V_0 and the volume $V(d)$ defined by all points at a distance d or greater to the object surface. The scale distribution is given by $E_3(d) = \frac{V_0 - V(d)}{V_0}$. The link between the scale distribution and the $V\varphi D$ can be express readily by $E_3(d) = \frac{F_V(\varphi=d)}{\alpha_l}$. Dumouchel et al. [195] worked on experimental data in 2D and more recently on numerical simulations to extract 3D results about the $E_3(d)$ function. A connection between the scale distribution and curvatures should be as well present.
Finally, the idea here proposed is to characterize the DSD, which is missing in the ELSA approach, when the switch to the lagrangian tracking takes place, by looking at the SCD transported by the $V\varphi D$.
In this chapter, this idea is discussed and its capabilities assessed using

data obtained through DNS on several test cases. The widely documented ARCHER code [145, 146], where a combined VOF-Level Set approach is used to capture the interface and a ghost-fluid method is applied to accurately represent the jump of variable across it, has been employed and it is briefly described in terms of governing equations later on. The Rayleigh-Plateau and droplet-collision test cases are first shown to clearly demonstrate the capabilities of interface curvatures and $V\varphi D$ in describing a basic breakup and collision events. Then, the Homogeneous Isotropic Turbulence (HIT) box is employed to generalize the link between the diameter and curvatures all along the atomization process.

6.2 Governing equations and numerical methods

In the ARCHER code, the joint level set/VOF method is coupled with a projection approach to carry out the Direct Numerical Simulations of incompressible Navier-Stokes equations [145, 146] shown here below. Such approach ensures mass conservation and a good description of the interface topology (see [146] for details).

$$\frac{\partial \boldsymbol{V}}{\partial t} + (\boldsymbol{V}\cdot\nabla)\boldsymbol{V} = -\frac{\nabla P}{\rho} + \frac{1}{\rho}\nabla\cdot(2\mu\boldsymbol{D}) + \boldsymbol{f} + \frac{1}{\rho}\sigma H\delta(G)\boldsymbol{n} \qquad (6.2)$$

where P is the fluid pressure, $\boldsymbol{V}$ is the velocity vector, and $\boldsymbol{D}$ is the viscous deformation tensor. At the interface, the effects of surface tension forces are represented through a Dirac function $\delta(G)$. This work benefits also for the latest improvements in the code: the convective term is solved using the improved Rudman technique presented by Vaudor et al. [131], allowing a better accuracy in the description of high density ratio flows. This method is based on the computation of mass fluxes from VOF, which can be then used to compute the convective term in a conservative formalism. Moreover, the viscous term is now calculated with the approach proposed by Sussman et al. [196], whose advantage is the implicit jump condition of the viscous tensor.

The proposed system of equations is solved in the context of a low Mach number approach using a projection method (for further details see [131]). As previously introduced, the interface is characterized through the distance function (namely the level set function), and jump conditions are extrapolated on few nodes on each side of the liquid-gas surface. The viscosity depends on the sign of the level set function according to each phase (liquid and gas). To finalize the description of the two-phase flow, jump conditions across the interface are taken into account with the Ghost Fluid (GF) method. In the GF approach, ghost cells are defined on each

side of the interface [197]. This prolongs each phase to allow smooth derivatives in the vicinity of the liquid-gas surface.

6.3 Rayleigh-Plateau test case

As a first configuration, the Rayleigh-Plateau instability, where a set of droplets is created from an initial column of liquid, is analysed. Here, the main results are summarized for this configuration and the interested reader can find further information in [198]. A quarter of a cylinder has been here computed and symmetric boundary conditions have been employed in a computational box of $1.5e-4m \times 1.0e-4m \times 1.0e-4m$ length. A mesh sizing of $96 \times 64 \times 64$ elements as in [145] has been chosen. This is a standard test case for the ARCHER code that proved to be able to correctly reproduce the dyspersion analysis diagram on this configuration [145]. The set of liquid and gas properties here selected is reported in Table 6.1.

ρ_l	μ_l	ρ_g	μ_g	σ
1000	$1,0.10^{-3}$	1.0	$1,879.10^{-3}$	$0,072$

Table 6.1: Physical properties of the Rayleigh Plateau instability. S.I. units.

The cylinder has a radius $R = 3.34 \times 10^{-5}m$ and the initial perturbation, essential to observe the instability, has an amplitude of the 10% of the radius of the cylinder and a wavelength of $R = 3.0 \times 10^{-4}m$ (twice the length of the box). The initial conditions have been chosen in order to have a wave number (k) satisfying $kR = 0.7$, which corresponds to the fastest growth mode.
Two methods have been used to extract the curvature distribution on this test case:

- **Method 1**: The first one is based on the distance function (φ) that is part of the numerical procedure in the resolution of the two-phase flow in the ARCHER code. The normal to the surface $\vec{n} = -\frac{\vec{\nabla}\varphi}{|\vec{\nabla}\varphi|}$ is first calculated. Then, the matrix $P = I - \vec{n}\vec{n}^T$ with I the identity matrix, and the Hessian matrix $H_m = \frac{\partial^2\varphi}{\partial x_i \partial x_j}$ are calculated in order to have the matrix $G_m = -\frac{PH_mP}{|\vec{\nabla}\varphi|}$. Finally, the two principal curvatures κ_1 and κ_2 are obtained as $\kappa_1 = \frac{T+\sqrt[2]{2F^2-T^2}}{2}$

and $\kappa_2 = \frac{T - \sqrt[2]{2F^2 - T^2}}{2}$ where T and F are respectilvely the trace and the Frobenius norm of the matrix G_m. The reader interested in a more detailed explanation of such method is addressed to Kindlmann et al. [199]. In this way, curvatures are calculated on the center of the mesh cells and then they are projected on the interface using φ.

- **Method 2**: The second one has been instead developed by Essadki et al. [194], where the gas-liquid interface is discretized with a 2D triangulated mesh using the marching cube algorithm. The curvature is computed at each vertex of the generated mesh through a spatial-averaging process that preserves some topological feature of the liquid-gas surface such as the Gauss-Bonnet formula [200] (see the previous section for further details). The topological features of the interface in computing the droplet number distribution from the bi-variate SCD, while filtering the noise, are in this way ensured.

On the other contrary, results for the $V\varphi D$ have been obtained directly from the distance function. The above two methods to extract the curvature distribution were compared on one time frame of the Rayleigh-Plateau test case, but no significant differences were observed as shown in Figure 6.2. The mean and Gauss curvatures are provided as dimensionless using the radius of the initial cylinder as reference length, whereas for the Gauss curvature the radius squared has been used to this end. Considering that the two approaches behave in a completely consistent manner, hereinafter all results have been obtained using Method 1. In the figure, the parabola represents the spherical shape (i.e. H^2=G) and the dotted black line the cylindrical one (G = 0).

6.3.1 Numerical Results and discussion

To have a deep insight in the evolution of the breakup event, four time frames have been selected and are shown in Figure 6.3. It is possible to see the initial configuration ($t_a = 3.92 \times 10^{-7} s$), the deformation of the cylinder with the generation of the bottle-neck ($t_b = 1.49 \times 10^{-4} s$), the break-up event ($t_c = 1.86 \times 10^{-4} s$) and the final generation of droplets ($t_d = 2.03 \times 10^{-4} s$).
It is significant to analyse the evolution of surface curvatures during this atomization process and each time frame has been individually investigated in order to ease the discussion. The distributions of points on the mean and Gauss curvatures graph, the PDF of distance function and the cumulative of total curvature (i.e. $2H$) are shown for each time frame. In these latter

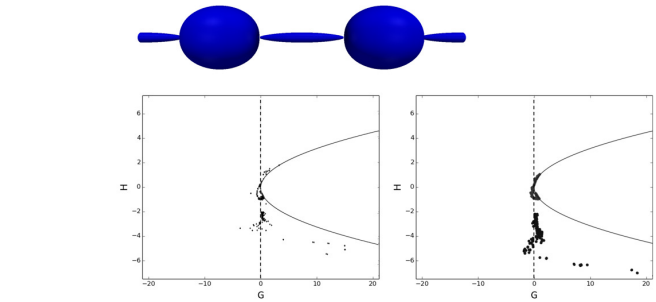

Figure 6.2: Rayleigh Plateau instability at $t = 1,88.10^{-4}$ (top) and mean curvature in function of Gauss curvature with Method 1 (bottom left) and with Method 2 (bottom right).

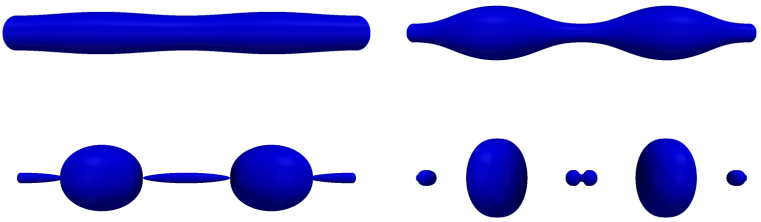

Figure 6.3: Rayleigh Plateau instability at t_a (top left), t_b (top right), t_c (bottom left) and t_d (bottom right).

figures, dx is used as reference length and curves are clipped between $-l_x$ and l_x.

- **Time frame** t_a: As long as the cylinder is weakly deformed, the shape of the PDF(φ) is very close to the one of a cylinder with a linear curve inside the liquid part (see Figure 6.4). In the image, line with markers represents the initial cumulative profile for a cylinder, whereas the dashed line separates the liquid (positive values) from the gas (negative values) side. For the cumulative of total curvature, a step profile at values corresponding to this cylinder has been obtained. Instead, in the H-G graph, all the points are gathered around the vertical line at G=0 (i.e. a cylindrical shape).

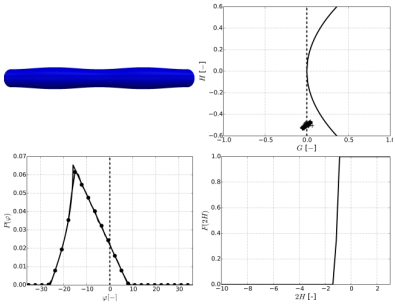

Figure 6.4: H-G plot, PDF(φ) and cumulative of 2H for time t_a.

- **Time frame** t_b: Now the cylinder is deformed and negative values for total curvature appear and are related to all the saddle points generated in the middle (see Figure 6.5). This portion of the cylinder is visible also on the mean and Gauss curvatures graph with the corresponding points that create an arc. Besides, on this graph, the points, which represent the big part of the cylinder, get closer to the parabola representing the spherical shape.

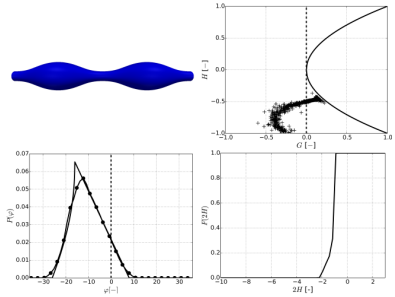

Figure 6.5: H-G plot, PDF(φ) and cumulative of 2H for time t_b.

- **Time frame** t_c: The break-up takes place and the arc described at time t_b is divided in two clouds of points with one set located on the black curve (see Figure 6.6). These points correspond to the big droplet predicted by numerical calculations. Indeed, the mean curvature is approximately 0.5 and the Gauss curvature about 0.25 that are related to a radius twice as big as the initial jet radius.

The other points, located below the parabola, represent the small ellipsoid generated in the middle. The big droplet appears also as a step on the total curvature cumulative and the small ellipsoid by all the high negative values. Such break-up process is clearly evident as well on the H-G plot since small variations on the interface geometry can lead to significant changes in the curvature values.

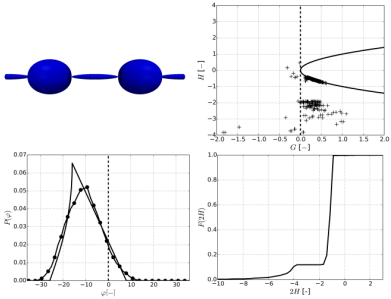

Figure 6.6: H-G plot, PDF(φ) and cumulative of 2H for time t_c.

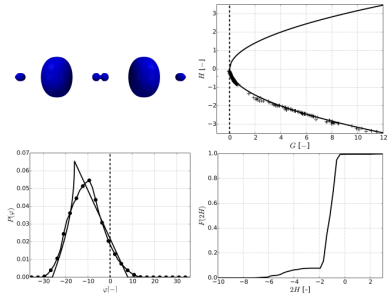

Figure 6.7: H-G plot, PDF(φ) and cumulative of 2H for time t_d.

- **Time frame** t_d: This represents the last configuration with a set of spherical droplet finally generated. On the mean and Gauss curvatures graph, most of the points are on the parabola corresponding to the spherical shape. Points related to the big droplet are located approximately at the same place as the previous time, while points determined by the small droplet are those having higher curvatures

(see Figure 6.7). The PDF(φ) becomes now parabolic in the liquid part, as expected for spheres, with higher values of the distance function because the generated droplet is bigger than the initial cylinder.

Hence, the analysis of the evolution of Gauss and mean curvatures can be reliably employed to describe a breakup event from a liquid jet to the final droplet suggesting that their evolution all along the atomization process can be characterized.

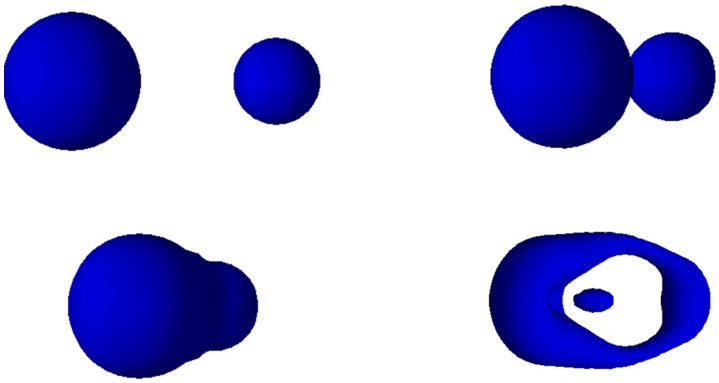

Figure 6.8: Top left : Surface evolution for droplet collision test case at t_a (top left), t_b (top right), t_c (bottom left) and t_d (bottom right).

The capabilities of such geometrical surface properties have been also tested for a collision test case, which represents another fundamental step in the deformation of a liquid surface. The ARCHER code has been already widely validated also on this configuration [126]. Here, a configuration with two spherical water droplets of initial radius of 100 μm, characterized by an impact factor I=0.35, a relative velocity $V_{coll} = 3.42 m/s$, a Weber liquid number $We_l = 33.5$ and an Ohnesorge of $Oh = 0.015$ has been considered.
In Figure 6.8 the resulting evolution of the liquid surface on four time frames is shown, where it is possible to recognize the initial configuration ($t_a = 2.97 \times 10^{-5} s$), the moment of coalescence ($t_b = 7.2 \times 10^{-5} s$), the generation of one deformed droplet ($t_c = 9.9 \times 10^{-5} s$) and its subsequent breakup with the generation of a torus structure ($t_d = 4.3562 \times 10^{-4} s$). In Figure 6.9 the corresponding evolution on the H-G plane is reported,

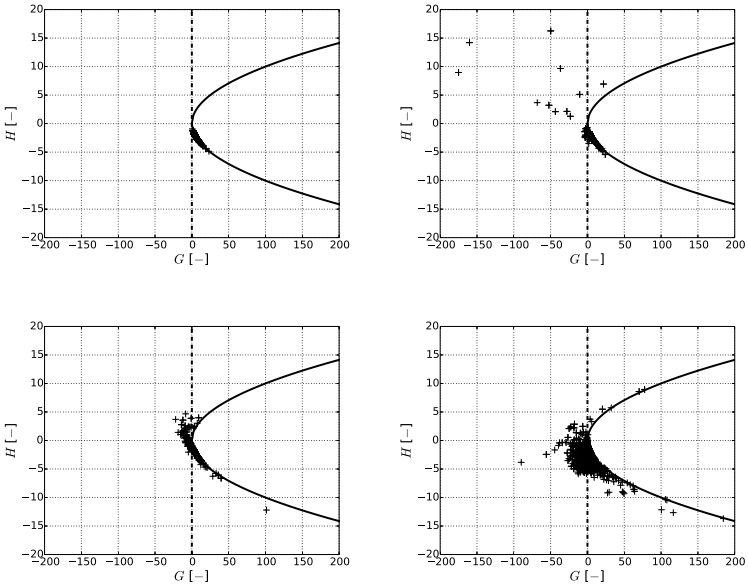

Figure 6.9: Mean curvature in function of Gauss curvature (Top left : at t_a ; Top right : at t_b ; Bottom left : at t_c ; Bottom right : at t_d)(solid line represents $\kappa_1 = \kappa_2$ so a sphere and the dashed line represents $G = 0$ so a cylinder).

where it can be pointed out that, similarly to the Rayleigh-Plateau test case, the curvatures evolve consistently with the investigated physical process.
Considering this preliminary assessment on fundamental test cases, in the next section, the same surface geometrical properties are employed to analyse a Homogeneous Isotropic Turbulence (HIT) box where breakup and coalescence events appear together due to the turbulence forcing.

6.4 Homogeneous Isotropic Turbulence Box

A further assessment and exploitation of the procedure regarding curvature extraction has been performed using a three dimensional cubical domain with periodic boundaries similar to the investigation of Duret

ρ_l/ρ_g	σ	μ_g	μ_l	k	L
30	0.0135	1.879e-05	5.65e-04	3.6	1.5e-04

Table 6.2: Properties for DNS simulations of HIT (S.I. units).

et al. [140, 201]. This configuration represents an extension of single phase mixing studies to two phase flow and it has been already analysed to improve the understanding of primary atomization (see [140, 201]).
The mesh resolution used in the present investigation is based on previous studies on the same test article and on single-phase flow simulations to correctly capture the Kolomogorov length scale [140, 201]. In [140], two mesh sizing are compared and here the fine computational domain counting $256 \times 256 \times 256$ mesh elements has been employed. The validation of this set-up for single-phase simulation is not here shown for the sake of clarity. The interested reader is addressed to [201], where this topic is discussed in detail.
In order to define a configuration with realistic interactions between the liquid surface and the turbulent gas flow-field, the following dimensionless parameters have been selected (i.e. coherently with [140]): gaseous Weber number $We_g = \rho_g \bar{k} L/\sigma = 1$, liquid Weber number $We_l = \rho_l \bar{k} L/\sigma = 30$, liquid based Reynolds number $Re_l = \sqrt{k} L/\nu_l = 310$ and liquid Ohnesorge number $Oh_l = \sqrt{We_l}/Re_l = 1.77e-02$, where $\bar{k}$ is the mean kinetic energy, σ the surface tension, ν the kinematic viscosity in liquid or gas phase, ρ the density and L is the length of the box. In Table 6.2 the corresponding set of physical properties is reported.
Several values of the liquid volume fraction inside the box have been studied for curvature extraction (i.e. ranging from 1% to 90%) in order to mimic the whole atomization process as shown in Figure 6.10.
Here, the main aim is the extraction of curvatures behaviour all along the jet evolution in order to point out firstly the link between the DSD and the $F_S(H, G)$ and also how curvatures evolve from the dense region up to the dispersed spray (i.e. reducing α_l).

6.4.1 Numerical Results and discussion

Results obtained for the HIT varying α_l are presented starting from the 1% test case, which can be reliably considered as representative of the diluted spray region. A snapshot of the liquid-gas interface distribution together with the evolution in time of $\bar{\Sigma}$ and $\bar{H}$, which represent the volume averaged for the whole domain of the liquid-gas interface and

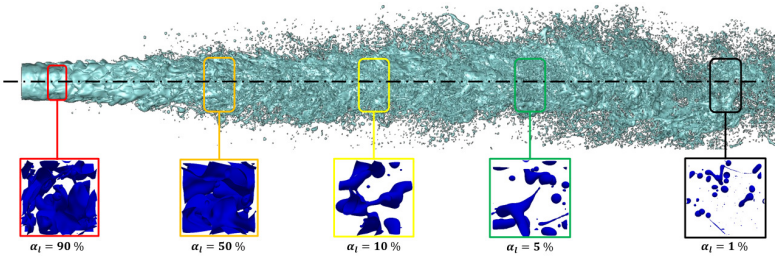

Figure 6.10: Regions considered for the extraction of curvature distribution all along the atomization process.

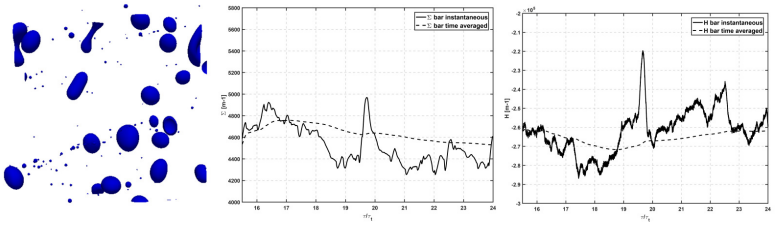

Figure 6.11: Visualization of liquid-gas interface for liquid volume fraction of 1%, together with time evolution of $\bar{\Sigma}$ and $\bar{H}$.

mean curvature, as well as their time-averaged values is reported in Figure 6.11. Hereinafter, τ^* is the time normalized by the turbulent time scale of the box, i.e. $\tau_t = \frac{\kappa}{\epsilon}$. It is possible to point out the augmentation and reduction of $\bar{\Sigma}$ in time related to breakup or coalescence events as well as the generation of a cloud of nearly spherical droplets from the instantaneous time frame.

The characteristic sizing of the generated liquid structures covers a wide range of diameters: big droplets, which carry the major part of the total mass, can be identified and from their turbulent collisions smaller particles are generated. Clearly, with respect to the Rayleigh-Plateau test case, the representation of the breakup process is here much more complex due to the local appearance of different values of the surface curvatures. Several nearly spherical droplets are generated together with some liquid structures characterized by high negative Gauss curvature values, leading to a non-straightforward discussion of physical phenomena on the H-G graph used in the previous section.

Therefore, in order to have a deeper insight into the evolution of surface characteristics in this test case, some statistical properties of H and G have been analysed.
In particular, in Figure 6.12 the time-averaged PDF of the mean curvature is shown. Such time-averaged distribution has been obtained by dividing the H-space in a user-defined number of classes and by collecting during the calculation the area of the liquid-gas interface associated to each class of H. Such procedure has been gathered for nearly 15 τ^* in order to reduce the statistical noise and to obtain a time-averaged distribution. Black dashed lines represent the mesh sizing, which can be considered as a numerical limit in the curvature calculation. A similar evolution has been obtained also for the PDF(G), which is not shown here for the sake of clarity.

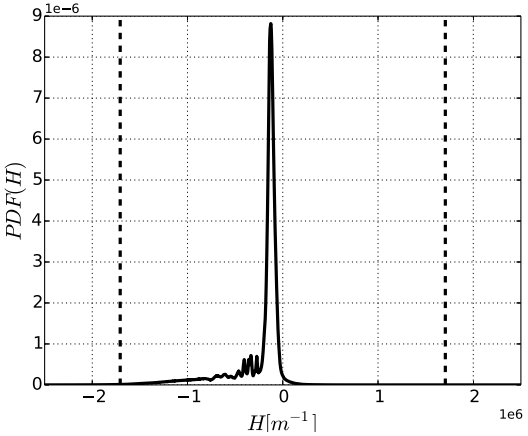

Figure 6.12: Time averaged PDF of mean curvature.

The peak of PDF(H) is located at negative values since a diluted spray is here considered, whereas the probability to have gas bubbles (i.e. $H > 0$) is negligible. Starting from such distribution, much more information about the evolution of the liquid-gas interface can be now extracted. For instance, the spray NDF can be now derived, associating to each curvature class (H_i) the corresponding number of spherical droplets ($N_{d.i}$) characterized by the class amount of liquid-gas surface (A_i) collected

during the calculation:

$$N_{d,i} = \frac{A_i}{4\pi(H_i)^{-2}} \tag{6.3}$$

This clearly represents an abrupt approximation since each curvature class is associated to the corresponding spherical shape, but it highlights a direct link between curvature distributions and the NDF. Using this formulation, it has been possible to extract the NDF and the Volume based Drop size Distribution (VDD) shown in Figure 6.13. The reader interested in the theoretical link between the NDF and the VDD is addressed to references [161, 162], where this topic is discussed in detail.

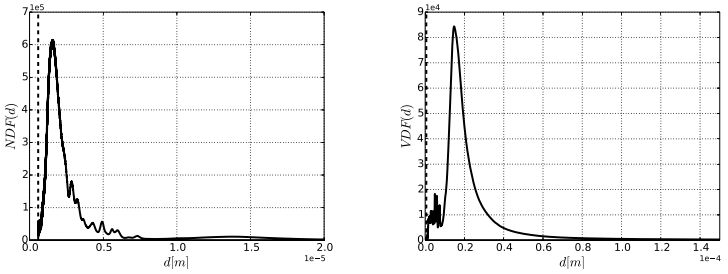

Figure 6.13: Extraction of NDF and VDF from PDF(H). Dashed lines represent dx.

A double peaked NDF is obtained from numerical calculations. It is representative of the generation of a huge number of nearly spherical droplets together with few ligaments, which bring the major part of the liquid volume. These small particles are generated through collisional events, which are enhanced by the turbulent liquid-gas interactions. The turbulence, acting on the liquid surface, increases the probability of collisions and determines the final spreading of the size distribution.
Log-normal probability distributions have been then calculated to fit the DNS data: first, two separate PDFs have been derived, i.e. PDF_1 for the diameter class 1×10^{-8}<d[m]<1×10^{-5} and PDF_2 for 1×10^{-5}<d[m]<1.5×10^{-4}. Thus, the complete probability distribution, expressed as $PDF_{tot} = V_1PDF_1 + V_2PDF_2$, where V_1 and V_2 represent the liquid volume associated to each class, has been obtained and it is shown in Figure 6.14. It is worth noting that V_1 represents nearly the 5% of the total liquid vol-

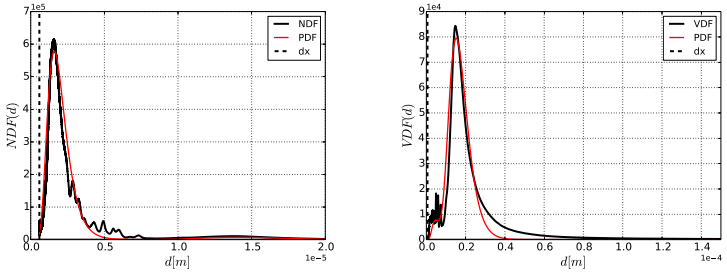

Figure 6.14: Extraction of NDF and VDF from the PDF(H). Dashed lines represent dx.

ume, showing that, even for such low value of liquid volume fraction, the contribution of collisions is not at all negligible. The resulting log-normal PDF_{tot}, both in terms of NDF or VDD, reliably agrees with DNS data as probably verified for other PDF shapes available for a dispersed spray. Hence, starting from the H-PDF it has been possible to derive a NDF that is consistent with a standard drop-size distribution in the diluted regime like the log-normal one. Furthermore, it is worth pointing out that the mean value calculated for PDF_{tot} is coherent with the characteristic Sauter Mean Diameter (SMD) of the box calculated as $SMD = 6\alpha_l/\Sigma$. Such evidence enforces the idea that curvatures PDF can be reliably used to characterize the spray distribution both in terms of mean value and dispersion.

This comparison clearly shows that, in a test article nearly representative for a diluted spray (i.e. α_l= 1%), a direct link between the spray NDF and the curvature evolution can be determined.

However, beyond the characterization of the spray distribution, such DNS analysis can also bring further information about the curvature evolution, which can be useful to better understand the topology of the liquid-gas interface under investigation as well as give some hints about the curvature modelling. In particular, in Figure 6.15 the time-averaged joined PDF(H,G) is shown together with the time-averaged joined PDF of the two principal curvatures (k_1,k_2). The red lines represent the spherical shape (i.e. $H^2 = G$ and $k_1 = k_2$), whereas the dotted one specifies a cylindrical topology (i.e. $G = 0$). The super-imposed blue lines represent instead different iso-values of the PDF(k_1, k_2). It is possible to extract several significant information about the evolution of the liquid-gas interface

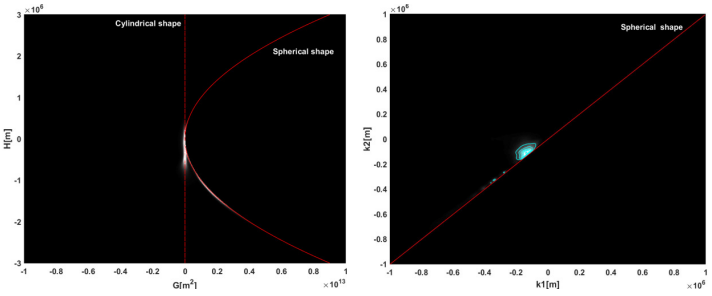

Figure 6.15: Joined PDF of the surface curvatures for $\alpha_1 = 1\%$: on the left the joined PDF(H,G) and on the right the PDF(k_1,k_2).

looking at such joined PDF distributions of surface curvatures:

- the PDF(H,G) shows that the topology of the liquid surface is mainly stretched along two directions, i.e. several points are collapsed on the parabola representative of the spherical shape and in a similar manner also the cylindrical asymptotic limit appears. Such bi-modal topological distribution derives from the presence of big cylindrical ligaments which, subjected on the action of the turbulence field, collide and generate a cloud of spherical droplets.

- the PDF(k_1, k_2) gives similar information in terms of time-averaged properties with respect to the PDF(H,G), but, looking now at the contour iso-lines, it should be pointed out that the most probable value of the two principal curvatures is not at all associated to a spherical shape (i.e. it is not collapsed on the $k_1 = k_2$ line).

Hence, the joined PDFs may give an idea about the topological evolution of the two phase flow together with some suggestions about the generated spray population. Considering these results, together with data already presented on the Rayleigh-Plateau test case, the capabilities of surface curvatures in describing the liquid breakup as well as its direct link with the NDF have been clarified.
Therefore, higher values of liquid volume fraction have been then investigated in order to understand how the curvatures PDFs evolve and if it is possible to determine a general behaviour all along the atomization process.
In Figure 6.16 the liquid-gas interface distribution together with the time-averaged PDF(H) is shown for $\alpha_l = 5\%$. Clearly, much more ligaments are generated now due to the augmentation of the liquid volume inside the

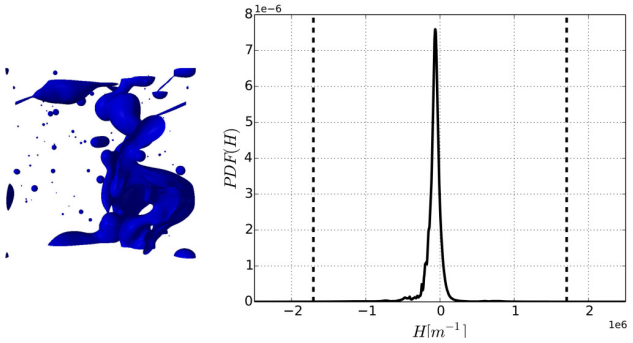

Figure 6.16: Visualization of liquid-gas interface for liquid volume fraction of 5%, together with time averaged PDF(H).

box with respect to the previous case: elongated and stretched cylindrical elements appear and from their turbulent breakup some spherical droplets are produced. The PDF(H) shows here an evolution in line with Figure 6.12 with a mode value shifted towards positive values of H. Now, the probability of finding H $>$ 0 is not negligible and this is linked to the presence of regions where gas bubbles are surrounded by the liquid phase leading to an opposite sign of curvatures.
In Figure 6.17 the joined PDF(H,G) and PDF(k_1, k_2) are reported for the 5% test article. Considering the PDF(H,G), with respect to Figure 6.15 less points tends now to collapse along the parabola and the probability peak is strongly stretched along the line at G=0. This is again representative of the topological variation in the liquid shape from a sphere to a deformed and elongated cylinder, while increasing the liquid volume fraction. In a similar fashion, looking at the PDF(k_1, k_2) the distribution is no more just collapsed on the spherical topology, but tends to be straightened also along the k_2=0 line. The PDF peak moves further away from the spherical asymptote with respect to the previous test point. Increasing further the liquid volume fraction, as shown in Figure 6.18 from the instantaneous snapshots of $\alpha_l = 10\%$ up to 90%, a huge number of continuous liquid structures appear and a set of bubbles is at the end generated for the very dense case. The time-averaged PDF(H) as well as the joined PDF(H,G) and PDF(k_1, k_2) are shown respectively in Figures 6.19 and 6.20.
Several considerations can be derived from these contour plots. For $\alpha_l = 10\%$, several pockets of gas are surrounded by continuous liquid

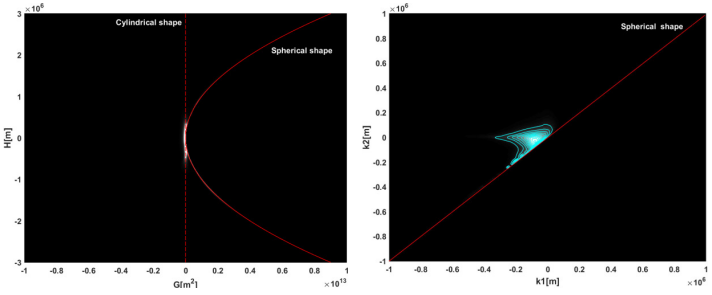

Figure 6.17: Joined PDF of the surface curvatures for $\alpha_l = 5\%$: on the left the joined PDF(H,G) and on the right the PDF(k_1,k_2).

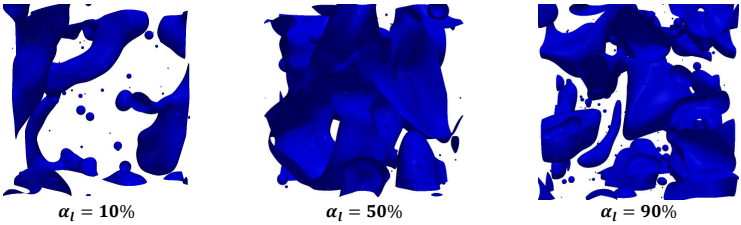

Figure 6.18: Visualization of liquid-gas interface for liquid volume fraction for $\alpha_l = 10\%$,$\alpha_l = 50\%$,$\alpha_l = 90\%$ from left to right.

structures and indeed, with respect to previous cases, now the probability of having H>0 is much higher. However, the queue is still stretched in the droplet direction.
The probability distribution of the mean curvature has a similar shape with respect to Figure 6.12 with the mode value that is shifted towards higher H-values. The topology of the interface is now strongly modified and the PDF(H,G) points out a leading cylindrical shape together with two clouds of points collapsed on the red parabola. They represents the generation of a set of bubbles and droplets nearly spherical. In terms of principal curvatures, the peak is further moved from the $k_1 = k_2$ limit, even if a significant stretch along the spherical line can be still pointed out.
As soon as the liquid volume fraction is further augmented (i.e. $\alpha_l = 50\%$), points characterized by a positive mean curvature disappear since the probability of having some isolated droplets is now negligible. The im-

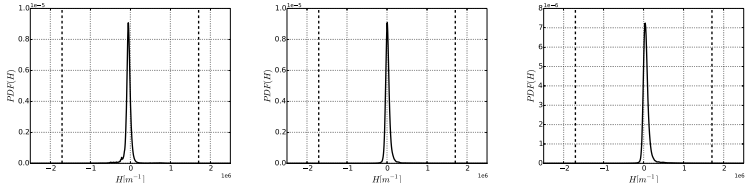

Figure 6.19: Time averaged PDF of mean curvature for $\alpha_l = 10\%$,$\alpha_l = 50\%$,$\alpha_l = 90\%$ from left to rigth.

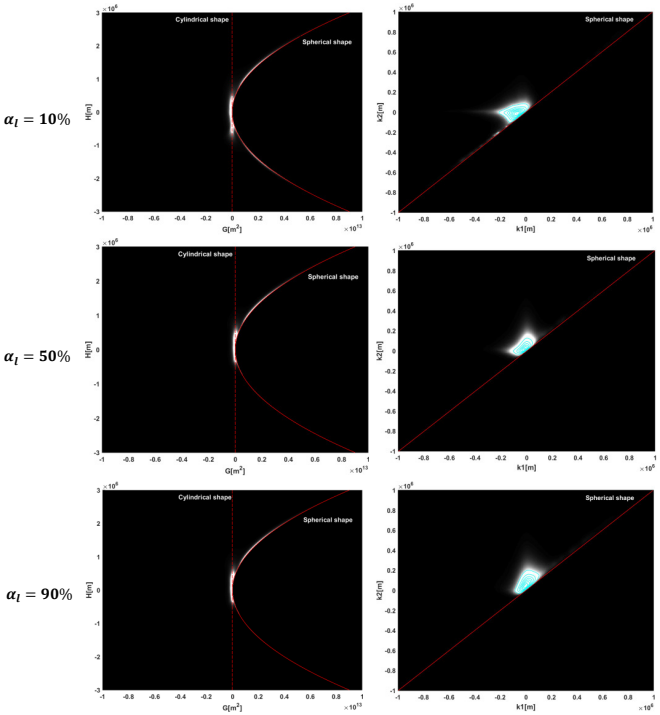

Figure 6.20: Time averaged joined PDF(H,G) (left) and PDF(κ_1,κ_2) (right) for $\alpha_l = 10\%$ up to $\alpha_l = 90\%$.

posed level of turbulent kinetic energy is not high enough to disrupt the

ligaments and the liquid-gas interface preserves its continuity. The gas phase is trapped inside these structures and on the H-G contour plot a huge amount of bubbles collapses on the spherical topology. Coherently, the principal curvatures change their sign. Finally, at $\alpha_l = 90\%$ the characteristic values of H and G are higher (i.e. bubbles with a smaller radius), the PDF(k_1,k_2) changes completely its orientation and the system is stretched on the positive principal curvatures direction. The HIT now behaves in terms of topology in a complementary manner with respect to the 10% case as shown also by the time-averaged PDF(H), where the peak is further stretched on the right because of the generated smaller bubbles.
By comparing all the results shown so far, it should be pointed out that the curvature evolution is completely consistent with the observed physical phenomena. Both the PFD(H) and the joined curvature probability distributions evolve all along the atomization process maintaining the same shape and moving the peak of the distribution from negative to positive values.
Moreover, as far as the spray becomes diluted, a link between the curvature evolution and a standard DSD is directly available. This surely represents a novel and general framework to study the atomization process and the obtained mathematical shape of the PDF(H) is particularly promising having in mind the introduction of such characteristics of the liquid-gas interface in the ELSA context.
So far, only the topology of the interface has been explored. The non symmetric behaviour of the positive/negative curvature statistics has been discussed considering the different values of liquid volume fraction and the difference of density of each phase. It is worth mentioning that in the present numerical simulations the level of turbulence is sustained by a forcing procedure that is not able to distinguish between phases. Accordingly, it is first expected that the turbulence characteristics are identical everywhere. However, due to the inertia and surface tension forces, the turbulence should be affected by the presence of the interface. In order to have a deeper insight in the achieved evolution of the surface curvatures and to better understand the impact of the liquid-gas interface, an analysis of the characteristics of the turbulence field is reported in the next section.

6.4.2 Effect of liquid-gas interface on turbulence

The goal of this last section is to to make a link between the curvature PDFs and the turbulence field. Here, some results are briefly summarized and the reader interested in further data is addressed to Annex-B.

It is worth pointing out that this represents a preliminary work on this topic and further investigations are required following the guidelines presented hereinafter. Indeed, several limitations of the present analysis should be highlighted: first, the Reynolds number of the proposed DNS simulations is not high enough to reach the asymptotic regime of infinite Reynolds. Furthermore, the forcing procedure here employed plays certainly a significant role on the obtained results. However, it is mandatory to reach an equilibrium state between the interface and turbulence, since, plugging directly on the interface, a non-physical stretching in the normal direction to the liquid surface would be generated. Moreover, the low Reynolds number does not allow to let the turbulence freely decreasing without any forcing, since all the turbulent structures would be rapidly dissipated. Further investigations are required on this point, verifying the obtained results with different forcing procedures.
Here, the main purpose is to show that the interface affects the turbulence on both liquid and gas sides in a non-symmetric manner.
In order to extract the effect of the liquid-gas interface on the turbulence field, second order structure function of velocity (S_2) has been studied for the case of $\alpha_l = 10\%$.
It is defined as $\overline{(u - u(r))^2}$ where u and $u(r)$ are the velocities at two points separated by a distance r. This quantity has been extracted using a set of 180 time steps, corresponding to approximately 5 τ^*, to ensure a proper statistical convergence.
Considering that the turbulence is homogeneous and isotropic in the HIT, to avoid too costly calculations in terms of time and memory, the structure function has been extracted only along one space direction (i.e. no transverse velocity has been analysed). In order to determine the effect of liquid-gas interface on turbulence, different configurations based on the distance function φ have been extracted. In the following figures, curves are normalized using $2\overline{u'^2}$ as reference, which corresponds to the theoretical limit when the velocities in the two selected points are totally uncorrelated (i.e $r \to \infty$).
In Figure 6.21 the second order structure function is shown. The r^2 curve has been also reported because S_2 should follow this asymptotic line for the smaller scales (i.e. where the dissipation of turbulence kinetic energy takes place). At these scales, a significant decorrelation can be observed for the elements close to the surface in the gas part. Conversely, far from the surface (i.e. $\varphi > 20dx$), such structure function follows the r^2-law suggesting that the energy dissipation occurs at bigger scales far from the interface. Further information about the evolution of S2 in the gas side can be found in Annex-B.

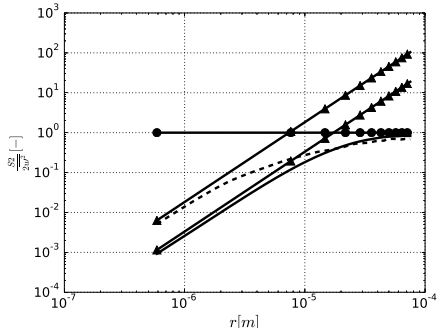

Figure 6.21: Second order structure function $S2$ in gas part. The dashed line represents $S2$ for $\varphi \in [0;4]dx$; the solid curve represents $S2$ for $\varphi > 20dx$; curves with ▲ represent the r^2 law ; the curve with ● represents the theoretical limit when $r \to \infty$.

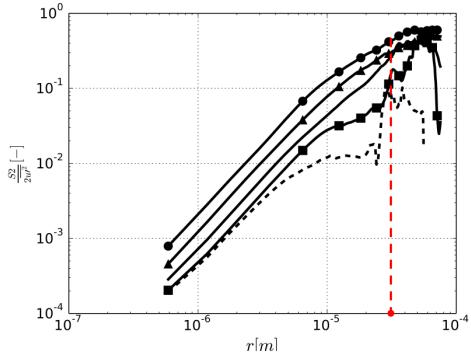

Figure 6.22: Second order structure function $S2$ in liquid part. The curve with ● represents $S2$ for $\varphi \in [0;5]dx$; the curve with ▲ represents $S2$ for $\varphi \in [5;10]dx$; solid curve represents $S2$ for $\varphi \in [10;15]dx$; the curve with ■ represents $S2$ for $\varphi \in [15;20]dx$; the dashed curve represents $S2$ for $\varphi \in [20;25]dx$)

Conversely, in Figure 6.22 the evolution of the structure function in the liquid phase is shown. Even if the statistical convergence is not completely ensured, a peak appears at a certain distance r (see the red curve), which

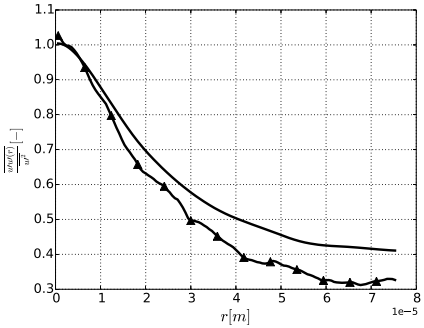

Figure 6.23: Autocorrelation function R_{uu} in gas part. The solid curve represents R_{uu} for $\varphi > 20dx$; the curve with ▲ represents R_{uu} for $\varphi \in [0; 4]dx$.

corresponds to the diameter of a droplet whose volume is the most probable according to the PDF(H) shown in Figure 6.19.
This observation highlights a possible link between the curvature evolution and the turbulence field: the scale where the turbulence acts in the liquid side (i.e. the auto-correlation function takes its maximum) corresponds to the mode value of H. This suggests an energy balance between the contribution transferred from the gas phase to the liquid and the answer of the liquid/gas interface in terms of curvature. Furthermore, it clearly shows that the liquid/gas interface has an impact on the turbulence field and that it can be related to the surface curvatures.
In order to complete this analysis, autocorrelation function R_{uu} was studied close and far from the interface. In Figure 6.23, the curves are normalized by their own values of $\overline{u'^2}$ ($\overline{u'^2} = 1.746m^2s^{-2}$ for $\varphi \in [0; 4]dx$ and $\overline{u'^2} = 2.363m^2s^{-2}$ for $\varphi > 20dx$) in order to compare the two shapes. Even if the zero value is not reached for great distance r, a faster decorrelation can be observed close to the surface (i.e. smaller area under the curve). This indicates a lower integral scale of turbulence as far as the distance from the interface is reduced, suggesting once again an impact of the interface on the turbulence field.
In the light of these results, some preliminary guidelines to relate the turbulence with the interface and to give some hints about curvature modelling can be introduced.
In particular, based on Figure 6.22, a completely novel definition of the

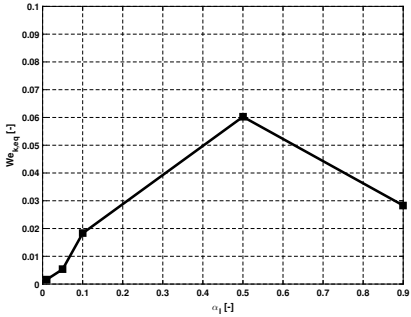

Figure 6.24: Evolution of $We_{k,eq}$ in the analysed HIT configurations.

equilibrium Weber number based on surface curvatures is proposed:

$$We_{k,eq}{}^{*} = 0.5 \frac{(\rho_l + \rho_g)\,\alpha_l\,(1-\alpha_l)\,k\bar{H}^{*}}{\sigma \bar{G}^{*}} \tag{6.4}$$

where $\bar{H}^{*}$ and $\bar{G}^{*}$ represent the equilibrium values of mean and Gauss curvature. This extended Weber number is defined everywhere (i.e. both in the dense and dispersed spray regions) and its mathematical proposal is similar to what has been already done for the liquid-gas interface by Duret et al. [140] (see Section 3.4.1). The idea arose considering that, locally, the turbulence acts on a length scale that corresponds to the deformation of the surface as given by the mean curvature. Such forcing is balanced by the effects of surface tension and this second contribution is proportional to the available liquid surface (i.e. related to G). Clearly, Equation 6.4 represents a first expression of such quantity that can be used as a starting point for further activities in the same framework.
The evolution of this Weber number in the analysed cases is shown in Figure 6.24, where for H^{*} and G^{*} values assumed at the end of the averaging window have here been used. It is interesting to notice that, at least in the investigated configurations, values of $We_{k,eq}{}^{*}$ are gathered in a reduced range with respect to previous studies on Weber number [140]. It is not possible to define, using the numerical data available up to now, a reliable value for this quantity. As proposed in [140], other cases varying the surface tension with respect to the reference here employed should be indeed investigated to increase the statistical database.
Nonetheless, Equation 6.4 states a significant relation between the geometrical characteristics of the liquid-gas interface in equilibrium conditions.

Such link between mean and Gauss curvatures can be particularly useful with the idea of introducing such quantities inside the ELSA framework to determine the DSD.
In fact, starting from this Weber number and assuming a spherical shape from a topological point of view at the equilibrium state (i.e. $H^{*2} = G^*$), the following transport equations can be introduced to determine the time derivative of mean and Gauss curvatures.

$$\begin{cases} \dfrac{\partial \bar{H}}{\partial t} = \dot{S}_{\bar{H}} = \dfrac{H^* - \bar{H}}{\tau_H} \\ \dfrac{\partial \bar{G}}{\partial t} = \dot{S}_{\bar{G}} = \dfrac{G^* - \bar{G}}{\tau_G} \end{cases} \tag{6.5}$$

where H^* can be determined as a function of $We_{k,eq}$ and $G^* = H^{*2}$. Characteristic times ($\tau_{H,G}$) are missing and, using the same approximation employed for Σ and in the ELSA approach, a dependence on the turbulent time scale (τ_t) can be assumed.
Once H and G distributions have been determined, as shown in [123] and in previous sections, using also the information in terms of liquid volume fraction and liquid-gas interface density, the diameter distribution to switch from the Eulerian region of ELSA to the lagrangian one can be extracted in a general way.
This surely represents a preliminary expression of such transport equations, that opens an important research topic on two-phase modelling. Further investigations are required to validate Equations 6.4 and 6.5 employing a wider DNS database.
Nevertheless, a link has been shown between the geometrical characteristics of the liquid-gas interface with the DSD together with the opportunity to model the evolution of H and G through the introduction of an equilibrium Weber number, representing the background and the starting point for next future perspectives of this activity.

6.5 Concluding remarks

This study shows how DNS of two-phase flows can be employed to improve understanding and modelling of primary atomization to be then used in RANS or LES framework. In particular, the study is aimed at enhancing the information available in ELSA framework through the introduction of liquid/gas interface curvatures.
Firstly, on a mathematical point of view, an extended definition of the drop size distribution to be used all along the atomization process is proposed, leading to the so-called surface curvature distribution. Hence,

the extraction of surface curvatures is shown for a simple Rayleigh-Plateau test case. Two different methods to extract the curvatures have been firstly tested and it has been shown that both approaches give the same results. This gives confidence on the computation of surface curvatures and it ensures that the mesh resolution is fine enough. Then, the evolution of Gauss and mean curvatures is analysed in detail in order to show how the breakup process from a liquid jet to the final droplet can be easily described in terms of such surface geometrical properties.
The same procedure has been applied on the HIT, where several cases, varying the liquid volume fraction, have been studied. The analysis has been firstly focused on a diluted case (i.e. $\alpha_1 = 1\%$), where the link between the DSD and SCD has been clarified. A bi-modal PDF(H) has been determined and it has been shown that log-normal distributions were able to fit each mode. This seems strange at first glance because only one phenomenon (i.e. the turbulence forcing) is promoting break-up and coalescence. However, a deeper look in the process clearly shows that one modal peak is related to the liquid-liquid actions and the other on the liquid-gas interactions. This is a significant result that has to be checked also in general for atomization. It worth mentioning that this effect is probably not captured by experiments since they directly investigate the droplet population as produced by collision and turbulence stretching, but for different levels of turbulence. Instead, thanks to the definition of the PDF of curvature, a local description of this mechanism can be carried out.
Nonetheless, after this preliminary assessment, sine the SCD is defined even if droplets or discrete elements are not present, higher values of α_l have been investigated up to 90%. It has been found that curvature distributions are able to describe the transition from a diluted spray to a bubbly flow and that the PDF(H) shows a very similar shape in all the studied cases. In order to have a deeper understanding about the interactions between the liquid-gas interface and the turbulence field, a detailed analysis has been performed in terms of structure function at different distances from the surface. As already mentioned, this last part of the investigation represents a preliminary attempt to show how the interface affects the turbulence field. A direct link between the peak of the structure function in the liquid side and the one of the mean curvature PDF has been pointed out. Then, a Weber number, based on curvature values, has been proposed, which has been then used to formulate two preliminary transport equations for H and G to be included in the ELSA context. The addition of such geometrical properties of the liquid/gas interface within an Eulerian-Eulerian framework represents a mandatory

step to be pursued to increase the level of description with respect to Eulerian-Lagrangian approaches.
This represents a first step in the analysis of curvature distributions, but surely a promising and powerful numerical framework for the extraction of the DSD has been proposed and validated through numerical data.

Conclusions

The research activity described in this dissertation has been aimed at deepening the knowledge about liquid phase modelling in ultra-low NO_x aero-engine combustors. In this context, the fuel preparation can have a significant effect on the reacting flow-field due to the fact that it directly affects the fuel-air mixing and the obtained distribution of equivalence ratio. Over the last years, this issue has been becoming increasingly important because of the strict regulations imposed by ICAO-CAEP in terms of pollutant emissions that are pushing towards the adoption of lean burn combustion systems. In this scenario, the atomization and evaporation of liquid fuel assumes a primary relevance since it completely determines the burning mode and the flame stability.
The development of numerical tools able to characterize the main phenomena associated to spray combustion from liquid injection up to a dispersed cloud is therefore of paramount importance. A reliable prediction of fuel preparation indeed requires to take into account all the complex physical processes related to the presence of a liquid-gas interface. In particular, strong attention should be devoted to the dense spray region that completely controls the subsequent breakup and the following reacting flow-field. Conversely, typical industrial calculations as well as a large amount of numerical contributions in technical literature neglect such near injection zone and are based on trial & error procedures to determine spray boundary conditions.
The present analysis has been carried out within this context and great attention has been therefore focused on the development of a general tool able to account for primary breakup as well as evaporation.
At first, a CFD campaign has been carried out on three different literature test cases with an increasing order of complexity to clearly point out the main limitations of the state of the art in the numerical analysis of spray flames. A LES-FGM approach based on an Eulerian-Lagrangian tracking for liquid phase has been here employed. The FGM combustion model

has been chosen since it may represent a good trade-off between CPU cost and accuracy mainly from an industrial perspective.
First, the Sydney Spray Burner allowed to validate the proposed numerical set-up on a basic geometrical configuration. The great agreement obtained with LES points out the intrinsic limitations of steady state approaches in the analysis of spray combustion together with the detailed insight that can be obtained with a scale-resolving method. Once validated this methodology, the Sheen Burner and the DLR-GSS combustor have been analysed. These test articles were particularly interesting since a swirled flow-field was involved and several measurements were available both on the gas phase and on the liquid distribution.
The Sheen Burner assessed that the proposed set-up was able of reasonably reproducing the main characteristics of such non-premixed flame in terms of burning and mixing regions as well as pollutant mass fraction.
The DLR-GSS combustor, which is completely representative for a lean aero-engine burner, instead bared the strong coupling between the liquid phase BCs and the reacting flow-field: just by means of a focused analysis on the fuel film evolution and atomization it has been possible to properly reproduce the breakup process and the subsequent spray distribution. On the contrary, trial & error procedures completely failed in representing the physics under investigation by totally misleading the spray PDF. Thanks to a proper description of the liquid evolution and of the fuel-air mixing, a fair agreement has been obtained also with regard to the gas phase.
The goal of this first part of the work has been therefore twofold:

- The capabilities of the FGM model in dealing with spray combustion have been assessed in order to propose it as a robust and reliable tool to deal with liquid fuelled flames mainly from an industrial perspective. To the best of the author's knowledge, the present work represents one of the first effort in technical literature focused on the analysis of the capabilities of FGM ranging from a laboratory flame up to a real aero-engine combustor.

- The impact of a correct spray characterization in reactive calculations has been pointed out. It has been clearly shown that the main source of uncertainty is related to the liquid breakup and that, without a general technique to deal with atomization, CFD tools lower their capabilities in a design context. This justifies the need of more advanced strategies to deal with the liquid evolution.

These observations have led the present research towards the development of a unified approach to deal with spray atomization in LES. This was the main topic of the second part of the work.

The Eulerian Lagrangian Spray Atomization (ELSA) model has been chosen to this end since it is able to deal with a pure liquid up to the generation of a dispersed phase within the same computational framework. It is based on a coupled DNS-LES approach, where a VOF method is combined with a diffuse interface approach and the switching criteria are defined using the available information about the liquid/gas interface (Σ) and the mesh sizing.
However, considering the flow field characteristics of the lean injection modules, several limitations of such approach have been pointed out for its application in the aero-engine context.
Firstly, the attention has been therefore focused on the impact of turbulent liquid flux, which introduces the effects of a slip velocity between phases inside the liquid volume fraction equation. A gradient based closure was initially employed for this term and results available on a PERM injection system have been used to underline that in lean devices this approach is completely unreliable.
A novel second order closure, where one equation is solved for each component of turbulent liquid flux, has been therefore developed and introduced inside the ELSA context. It is worth pointing out that, in this part of the work, both theoretical and numerical aspects related to the physics of a two-phase flow have been deeply investigated to develop the proposed methodology. The capabilities of the resulting Quasi Multiphase Eulerian (QME) approach have been assessed on a jet in crossflow test case. Two different momentum flux ratio have been analysed, pointing out an overall good agreement with experiments and a significant enhancement with respect to the gradient based closure results.
The resulting QME-VOF approach based on ELSA has been introduced as a reliable tool to deal with spray atomization. This method fills the gap between single Eulerian mixture flow and fully two-phase Eulerian-Eulerian approaches with the benefit to be applicable for a wide range of liquid volume fraction, addressing both dense and dispersed flows. Based on the operating conditions, the solver is able to switch between VOF and QME also providing a reliable initialization to the lagrangian particles injected in the dispersed spray region.
A further achievement towards the development of a general framework for spray atomization has been also represented by the proposition and the assessment of a novel evaporation model to deal with the dense spray region. This step represents the link between the liquid phase and the reacting flow-field. For this reason, it can be considered of paramount importance in the development of an approach able to account for all the phenomena going from the near injection region up to a dispersed spray.

Several approaches are indeed already available for a dispersed cloud of droplets, but no efforts have been carried out so far for the near injection zone. A novel evaporation model, based on an implicit formulation and on the computation of an equilibrium state, has been here introduced and assessed on the experimental data provided in the ECN database.
Finally, in order to further extend the capabilities of the proposed approach in the aero-engine context, an innovative way to determine the Drop Size Distribution (DSD) in the ELSA context has been proposed, based on surface curvatures. Firstly, it has been shown that, from a theoretical perspective, the DSD represents a particular case of the more general Surface Curvature Distribution (SCD), which is defined from the near injection region up to the final spray. Hence, DNS data obtained on several numerical configurations have been used to show that curvatures can be reliably employed to describe fundamental breakup or coalesce events. It has been pointed out that a general shape of the SCD can be evaluated all along the atomization process. This represents a completely novel frame to study a two phase flow and, therefore, further investigations have to be pursued in future works.
In conclusion, a QME-VOF approach, based on ELSA together with the inclusion of evaporation modelling, has been proposed as a general tool to deal with spray atomization and as a basis towards a unified approach for LES of turbulent spray flames for aero-engine applications. The introduction of surface curvatures should help in further extending the capabilities of such method mainly regarding the characterization of the drop size distribution.
Validations with experimental and numerical test cases have shown that the proposed developments allow a reliable representation of the main physical phenomena regulating liquid injection systems and, together with previous studies in technical literature, further assess ELSA for atomization modelling.
In order to better explain the contributions of the present research work, it is worth giving a picture of the approaches employed for the numerical analysis of turbulent lean spray flames before and after this study. An overview about future perspectives of the study is finally reported at the end.

Before this research...

As well described in Chapter 1, in technical literature the atomization of the liquid phase was usually neglected in scale-resolving simulations of spray flames. Calculations normally relied on trial & error procedures or on a fitting of experimental data to define the BCs for an equivalent

injector placed at the end of the near injection zone. The characteristics of droplets generated were imposed by the user and the unsteady and locally defined interactions between liquid and gas phases were completely overlooked. This approach strongly lowered the reliability of scale resolving methods mainly in an industrial context, since a case-dependent and time consuming sensitivity on liquid breakup was required. Much more attention was instead devoted to the following reacting flow-field and to the correct prediction of the turbulence-chemistry interactions. However, the uncertainty introduced in this way with atomization modelling on the flame shape and, therefore, on pollutant emissions could be of the same order of magnitude of the expected improvements in a design context.

After this research...

The impact of liquid phase modelling on scale resolving simulations of spray flames has been investigated. It has been shown that, without a detailed insight on atomization modelling, the flame shape and the interactions between fuel and the reacting flow-field can be completely misled. The breakup represents a leading phenomenon to be included and requires strong attention in the numerical prediction of aero-engine performances. It has been demonstrated that, based on a proper description of fuel atomization, the FGM model can be considered a reliable strategy for combustion modelling mainly from an industrial perspective.
A unified approach, which includes the primary breakup up to the generation of a diluted spray, based on ELSA, has been therefore proposed focusing the attention on the inclusion of the most important interactions among liquid and gas. Important phenomena for liquid fuel preparation and evolution, such as slip velocity as well as evaporation and heat transfer between phases, can be now included in the simulation of the dense zone of injection systems. A novel method to extract the DSD has been as well introduced pointing the way for an innovative approach to determine the size distribution all along the atomization process.
This work clearly represents a first step towards a unified approach for spray flames calculation and several aspects still deserve to be further investigated after this research:

- As well deepened in Annex-A, in the mixture momentum equation of ELSA, several density correlations terms, which are linked to the turbulent liquid flux, appear and represent still today an important unclosed problem in a multiphase context. The work shown in the present thesis on the QME opens important perspectives to close this modelling issue.

- The further validation of the QME-VOF approach on different geometrical configurations with respect to the jet breakup here investigated. Prefilming airblast atomizers, which represent another widely employed solution in the aero-engine context, have to be analysed for this purpose. The test article experimentally studied by Gepperth et al. [51], which presents detailed experimental data also as far as the drop size distribution is concerned, is already under investigation in our research group using the numerical tools developed in the present activity.

- The coupling of the QME-VOF approach with a turbulent combustion model and, based on results shown in Chapter 2, the FGM represents surely a valuable choice in this context. Obtained results prove that, mainly in an industrial perspective, it can be considered a suitable trade-off between accuracy and CPU cost, in the context of spray combustion.
  This step should be straightforward thanks to the single-phase formalism employed in ELSA that ease the coupling with combustion models and should benefit also of the deep understanding established in this work on the characteristics of FGM.
  This point should finally make possible a total flame calculation from liquid injection up to the reacting flow field. To the best of the author's knowledge, this is now out of reach of the available multiphase approaches.

- The addition of the proposed set of transport equations for interface curvatures in the ELSA framework and the assessment of the proposed equilibrium Weber number on a wider set of DNS data. The curvature formulation is extremely promising to better predict the lagrangian population to be injected as soon as the spray becomes diluted. Such formulation should be coupled with the rest of the code and validated on an experimental test case to further enhance the reliability of the ELSA model.

Annex-A

Favre averaging

The goal of this annex is to make a focus on Favre averaging when a two-phase system is under investigation. In fact, in Chapter 3, when the filtered momentum equation is derived (see Equation A.1), it is clearly stated that with $\tau_{\rho u_i u_j}$ and $\tau_{\rho u_i}$ all the terms coming from turbulent fluctuations, comprising also the density sub-grid correlation terms, are included.

$$\begin{aligned}\frac{\partial \bar{\rho}\bar{U}_i + \tau_{\rho u_i}}{\partial t} + \frac{\partial \bar{\rho}\bar{U}_i\bar{U}_j + \tau_{\rho u_i u_j}}{\partial x_j} = &- \frac{\partial \bar{P}}{\partial x_i} + \\ &+ \frac{\partial}{\partial x_j}\left(\mu\left(\frac{\partial \bar{U}_i}{\partial x_j} + \frac{\partial \bar{U}_j}{\partial x_i}\right) + \tau_{S_{ij}}\right) + \\ &+ \bar{\rho} f_i\end{aligned} \tag{A.1}$$

This represents a strong approximation and the Favre averaging can be considered as a valuable alternative in this context. However, even if it has been widely employed in technical literature for atomization modelling, it hides in the momentum equation a similar problem and in this section it is clearly shown.
The well-known transport equation for mixture velocity that can be obtained in Favre context is the following one:

$$\begin{aligned}\frac{\partial \bar{\rho}\tilde{U}_i}{\partial t} + \frac{\partial \bar{\rho}\tilde{U}_i\tilde{U}_j}{\partial x_j} = &- \frac{\partial \bar{P}}{\partial x_i} + \\ &+ \frac{\partial}{\partial x_i}\left(\mu\left(\frac{\partial \tilde{U}_i}{\partial x_j} + \frac{\partial \tilde{U}_j}{\partial x_i}\right) + \tau_{S_{ij}}\right) + \frac{\partial \bar{\rho}\tilde{R}_{ij}}{\partial x_j} + \\ &+ \bar{\rho} f_i\end{aligned} \tag{A.2}$$

The relation between each term of Equations A.1 and A.2 is specified in the following in order to clearly point out the appearance of some unclosed terms even if a Favre averaging is applied.

- **Transient term**: starting from first term on the LHS of Equation A.2:

$$\bar{\rho}\tilde{U}_i = \overline{\rho U_i} = \bar{\rho}\bar{U}_i + \tau_{\rho u_i} \tag{A.3}$$

and applying now a liquid-gas decomposition based on the liquid volume fraction, the following equation can be derived:

$$\begin{aligned}\overline{\rho U_i} = \rho_l\bar{\alpha}_l\bar{U}_i|_l + \rho_g\bar{\alpha}_g\bar{U}_i|_g = \rho_l\bar{\alpha}_l\bar{U}_i + \rho_l\underbrace{\bar{\alpha}_l\left(\bar{U}_i|_l - \bar{U}_i\right)}_{\bar{R}_{li}} + \\ + \rho_g\bar{\alpha}_g\bar{U}_i + \rho_g\underbrace{\bar{\alpha}_g\left(\bar{U}_i|_g - \bar{U}_g\right)}_{\bar{R}_{gi}}\end{aligned} \tag{A.4}$$

where R_{li} and R_{gi} represent respectively the contribution of turbulent flux in liquid and gas phases. It is possible to demonstrate that $R_{gi} = -R_{li}$. This shows the primary importance of the liquid turbulent flux on density-velocity based correlation on the transient term:

$$\bar{\rho}\tilde{U}_i = \overline{\rho U_i} = \bar{\rho}\bar{U}_i + \tau_{\rho u_i} = \bar{\rho}\bar{U}_i + \bar{R}_{li}\left(\rho_l - \rho_g\right) \tag{A.5}$$

- **Convective term**: considering now the second term on the LHS of Equation A.2:

$$\begin{aligned}\bar{\rho}\widetilde{U_iU_j} = \overline{\rho U_iU_j} = \bar{\rho}\bar{U}_i\bar{U}_j + \tau_{\rho u_iu_j} &= \bar{\rho}\tilde{U}_i\tilde{U}_j + \bar{\rho}\left(\widetilde{U_iU_j} - \tilde{U}_i\tilde{U}_j\right) \\ &= \bar{\rho}\tilde{U}_i\tilde{U}_j + \bar{\rho}\tilde{R}_{ij}\end{aligned} \tag{A.6}$$

where $\tilde{R}_{ij}$ is the Reynolds stress tensor. The same liquid-gas decomposition previously introduced can be here applied:

$$\begin{aligned}\overline{\rho U_iU_j} = \rho_l\bar{\alpha}_l\overline{U_iU_j}|_l + \rho_g\bar{\alpha}_l\overline{U_iU_j}|_g = \rho_l\bar{\alpha}_l\left(\bar{U}_i|_l\bar{U}_j|_l + \bar{R}_{ij}|_l\right) + \\ + \rho_g\bar{\alpha}_g\left(\bar{U}_i|_g\bar{U}_j|_g + \bar{R}_{ij}|_g\right)\end{aligned} \tag{A.7}$$

and then:

$$\begin{aligned}
&\rho_l\bar{\alpha}_l\bar{U}_i|_l\bar{U}_j|_l + \rho_g\bar{\alpha}_g\bar{U}_i|_g\bar{U}_j|_g = \\
&= \left(\rho_l\bar{\alpha}_l + \rho_g\bar{\alpha}_g\right)\bar{U}_i\bar{U}_j + \rho_l\bar{\alpha}_l\left(\bar{U}_i|_l\bar{U}_j|_l - \bar{U}_i\bar{U}_j\right) + \\
&+ \rho_g\bar{\alpha}_g\left(\bar{U}_i|_g\bar{U}_j|_g - \bar{U}_i\bar{U}_j\right) = \\
&= \bar{\rho}\bar{U}_i\bar{U}_j + \rho_l\bar{\alpha}_l\left(\bar{U}_i|_l\bar{U}_j|_l - \bar{U}_i\bar{U}_j\right) + \rho_g\bar{\alpha}_g\left(\bar{U}_i|_g\bar{U}_j|_g - \bar{U}_i\bar{U}_j\right)
\end{aligned} \tag{A.8}$$

leading to:

$$\begin{aligned}
&\rho_l\bar{\alpha}_l\bar{U}_i|_l\bar{U}_j|_l + \rho_g\bar{\alpha}_g\bar{U}_i|_g\bar{U}_j|_g = \bar{\rho}\bar{U}_i\bar{U}_j + \\
&+ \rho_l\bar{\alpha}_l\left(\left(\frac{\bar{R}_{li}}{\bar{\alpha}_l} + \bar{U}_i\right)\left(\frac{\bar{R}_{li}}{\bar{\alpha}_l} + \bar{U}_j\right) - \bar{U}_i\bar{U}_j\right) + \\
&+ \rho_g\bar{\alpha}_g\left(\frac{\bar{R}_{gi}\bar{R}_{gj}}{\bar{\alpha}_g^2} + \frac{\bar{R}_{gi}\bar{U}_j}{\bar{\alpha}_g} + \frac{\bar{R}_{gj}\bar{U}_i}{\bar{\alpha}_g} + \bar{U}_i\bar{U}_j - \bar{U}_i\bar{U}_j\right) = \\
&= \bar{\rho}\bar{U}_i\bar{U}_j + \bar{R}_{li}\bar{R}_{lj}\left(\frac{\rho_l}{\bar{\alpha}_l} + \frac{\rho_g}{\bar{\alpha}_g}\right) + \left(\rho_l - \rho_g\right)\left(\bar{R}_{li}\bar{U}_j + \bar{U}_i\bar{R}_{lj}\right)
\end{aligned} \tag{A.9}$$

The final reconstruction is therefore that:

$$\begin{aligned}
\widetilde{\bar{\rho}\bar{U}_i\bar{U}_j} = \overline{\rho U_i U_j} = \bar{\rho}\bar{U}_i\bar{U}_j + \tau_{\rho u_i u_j} = \bar{\rho}\bar{U}_i\bar{U}_j + \rho_l\bar{\alpha}_l\bar{R}_{ij}|_l + \rho_g\bar{\alpha}_g\bar{R}_{ij}|_g + \\
+ \bar{R}_{li}\bar{R}_{lj}\left(\frac{\rho_l}{\bar{\alpha}_l} + \frac{\rho_g}{\bar{\alpha}_g}\right) + \left(\rho_l - \rho_g\right)\left(\bar{R}_{lj}\bar{U}_j + \bar{U}_i\bar{R}_{li}\right)
\end{aligned} \tag{A.10}$$

This equation clearly shows once again the strong coupling of Favre averaging with the turbulent liquid flux and normally this contribution is neglected using standard gradient based closures (i.e. Boussinesq approach for $\bar{R}_{ij}$). Further work is required in this direction to detail this problem and to introduce the contribution of turbulent liquid flux.

- **Pressure term**: The pressure term, as well as the one related to volume forces, is directly obtained from averaging:

$$\overline{\frac{\partial P}{\partial x_i}} = \frac{\partial \bar{P}}{\partial x_i} \tag{A.11}$$

- **Viscous term**: considering now the second term on RHS of Equa-

tions A.2 and A.1 the following relation stands:

$$\bar{\rho}\left(\nu\left(\widetilde{\frac{\partial U_j}{\partial x_i}+\frac{\partial U_i}{\partial x_j}}\right)\right)=\overline{\rho\nu\left(\frac{\partial U_j}{\partial x_i}+\frac{\partial U_i}{\partial x_j}\right)} \tag{A.12}$$

where ν is the kinematic viscosity. In this case the phase decomposition leads to:

$$\overline{\rho\nu\left(\frac{\partial U_j}{\partial x_i}+\frac{\partial U_i}{\partial x_j}\right)}=\rho_l\nu_l\bar{\alpha}_l\left(\frac{\partial\bar{U}_j|_l}{\partial x_i}+\frac{\bar{U}_i|_l}{\partial x_j}\right)+\rho_g\nu_g\bar{\alpha}_g\left(\frac{\partial\bar{U}_j|_g\partial x_i+\bar{U}_i|_g}{\partial x_j}\right) \tag{A.13}$$

Then, replacing the conditioned average velocity by the corresponding turbulent flux (i.e. $\bar{U}_i|_l=\frac{\bar{R}_{li}}{\bar{\alpha}_l}+\bar{U}_i$):

$$\bar{\alpha}_l\frac{\partial\bar{U}_i|_l}{x_j}=\frac{\bar{R}_{li}}{\partial x_j}-\frac{\bar{R}_{li}}{\bar{\alpha}_l}\frac{\partial\bar{\alpha}_l}{\partial x_j}+\bar{\alpha}_l\frac{\bar{U}_i}{\partial x_j} \tag{A.14}$$

It leads to:

$$\begin{aligned}\overline{\rho\nu\left(\frac{\partial U_j}{\partial x_i}+\frac{\partial U_i}{\partial x_j}\right)}=&\left(\rho_l\nu_l\bar{\alpha}_l+\rho_g\nu_g\bar{\alpha}_g\right)\left(\frac{\partial\bar{U}_j}{\partial x_i}+\frac{\partial\bar{U}_i}{\partial x_j}\right)+\\&+\rho_l\nu_l\left(\frac{\partial\bar{R}_{lj}}{\partial x_i}-\frac{\bar{R}_{lj}}{\bar{\alpha}_l}\frac{\partial\bar{\alpha}_l}{\partial x_i}+\frac{\partial\bar{R}_{li}}{\partial x_j}-\frac{\bar{R}_{li}}{\bar{\alpha}_l}\frac{\partial\bar{\alpha}_l}{\partial x_j}\right)+\\&+\rho_g\nu_g\left(\frac{\partial\bar{R}_{gj}}{\partial x_i}-\frac{\bar{R}_{gj}}{\bar{\alpha}_g}\frac{\partial\bar{\alpha}_g}{\partial x_i}+\frac{\partial\bar{R}_{gi}}{\partial x_j}-\frac{\bar{R}_{gi}}{\bar{\alpha}_g}\frac{\partial\bar{\alpha}_g}{\partial x_j}\right)\end{aligned} \tag{A.15}$$

that after some further mathematical passages takes the following final form:

$$\begin{aligned}\overline{\rho\nu\left(\frac{\partial U_j}{\partial x_i}+\frac{\partial U_i}{\partial x_j}\right)}=&\bar{\rho}\bar{\nu}\left(\frac{\partial\bar{U}_j}{\partial x_i}+\frac{\partial\bar{U}_i}{\partial x_j}\right)+\\&+\left(\frac{\partial\bar{R}_{lj}}{\partial x_i}+\frac{\partial\bar{R}_{li}}{\partial x_j}\right)\left(\rho_l\nu_l-\rho_g\nu_g\right)+\\&-\left(\bar{R}_{li}\frac{\partial\bar{\alpha}_l}{\partial x_j}+\bar{R}_{lj}\frac{\partial\bar{\alpha}_l}{\partial x_i}\right)\left(\frac{\rho_l\nu_l}{\bar{\alpha}_l}+\frac{\rho_g\nu_g}{\bar{\alpha}_g}\right)\end{aligned} \tag{A.16}$$

Once again, even in the viscous term a direct dependency on the turbulent liquid flux can be pointed out.

Using this procedure, the momentum equation using a Reynolds averaging can be written again with all the density correlation terms expressed in terms of liquid and gas Reynolds stress tensors as well as turbulent liquid

flux:

$$\begin{aligned}\frac{\partial\bar{\rho}\bar{U}_i}{\partial t}+\frac{\partial\bar{\rho}\bar{U}_i\bar{U}_j}{\partial x_j}=&-\frac{\partial\bar{P}}{\partial x_i}+\\&+\frac{\partial}{\partial x_i}\underbrace{\left(-\rho_l\bar{\alpha}_l\bar{R}_{ij}|_l-\rho_g\bar{\alpha}_g\bar{R}_{ij}|_g\right)}_{\text{Reynolds Stress tensor}}+\\&+\frac{\partial}{\partial x_i}\underbrace{\left(\bar{\rho}\bar{\nu}\left(\frac{\partial\bar{U}_j}{\partial x_i}+\frac{\partial\bar{U}_i}{\partial x_j}\right)\right)}_{\text{Viscous term}}+\bar{\rho}f_i+\\&-\frac{\partial}{\partial t}\left(\bar{R}_{li}\left(\rho_l-\rho_g\right)\right)+\frac{\partial}{\partial x_j}\left(-\bar{R}_{li}\bar{R}_{lj}\left(\frac{\rho_l}{\bar{\alpha}_l}+\frac{\rho_g}{\bar{\alpha}_g}\right)\right)+\\&-\frac{\partial}{\partial x_j}\left(\left(\rho_l-\rho_g\right)\left(\bar{R}_{li}\bar{U}_j+\bar{U}_i\bar{R}_{li}\right)\right)+\\&+\frac{\partial}{\partial x_j}\left(\left(\frac{\partial\bar{R}_{lj}}{\partial x_i}+\frac{\partial\bar{R}_{li}}{\partial x_j}\right)\left(\rho_l\nu_l-\rho_g\nu_g\right)\right)+\\&-\frac{\partial}{\partial x_j}\left(\left(\bar{R}_{li}\frac{\partial\bar{\alpha}_l}{\partial x_j}+\bar{R}_{lj}\frac{\partial\bar{\alpha}_l}{\partial x_i}\right)\left(\frac{\rho_l\nu_l}{\bar{\alpha}_l}+\frac{\rho_g\nu_g}{\bar{\alpha}_g}\right)\right)\end{aligned}\tag{A.17}$$

This re-formulation, beyond the contribution of Reynolds stress tensor and viscous stresses, makes apparent the strong coupling between the turbulent liquid flux and the momentum equation in a two phase flow. Based on Equations A.5 and A.6, the same problem arises even employing a Favre averaging procedure.
Therefore, to summarize, starting from Equation 4.29 in Chapter 4, beyond the specific adopted averaging strategy, several unclosed terms, which are linked to the density correlation and to turbulent liquid flux, appear. Some modelling assumptions can be used to overcome this modelling issue:

- The Reynolds stress term can be studied assuming a first order gradient closure. It means that:

$$\begin{aligned}-\rho_l\bar{\alpha}_l\bar{R}_{ij}|_l-\rho_g\bar{\alpha}_g\bar{R}_{ij}|_g=&\rho_l\bar{\alpha}_l\nu_t|_l\left(\frac{\partial\bar{U}_j|_l}{\partial x_i}+\frac{\partial\bar{U}_i|_l}{\partial x_j}\right)+\\&+\rho_g\bar{\alpha}_g\nu_t|_g\left(\frac{\partial\bar{U}_j|_g}{\partial x_i}+\frac{\partial\bar{U}_i|_g}{\partial x_j}\right)\end{aligned}\tag{A.18}$$

  and if the turbulent viscosity is assumed to be the same in each

phase:

$$-\rho_l\bar{\alpha}_l\bar{R}_{ij}|_l - \rho_g\bar{\alpha}_g\bar{R}_{ij}|_g \approx \bar{\rho}\nu_t\left(\frac{\partial\bar{U}_j}{\partial x_i}+\frac{\partial\bar{U}_i}{\partial x_j}\right) \tag{A.19}$$

- The time derivative of R_{li} determines a strong coupling between momentum and turbulent liquid flux equations. Its effect can be better explained considering for instance a mixing layer in a two phase flow with a constant slip velocity between gas and liquid phases. The mixing of the liquid volume fraction should modify the Reynolds average velocity and it is related to the turbulent liquid flux. A direct link between this term and the source term in the equation of R_l ($\bar{S}_{Rli}$, see Chapter 4) can be introduced:

$$\frac{\partial}{\partial t}\left(\bar{R}_{li}\left(\rho_l-\rho_g\right)+\frac{\partial}{\partial x_j}\left(\rho_l-\rho_g\right)R_{li}\bar{U}_j\right)=\left(\rho_l-\rho_g\right)\bar{S}_{Rli} \tag{A.20}$$

- Another modelling choice to simplify Equation A.17 can be the adoption of a first order closure for turbulent liquid flux. However, it has been widely demonstrate in Chapter 4 that this approximation leads to neglect the significant contribution of the slip velocity. As shown for the jet in crossflow configuration, the error determined in this way can completely modify the predicted atomization process.

However, the present section represents just a first effort in this direction since in technical literature a straightforward way to include the effects of turbulent liquid flux in the momentum equation is not yet available. It represents an important limitation of this class of multiphase approaches and it holds independently from the adopted averaging procedure.
Having in mind this scenario, since an established theoretical background on this point is not present up to now, in this work it has been decided to include all the density correlation terms inside the Reynolds stress tensor and to apply a standard Boussinesq based closure. Using this approximation, Equation A.17 is strongly simplified and Equation 4.33 for the mixture momentum can be recast. Further investigation are surely required to better understand the impact of this modelling choice and to propose a coupling with the turbulent liquid flux equation proposed in Chapter 4.

Annex-B

Direction to analyse turbulence/interface interactions and curvature distributions

In this annex further results about the analysis of structure function for the HIT case shown in Chapter 6 are reported. Together with the guidelines detailed in Section 6.4.2, these data can be used as starting point to deepen the knowledge about the impact on the liquid-gas interface on the turbulence field and to clarify the modelling of surface curvatures. As already detailed in Section 6.4.2, in order to determine the effect of liquid-gas interface on turbulence, different configurations based on the distance function φ have been extracted. All the curves are normalized using $2\overline{u'^2}$ as reference, which corresponds to the theoretical limit when the velocities in the two selected points are totally uncorrelated so when $r \to \infty$.
In Figure B.1 the second order structure function is shown and the r^2 curve has been also reported because S_2 should follow this asymptotic line for the smaller scales (i.e. where dissipation of turbulence kinetic energy takes place). At these scales, a significant decorrelation can be observed for the elements close to the surface in the gas part. Conversely, far from the surface (i.e. $\varphi > 20dx$), such structure function follows the r^2-law suggesting that the energy dissipation occurs at bigger scales far from the interface. This is confirmed in Figure B.2 where the inertial sub-range, characterized by a $r^{\frac{2}{3}}$ slope, is specified by vertical lines in order to point out that it is smaller and at higher scales while increasing the distance from the interface. This idea is as well represented in Figure B.3 where the evolution of the structure function close to the interface is plotted.
In the liquid part (Figure B.4), the shape of the structure function does not change close to the surface. This suggests a more significant influence of the liquid-gas interface on the turbulence in the gas phase than in the

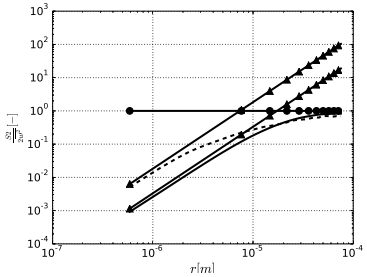

Figure B.1: Second order structure function $S2$ in gas part. Dashed curve represents $S2$ for $\varphi \in [0;4]dx$; solid curve represents $S2$ for $\varphi > 20dx$; curves with ▲ represent the r^2 law; curve with • represents the theoretical limit when $r \to \infty$.

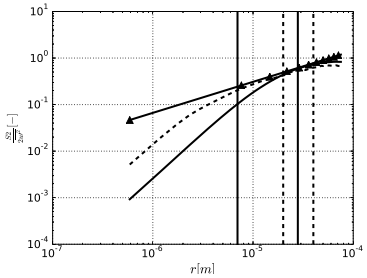

Figure B.2: Second order structure function $S2$ in gas part. The dashed curve represents $S2$ for $\varphi \in [0;4]dx$; the solid curve represents $S2$ for $\varphi > 20dx$; the curve with ▲ represents the $r^{\frac{2}{3}}$ law; the dashed vertical lines represent the inertial range for $\varphi > 20dx$; the solid vertical lines represent the inertial range for $\varphi \in [0;4]dx$.

liquid one. In the gas side, the effects of the surface is lost while increasing the distance and in Figure B.5 the evolution of structure function is reported at increasing windows of $5dx$. After $15dx$ approximately, the impact of the interface is negligible.
However, analysing more in detail the evolution of the structure function in the liquid phase (Figure B.6), even if the statistical convergence is not completely ensured, a peak appears at a certain distance r which corresponds to the diameter of a droplet whose volume is the most probable

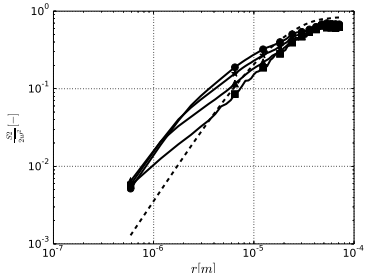

Figure B.3: Second order structure function $S2$ in gas part. The dashed curve represents $S2$ for the total gas part ; curve with ■ represents $S2$ for $\varphi \in [0;1]dx$; the curve with ▲ represents $S2$ for $\varphi \in [0;2]dx$; the curve with ★ represents $S2$ for $\varphi \in [0;3]dx$; the curve with • represents $S2$ for $\varphi \in [0;4]dx$.

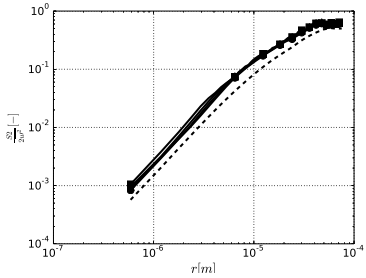

Figure B.4: Second order structure function $S2$ in liquid part. The dashed curve represents $S2$ for the total liquid part; the curve with ■ represents $S2$ for $\varphi \in [0;1]dx$; the curve with ▲ represents $S2$ for $\varphi \in [0;2]dx$; the curve with ★ represents $S2$ for $\varphi \in [0;3]dx$; the curve with • represents $S2$ for $\varphi \in [0;4]dx$.

from the PDF(H) shown in Figure 6.19. As already mentioned, this observation highlights the link between liquid-gas interface and turbulence field and it gives some hints for further perspectives on this topic as suggested in Section 6.4.2.

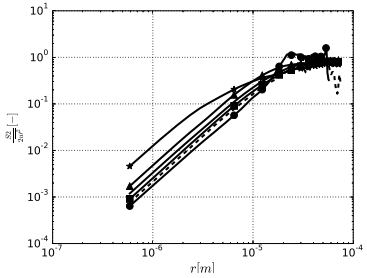

Figure B.5: Second order structure function $S2$ in gas part. The curve with ★ represents $S2$ for $\varphi \in [0;5]dx$; line with ▲ represents $S2$ for $\varphi \in [5;10]dx$; the solid curve represents $S2$ for $\varphi \in [10;15]dx$; the curve with ■ represents $S2$ for $\varphi \in [35;40]dx$; the dashed curve represents $S2$ for $\varphi \in [60;65]dx$; the curve with • represents $S2$ for $\varphi \in [65;70]dx$)

Figure B.6: Second order structure function $S2$ in liquid part. The curve with • represents $S2$ for $\varphi \in [0;5]dx$; the curve with ▲ represents $S2$ for $\varphi \in [5;10]dx$; the solid curve represents $S2$ for $\varphi \in [10;15]dx$; the curve with ■ represents $S2$ for $\varphi \in [15;20]dx$; the dashed curve represents $S2$ for $\varphi \in [20;25]dx$)

Bibliography

[1] Boeing. Current market outlook 2017-2036, 2017. URL `http://www.boeing.com/resources/boeingdotcom/commercial/market/current-market-outlook-2017/assets/downloads/2017-cmo-compressed_091917.pdf`.

[2] Lefebvre, A.H. *Gas turbine combustion*. CRC Press, 2010.

[3] Duane, S. FAA CLEEN II Technologies, 2016.

[4] Mongia, H. "TAPS - A 4th Generation Propulsion Combustor Technology for Low Emissions." *The next 100 years, International Air and Space Symposium and Exposition.*, 2003.

[5] Cooper, J.N., Duncan, B.S., Hura, H.S., Lohmueller, S.J., Mongia, H.C., and Sabla, P.E. *Fuel nozzle assembly for reduced exhaust emissions*. Google Patents, April 2002.

[6] General Electric, TAPS II combustor final report, 2013.

[7] Marinov, S., Kern, M., Merkle, K., Zarzalis, N., Peschiulli, A., Turrini, F., and Sara, ON. On swirl stabilized flame characteristics near the weak extinction limit. In *Proc. ASME Turbo Expo*, number GT2010-22335, pages 259–268, 2010.

[8] Kern, M., Marinov, S., Merkle, K., Zarzalis, N., Peschiulli, A., and Turrini, F. Characteristics of an ultra-lean swirl combustor flow by LES and comparison to measurements. In *Proc. ASME Turbo Expo*, number GT2011-45300, pages 321–330, 2011.

[9] Andreini, A., Caciolli, G., Facchini, B., Picchi, A., and Turrini, F. "Experimental investigation of the flow field and the heat transfer on a scaled cooled combustor liner with realistic swirling flow generated

by a lean-burn injection system." *Journal of Turbomachinery*, 137 (3), 2014.

[10] Jenny, P., Roekaerts, D., and Beishuizen, N. "Modeling of turbulent dilute spray combustion." *Progress in Energy and Combustion Science*, 38(6):846–887, 2012.

[11] Jiang, X., Siamas, G.A., Jagus, K., and Karayiannis, T.G. "Physical modelling and advanced simulations of gas–liquid two-phase jet flows in atomization and sprays." *Progress in Energy and Combustion Science*, 36(2):131 – 167, 2010. ISSN 0360-1285. doi: http://dx.doi.org/10.1016/j.pecs.2009.09.002.

[12] Lefebvre, A. *Atomization and Sprays*. Combustion (Hemisphere Publishing Corporation). Taylor & Francis, 1988.

[13] Faeth, G. M. "Evaporation and combustion of sprays." *Progress in Energy and Combustion Science*, 9(1-2):1–76, 1983.

[14] Chiu, H. H. and Liu, T. M. "Group combustion of liquid droplets." *Combustion Science and Technology*, 17(3-4):127–142, 1977. doi: 10.1080/00102207708946823.

[15] Chiu, H.H., Kim, H.Y., and Croke, E.J. "Internal group combustion of liquid droplets." *Symposium (International) on Combustion*, 19 (1):971 – 980, 1982. ISSN 0082-0784. 19th Symposium (International) on Combustion.

[16] Borghi, R. *Background on droplets and sprays. Combustion and Turbulence in Two-phase Flows*. Lecture series 1996-02. Von Karman Institute for Fluid Dynamics, 1996.

[17] Reveillon, J. and Vervish, L. "Analysis of weakly turbulent dilute-spray flames and spray combustion regimes." *Journal of Fluid Mechanics*, 537:317–347, 2005. doi: 10.1017/S0022112005005227.

[18] Beck, C.H., Koch, R., and Bauer, H.-J. "Identification of droplet burning modes in lean, partially prevaporized swirl-stabilized spray flames." *Proceedings of the Combustion Institute*, 32(2):2195 – 2203, 2009. ISSN 1540-7489. doi: http://dx.doi.org/10.1016/j.proci.2008.06.030.

[19] Luo, K., Pitsch, H., Pai, M.G., and Desjardins, O. "Direct Numerical Simulations and analysis of three-dimensional n-heptane

spray flames in a model swirl combustor." *Proceedings of the Combustion Institute*, 33(2):2143 – 2152, 2011. ISSN 1540-7489. doi: http://dx.doi.org/10.1016/j.proci.2010.06.077.

[20] Mastorakos, E. "Ignition of turbulent non-premixed flames." *Progress in Energy and Combustion Science*, 35(1):57 – 97, 2009. ISSN 0360-1285. doi: http://dx.doi.org/10.1016/j.pecs.2008.07.002.

[21] Stepowski, D., Cessou, A., and Goix, P. "Flame stabilization and OH fluorescence mapping of the combustion structures in the near field of a spray jet." *Combustion and Flame*, 99(3):516 – IN1, 1994. ISSN 0010-2180. doi: http://dx.doi.org/10.1016/0010-2180(94)90044-2. 25th Symposium (International) on Combustion.

[22] Marley, S., Lyons, K., and Watson, K. "Leading-edge reaction zones in lifted-jet gas and spray flames." *Flow Turbulence and Combustion*, 72(29), 2004.

[23] Masri, A. R. "Turbulent combustion of sprays: From dilute to dense." *Combustion Science and Technology*, 188(10):1619–1639, 2016.

[24] Merci, B., Roekaerts, D., and Sadiki, A. *Experiments and Numerical Simulations of Diluted Spray Turbulent Combustion*. Springer Link, 2009.

[25] Jones, W.P., Lyra, S, and Marquis, AJ. "Large-Eddy Simulation of evaporating kerosene and acetone sprays." *International Journal of Heat and Mass Transfer*, 53(11):2491–2505, 2010.

[26] Jones, W.P., Marquis, A.J., and Vogiatzaki, K. "Large-Eddy Simulation of spray combustion in a gas turbine combustor." *Combustion and Flame*, 161(1):222–239, 2014.

[27] Colin, O., Ducros, F., Veynante, D., and Poinsot, T. "A thickened flame model for Large-Eddy Simulations of turbulent premixed combustion." *Physics of Fluids (1994-present)*, 12(7):1843–1863, July 2000.

[28] Boileau, M., Staffelbach, G., Cuenot, B., Poinsot, T., and Bérat, C. "LES of an ignition sequence in a gas turbine engine." *Combustion and Flame*, 154(1):2 – 22, 2008. ISSN 0010-2180. doi: http://dx.doi.org/10.1016/j.combustflame.2008.02.006. URL `http://www.sciencedirect.com/science/article/pii/S0010218008000497`.

[29] Knudsen, E. and Pitsch, H. "Large-Eddy Simulation for Combustion Systems: Modeling Approaches for Partially Premixed Flows." *The Open Thermodynamics Journal*, 4(1):76–85, January 2010.

[30] Kuenne, G., Ketelheun, A., and Janicka, J. "LES modeling of premixed combustion using a thickened flame approach coupled with FGM tabulated chemistry." *Combustion and Flame*, 158(9): 1750 – 1767, 2011. ISSN 0010-2180. doi: http://dx.doi.org/10.1016/j.combustflame.2011.01.005. URL `http://www.sciencedirect.com/science/article/pii/S0010218011000204`.

[31] Fiorina, B., Vicquelin, R., Auzillon, P., Darabiha, N., Gicquel, O., and Veynante, D. "A filtered tabulated chemistry model for LES of premixed combustion." *Combustion and Flame*, 157(3):465 – 475, 2010. ISSN 0010-2180. doi: http://dx.doi.org/10.1016/j.combustflame.2009.09.015. URL `http://www.sciencedirect.com/science/article/pii/S0010218009002739`.

[32] Van-Oijen, J.A., Donini, A., Bastiaans, R.J.M., Boonkkamp, J.H.M., and de Goey, L.P.H. "State of the art in premixed combustion modeling using flamelet generated manifolds." *Progress in Energy and Combustion Science*, 57:30 – 74, 2016. ISSN 0360-1285. doi: http://dx.doi.org/10.1016/j.pecs.2016.07.001. URL `http://www.sciencedirect.com/science/article/pii/S0360128515300137`.

[33] Van-Oijen, J.A., Lammers, F.A., and De Goey, L.P.H. "Modeling of complex premixed burner systems by using flamelet-generated manifolds." *Combustion and Flame*, 127(3):2124–2134, 2001.

[34] Ihme, M. and Pitsch, H. "Modeling of radiation and nitric oxide formation in turbulent non-premixed flames using a flamelet/progress variable formulation." *Physics of Fluids*, 20, 2008.

[35] Ihme, M., Cha, C.M., and Pitsch, H. "Prediction of local extinction and re-ignition effects in non-premixed turbulent combustion using a flamelet/progress variable approach." *Proceedings of the Combustion Institute*, 30(1):793 – 800, 2005. ISSN 1540-7489. doi: http://dx.doi.org/10.1016/j.proci.2004.08.260. URL `http://www.sciencedirect.com/science/article/pii/S0082078404003145`.

[36] Esclapez, L., Ma, P. C., Mayhew, E., Xu, R., Stouffer, S., Lee, T., Wang, H., and Ihme, M. "Fuel effects on lean blow-out in a realistic gas turbine combustor." *Combustion and Flame*, 181:82 – 99, 2017. ISSN 0010-2180. doi: http://dx.doi.org/10.1016/j.

combustflame.2017.02.035. URL http://www.sciencedirect.com/science/article/pii/S0010218017300822.

[37] Chrigui, M., Gounder, J., Sadiki, A., Masri, A. R., and Janicka, J. "Partially premixed reacting acetone spray using LES and FGM tabulated chemistry." *Combustion and flame*, 159(8):2718–2741, 2012.

[38] Ma, L. and Roekaerts, D. "Modeling of spray jet flame under mild condition with non-adiabatic FGM and a new conditional droplet injection model." *Combustion and Flame*, 165:402 – 423, 2016. ISSN 0010-2180. doi: http://dx.doi.org/10.1016/j.combustflame.2015.12.025. URL http://www.sciencedirect.com/science/article/pii/S001021801500468X.

[39] Domingo, P., Vervish, L., and Bray, K. "Partially premixed flamelets in LES of non-premixed turbulent combustion." *Combustion Theory and Modelling*, 6(4):529–551, 2002.

[40] Knudsen, E. and Pitsch, H. "Modeling partially premixed combustion behavior in multiphase LES." *Combustion and Flame*, 162(1):159 – 180, 2015. ISSN 0010-2180. doi: http://dx.doi.org/10.1016/j.combustflame.2014.07.013. URL http://www.sciencedirect.com/science/article/pii/S0010218014002089.

[41] Franzelli, B., Fiorina, B., and Darabiha, N. "A tabulated chemistry method for spray combustion." *Proceedings of the Combustion Institute*, 34(1):1659 – 1666, 2013. ISSN 1540-7489. doi: https://doi.org/10.1016/j.proci.2012.06.013. URL http://www.sciencedirect.com/science/article/pii/S1540748912001216.

[42] Klimenko, A.Y. and Bilger, R.W. "Conditional moment closure for turbulent combustion." *Progress in Energy and Combustion Science*, 25(6):595 – 687, 1999. ISSN 0360-1285. doi: http://dx.doi.org/10.1016/S0360-1285(99)00006-4. URL http://www.sciencedirect.com/science/article/pii/S0360128599000064.

[43] Zhang, H. and Mastorakos, E. "Prediction of global extinction conditions and dynamics in swirling non-premixed flames using LES/CMC modelling." *Flow, Turbulence and Combustion*, 96(4):863–889, Jun 2016. ISSN 1573-1987. doi: 10.1007/s10494-015-9689-y. URL https://doi.org/10.1007/s10494-015-9689-y.

[44] Giusti, A. and Mastorakos, E. "Detailed chemistry LES/CMC simulation of a swirling ethanol spray flame approaching blow-off." *Proceedings of the Combustion Institute*, 36(2):2625 – 2632, 2017. ISSN 1540-7489. doi: http://dx.doi.org/10.1016/j.proci.2016.06.035. URL http://www.sciencedirect.com/science/article/pii/S1540748916300931.

[45] Klimenko, A.Y. and Pope, S.B. "The modeling of turbulent reactive flows based on multiple mapping conditioning." *Physics of Fluids*, 15(7):1907–1925, 2003.

[46] Knudsen, E. and Pitsch, H. "A general flamelet transformation useful for distinguishing between premixed and non-premixed modes of combustion." *Combustion and Flame*, 156(3):678 – 696, 2009. ISSN 0010-2180. doi: http://dx.doi.org/10.1016/j.combustflame.2008.10.021. URL http://www.sciencedirect.com/science/article/pii/S0010218008003246.

[47] Patel, N. and Menon, S. "Simulation of spray–turbulence–flame interactions in a lean direct injection combustor." *Combustion and Flame*, 153(1):228 – 257, 2008. ISSN 0010-2180. doi: http://dx.doi.org/10.1016/j.combustflame.2007.09.011. URL http://www.sciencedirect.com/science/article/pii/S0010218007002647.

[48] Moin, P. and Apte, S. V. "Large-Eddy Simulation of realistic gas turbine combustors." *American Institute of Aeronautics and Astronautics Journal*, 2006.

[49] Prasad, V.N., Masri, A.R., Navarro-Martinez, S., and Luo, K.H. "Investigation of auto-ignition in turbulent methanol spray flames using Large-Eddy Simulation." *Combustion and Flame*, 160(12):2941 – 2954, 2013. ISSN 0010-2180. doi: http://dx.doi.org/10.1016/j.combustflame.2013.07.004. URL http://www.sciencedirect.com/science/article/pii/S0010218013002629.

[50] Chaussonnet, G., Vermorel, O., Riber, E., and Cuenot, B. "A new phenomenological model to predict drop size distribution in Large-Eddy Simulations of airblast atomizers." *International Journal of Multiphase Flow*, 80:29 – 42, 2016. ISSN 0301-9322. doi: http://dx.doi.org/10.1016/j.ijmultiphaseflow.2015.10.014. URL http://www.sciencedirect.com/science/article/pii/S0301932215002566.

[51] Gepperth, S., Barow, E., Koch, R., and Bauer, H.J. Primary atomization of prefilming airblast nozzles: Experimental studies using

advanced image processing techniques. In *26th Annual Conference on Liquid Atomization and Spray Systems, (ILASS Europe), Bremen, Germany, Sept*, pages 8–10, 2014.

[52] Sanjosé, M., Senoner, J.M., Jaegle, F., Cuenot, B., Moreau, S., and Poinsot, T. "Fuel injection model for Euler–Euler and Euler–Lagrange Large-Eddy Simulations of an evaporating spray inside an aeronautical combustor." *International Journal of Multiphase Flow*, 37(5):514 – 529, 2011. ISSN 0301-9322. doi: http://dx.doi.org/10.1016/j.ijmultiphaseflow.2011.01.008. URL `http://www.sciencedirect.com/science/article/pii/S0301932211000280`.

[53] Fuster, D., Bagué, A., Boeck, T., Moyne, L. Le, Leboissetier, A., Popinet, S., Ray, P., Scardovelli, R., and Zaleski, S. "Simulation of primary atomization with an octree adaptive mesh refinement and VOF method." *International Journal of Multiphase Flow*, 35(6): 550 – 565, 2009. ISSN 0301-9322. doi: http://dx.doi.org/10.1016/j.ijmultiphaseflow.2009.02.014. URL `http://www.sciencedirect.com/science/article/pii/S0301932209000305`.

[54] Herrmann, M., Arienti, M., and Soteriou, M. "The impact of density ratio on the liquid core dynamics of a turbulent liquid jet injected into a crossflow." *ASME J. Gas Turb. Pwr*, 133(6):061501–9, 2011. ISSN 0742-4795.

[55] Ishimoto, J., Hidehiro, H., Tadashi, T., Hideyuki, W., Asako, H., and Fuminori, S. "Integrated simulation of the atomization process of a liquid jet through a cylindrical nozzle." *Interdisciplinary Information Sciences*, 13(1):7–16, 2007. doi: 10.4036/iis.2007.7.

[56] Gorokhovski, M. and Herrmann, M. "Modeling Primary Atomization." *Annual Review of Fluid Mechanics*, 40(1):343–366, jan 2008.

[57] Vallet, A. and Borghi, R. "Modélisation eulerienne de l'atomisation d'un jet liquide." *Comptes Rendus de l'Académie des Sciences - Series IIB - Mechanics-Physics-Astronomy*, 327(10):1015 – 1020, 1999. ISSN 1287-4620.

[58] Vallet, A., Burluka, A. A., and Borghi, R. "Development of a eulerian model for the atomization of a liquid jet." *Atomization and Sprays*, 11(6):619–642, 2001. ISSN 1044-5110.

[59] Lebas, R. *Modélisation Eulérienne de l'Atomisation Haute Pression-Influences sur la Vaporisation et la Combustion Induite*. PhD thesis, Université de Rouen, 2007.

[60] Lebas, R., Menard, T., Beau, P.A., Berlemont, A., and Demoulin, F.X. "Numerical simulation of primary break-up and atomization: DNS and modelling study." *International Journal of Multiphase Flow*, 35(3):247 – 260, 2009. ISSN 0301-9322.

[61] Blanco, A. P. *Implementation and Development of an Eulerian Spray Model for CFD simulations of diesel Spray*. PhD thesis, Universitat Politécnica de Valéncia, 2016.

[62] Mazzei, L., Puggelli, S., Bertini, D., Andreini, A., Facchini, B., Vitale, I., and Santoriello, A. Numerical and experimental investigation on an effusion-cooled lean burn aeronautical combustor: Temperature profiles and emissions. In *Proceedings of ASME Turbo Expo 2018, Paper No. GT2018-76765*. American Society of Mechanical Engineers, 2018.

[63] Bertini, D., Mazzei, L., Puggelli, S., Andreini, A., Facchini, B., Bellocci, L., and Santoriello, A. Numerical and experimental investigation on an effusion-cooled lean burn aeronautical combustor: aerothermal field and metal temperature. In *Proceedings of ASME Turbo Expo 2018, Paper No. GT2018-76779*. American Society of Mechanical Engineers, 2018.

[64] Sagaut, P., Adams, N., and Garnier, E. *Large Eddy Simulation for Compressible Flows*. Springer book, 2009.

[65] Lilly, D.K. "A proposed modification of the Germano subgrid-scale closure method." *Physics of Fluids A: Fluid Dynamics (1989-1993)*, 4(3):633–635, 1992.

[66] Koch, R. "Spray combustion." *In Turbulent combustion,Lecture Series 2011-03, Von Karman Institute for Fluid Dynamics*.

[67] Kralj, C. *Numerical Simulation Of Diesel Spray Processes*. PhD thesis, University of London, 1995.

[68] Morsi, S.A. and Alexander, A.J. "An investigation of particle trajectories in two-phase flow systems." *Journal of Fluid Mechanics*, 55(02):193–208, 1972.

[69] Abramzon, B. and Sirignano, W.A. "Droplet vaporization model for spray combustion calculations." *International journal of heat and mass transfer*, 32(9):1605–1618, 1989.

[70] Sazhin, S.S. "Advanced models of fuel droplet heating and evaporation." *Progress in energy and combustion science*, 32(2):162–214, 2006.

[71] Gosman, A. D. and Ioannides, E. "Aspects of computer simulation of liquid-fuelled combustors." *Journal of Energy*, 1983.

[72] Ramaekers, W.J.S., Albrecht, B.A., van Oijen, J.A., de Goey, L.P.H., and Eggels, R.G.L.M. "The application of flamelet generated manifolds in modelling of turbulent partially premixed flames." *Proceedings of the Fluent Benelux User Group Meeting*, 2005.

[73] Donini, A., Bastiaans, R. J. M., Van Oijen, J. A., and de Goey, L. P. H. The Implementation of Five-Dimensional FGM Combustion Model for the Simulation of a Gas Turbine Model Combustor. In *Proc. ASME Turbo Expo*, number GT2015-42037, June 2015.

[74] Ansys, Fluent. *15.0 Theory Guide*. 2013.

[75] Masri, A.R. and Gounder, J.D. Details and complexities of boundary conditions in turbulent piloted dilute spray jets and flames. In *Experiments and Numerical Simulations of Diluted Spray Turbulent Combustion*, pages 41–68. Springer, 2011.

[76] Gounder, J.D., Kourmatzis, A., and Masri, A.R. "Turbulent piloted dilute spray flames: Flow fields and droplet dynamics." *Combustion and flame*, 159(11):3372–3397, 2012.

[77] Ukai, S., Kronenburg, A., and Stein, O. LES-CMC of a dilute acetone spray flame with pre-vapor using two conditional moments. In *Proc. 6th Europ. Combust. Meeting, Lund*, 2013.

[78] Rittler, A., Proch, F., and Kempf, A. M. "LES of the sydney piloted spray flame series with the PFGM/ATF approach and different subfilter models." *Combustion and Flame*, 162(4):1575–1598, 2015.

[79] Puggelli, S., Bertini, D., Andreini, A., and Facchini, B. "Large-Eddy Simulation of a turbulent spray flame using the Flamelet Generated Manifold approach." *Energy Procedia*, 82:395 – 401, 2015. ISSN 1876-6102.

[80] Bertini, D. Large Eddy Simulation of turbulent spray flames. Master's thesis, University Of Florence, 2014. URL `https://sol.unifi.it/tesi/consultazione`. Relators: S.Puggelli, L.Mazzei, A. Andreini, B.Facchini.

[81] Reid, R.C., Prausnitz, J.M., and Poling, B.E. *The properties of gases and liquids*. McGraw Hill Book Co., New York, NY, 1987.

[82] Smirnov, A., Shi, S., and Celik, I. "Random flow generation technique for Large-Eddy Simulations and particle-dynamics modeling." *Journal of Fluids Engineering*, 123(2):359–371, 2001.

[83] De, S., Lakshmisha, K.N., and Bilger, R.W. "Modeling of nonreacting and reacting turbulent spray jets using a fully stochastic separated flow approach." *Combustion and Flame*, 158(10):1992–2008, 2011.

[84] Pichon, S., Black, G., Chaumeix, N., Yahyaoui, M., Simmie, J.M., Curran, H.J., and Donohue, R. "The combustion chemistry of a fuel tracer: Measured flame speeds and ignition delays and a detailed chemical kinetic model for the oxidation of acetone." *Combustion and Flame*, 156(2):494–504, 2009.

[85] Pope, S. B. "Ten questions concerning the Large-Eddy Simulation of turbulent flows." *New Journal of Physics*, 35, March 2004.

[86] Sheen, D. *Swirl-stabilised turbulent spray flames in an axisymmetric model combustor*. PhD thesis, Imperial College, 1993.

[87] Puggelli, S., Bertini, D., Andreini, A., and Facchini, B. "Scale adaptive simulations of a swirl stabilized spray flame using flamelet generated manifold." *Energy Procedia*, 101(Supplement C):1143 – 1150, 2016.

[88] Puggelli, S., Bertini, D., Mazzei, L., and Andreini, A. "Modelling strategies for Large-Eddy Simulation of lean burn spray flames." *ASME J Gas Turb Pwr*, 140(5)(GTP-17-1396), 2017.

[89] Jones, W.P., Lyra, S., and Navarro-Martinez, S. "Numerical investigation of swirling kerosene spray flames using Large-Eddy Simulation." *Combustion and Flame*, 159(4):1539 – 1561, 2012. ISSN 0010-2180.

[90] Jones, W.P., Lyra, S., and Navarro-Martinez, S. "Large-Eddy Simulation of turbulent confined highly swirling annular flows." *Flow Turbulence Combustion*, 89:361, 2012.

[91] O'Brien, E.E. *The probability density function (pdf) approach to reacting turbulent flows.* In: Libby P.A., Williams F.A. (eds) Turbulent Reacting Flows. Topics in Applied Physics, vol 44. Springer, Berlin, Heidelberg, 1980.

[92] Jones, W. P., Marquis, A. J., and Vogiatzaki, K. "Large-Eddy Simulation of spray combustion in a gas turbine combustor." *Combustion and Flame*, 161(1):222–239, January 2014.

[93] Lyra, S. *Large-Eddy Simulation of Isothermal and Reacting Sprays.* PhD thesis, Imperial College London, 2010.

[94] Jacek, P. and Apte, S.V. "Filtered particle tracking in isotropic turbulence and stochastic modeling of subgrid-scale dispersion." *International Journal of Multiphase Flow*, 35(2):118 – 128, 2009. ISSN 0301-9322. doi: http://dx.doi.org/10.1016/j.ijmultiphaseflow.2008.10.005. URL `http://www.sciencedirect.com/science/article/pii/S0301932208001511`.

[95] Sankaran, V. and Menon, S. "LES of spray combustion in swirling flows." *Journal of Turbulence*, 3(11):1–23, 2002.

[96] Fossi, A., DeChamplain, A., Paquet, B., Kalla, S., and Bergthorson, J. M. Scale-Adaptive and Large-Eddy Simulations of a turbulent spray flame in a scaled swirl-stabilized gas turbine combustor using strained flamelets. In *Proc. ASME Turbo Expo*, number GT2015-42535. American Society of Mechanical Engineers, 2015.

[97] Saha, A., Lee, J.D., and Basu, R. S.and Kumar. "Breakup and coalescence characteristics of a hollow cone swirling spray." *Physics of fluids*, 24(12):124103, 2012.

[98] Sirjean, B., Dames, E., Sheen, D. A., Wang, H., Lu, T. F., and Law, T. F. Jetsurf 1.0-ls: Simplified chemical kinetic models for high-temperature oxidation of C5 to C12 n-Alkanes. Technical report, http://melchior.usc.edu/JetSurF1.0/JetSurF1.0-ls, 2009.

[99] Smith, T.F., Shen, Z.F., and Friedman, J.N. "Evaluation of coefficients for the weighted sum of gray gases model." *J Heat Transf*, 602-8:159 – 180, 1982.

[100] Freitag, S., Meier, U., Heinze, J., Behrendt, T., and Hassa, C. Measurement of initial conditions of a kerosene spray from a generic aeroengine injector at elevated pressure. In *23rd Annual Conference on Liquid Atomization and Spray Systems, (ILASS Europe)*, 2010.

[101] Meier, U., Heinze, J., Freitag, S., and Hassa, C. "Spray and flame structure of a generic injector at aeroengine conditions." *ASME J Gas Turb Pwr*, 134(031503), March 2012.

[102] Puggelli, S., Bertini, D., Mazzei, L., and Andreini, A. "Assessment of scale-resolved computational fluid dynamics methods for the investigation of lean burn spray flames." *ASME J Gas Turb Pwr*, 139(2)(GTP-16-1237), 2016.

[103] Puggelli, S., Paccati, S., Bertini, D., Mazzei, L., Andreini, A., and Giusti, A. "Multi-coupled numerical simulations of the DLR Generic Single Sector Combustor." *Accepted for Combustion Science and Technology, Transaction from Tenth Mediterranean Combustion Symposium*, 2017.

[104] Jones, W. P., Marquis, A. J., and Vogiatzaki, K. Deliverable D3.2.4: Report on LES results of the DLR experiment of task 2.3. Technical report, Imperial College, 2010.

[105] Menter, F.R. and Egorov, Y. "Flow turbulence combustion." *The Scale-Adaptive Simulation Method for Unsteady Turbulent Flow Predictions. Part 1: Theory and Model Description*, 85(113), 2010.

[106] Joseph, D., Belanger, J., and Beavers, G.S. "Breakup of a liquid drop suddenly exposed to a high-speed airstream." *International Journal of Multiphase Flow*, 25(6):1263–1303, 1999.

[107] Rachner, M. Die Stoffeigenschaften von Kerosin Jet A-1. Technical report, DLR, Institut für Antriebstechnik, März 1998.

[108] Wang, G., Boileau, M., and Veynante, D. "Implementation of a dynamic thickened flame model for Large-Eddy Simulations of turbulent premixed combustion." *Combustion and Flame*, 158 (11):2199–2213, November 2011. ISSN 0010-2180. doi: 10.1016/j.combustflame.2011.04.008.

[109] Zimont, V., Polifke, W., Bettelini, M., and Weisenstein, W. "An Efficient Computational Model for Premixed Turbulent Combustion at High Reynolds Numbers Based on a Turbulent Flame Speed Closure." *ASME J Gas Turb Pwr*, 120(3):526–532, July 1998.

[110] Westbrook, C. K. and Dryer, F. L. "Simplified reaction mechanisms for the oxidation of hydrocarbon fuels in flames." *Combustion science and technology*, 27(1-2):31–43, 1981.

[111] Moghaddas, A., Eisazadeh-Far, K., and Metghalchi, H. "Laminar burning speed measurement of premixed n-decane/air mixtures using spherically expanding flames at high temperatures and pressures." *Combustion and Flame*, 159(4):1437 – 1443, 2012. ISSN 0010-2180.

[112] Nakod, P. and Yadav, R. Numerical computation of a turbulent lifted flame using flamelet generated manifold with different progress variable definitions. In *Proc. India ASME Turbo Expo*, number GTINDIA2015-1406. American Society of Mechanical Engineers, 2015.

[113] Domingo, P., Vervisch, L., and Réveillon, J. "DNS analysis of partially premixed combustion in spray and gaseous turbulent flame-bases stabilized in hot air." *Combustion and Flame*, 140(3):172–195, February 2005.

[114] Giusti, A. *Development of numerical tools for the analysis of advanced airblast injection systems for lean burn aero-engine combustors*. PhD thesis, Department of Industrial Engineering of University of Florence, 2013.

[115] Magnussen, Bjørn F and Hjertager, BW. On the structure of turbulence and a generalized eddy dissipation concept for chemical reaction in turbulent flow. In *19th AIAA Aerospace Meeting, St. Louis, USA*, 1981.

[116] Magnussen, B. F. The eddy dissipation concept: a bridge between science and technology. In *ECCOMAS Thematic Conference on Computational Combustion*, 2005.

[117] Shinjo, J. and Umemura, A. "Surface instability and primary atomization characteristics of straight liquid jet sprays." *International Journal of Multiphase Flow*, 37(10):1294 – 1304, 2011. ISSN 0301-9322.

[118] Williams, F. A. "Spray combustion and atomization." *Physics of Fluids*, 1(6):541–545, 1958. URL `http://scitation.aip.org/content/aip/journal/pof1/1/6/10.1063/1.1724379`.

[119] Bird, G.A. *Molecular gas dynamics and the direct simulation of gas flows*. Oxford University Press, 1994.

[120] Ham, F., Apte, S., Iaccarino, G., Wu, X., and Herrmann, M. Unstructured LES of reacting multiphase flows in realistic gas turbine combustors. Technical report, Center for Turbulence Research Annual Research Briefs, 2003.

[121] Laurent, F. and Massot, M. "Multi-fluid modelling of laminar polydisperse spray flames: origin, assumptions and comparison of sectional and sampling methods." *Combustion Theory and Modelling*, 5(4):537–572, 2001.

[122] Yuan, C., Laurent, F., and Fox, R.O. "An extended quadrature method of moments for population balance equations." *Journal of Aerosol Science*, 51:1 – 23, 2012. ISSN 0021-8502.

[123] Essadki, M., De Chaisemartin, S., Laurent, F., and Massot, M. "High Order Moment Model for Polydisperse Evaporating Sprays Towards Interfacial Geometry." *ArXiv e-prints*, 1608, 2016. URL `http://adsabs.harvard.edu/abs/2016arXiv160807148E`.

[124] Drew, D.A. and Passman, S.L. *Theory of Multicomponent Fluids*. Springer-Verlag New York, 1999.

[125] Sagaut, P., Adams, N., and Garnier, E. *Large Eddy Simulation for Incompressible Flows*. Springer book, 1998.

[126] Chesnel, J. *Simulation aux Grandes Échelles de l'Atomisation. Application á l'Injection Automobile.* PhD thesis, University of Rouen, 2010.

[127] Hecht, N. *Simulation aux grandes échelles des écoulements liquide-gaz : application à l'atomisation*. PhD thesis, University of Rouen, 2014.

[128] Herrmann, M. "Detailed numerical simulations of the primary atomization of a turbulent liquid jet in crossflow." *ASME J. Gas Turb. Pwr*, 132(6):061506.1–10, 2010.

[129] Dabonneville, F., Reveillon, J., Hecht, N., Pinon, G., Rivoalen, E., and Demoulin, F.X. A zonal grid method for liquid atomization modeling using OpenFOAM. 12th OpenFOAM Workshop, 2017.

[130] Chesnel, J., Reveillon, J., Menard, T., and Demoulin, F.X. "Large Eddy Simulation of liquid jet atomization." *Atomization and Sprays*, 21(9):711–736, 2011. ISSN 1044-5110.

[131] Vaudor, G., Ménard, T., Aniszewski, W., Doring, M., and Berlemont, A. "A consistent mass and momentum flux computation method for two phase flows. Application to atomization process." *Computers & Fluids*, 152:204–216, July 2017. ISSN 0045-7930. doi: 10.1016/j.compfluid.2017.04.023. URL `http://www.sciencedirect.com/science/article/pii/S0045793017301494`.

[132] Rusche, H. *Computational Fluid Dynamics of Dispersed Two-Phase Flows at High Phase Fractions*. PhD thesis, Imperial College of Science, Technology and Medicine, 2002.

[133] Ishii, M. and Hibiki, T. *Thermo-Fluid Dynamics of Two-Phase Flow*. Springer-Verlag, 1975.

[134] Demoulin, F. X., Reveillon, J., Duret, B., Bouali, Z., Desjonqueres, P., and Menard, T. "Toward using Direct Numerical Simulation to improve primary break-up modeling." *Atomisation and Sprays*, 23(11):957–980, 2013.

[135] Morel, C. "On the surface equations in two-phase flows and reacting single-phase flows." *International Journal of Multiphase Flow*, 33(10):1045 – 1073, 2007. ISSN 0301-9322. doi: http://dx.doi.org/10.1016/j.ijmultiphaseflow.2007.02.008. URL `http://www.sciencedirect.com/science/article/pii/S0301932207000560`.

[136] Iyer, V. and Abraham, J. "An evaluation of a Two-Fluid Eulerian-Liquid Eulerian-Gas Model for Diesel Sprays." *Journal of Fluids Engineering*, 125(10):660 – 669, 2003. ISSN 0301-9322. doi: 10.1115/1.1593708.

[137] Candel, S. M. and Poinsot, T. J. "Flame stretch and the balance equation for the flame area." *Combustion Science and Technology*, 70(1-3):1–15, 1990.

[138] Demoulin, F.X., Beau, P.A., Blokkeel, G., Mura, A., and Borghi, R. "A new model for turbulent flows with large density fluctuations: application to liquid atomization." *Atomization and Sprays*, 17(4): 315–345, 2007. ISSN 1045-5110. doi: 10.1615/AtomizSpr.v17.i4.20.

[139] Vallet, A., Burluka, A. A., and Borghi, R. Development of a Eulerian model for the atomization of a liquid jet, 2001.

[140] Duret, B., Reveillon, J., Menard, T., and Demoulin, F. X. "Improving primary atomization modeling through DNS of two-phase flows." *International Journal of Multiphase Flow*, 55:130–137, 2013.

[141] Chrigui, M. *Eulerian-Lagrangian approach for modeling and simulations of turbulent reactive multi-phase flows under gas turbine combustor conditions*. PhD thesis, Technische Universität Darmstadt, 2005.

[142] Faeth, G. M. "Current status of droplet and liquid combustion." *Progress in Energy and Combustion Science*, 3(4):191–224, 1977.

[143] Ranz, W.E. and Marshall, W.R. "Evaporation from drops." *Chem. Eng. Prog*, 48(3):141–146, 1952.

[144] Borman, G. L. and Johnson, J. H. Unsteady vaporization histories and trajectories of fuel drops injected into swirling air. In *SAE Technical Paper*. SAE International, 1962. doi: 10.4271/620271.

[145] Thibaut, M. *Développement d'une méthode Level Set pour le suivi d'interface. Application de la rupture de jet liquide*. PhD thesis, Université de Rouen, 2007.

[146] Ménard, T., Tanguy, S., and Berlemont, A. "Coupling level set/VOF/ghost fluid methods: Validation and application to 3D simulation of the primary break-up of a liquid jet." *International Journal of Multiphase Flow*, 33(5):510–524, May 2007. ISSN 03019322. doi: 10.1016/j.ijmultiphaseflow.2006.11.001.

[147] Hecht, N., Puggelli, S., Demoulin, F.X., and Reveillon, J. Towards general purpose LES model of atomization. In *Proceedings of 9th International Conference on Multiphase Flows*, 2016.

[148] Anez, J., Puggelli, S., Hecht, N., Reveillon, J., Demoulin, F.X., and Andreini, A. *11th OpenFOAM workshop book*, chapter : Liquid atomization modelling in OpenFOAM. Springer International Publishing, 2017.

[149] Ahmed, A., Anez, J., de Motta, J. B., Puggelli, S., Reveillon, J., and Demoulin, F.X. Subgrid liquid flux and interface modelling of atomization. In *28th Conference on Liquid Atomization and Spray System, (ILASS-Europe), Paper No. 4694*, 2017.

[150] Hoyas, S., Gil, A., Margot, X., Khuong-Anh, D., and Ravet, F. "Evaluation of the Eulerian–Lagrangian Spray Atomization (ELSA) model in spray simulations: 2D cases." *Mathematical and Computer Modelling*, 57(7-8):1686–1693, apr 2013.

[151] García-Oliver, J. M., Pastor, J. M., Pandal, A., Trask, N., Baldwin, E., and Schmidt, D. P. "Diesel spray CFD simulations based on the Σ-Y eulerian atomization model." *Atomization and Sprays*, 23(1):71–95, 2013.

[152] Desantes, J. M., Garcia-Oliver, J. M., Pastor, J. M., and Pandal, A. "A comparison of diesel sprays CFD modeling approaches: Ddm versus Σ-Y eulerian atomization model." *Atomization and Sprays*, 26(7), 2016.

[153] Moulai, M., Grover, R., Parrish, S., and Schmidt, D. Internal and near-nozzle flow in a multi-hole gasoline injector under flashing and non-flashing conditions. In *SAE Technical Paper*. SAE International, 04 2015. doi: 10.4271/2015-01-0944.

[154] Xue, Q., Battistoni, M., Powell, C.F., Longman, D.E., Quan, S.P., Pomraning, E., Senecal, P.K., Schmidt, D.P., and Som, S. "An eulerian CFD model and x-ray radiography for coupled nozzle flow and spray in internal combustion engines." *International Journal of Multiphase Flow*, 70:77 – 88, 2015. ISSN 0301-9322. doi: https://doi.org/10.1016/j.ijmultiphaseflow.2014.11.012. URL `https://www.sciencedirect.com/science/article/pii/S0301932214002328`.

[155] Deutsch, E. and Simonin, O. "Large Eddy Simulation applied to the motion of particles in stationary homogeneous fluid turbulence." *Turbulence Modification in Multiphase Flows-ASME FED*, 110(35), 1991.

[156] Simonin, O. "Statistical and continuum modelling of turbulent reactive particulate flows." *Lecture Series 1996-02, Von Karman Institute for Fluid Dynamics*, 2000.

[157] Bailly, P., Champion, M., and Garréton, D. "Counter-gradient diffusion in a confined turbulent premixed flame." *Physics of Fluids (1994-present)*, 9(3):766–775, March 1997. ISSN 1070-6631, 1089-7666.

[158] Beau, P.A. *Modelisation de l'atomisation d'un jet liquide. Application aux sprays Diesel*. PhD thesis, University of Rouen, France, 2006.

[159] Andreini, A., Bianchini, C., Caciolli, G., Facchini, B., Giusti, A., and Turrini, F. Multi-coupled numerical analysis of advanced lean burn injection systems. In *Proc. ASME Turbo Expo*, number GT2014-26808, 2014.

[160] Andreini, A., Bianchini, C., Puggelli, S., and Demoulin, F.X. "Development of a turbulent liquid flux model for Eulerian–Eulerian multiphase flow simulations." *International Journal of Multiphase Flow*, 81:88 – 103, 2016. ISSN 0301-9322. doi: http://dx.doi.org/10.1016/j.ijmultiphaseflow.2016.02.003. URL `http://www.sciencedirect.com/science/article/pii/S0301932216300817`.

[161] Babinsky, E. and Sojka, P.E. "Modeling drop size distributions." *Progress in Energy and Combustion Science*, 28(4):303 – 329, 2002. ISSN 0360-1285. doi: http://dx.doi.org/10.1016/S0360-1285(02)00004-7. URL `http://www.sciencedirect.com/science/article/pii/S0360128502000047`.

[162] Dumouchel, C. "A new formulation of the maximum entropy formalism to model liquid spray drop-size distribution." *Particle & Particle Systems Characterization*, 23(6):468–479, 2006. ISSN 1521-4117. doi: 10.1002/ppsc.200500989. URL `http://dx.doi.org/10.1002/ppsc.200500989`.

[163] Drew, D.A. "Mathematical modelling of two-phase flow." *Annual review of fluid mechanics*, 1983.

[164] Simonin, O. "Continuum modelling of dispersed turbulent two phase flows." *Combustion and turbulence in two-phase flow, Lecture Series 1996-02., Von Karman Institute for Fluid Dynamics*, 1996.

[165] Beau, P.A., Funk, M., Lebas, R., and Demoulin, F.X. Applying Quasi-Multiphase Model to simulate atomization processes in diesel engines: Modeling of the slip velocity. Technical Report 2005-01-0220, SAE International, April 2005.

[166] Rusche, H. *Computational Fluid Dynamics of dispersed two-phase flows at high phase fractions*. PhD thesis, Imperial College of London, England, 2002.

[167] Garcia-Oliver, J. M., Pastor, J. M., Pandal, A., Trask, N., Baldwin, E., and Schmidt, D. P. "Diesel spray CFD simulations based on the Σ-Y Eulerian atomization model." *Atomization and Sprays*, 23(1):71–95, 2013. ISSN 1044-5110.

[168] Pandal, A., Pastor, J.M., García-Oliver, J.M., Baldwin, E., and Schmidt, D.P. "A consistent, scalable model for Eulerian spray modeling." *International Journal of Multiphase Flow*, 83:162 – 171, 2016. ISSN 0301-9322. doi: http://dx.doi.org/10.1016/j.ijmultiphaseflow.2016.04.003. URL `http://www.sciencedirect.com/science/article/pii/S030193221530210X`.

[169] Brown, C.T. and McDonell, V.G. "Near field behaviour of a liquid jet in a crossflow." *19th Annual Conference on Liquid Atomization and Sprays systems, (ILASS Americas), Canada*, 2006.

[170] Wu, P.K., Kirkendall, K. A., Fuller, R. P., and Nejad, A. S. "Breakup processes of liquid jets in subsonic crossflows." *Journal of Propulsion and Power*, 13(1):64–73, 1997. ISSN 0748-4658. doi: 10.2514/2.5151.

[171] Stenzler, J. N., Lee, J. G., Santavicca, D. A., and Lee, W. "Penetration of liquid jets in a cross-flow." *Atomization and Sprays*, 16 (8), 2006.

[172] Launder, B.E., Reece, G., and Rodi, W. "Progress in the development of a Reynolds-stress turbulence closure." *Journal of fluid mechanics*, 68(03):537–566, 1975.

[173] Launder, B.E. and Sharma, B.I. "Application of the energy-dissipation model of turbulence to the calculation of flow near a spinning disc." *Letters in heat and mass transfer*, 1(2):131–137, 1974.

[174] Bianchini, C., Andrei, L., Andreini, A., and Facchini, B. "Numerical Benchmark of Non conventional RANS Turbulence Models for Film and Effusion Cooling." *Journal of Turbomachinery*, 135(4), June 2013. ISSN 0889-504X. doi: 10.1115/1.4007614. URL `http://dx.doi.org/10.1115/1.4007614`.

[175] Lubarsky, E., Zinn, B. T., Shcherbik, D., Bibik, O., and Gopala, Y. *Fuel Jet in Cross Flow-Experimental Study of Spray Characteristics*. INTECH Open Access Publisher, 2012.

[176] Freitag, S. and Hassa, C. Spray characteristics of a kerosene jet in cross flow of air at elevated pressure. In *22nd Annual Conference on Liquid Atomization and Spray Systems, (ILASS-Europe)*, 2008.

[177] Puggelli, S., Mazzei, L., Andreini, A., and Demoulin, F.X. Large Eddy Simulation of a liquid jet in crossflow using a quasi multiphase

eulerian approach for atomization modelling. In *Proceedings of the 1st Global Power and Propulsion Forum, Paper No. GPPF-2017-29*. Global Power and Propulsion Society, 2017.

[178] Kornev, N., Kröger, H., and Hassel, E. "Synthesis of homogeneous anisotropic turbulent fields with prescribed second-order statistics by the random spots method." *International Journal for Numerical Methods in Biomedical Engineering*, 24(10):875–877, 2008.

[179] Xiao-Shu, C., Nai-Ning, W., Jing-Ming, W., and Gang, Z. "Experimental investigation of the light extinction method for measuring aerosol size distributions." *Journal of Aerosol Science*, 23 (7):749 – 757, 1992. ISSN 0021-8502. doi: http://dx.doi.org/10.1016/0021-8502(92)90041-S. URL `http://www.sciencedirect.com/science/article/pii/002185029290041S`.

[180] Kuanfang, R., Feng, X., Xiaoshu, C., and Jean-Marc, D. "Development of a precise and in situ turbidity measurement system." *Chemical Engineering Communications*, 197(2):250–259, 2009. doi: 10.1080/00986440902938865.

[181] Wang, Q., Mondragon, U.M., Brown, C.T., and McDonell, V.G. "Characterization of trajectory, break point, and break point dynamics of a plain liquid jet in a crossflow." *Atomization and Sprays*, 21(3):203–219, 2011. ISSN 1044-5110.

[182] Palanti, L. Development of an evaporation model for the dense spray region in Eulerian-Eulerian multiphase flow simulations. Master's thesis, University Of Florence, 2016. URL `https://sol.unifi.it/tesi/consultazione`. Relators: S.Puggelli, A. Andreini, F.X. Demoulin, B. Facchini.

[183] Abraham, J. and Pickett, L. M. "Computed and Measured Fuel Vapor Distribution in a Diesel Spray." *Atomization and Sprays*, 20 (3):241–250, 2010.

[184] Puggelli, S., Palanti, L., Andreini, A., and Demoulin, F.X. Development of an evaporation model for the dense spray region in eulerian-eulerian multiphase flow simulations. In *28th Conference on Liquid Atomization and Spray System, (ILASS-Europe), Paper No. 4652*, 2017.

[185] Kösters, A. and Karlsson, A. A comprehensive numerical study of diesel fuel spray formation with OpenFOAM. In *SAE Technical Paper 2011-01-0842*, 2011.

[186] Cengel, Y. A. and Boles, M. A. *Thermodynamics: an Engineering Approach 8th Edition*. 2015.

[187] Moran, M. J. and Shapiro, H. N. *Fundamentals of Engineering Thermodynamics*, volume 181. 7 edition, 2006.

[188] Chin, J.S. and Lefebvre, A.H. "The Role of the Heat-up Period in Fuel Drop Evaporation." *International Journal of Turbo and Jet Engines*, 2(4), jan 1985.

[189] ECN. Engine Combustion Network, 2012. URL `https://ecn.sandia.gov/`.

[190] Kastengren, A. L., Tilocco, F. Z., Powell, C. F., Manin, J., Pickett, L. M., Payri, R., and Bazyn, T. "Engine Combustion Network (ECN): measurements of nozzle geometry and hydraulic behavior." *Atomization and Sprays*, 22(12):1011–1052, 2012.

[191] Pandal, A. *Implementation and Development of an Eulerian Spray Model for CFD simulations of diesel Sprays*. PhD thesis, Universitat Politècnica de València, 2016.

[192] Lounnaci, K., Idlahcen, S., Sedarsky, D., Roze, C., Blaisot, J.B., and Demoulin, F.X. "Image processing techniques for velocity, interface complexity, and droplet production measurement in the near-nozzle region of a diesel spray." *Atomization and Sprays*, 25(9):753–775, 2015. ISSN 1044-5110.

[193] Essadki, M., De Chaisemartin, S., Massot, M., Laurent, F., Larat, A., and Jay, S. "Adaptive Mesh Refinement and High Order Geometrical Moment Method for the Simulation of Polydisperse Evaporating Sprays." *Oil & Gas Science and Technology*, 71(5):61, September 2016. ISSN 1294-4475, 1953-8189. doi: 10.2516/ogst/2016012.

[194] Essadki, M., Drui, F., De Chaisemartin, S., Larat, A., Menard, T., and Massot, M. "Statistical modeling of the gas-liquid interface: Toward a unified description of the disperse and separated phases flows." *submitted for International Journal for Multiphase Flow*, page available on HAL, 2017.

[195] Dumouchel, C., Aniszewski, W., Vu, T.T., and Ménard, T. "Multiscale analysis of simulated capillary instability." *International Journal of Multiphase Flow*, 92:181–192, June 2017. ISSN 03019322. doi: 10.1016/j.ijmultiphaseflow.2017.03.012.

[196] Sussman, M., Smith, K. M., Hussaini, M. Y., Ohta, M., and Zhi-Wei, R. "A sharp interface method for incompressible two-phase flows." *Journal of Computational Physics*, 221(2):469–505, February 2007. ISSN 0021-9991. doi: 10.1016/j.jcp.2006.06.020. URL http://www.sciencedirect.com/science/article/pii/S0021999106002981.

[197] Liu, X.D., Fedkiw, R. P., and Kang, M. "A boundary condition capturing method for Poisson's equation on irregular domains." *Journal of Computational Physics*, 160(1):151 – 178, 2000. ISSN 0021-9991. doi: DOI:10.1006/jcph.2000.6444. URL http://www.sciencedirect.com/science/article/B6WHY-45FC8N8-67/2/8150a32474158fecfa1866806f0576f6.

[198] Canu, R., Puggelli, S., Duret, B., Essadki, M., Massot, M., Ménard, T., Reveillon, J., and Demoulin, F.X. Where does the drop size distribution come from? In *28th Conference on Liquid Atomization and Spray System, (ILASS-Europe), Paper No. 4706*, 2017.

[199] Kindlmann, G., Whitaker, R., Tasdizen, T., and Moller, T. Curvature-based transfer functions for direct volume rendering: Methods and applications. In *Visualization, 2003. VIS 2003. IEEE*, pages 513–520. IEEE, 2003.

[200] Meyer, M., Desbrun, M., Schröder, P., Barr, A. H., and others. "Discrete differential-geometry operators for triangulated 2-manifolds." *Visualization and mathematics*, 3(2):52–58, 2002.

[201] Duret, B., Luret, G., Reveillon, J., Menard, T., Berlemont, A., and Demoulin, F.X. "DNS analysis of turbulent mixing in two-phase flows." *International Journal of Multiphase Flow*, 40:93 – 105, 2012. ISSN 0301-9322. doi: http://dx.doi.org/10.1016/j.ijmultiphaseflow.2011.11.014. URL http://www.sciencedirect.com/science/article/pii/S0301932211002448.